

# **Material Interactions in a Novel Refill Friction Stir Spot Welding Approach to Joining Al-Al and Al-Mg Automotive Sheets**

---

A thesis submitted to the University of Manchester for the degree of Doctor  
of Philosophy in the Faculty of Sciences and Engineering

2016

BY

Basem Mohysen Mohammed Al-Zubaidy

---

SCHOOL OF MATERIALS



## **Contents**

Contents .....	3
List of Tables.....	7
List of Figures .....	8
List of Abbreviations.....	15
Abstract .....	16
Associated Publications .....	17
Declaration .....	18
Copyright .....	19
Acknowledgements .....	20
Chapter 1: Introduction .....	23
1.1 The Effects of Automobiles on Global Warming (Greenhouse Gas Emissions) ..	23
1.2 Lightweight Materials in Automobile Body Applications.....	25
1.2.1 Influence on Emissions .....	25
1.2.2 Multi-Material Automotive Structures.....	30
1.3 Objectives of this Study .....	35
1.4 Thesis Overview.....	36
Chapter 2: Literature Review .....	37
2.1 Introduction .....	37
2.2 Joining Overview .....	37
2.3 Fusion Spot Welding.....	39
2.3.1 Resistance Spot Welding (RSW) .....	39
2.3.2 Laser Welding .....	42
2.4 Mechanical Fastening.....	45
2.4.1 Self-Piercing Riveting .....	45
2.4.2 Clinching .....	46
2.5 Solid State Spot Welding .....	47
2.5.1 Ultrasonic welding (USW).....	47
2.6 Friction Stir Spot Welding (FSSW) Techniques.....	50
2.6.1 Background: Friction Stir Welding (FSW) .....	50
2.6.2 Friction Stir Spot Welding (FSSW) .....	54
2.6.3 Refill Friction Stir Spot Welding (RFSSW) .....	58
2.7 Heat Generation in FSSW and RFSSW .....	61
2.8 Effects of Welding Parameters on the RFSSW process.....	68
2.9 Material Flow in FSSW and RFSSW .....	72

2.10 Microstructure Formation and Weld Defects in Al-Al Similar Friction Stir Spot Welds .....	78
2.10.1 Microstructure Formation in Al-Al Similar Welds.....	78
2.10.2 Weld Defects in Al-Al Similar Welds .....	80
2.11 Microstructure Formation of Dissimilar Al-Mg Spot Welds.....	83
2.12 Al Alloys .....	86
2.12.1 Overview and Classification of Al Alloys .....	86
2.12.2 Precipitation Hardening of Al Alloys .....	90
2.12.3 Aluminium Alloy AA6111 .....	94
2.12.4 The Microstructures of AA6111 FSSWs .....	97
2.13 Magnesium Alloys .....	99
2.13.1 Overview and Classification of Mg Alloys.....	99
2.13.2 Magnesium Alloy AZ31 .....	103
2.14 Aluminium and Magnesium Intermetallic Compounds.....	106
2.14.1 Al-Mg Binary Phase Diagram.....	106
2.14.2 Gamma Phase.....	107
2.14.3 Beta Phase .....	108
2.14.4 Other Phases.....	109
2.15 FE Modelling of the Mechanical Behaviour of RFSSW Joints .....	110
Chapter 3: Experimental Methods .....	115
3.1 Introduction.....	115
3.2 Materials.....	115
3.2.1 Surface Preparation for Welding.....	116
3.3 Welding Method: Refill Friction Stir Spot Welding (RFSSW) and Modified FSSW .....	116
3.4 Heat Treatments .....	121
3.5 Thermal Measurements.....	121
3.6 Hardness Test.....	123
3.7 Mechanical Testing .....	124
3.8 Metallographic Examination.....	125
3.8.1 Sample Preparation .....	125
3.8.2 Optical Microscopy.....	126
3.8.3 Scanning Electron Microscopy (SEM) .....	126
3.8.4 Energy Dispersive X-ray (EDX).....	128
3.8.5 Electron Backscatter Diffraction (EBSD).....	128
3.8.6 Focused Ion Beam (FIB) Milling.....	129
3.8.7 Transmission Electron Microscopy (TEM) .....	130



3.9 Material Flow during RFSSW .....	131
3.9.1 Sample Preparation for Dissimilar Aluminium Alloy Flow Experiments ...	131
3.9.2 Sample Preparation for X-Ray Tomography .....	132
3.9.3 Description of the X-Ray Computational Tomography Technique (XCT) .	133
3.10 FE Modelling of the Lap Tensile-Shear Test of RFSSW Joints .....	135
Chapter 4: Refill Friction Stir Welding of Al-Al Similar Welding (Results and Discussion).....	137
4.1 Introduction .....	137
4.2 Welding Optimisation .....	137
4.3 Effect of the Process Parameters on Material Flow in Refill Friction Stir Spot Welding and Weld Defects .....	139
4.4 Effect of Welding Variables on the Weld Thermal Field and Thermal History .	158
4.5 Weld Microstructure .....	163
4.6 Effect of Welding Variables on Joint Hardness Profiles in the as-Welded, Naturally Aged, and Artificially Aged Conditions .....	168
4.7 Effect of Welding Variables on Weld Strength .....	176
4.8 Effect of Natural and Artificial Ageing on Weld Strength .....	182
4.9 Weld Fracture Surfaces and Cross-Sections in the As-Welded, Naturally Aged, and Artificially Aged Conditions .....	187
4.10 Summary and Conclusions.....	190
Chapter 5: Refill Friction Stir Welding of Mg-Al Dissimilar and Mg-Mg Similar Welding (Results and Discussion) .....	193
5.1 Introduction .....	193
5.2 Welding Optimisation and RFSSW Modification .....	194
5.3 Effect of Welding Variables on the Weld Thermal Field and Thermal History of Mg-Al Dissimilar Joints.....	196
5.4 Effect of Welding Variables on Joint Hardness Profile of the Mg-Al Dissimilar Weld in the As-Welded Condition.....	201
5.5 Effect of Welding Variables on the Interface Microstructure of the Mg-Al Dissimilar Welds.....	203
5.6 Effect of Welding Variables on the Weld Strength of Mg-Al RFSSWs and Modified RFSSWs .....	212
5.7 Comparison of the Effect of the Tool Rotation Rate on the Strength of Mg-Al and Mg-Mg Modified RFSSWs.....	220
5.8 Weld Failure Modes.....	222
5.9 Summary and Conclusions.....	225
Chapter 6: FE Modelling of the Mechanical Behaviour of Refill Friction Stir Spot Welds (Al-Al and Mg-Al).....	229
6.1 Introduction .....	229

6.1	Model Characteristics.....	229
6.1.1	Geometry and Dimensions of the Similar Al-Al Lap-Shear Specimen and Weld Regions (SZ, HAZ, BM) .....	230
6.1.2	Geometry and Dimensions of Dissimilar Mg-Al Lap-Shear Specimen and Weld Regions (SZ, HAZ, BM) .....	233
6.2	Material Properties .....	235
6.2.1	Al-Al welds .....	235
6.2.2	Mg-Al welds .....	242
6.3	Boundary Loading Conditions in the Model.....	244
6.4	Mesh building.....	245
6.5	Results and Discussion.....	249
6.5.1	As-welded similar Al joints .....	249
6.5.2	Artificially-aged Similar Joints .....	258
6.5.3	Mg-Al Dissimilar Welds .....	264
6.6	Summary and Conclusions.....	270
Chapter 7:	Conclusions and Recommendations for Further Work .....	273
7.1	General Conclusion.....	273
7.1.1	Al to Al similar welds .....	273
7.1.2	Mg to Al dissimilar welds .....	276
7.1.3	FE Model of the Similar and Dissimilar Joints.....	277
7.2	Recommendations for Further Work .....	279
Chapter 8:	References .....	281

(79,971 words)

## **List of Tables**

Table 1-1: Vehicle mass analysis by system and components.....	27
Table 2-1: Properties of pure aluminium, magnesium and iron at their melting points .	41
Table 2-2: Aluminium Alloy Designation Systems .....	88
Table 2-3: Aluminium Association and European Union (EN) Aluminium Alloy Temper Designation System .....	88
Table 2-4: Some of the common aluminium precipitation hardening systems.....	93
Table 2-5: Composition of some of the 6xxx series aluminium alloys used for automotive panel applications.....	95
Table 2-6: Literal symbols for alloying elements in magnesium alloys .....	102
Table 2-7: General divisions of the temper designations for magnesium alloys .....	103
Table 2-8: Composition of magnesium wrought alloys used for sheets and plates .....	104
Table 2-9: Mechanical properties of an AZ31 sheet at room temperature .....	104
Table 3-1: Chemical compositions of the alloys used in this study. ....	116
Table 3-2: Range of welding parameters used in this study. ....	119
Table 4-1: The range of welding parameters used in RFSSW of AA6111 similar joints. .....	139
Table 5-5-1: The range of welding parameters used in the RFSSW and modified RFSSW process for welding AZ31 to AA6111 dissimilar joints. ....	196
Table 6-1: True stress-strain data used for modelling the RFSSW joint in the as-welded condition.....	239
Table 6-2: True stress-strain data used for modelling the RFSSW joint in the paint- baked condition. ....	242
Table 6-3: True stress-strain data used for modelling the AZ31-H24 magnesium alloy in the dissimilar RFSSW joint of Mg-Al. ....	243

## List of Figures

Figure 1-1: Greenhouse gases emitted by transportation.....	24
Figure 1-2: Grams of CO <sub>2</sub> emitted by transportation according to the region and projected future targets.....	25
Figure 1-3: Typical energy consumption during the life cycle of a vehicle .....	26
Figure 1-4: Mercedes-Benz AMG SL63 aluminium body structure .....	29
Figure 1-5: Vehma/Ford MMLV a) Mach I BIW b) Mach II BIW .....	31
Figure 1-6: Schematic illustration of the RFSSW processes .....	34
Figure 2-1: Classes of methods used to join similar and dissimilar materials .....	38
Figure 2-2: Schematic illustration of the resistance spot welding (RSW) process .....	39
Figure 2-3: Schematic illustration of laser welding .....	43
Figure 2-4: Laser weld bonding process .....	45
Figure 2-5: a) Schematic illustration of the self-piercing riveting process; b) Cross-section of two sheets joined by a self-piercing rivet.....	46
Figure 2-6: Schematic illustration of the clinching process.....	46
Figure 2-7: Schematic illustration of the ultrasonic welding (USW) process .....	48
Figure 2-8: The effect of welding time on the cross-sectional appearance of USWs of Al-Al .....	49
Figure 2-9: Schematic diagram of the friction stir welding (FSW) process .....	50
Figure 2-10: Friction stir welding tool.....	51
Figure 2-11: Some selected tools designed at TWI .....	52
Figure 2-12: Schematic illustration of the friction stir spot welding (FSSW) process ...	55
Figure 2-13: The typical macrostructure of a cross-section of a friction stir spot weld. ....	56
Figure 2-14: Failure loads of AA6111-T4 sheets joined using FSSW .....	57
Figure 2-15: Schematic illustration of the friction stir spot welding refilling process ...	57
Figure 2-16: Schematic illustration of the RFSSW tool system .....	59
Figure 2-17: Schematic illustration of the two RFSSW process variants.....	60
Figure 2-18: Constitutive behaviour of an AA6056 during FSW.....	62
Figure 2-19: Temperature cycle during the complete welding process (a) in different distances from the SZ and (b) at a distance of 2.66 mm (Shen, et al., 2015). ....	64
Figure 2-20: (a) Results of the simulated temperature distribution in the RFSSW process for a half weld at the welding time of 3 s and (b) thermal cycles in different tracked positions .....	65
Figure 2-21: Results of the simulated strain rate distribution in an RFSSW process for a welding time of 3 s.....	66
Figure 2-22: A schematic illustration of the RFSSW process with the placement of the thermocouples during the temperature measurements.....	67
Figure 2-23: The temperature profile during RFSSW of an Al-Mg dissimilar joint .....	67
Figure 2-24: The effect of key welding parameters on the tensile shear strength of RFSSW joints.....	69
Figure 2-25: The effect of plunge depth and welding time on the lap shear strength of RFSSW joints.....	70
Figure 2-26: Effect of the RFSSW process parameters on the lap shear strength of AA5754 to AZ31 joints.....	71
Figure 2-27: Interlamellar regions produced during dissimilar Al 5754-Al 6111 FSSW using a threaded pin tool .....	73
Figure 2-28: Schematic illustration of a material flow model during FSSW .....	73

Figure 2-29: Material flow observed with a pinless tool from welds produced with the upper and lower sheets split though the weld centre into dissimilar copper content alloys .....	75
Figure 2-30: X-ray tomography results showing the dished nature developed by the weld interface for welds produced with the pinless tool.....	75
Figure 2-31: Cross-sectional views of a kinematic model after different numbers of tool rotations, for three surface stick-slip conditions .....	76
Figure 2-32: Simulation results of material flow during RFSSW.....	77
Figure 2-33: Material flow in RFSSW during sleeve-plunging.....	78
Figure 2-34: Optical micrograph of the cross-section of an RFSSW joint, of AA6181-T4 .....	79
Figure 2-35: Microhardness profile measured in the middle of the upper sheet at the cross-section of an RFSSW joint of AA6181-T4 .....	80
Figure 2-36: Macrographs of RFSSW joint cross-section showing detrimental weld zone, geometric/metallurgical features and weld defects .....	80
Figure 2-37: Different types of hook defect in RFSSW welds .....	81
Figure 2-38: The effect of welding parameters on the hook height.....	82
Figure 2-39: Cross-section of an Al5754-AZ31 RFSSW joint: (a) as-welded sample, (b) micrographs of the eutectic structure in the IMC layer.....	84
Figure 2-40: (a) Macrograph of an RFSSW joint between AA5754 Al and AZ31 Mg, (b) enlarged microstructures from region 2, and (c) the chemical composition distribution across the interface .....	84
Figure 2-41: Cross-section of an Al5754-AZ31 RFSSW joint.....	85
Figure 2-42: Typical SEM images of (a) the interfacial layers in low- and high-rotational-rate welds; (b) the corresponding interfacial layer in the fractured welds .....	85
Figure 2-43: The increase in aluminium content in North American small vehicles over the last three decades.....	87
Figure 2-44: Typical aluminium alloy applications in an automobile .....	90
Figure 2-45: (a) The Al-rich side of an Al-Cu binary diagram showing GP zone, $\theta''$ and $\theta'$ solvus lines (dotted lines), (b) $\theta$ unit cell, (c) GP zone, (d) $\theta''$ unit cell and (e) $\theta'$ unit cell .....	91
Figure 2-46: Activation energy barriers to the nucleation of precipitate phases in Al-Cu binary alloys .....	93
Figure 2-47: The effect of copper percentage and ageing time on the hardness of Al-Cu binary alloys on ageing at (a) 130°C and (b) 190°C.....	94
Figure 2-48: The pseudo-binary Al-Mg <sub>2</sub> Si system .....	96
Figure 2-49: SEM images showing coarse precipitates of the second phase present in weld zones of the AA6111 FSSW joints .....	98
Figure 2-50: TEM micrographs for: the AA6111 parent material (a) in the T4 condition and (b) after the paint-bake treatment, and from the pinless FSSW joint centre of a 0.5 second dwell-time weld (c) in the as-welded condition, and (d) after the paint-bake treatment.....	99
Figure 2-51: Comparison of the specific stiffness and specific strength of pure Mg with Al and iron .....	100
Figure 2-52: Magnesium production data in the period 1938–2008.....	100
Figure 2-53: Timeline summarising magnesium automotive applications .....	101
Figure 2-54: Schematic of magnesium's hexagonal close-packed (HCP) crystal lattice and major planes .....	102

Figure 2-55: Typical microstructures for an AZ31 sheet.....	104
Figure 2-56: The effects of Al and Zn additions on the mechanical properties of Mg in annealed and hard rolled conditions.....	105
Figure 2-57: Al-Mg equilibrium phase diagrams .....	106
Figure 2-58: The Al-Mg binary phase diagram drawn by Okamoto using calculated data from Murray and experimental results from Su et al .....	107
Figure 2-59: Crystal structure of the gamma phase ( $\text{Al}_{12}\text{Mg}_{17}$ ).....	108
Figure 2-60: Complete unit cell of $\beta\text{-Al}_3\text{Mg}_2$ phase .....	109
Figure 2-61: The middle section of the Mg-Al phase diagram proposed by Su et al ...	109
Figure 2-62: $\epsilon\text{-Al}_{30}\text{Mg}_{23}$ phase crystal structure .....	110
Figure 2-63: The geometric features of the welded joint.....	111
Figure 2-64: The engineering stress-strain curves assumed for the BM, SZ, and TMAZ .....	113
Figure 2-65: Stress distribution in the RFSSW joint under loading .....	113
Figure 2-66: Finite-element model of a FSSW joint with 5 different material property regions.....	114
Figure 3-1: The refill friction stir spot welding machine.....	117
Figure 3-2: Typical monitoring chart for the RFSSW process. ....	117
Figure 3-3: Welding head for the RFSSW process.....	118
Figure 3-4: The RFSSW tool parts. ....	118
Figure 3-5: The RFSSW machine variable control table.....	119
Figure 3-6: Schematic illustration of the modified RFSSW process .....	120
Figure 3-7: Schematic illustration of the different thermocouple locations for AA6111 similar welding.....	122
Figure 3-8: Schematic illustration of the thermocouple location for the dissimilar AZ31-H24 to AA6111-T4 welding. ....	122
Figure 3-9: Schematic illustration of the locations of the microhardness measurements .....	123
Figure 3-10: Schematic of the Vickers Microhardness indentation test. ....	124
Figure 3-11: Schematic illustration of lap-shear test specimens.....	125
Figure 3-12: Effects produced by the electron beam–specimen interaction .....	127
Figure 3-13: Schematic diagram illustrating the FIB procedure of TEM sample preparation .....	130
Figure 3-14: Schematic diagram illustrating the TEM optical system .....	131
Figure 3-15: Schematic illustration of one of the material flow sample alignments ....	132
Figure 3-16: Schematic illustration of the alignment for the X-ray Tomography sample .....	133
Figure 3-17: (a) Principle of X-ray tomography; (b) synchrotron and laboratory tomography .....	134
Figure 4-1: The effect of plunge time and tool rotation rate on the weld surface appearance and the completeness of the refilling process. ....	139
Figure 4-2: The output of the kinematic model, showing the surface velocity profile by assuming complete sticking .....	141
Figure 4-3: Effect of weld plunge depth and process interruption on the material flow .....	143
Figure 4-4: Effect of sleeve plunge depth and process interruption on material flow in the lower sheet .....	144

Figure 4-5: Cross-section of an AA6111 similar interrupted RFSSW, showing the joint interface flow in the upper sheet .....	145
Figure 4-6: The results of X-ray tomography showing the distribution of gold at the weld interface, for interrupted welds .....	147
Figure 4-7: A schematic diagram indicating the material flow during the plunging stage .....	149
Figure 4-8: Effect of welding parameters on the material flow .....	151
Figure 4-9: Development of the shape of the weld line as a function of plunge depth with 1.0 s welding time and 2000 rpm tool rotation rate .....	153
Figure 4-10: Hook development as a function of plunge depth.....	154
Figure 4-11: The effect of plunge depth on hook height .....	154
Figure 4-12: The results of X-ray tomography showing the distribution of gold at the weld interface for welds produced with 2000 rpm tool rotation rate.....	155
Figure 4-13: A schematic diagram indicating the material flow during the retraction stage.....	157
Figure 4-14: Typical temperature history curve recorded for the welding process .....	159
Figure 4-15: Thermal histories at different distances from the weld centre for RFSSW .....	161
Figure 4-16: The relationship between peak temperature, rotation rate, and distance from the centre of RFSSW .....	162
Figure 4-17: (a) Typical macrostructure of a RFSSW joint cross-section (0.55 s, 2000 rpm, and 1.0 mm .....	164
Figure 4-18: (a) Band contrast map at the weld edge for a sample welded with a 2500 rpm and 2.0 s, showing the main three regions SZ, TMAZ, and HAZ; (b) an EDS line scan data for the yellow line shown in (a); and (c) x-direction IPF coloring orientation map from the same region as (a). .....	166
Figure 4-19: SEM (BSE) images for a sample welded with a 2500 rpm and 2.0 s: (a) OM image for the full joint; (b) HAZ in the as-welded condition; (c) artificially aged at 180 °C for 30 min. at the same location as (b); and (d) the parent material also artificially aged at 180 °C for 30 min., for comparison. ....	167
Figure 4-20: Hardness profiles of welds produced with different tool rotation rates and welding times, measured immediately after welding.....	170
Figure 4-21: The relationship between the welding time and the average hardness at the weld centre after welding with different tool rotation rates, measured immediately after welding.....	171
Figure 4-22: The effect of welding time on the width of the HAZ, measured immediately after welding.....	172
Figure 4-23: Hardness profiles for samples naturally aged for 30 days .....	174
Figure 4-24: The average hardness of the weld zone centre of the upper sheet. The samples were naturally aged for 30 days. ....	175
Figure 4-25: Hardness profiles of AA6111 RFSSWs produced with 1500 rpm, 1.0 s and 1.0 mm, immediately after welding and after artificial ageing at 180 °C for 30 min. ..	176
Figure 4-26: Example of load-extension curves for the tensile lap-shear test of RFSSW joints in the as-welded condition.....	177
Figure 4-27: Effect of welding time and sleeve plunge depth on the joints' average lap-shear test peak load, in the as-welded condition .....	179
Figure 4-28: Effect of welding time and sleeve plunge depth on the average fracture energy of the joints in the as-welded condition .....	181

Figure 4-29: Example of load-extension curves for the tensile-shear test from RFSSW joints in the as-welded, naturally aged, and artificially aged conditions. ....	182
Figure 4-30: Effect of welding time and rotation rate on average peak load in the lap-shear tests of RFSSW joints in the as-welded, naturally aged, and artificially aged conditions. ....	185
Figure 4-31: Effect of welding time and rotation rate on the average fracture energy of the RFSSW joints in the as-welded, naturally, and artificially aged conditions.....	186
Figure 4-32: Examples of joint failure behaviours, showing both halves of the fractured lap-shear test samples welded with a 2000 rpm and different plunge depths.....	188
Figure 4-33: Examples of the failure behaviour showing both halves of the fractured lap-shear test samples tested in the as-welded condition.....	189
Figure 4-34: Macroscopic cross-sections through the weld centre lines for fractured samples.....	190
Figure 5-1: Examples of nugget pull-out holes left after RFSSW of 1.0 mm AA6111 to AZ31 .....	194
Figure 5-2: Macrostructure of a cross-section of an early RFSSW dissimilar Al to Mg joint produced with a 2.0 mm thick Al upper sheet, using a 2500 rpm and 2.5 s; (b) the thick IMC layer formed at the joint interface; and (c) example of cracks propagated through the IMC layer.....	195
Figure 5-3: Example of a thermal history measured for the modified RFSSW process for Mg-Al.....	198
Figure 5-4: The effect of tool rotation rate on the peak temperature measured for the modified RFSSW process .....	200
Figure 5-5: Hardness profiles of cross-sections across a typical Mg-Al joint in the as-welded condition.....	201
Figure 5-6: Backscattered SEM micrographs of the cross-section of Mg to Al welds produced using welding conditions of 1900 rpm, 1.0 s, 1.0 mm.....	204
Figure 5-7: Backscattered SEM micrographs of the cross-section of Mg to Al welds produced using the welding condition of 2500 rpm, 1.0 s, and 1.0 mm.....	206
Figure 5-8: Backscattered SEM micrographs of the interfacial reaction IMC layer seen between the Mg and Al sheets .....	207
Figure 5-9: (a) TEM image of the bond-line between the Mg and Al sheets showing the IMC layer .....	208
Figure 5-10: Backscattered SEM micrographs of the cross-section of Mg to Al joints produced using the modified RFSSW process with welding conditions of 2800 rpm, 1.0 s, 1.0 mm.....	210
Figure 5-11: Effect of tool rotation rate on the thickness of the interfacial IMC reaction layer in the Mg-Al joints.....	211
Figure 5-12: Backscattered SEM micrographs showing the development of weld defects at the edge of Mg and Al joints, as a function of the sleeve plunge depth .....	212
Figure 5-13: Example load-extension curves for the tensile-shear test from dissimilar Mg-Al and similar Mg-Mg joints.....	213
Figure 5-14: Effect of tool rotation rate and sleeve plunge depth on the average lap shear peak load of Mg-Al joints produced using a 1.0 s total welding time.....	215
Figure 5-15: Effect of sleeve plunge depth and tool rotation rate on the average lap shear peak load of Mg-Al joints produced using the modified RFSSW process.....	216
Figure 5-16: Effect of total welding time and tool rotation rate on the average lap shear peak load of Mg-Al joints produced using the modified RFSSW process .....	217



Figure 5-17: Effect of tool rotation rate and sleeve plunge depth on the average fracture energy of Mg-Al joints produced using a 1.0 s total welding time.....	218
Figure 5-18: Effect of sleeve plunge depth and tool rotation rate on the average fracture energy of Mg-Al joints produced using the modified RFSSW process.....	219
Figure 5-19: Effect of total welding time and tool rotation rate on the average fracture energy of Mg-Al lap joints produced using the modified RFSSW process.....	220
Figure 5-20: Effect of tool rotation rate on the average peak load of the Mg-Mg and Mg-Al joints produced using the modified RFSSW process.....	221
Figure 5-21: Effect of tool rotation rate on the average fracture energy of the Mg-Mg and Mg-Al joints produced using the modified RFSSW process .....	222
Figure 5-22: Examples of typical joint failure behaviours, showing both halves of the fractured lap shear test samples produced using a 1.0 mm and 1.0 s.....	223
Figure 5-23: Backscattered SEM micrographs and EDS maps of a quarter of both halves of the fractured Mg to Al welds .....	224
Figure 5-24: Examples of typical joint failure behaviours from similar Mg-Mg welds showing both halves of the fractured lap-shear test samples .....	225
Figure 6-1: Geometry definition of the different material partition zones used for the similar AA6111 RFSSW joint model of the lap-shear test .....	232
Figure 6-2: Geometry definition of the heat-affected zones for a similar RFSSW joint of AA6111 for modelling a lap-shear test, showing the detail of the hook defect.....	233
Figure 6-3: Geometry definition of the SZ of the dissimilar AZ31 to AA6111 RFSSW joint, for modelling the lap-shear test .....	234
Figure 6-4: Hardness profiles of an RFSSW joint produced using a 2000 rpm, 1.0 s and 1.0 mm, measured immediately after welding .....	236
Figure 6-5: Stress-strain curves for AA6111 heat-treated using different treatments ..	237
Figure 6-6: Plastic region of the true stress-strain curves and their curve fits for AA6111 heat-treated using different treatments.....	238
Figure 6-7: Hardness profiles of an RFSSW joint produced using a 2000 rpm, 1.0 s, and 1.0 mm, artificially aged at 180 °C for 30 min .....	240
Figure 6-8: Stress-strain curves for the simulated paint-baked for the AA6111 weld zones.....	241
Figure 6-9: (a) Stress-strain curve for the AZ31-H24, and (b) plastic region of the true stress-strain curve for the AZ31-H24 and its curve fit.....	243
Figure 6-10: Boundary condition applied to the model. ....	245
Figure 6-11: Mesh distribution for the similar Al joint.....	246
Figure 6-12: The effect of mesh number on computing time and the difference between the force predicted by the model and the experimentally measured force at the peak load.....	247
Figure 6-13: Mesh distribution through the cross-section of Al-Al joints.....	248
Figure 6-14: Mesh distribution through the cross-section of the model used to replicate a dissimilar joint of Mg to Al.....	248
Figure 6-15: Stress and strain distribution on the longitudinal cross-section of an RFSSW joint under tensile-shear loading. ....	250
Figure 6-16: Predicted Von-mises stress and strain distribution in an RFSSW joint under tensile-shear loading (top view).....	252
Figure 6-17: Effect of a hook defect on the stress and strain distribution on the longitudinal cross-section of an RFSSW joint under tensile-shear loading.....	253

Figure 6-18: Examples of the failure behaviour, showing both halves of the fractured lap shear test.....	254
Figure 6-19: Comparison of the stress and strain distribution predicted in the longitudinal cross-section of an RFSSW joint.....	255
Figure 6-20: Comparison of the stress and strain distribution predicted in two lines of nodes passing through the longitudinal cross-section at 0.33 mm above and below the interface of an RFSSW joint in the as-welded condition.....	256
Figure 6-21: Comparison of experimental and modelled force-extension curves for the tensile lap shear test of RFSSW joints in the as-welded condition.....	257
Figure 6-22: Stress and strain distribution modelled in the longitudinal cross section of an artificially-aged RFSSW joint.....	259
Figure 6-23: Effect of the hook defect on the stress and strain distribution modelled in the longitudinal cross-section of an artificially-aged RFSSW joint .....	260
Figure 6-24: Comparison of the stress and strain distribution predicted in two lines of nodes passing through the longitudinal cross-section at 0.33 mm above and below the interface of an RFSSW joint in the artificially aged condition.....	261
Figure 6-25: Stress and strain distribution on an artificially-aged RFSSW joint under tensile-shear loading (top view).....	262
Figure 6-26: Experimental and modelled force-extension curves for the tensile lap shear test of RFSSW joints in the as-welded and artificially aged conditions .....	263
Figure 6-27: Predicted stress and strain distribution in the longitudinal cross section of an RFSSW dissimilar Mg-Al joint.....	265
Figure 6-28: Comparison of the stress and strain distributions predicted in two lines of nodes passing through the longitudinal cross-section at 0.33 mm above and below the interface of a dissimilar Mg-Al RFSSW joint of under tensile-shear loading.....	266
Figure 6-29: Comparison of the predicted maximum principal stress-strain curves in two nodes located at the interface at 0.35 mm from the edges of the dissimilar Mg-Al RFSSW joint. ....	267
Figure 6-30: Predicted stress distribution in an RFSSW dissimilar Mg-Al joint in two different steps under tensile-shear loading.....	268
Figure 6-31: Predicted strain distribution in an RFSSW dissimilar Mg-Al joint in two different steps under tensile-shear loading.....	268
Figure 6-32: Experimental and numerical force-extension curves for the tensile lap shear test of RFSSW joints of dissimilar Mg-Al .....	269

## List of Abbreviations

Al	Aluminium
BM	Base metal
BIW	Body-in-white
BSE	Backscattered electron
EBSD	Electron backscatter diffraction
EDX (EDS)	Energy dispersive x-ray
FE	Finite elements
FEGSEM	Field emission gun scanning electron microscope
FIB	Focused ion beam
FSSW	Friction stir spot welding
FSW	Friction stir welding
GP	Guinier-Preston
HAZ	Heat affected zone
HCP	Hexagonal close packed
HV	Vickers hardness
IMC	Intermetallic compound
Mg	Magnesium
OM	Optical microscopy
PBC	Paint-bake thermal cycle
PP	Pin-plunge
$Q_{\text{total}}$	Total energy generated during friction stir spot welding
RFSSW (FSpW)	Refill friction stir spot welding
RSW	Resistance spot welding
SEM	Scanning electron microscope
SE	Secondary electron
SP	Sleeve-plunge
SSSS	Supersaturated solid solution
SZ	Stir zone
TEM	Transmission electron microscopy
TMAZ	Thermomechanical affected zone
USW	Ultrasonic welding
XCT	X-ray computational tomography
XRD	X-ray diffraction

## **Abstract**

The University of Manchester. **Basem Mohysen Mohammed Al-Zubaidy**. Doctor of Philosophy (PhD). September 2016. **Material Interactions in a Novel Refill Friction Stir Spot Welding Approach to Joining Al-Al and Al-Mg Automotive Sheets**

Refill Friction Stir Spot Welding (RFSSW) is a new solid-state joining technology, which is suitable for joining similar and dissimilar overlap sheets connections, particularly in aluminium and magnesium alloys. This welding method is expected to have wide applications in joining of body parts in the automotive industry.

In the present study, RFSSW has been used to join 1.0 mm gauge sheets of two material combinations: similar AA6111-T4 automotive aluminium alloy joints and a dissimilar aluminium AA6111-T4 to magnesium AZ31-H24 alloy combinations. The performance of the joints was investigated in terms of the effect of the welding parameters (including tool rotation rate, sleeve plunge depth, and welding time etc.) to improve current understanding and allow optimisation of the process for short welding-cycles when joining similar and dissimilar light alloys.

The results of the investigations on similar AA6111 welds showed the ability to use a wide window of process parameters that resulted in joints with a successfully refilled keyhole and flat weld surface, even when using a welding time as short as 0.5 s. The joints in the as-welded condition showed strengths as high as 4.2 kN, when using welding parameters of 1500 rpm, 1.0 mm with a range of welding times from 0.55 to 2.0 s. All joints showed a nugget pull-out failure mode when using a sleeve plunge depth of 0.8 mm or more, as a result of increasing the joint area. The strength of the joints further improved and reached peak loads of 5.15 and 6.43 kN after natural and artificial ageing, respectively, for welds produced using optimised welding parameters of a 2500 rpm tool rotation rate, a 1.5 s welding time and a 1.0 mm plunge. This improvement in strength resulted from the improvement in the local mechanical properties in the HAZ and other regions, which results from a minimal HAZ due to the rapid weld cycle and the re-precipitation of GPZs and clustering on natural ageing, or  $\beta''$  on artificial ageing.

A modification to the RFSSW process was developed in this project to solve the problems faced when dissimilar welding Mg to Al. This modified process involved adding a final brief pin plunge stage to consolidate refill defects and it was successful in producing nearly defect-free joints with improved mechanical properties, using a wide range of the process parameters. The average peak load of the joints increased with increasing tool rotation rate, to reach a maximum value at 2500 rpm due to eliminating the weld defects by increasing the material plasticity. However, increasing the tool rotation rate further to 2800 rpm led to a decrease in the average peak failure load due to eutectic melting at the weld interface. The optimum welding condition was thus found to be: 2500 rpm, 1.0 s, and 1.0 mm, which gave an average peak failure load of 2.4 kN and average fracture energy of 1.3 kN.mm. These values represent an improvement of about 10 % and 27 %, respectively, compared to welds produced with the conventional RFSSW process, and about 112 % and 78 % of the Mg-Mg similar joints produced using the same welding conditions.

A FE model developed in this project was successful in increasing understanding of the behaviour of the RFSSW joints when subjected to lap tensile-shear loading. The stress and strain distribution in the modelled samples showed that the highest concentration occurring in the region of the confluence of the SZ with the two sheets. With increasing extension, these regions of highest stress and strain propagated to the outer surfaces of the two sheets and then annularly around the weld nugget. This annular ring of high strain concentration agreed well with the failure path and results in the full plug pull-out fracture mode shown by the experimentally tested samples. The predicted force-extension curves showed high agreement with the experimental results, especially when including the effect of the hook defect and correction of compliance in the experimental results.

## **Associated Publications**

- Al-Zubaidy, B. M., Chen, Y. C. and Prangnell, P. B. (2014) Assessment of Rapid Refill FSSW for 6111-T4 Aluminium Automotive Alloys, in 14<sup>th</sup> International Friction Stir Welding Symposium, Beijing, China, Publ. TWI on CD.
- Chen, Y. C., Al-Zubaidy, B. M. and Prangnell, P. B. (2014) Dissimilar Friction Spot Welding of Aluminium and Magnesium for Automotive applications Using Novel Approaches - Abrasion Circle FSSW and Refill FSSW, in 14<sup>th</sup> International Friction Stir Welding Symposium, Beijing, China, Publ. TWI on CD.
- Wang, Y., Wang, L., Robson, J., Al-Zubaidy, B. M. and Prangnell, P. (2015) Coating Design for Controlling  $\beta$  Phase IMC Formation in Dissimilar Al-Mg Metal Welding, in Friction Stir Welding and Processing VIII (eds R. S. Mishra, M. W. Mahoney, Y. Sato and Y. Hovanski), John Wiley & Sons, Inc., Hoboken, NJ, USA. doi: 10.1002/9781119093343.ch19

## **Declaration**

No portion of the work referred to in this thesis has been submitted in support of an application for another degree or qualification of this or any other university or institute of learning.

## **Copyright**

The author of this thesis (including any appendices and/or schedules to this thesis) owns certain copyright or related rights in it (the “Copyright”) and s/he has given The University of Manchester certain rights to use such Copyright, including for administrative purposes.

Copies of this thesis, either in full or in extracts and whether in hard or electronic copy, may be made only in accordance with the Copyright, Designs and Patents Act 1988 (as amended) and regulations issued under it or, where appropriate, in accordance with licensing agreements which the University has from time to time. This page must form part of any such copies made.

The ownership of certain Copyright, patents, designs, trademarks and other intellectual property (the “Intellectual Property”) and any reproductions of copyright works in the thesis, for example graphs and tables (“Reproductions”), which may be described in this thesis, may not be owned by the author and may be owned by third parties. Such Intellectual Property and Reproductions cannot and must not be made available for use without the prior written permission of the owner(s) of the relevant Intellectual Property and/or Reproductions.

Further information on the conditions under which disclosure, publication and commercialisation of this thesis, the Copyright and any Intellectual Property and/or Reproductions described in it may take place is available in the University IP Policy (see <http://www.campus.manchester.ac.uk/medialibrary/policies/intellectual-property.pdf>), in any relevant Thesis restriction declarations deposited in the University Library, The University Library’s regulations (see <http://www.manchester.ac.uk/library/aboutus/regulations>) and in The University’s policy on presentation of Theses.

## **Acknowledgements**

It is with immense gratitude that I acknowledge my supervisor Professor Phil Prangnell whose support, help and guidance enabled me to finish my project. Thanks are also due to Professor Joseph Robson for his support throughout my PhD.

This study was sponsored by The Higher Committee for Education Development in Iraq \ Prime Minister's Office. I owe to you all.

I owe my deepest gratitude to Dr. Yingchun Chen, Dave Strong and Yin Wang who have contributed immensely to the contents of this thesis.

I also wish to acknowledge colleagues and friends in Manchester for all the support and assistance they have given me, especially, Dr. Abdul Sameea Jilabi and Dr. Hameed Ala'asam.

I would like to thank all of the people in C7-Material Science Centre, who supported me during my study.

Last but not least, I would like to thank my family for their unwavering support in my life.



**To**

**My Family**



## **Chapter 1: Introduction**

---

This chapter provides an introduction to the motivation for this work, a clarification of the aims of the study, and an overview of the contents of this thesis.

### **1.1 The Effects of Automobiles on Global Warming (Greenhouse Gas Emissions)**

There is a growing body of literature that recognises the dangerous effect of man-made emissions of greenhouse gases on the Earth's climate (Lashof & Ahuja, 1990; T&E, 2008; Meinshausen, et al., 2009; Dodman, 2009; Solomon, et al., 2009). This literature predicts an increase of 1.8 – 4.0°C in the earth's mean temperature during the 21st century. Both the environment and society will be affected by the negative consequences of climate change. Examples of these consequences are many, including health issues, due to heat waves, in addition to the increasing frequency of droughts in dry regions and, conversely, an increased risk of flooding in other places. It is also expected that the increase in the average global temperature between 1.5 and 2.5°C will lead to a 20 to 30 percent increase in the extinction risk faced by plant and animal species (T&E, 2008).

The transport sector is one of the main sources of greenhouse gas emissions. It contributes about a quarter of domestic greenhouse gas emissions in the UK (Greene & Plotkin, 2011; GOV.UK, 2015). The most important greenhouse gas, by volume, is carbon dioxide (CO<sub>2</sub>), as shown in Figure 1-1 (Greene & Plotkin, 2011). CO<sub>2</sub> emissions are directly related to the consumption of fossil fuel. For example, burning one kilogram of any type of organic fuel, like petrol, diesel or kerosene, in a car, van, lorry, aircraft or ship results in the emission of about 3 kg of CO<sub>2</sub> (T&E, 2007).

CO<sub>2</sub> emissions from the transport sector represented 21% of the total emissions for the EU in 1990, but this rose to 27% by 2005, which is an increase of about 32% overall. Passenger cars and vans are responsible for about half of these emissions. The transport is thus considered the worst sector in terms of meeting the requirements of the Kyoto Protocol (T&E, 2007).

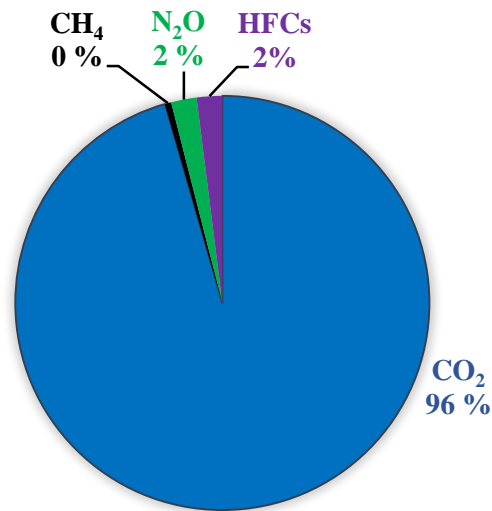


Figure 1-1: Greenhouse gases emitted by transportation (Greene, 2006).

Europe and its automobile manufacturers have taken a leading role in the international challenge to reduce CO<sub>2</sub> emissions (ACEA, 2015 a). The target for the EU to reduce the average emissions for new automobiles to 120 g/km was first suggested by Germany in October 1994, during the meeting of European environment ministers, but it was officially announced by the European Commission communication in 1995. This target can be converted into fuel consumption figures of 5.0 litres/100 km for petrol cars and 4.5 litres/100 km for diesel cars. Initially, 2005 was set as a target date for the objective to be reached (T&E, 2007), and this figure has largely been met by automotive manufacturers.

Globally, the most challenging targets for decreasing vehicle CO<sub>2</sub> emissions in the world have been set by the EU (see Figure 1-2) (ACEA, 2015 b). The Council of the European Union and the European Parliament reached an agreement, at the end of 2013, about two further regulatory requirements that will become mandatory CO<sub>2</sub> emission targets for light-commercial vehicles and new passenger cars by 2020 (ICCT, 2014). European car manufacturers will have to reduce fleet average CO<sub>2</sub> emissions from 186 g/km in 1995 down to 95 g/km (about 3.8 l/100 km in terms of fuel consumption) for passenger cars, and from 181 g/km in 2010 down to 147 g/km for vans by 2020 (effectively 2021) (ICCT, 2014; ACEA, 2015 b).

These objectives have since been modified to a prescribed more gradual improvement in performance down to 95 percent of the target by 2020 and 100% by 2021.

In spite of the reductions in CO<sub>2</sub> emissions delivered by manufacturers for new vehicles, progress in decreasing the overall emissions of road transport has been slow owing to growth in demand. Because early targets were relatively easy to achieve, car manufacturers now have a real challenge, in terms of continuing to reduce CO<sub>2</sub> emissions from individual vehicles to reach these targets (ACEA, 2015 b).

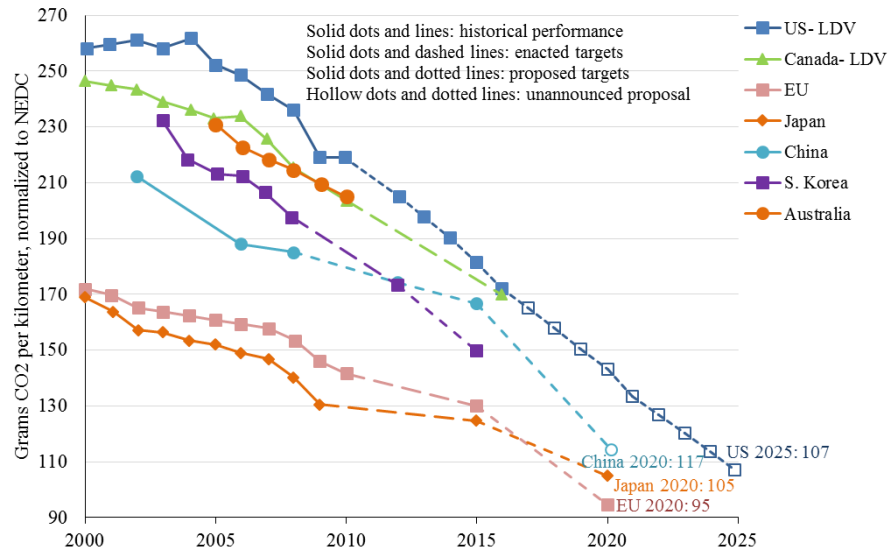


Figure 1-2: Grams of CO<sub>2</sub> emitted by transportation according to the region and projected future targets (ACEA, 2015 a).

## 1.2 Lightweight Materials in Automobile Body Applications

### 1.2.1 Influence on Emissions

While automobile manufacturers are under substantial pressure to reduce the greenhouse gas emissions produced by their vehicles through increasing fuel efficiency (Jambor & Beyer, 1997; T&E, 2008; ACEA, 2015 b), at the same time, there is pressure on car companies to maintain safety systems, improve crashworthiness and passenger comfort (Kim, et al., 2010; Amancio-Filho, et al., 2011 a).

Energy consumption during a vehicle's full life cycle is basically determined by the fuel consumed throughout its active use. As seen in Figure 1-3, the highest percentage of energy is consumed in the driving period of the life cycle of a car. Therefore, this amount has to be reduced. Reductions can be achieved by several means, including a more economical driving style, improvement of tyre rolling resistance and drive

efficiency, optimisation and improvement of the ancillary components, improvement of the aerodynamics, reduction of drag, increasing the efficiency of the engine and reduction of vehicle weight (Jambor & Beyer, 1997; Lathabai, et al., 2006; Cui, et al., 2008; ACEA, 2015 b). There are limits as to what degree the internal combustion engine can be additionally developed while delivering inexpensive consumer product. Additional changes will be even more difficult. Furthermore, continuing to produce lighter vehicles is challenging when customers continue to demand the best possible safety from the cars they purchase (ACEA, 2015 b).

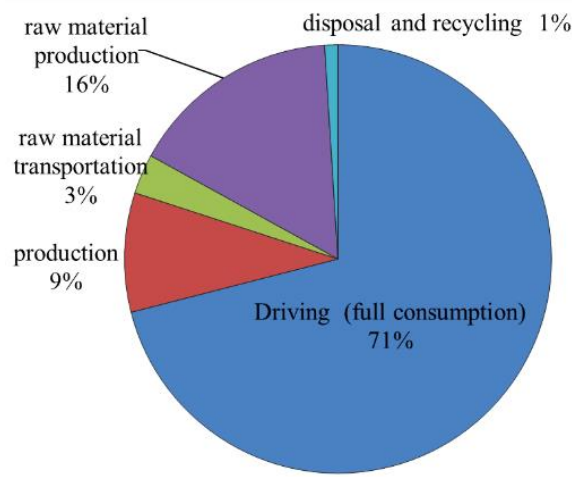


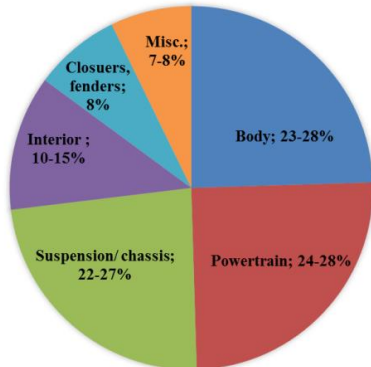
Figure 1-3: Typical energy consumption during the life cycle of a vehicle (Jambor & Beyer, 1997).

Building lightweight cars is not a new trend. The use of lighter materials to reduce the mass of components has taken place since the foundation of the automobile industry; however, this trend has gradually increased over the past fifty years (CAR, 2011). Until now, weight reduction is still the most economic means for the transport sector to decrease fuel consumption and greenhouse gas emissions (Cui, et al., 2008; Ghassemieh, 2011). Several studies have shown that there is a physical relationship between car mass and its technical efficiency (measured by either its fuel consumption or CO<sub>2</sub> emission rate). Research has consistently shown that every 10% decrease in the total mass of a conventional vehicle leads to a reduction of 6% to 8% in fuel consumption (Lutsey, 2010; Ghassemieh, 2011).

Table 1-1 shows an approximate analysis of the mass breakdown of structures for various existing vehicle designs. In general, the car body, also known as the “body-in-white” (BIW), represents about 23-28 percent of the overall mass of the car, depending

generally on the installed options, the engine size, comfort features and integrated safety systems (Carle & Blount, 1999; Kelkar, et al., 2001; Fuchs, et al., 2008; Lutsey, 2010; Hirsch, 2011). A reduction in body weight can also lead to savings in other components. For example, a smaller engine can be used to obtain the same performance. Therefore, a reduction in car body weight provides a promising way to reduce fuel consumption, lower car emissions and improve driving performance (Cui, et al., 2008; Fuchs, et al., 2008; Gould, 2012).

Table 1-1: Vehicle mass analysis by system and components (Lutsey, 2010).

Approximate vehicle mass breakdown	System	Major component in system
	Body-in-white	Passenger compartment frame, cross and side beam, roof structure, front-end structure, underbody floor structure, panels
	Powertrain	Engine, transmission, exhaust system, fuel tank
	Chassis	Chassis, suspension, tires, wheels, steering, brakes
	Interior	Seats, instrument panel, insulation, trim, airbags
	Closures	Front and rear doors, hoods, liftgate
	Miscellaneous	Electrical, lighting, thermal, windows, glazing

However, the lightweight design must meet some important criteria including an acceptable production cost for large volume manufacturing, combined with sufficient strength, stiffness and crash resistance, durability, recycling, repair-ability and acoustic properties (Cole & Sherman, 1995; Jambor & Beyer, 1997).

The main strategic approaches for body-in-white lightweighting, without compromising rigidity, are architectural changes and material replacement. The unibody is the most mass-efficient of all possible architecture variations, but it is already largely optimised (Jambor & Beyer, 1997; Fontaras & Samaras, 2007). Consequently, the most important method available for further reducing the weight of the car body is through the use of lightweight materials (Jambor & Beyer, 1997; Cui, et al., 2008; Gould, 2012), such as ultra-high-strength steels, aluminium alloys, magnesium alloys, titanium alloys, composites and foams (Li, et al., 2003; Uematsu, et al., 2008; Kim, et al., 2010; Tozaki, et al., 2010; CAR, 2011; Ghassemieh, 2011).

The environmental aspect of different materials can be measured by a comparison of the energy consumed by cars made from these materials, during manufacture and over the

entire life cycle of the product. All processes that result in energy consumption during fabrication and production should be taken into consideration to obtain an accurate assessment of the eco-friendliness of a vehicle. This includes the energy needed to construct and maintain a car during its operating lifetime, in addition to that recovered in material recycling (see Figure 1-3) (Carle & Blount, 1999).

It is possible to reduce the weight of the vehicle body by about 7% when an all-steel body in white is optimised. It is clear that the impact from this on reducing fuel consumption and emissions will be insufficient (Jambor & Beyer, 1997). Therefore, mild steel has been replaced by more advanced steels, such as high and ultra-high strength steels, due to their higher yield strength (Jambor & Beyer, 1997; Li, et al., 2003; Ghassemieh, 2011).

Aluminium usage has seen a significant increase in automotive industry applications in recent years. The amount of aluminium used in an average vehicle in 1996 was about 110 kg; this amount is predicted to rise to about 250 - 340 kg by 2015 (Fridlyander, et al., 2002; Ghassemieh, 2011). Aluminium is attractive in automotive applications for many reasons. The most important of these is the decrease in density by 3:1 offered by aluminium alloys over steel in terms of strength-to-weight ratio, which means that for an equivalent design, up to 70% of the body-in-white weight could be reduced by direct replacement of steel by aluminium. Even when taking into consideration the difference in strength and stiffness between aluminium and steel, a weight reduction of 40 to 60% can still be achieved (Miller, et al., 2000; Gould, 2012). When added to other mass-reduction opportunities, this substitution can reduce the total vehicle weight by around 30% (Miller, et al., 2000). This advantage of aluminium over steel is causing many manufacturers to design vehicles with bodies made entirely of aluminium (see Figure 1-4), such as the Mercedes-Benz CL Coupé, the Audi A-2, Audi A-8, Jaguar XJ, BMW Ford AIV and the General Motors EV-1 (Miller, et al., 2000; Lutsey, 2010; CAR, 2011; Gould, 2012).





Figure 1-4: Mercedes-Benz AMG SL63 aluminium body structure (Mercedes-Benz.USA, 2016).

Magnesium alloys are very attractive materials for automotive applications because they are the least dense structural metal (Aghion & Bronfin, 2000; Aghion, et al., 2001; Lutsey, 2010). Magnesium components are less dense than aluminium and steel/cast iron by 33% and 75%, respectively (Cole & Sherman, 1995; Lutsey, 2010; CAR, 2011). Moreover, magnesium has a significantly higher specific strength, at about 14.1% higher than aluminium and 67.7% higher than steel/cast iron (Ghassemieh, 2011). Several vehicle models now contain magnesium parts (Lutsey, 2010). However, because of the galvanic corrosion problem, most of the magnesium applications can be found in the vehicle interior, in components such as instrument panels, steering, cross-car beams and seat structures (Blawert, et al., 2004; CAR, 2011).

Polymer composite materials have been used in automotive manufacturing for a long time. The use of these materials has significantly grown in many applications due to their ability to reduce part weight. In addition to their design flexibility, they have the advantage of better corrosion resistance, low-velocity impact cushioning and noise attenuation (Jambor & Beyer, 1997; Li, et al., 2004; Ghassemieh, 2011). However, these applications are typically confined to cosmetic components, rather than structural performance components, because only expensive continuous fibre reinforced materials have sufficient stiffness for structural applications. Glass fibre-reinforced plastics are the most widely used material in this category, but they have limitations in terms of stiffness and strength (Lutsey, 2010; CAR, 2011). Recently, there has been much more interest in advanced composites (mainly carbon fibre-reinforced polymers) in structural vehicle body applications (Fuchs, et al., 2008; CAR, 2011). Even though these benefits

are well known by the automotive manufacturers, the use of polymer composite in large scale automotive applications has been hindered by high material costs (when using carbon fibres, the cost can be up to 10 times higher than that of conventional metals), slow production rates, and concerns about recyclability (Ghassemieh, 2011).

### **1.2.2 Multi-Material Automotive Structures**

The main method for vehicle body lightweighting is using lightweight materials. However, an obstacle in the replacement of commonly used steel with lightweight materials is their high cost compared to steel. For example, the cost required to build an entirely aluminium vehicle body similar to that of the Audi A8 is considerably higher than that of a traditional steel body (Cui, et al., 2008). As an alternative to the all-aluminium BIW designs, there is a new concept of “multi-material designs” (Hirsch, 2011), which refers to the selection of the best material for the functions of the intended part (Cui, et al., 2008; Hirsch, 2011). Therefore, nowadays, a vehicle structure is often made up of a variety of materials (Gould, 2012). This includes a range of steels (mild steel, high- and ultra-high-strength steels) (Hirsch, 2011), aluminium alloys, magnesium alloys and plastic composites (Hirsch, 2011; Gould, 2012). Representing the state-of-the-art in this area, Ford and Vehma developed the MMLV Mach I BIW (see Figure 1-5 a) which targeted a 40% vehicle mass (Mascarin, et al., 2015). A 30% mass reduction was achieved by the panel and closure set through the use of aluminium extrusions, aluminium panels, magnesium castings, and boron steel stampings. In the Mach II design concept (with a vehicle mass reduction target of 45%; see Figure 1-5 b) an additional decrease of BIW mass was obtained by increasing the use of carbon-fibre composites, together with aluminium, ultra-high-strength steel, and press-hardened boron steel, which achieved a mass reduction of 44%. In addition, the use of magnesium sheet, castings, and extrusions accompanied by sheet aluminium and boron-steel intrusion beams in the closure panels gave total mass savings of 46% (Mascarin, et al., 2015).

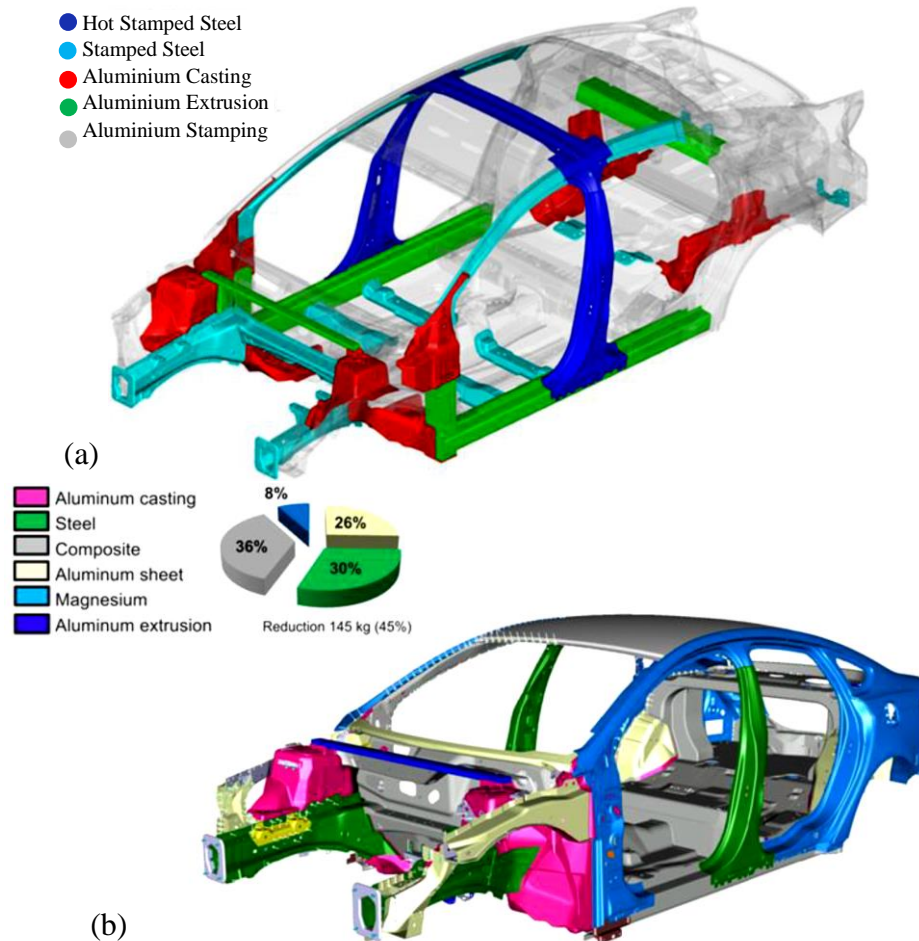


Figure 1-5: Vehma/Ford MMLV a) Mach I BIW b) Mach II BIW (Mascarin, et al., 2015).

After the completion of their manufacture, vehicle parts must be assembled into the complete body (Hadley, et al., 2000). Resistance spot welding is the conventional technique used to assemble steel vehicle bodies. However, the welding of aluminium alloys by this method presents several challenges owing to their high reactivity and low resistivity. As a result, joining aluminium requires a different set of technologies from that used for steel (Carle & Blount, 1999; Hadley, et al., 2000; Gould, 2012). In addition, the use of multi-materials in vehicle-body manufacturing requires specific techniques to join dissimilar materials (Hadley, et al., 2000). This finding has resulted in a new challenge to develop alternative joining methods that are low cost and have high productivity.

Proposed techniques to join dissimilar materials include mechanical fastening and welding methods which can be classified into two types: fusion welding and solid-state welding. (Tozaki, et al., 2007; Badarinarayan, et al., 2009; Uematsu & Tokaji, 2009).

Fusion welding methods under consideration include resistance spot welding (RSW) and laser welding. RSW has some limitations when used to join aluminium alloys, such as the need to use machines with greater capacity and very high welding currents and a reduced life of the electrode tips (Qiu, et al., 2009). Moreover, RSW joints suffer from poor weld microstructures (Gould, 2012) and inconsistencies in joint strength (Uematsu, et al., 2009). On the other hand, limitations of using laser welding are the low absorption of Al metal surfaces and their high conductivity (Kou, 2003) which results in a limited penetration depth.

Mechanical fastening technologies involve the completion of a connection by mechanical interference instead of metallurgical bonding (Gould, 2012). Such techniques have some important limitations; for example, when using self-piercing riveting, the weight is increased by introducing additional consumable substances (rivets) (Barnes & Pashby, 2000b). In contrast, clinching faces different problems because the joint strength is not high (Abe, et al., 2009 b).

In solid-state welding, a joint is produced without the use of filler metals through the application of pressure and heat (below the melting temperature). Friction welding and ultrasonic welding are examples of this type of welding process (Khan, 2007).

The capability of the ultrasonic power source to deliver the power appears to be the main limitation of ultrasonic welding. Therefore, the use of USW is limited to comparatively thin sheets (Gould, 2012). A potential alternative is the friction stir welding (FSW) technique, which uses a non-consumable rotating tool to generate heat through friction and mechanical deformation in the welding area, resulting in the joining of welded pieces without reaching the melting point of the welded members (Shivaraj, et al., 2011).

Friction stir spot welding (FSSW) is a relatively new technique derived from the “linear” friction stir welding (FSW) technique (Badarinarayan, et al., 2009; Lee, et al., 2011). FSSW and FSW share the same advantages, such as the ability to join dissimilar materials and materials that are difficult to fusion weld (Shen, et al., 2011), low distortion, excellent mechanical properties and ease of handling (Tozaki, et al., 2007; Uematsu & Tokaji, 2009). However, the keyhole that results from the pin on the tool used in this process, which almost penetrates the lower sheet, is undesirable (Prangnell

& Bakavos, 2010; Bilici & Yüklér, 2012) and represents the main limitation associated with FSSW.

Refill friction stir spot welding (RFSSW) is a new solid-state joining technology, which is suitable for joining similar and dissimilar overlap sheet connections (Parra, et al., 2011), particularly in aluminium alloys and magnesium alloys (Rosendo, et al., 2011). This welding method is expected to have wide applications for joining body parts in the automotive industry (Uematsu, et al., 2008).

The RFSSW process (Figure 1-6) is accomplished using a non-consumable welding tool consisting of three parts that are independently movable in the upward and downward directions: these consist of a clamping ring, sleeve and pin (Amancio-Filho, et al., 2011 a; Parra, et al., 2011; Rosendo, et al., 2011; Shen, et al., 2013). The RFSSW process consists of the following four stages (a) the two sheets are clamped together by the clamping ring and the tool begins to rotate (the sleeve and the pin); (b) the sleeve plunges and deforms the sheet material plastically and the pin is retracted to create a cylindrical space which accommodates the displaced plasticised material; (c) the sleeve reaches a predetermined depth and then both the sleeve and the pin are retracted to their original position; (d) finally, the rotation of the tool is stopped and the welding head removed (Mazzaferro, et al., 2009; Oliveira, et al., 2010; Parra, et al., 2011; Shen, et al., 2013).

RFSSW was developed to reduce, or eliminate, the disadvantages incurred by other spot-joining methods (Campanelli, et al., 2013a). It has many advantages, such as the absence of a keyhole (the joint is likely to be flat with a defect-free surface) (Rosendo, et al., 2011; Campanelli, et al., 2012a), low heat distortion (Uematsu, et al., 2008), excellent mechanical properties (Parra, et al., 2011), minimum material loss (Campanelli, et al., 2012a), and is more environmentally friendly (no fumes and little waste or pollution are generated) compared to conventional RSW (Uematsu, et al., 2008; Parra, et al., 2011). RFSSW also benefits from short production cycles (Oliveira, et al., 2010), no pre-cleaning or post-processing requirements, ease of automation (Parra, et al., 2011), and low energy consumption compared with fusion welding methods (Amancio-Filho, et al., 2011 a).

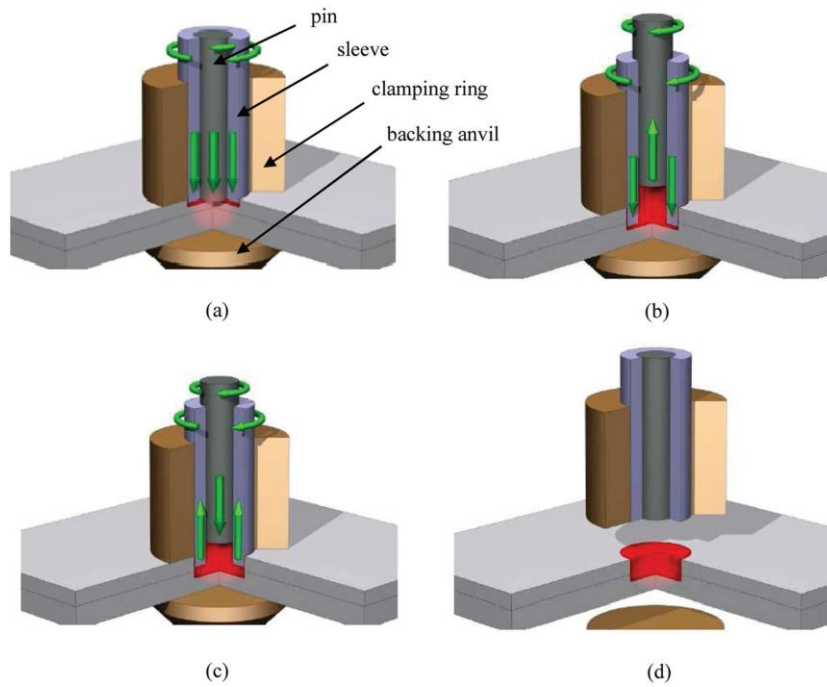


Figure 1-6: Schematic illustration of the RFSSW processes: (a) clamping and tool rotation, (b) sleeve plunging and pin retraction, (c) sleeve retraction and pin plunging, (d) tool removal (Qiao, et al., 2015).

The RFSSW process is an area of growing interest and a great amount of work is being conducted to improve the process for joining different combinations of materials, such as aluminium to aluminium (Uematsu, et al., 2008; Mazzaferro, et al., 2009; Parra, et al., 2011; Shen, et al., 2013), magnesium to magnesium (Campanelli, et al., 2013a), magnesium to fibre-reinforced polymers (Amancio-Filho, et al., 2011 b) polymers to polymers (Oliveira, et al., 2010), aluminium to steel (Qiao, et al., 2015; Verastegui, et al., 2015) aluminium alloy to galvanised steel (Dong, et al., 2016) and aluminium to magnesium (Suhuddin, et al., 2014). In spite of a large body of work being carried out, the literature review in Chapter 2 will show that most of these studies have focused on two main things: the mechanical properties and the microstructure of the welded joints and the relationship between them. However, the RFSSW process still has some issues to resolve including reducing the welding time of aluminium to aluminium sheets to 1.0 s or less and developing the ability to join dissimilar thin sheets of aluminium to magnesium (1.0 mm or less), in order to fulfil the automotive industry requirements for multi-material designs. Therefore, there is a necessity to develop the current understanding of the aluminium-to-aluminium and aluminium-to-magnesium interactions during the RFSSW joining processes and to investigate the feasibility of modifying the process so as to take steps towards a solution.

### **1.3 Objectives of this Study**

There are two primary aims of this study: firstly, to identify the most important factors influencing joint performance, when rapidly joining similar (aluminium to aluminium) and dissimilar (magnesium to aluminium) material combinations using the refill friction stir spot welding (RFSSW) technique. Secondly, this study aims to develop the understanding required to optimise the welding process parameters for a shorter weld-cycle time and any process modifications required to achieve higher performance. The literature review will show that several alternative joining techniques, such as refill friction stir spot welding (RFSSW), friction stir spot welding (FSSW) and ultrasonic welding (USW) can be used to join dissimilar materials, but these methods still have many problems. For example, welding aluminium takes longer than one second using these techniques; even though the welding process could be completed in less than one second, the strength of the resultant joints was found to be unacceptable. On the other hand, the welding of magnesium to aluminium has revealed another problem, which is the brittle intermetallic phases that rapidly form at the weld interface, leading to a poor quality joint. In order to solve some of these problems, this thesis aims to systematically develop and modify the refill friction stir spot welding (RFSSW) technique to achieve aluminium-to-aluminium and aluminium-to-magnesium joints with higher performance. Key to the approach adopted in this study was to fully understand the microstructure development at the weld interface, the material flow during welding, and the relationship to the process parameters and the weld cycle. In addition, the failure behaviour of both similar and dissimilar welds have been studied and modelled in order to better understand the factors that affect weld performance.

## **1.4 Thesis Overview**

### **Chapter 2: Literature Review**

This chapter gives a review of the literature related to Al and dissimilar Al-Mg materials so as to understand the existing information about the subject and discover the areas that require further research.

### **Chapter 3: Experimental Methods**

The materials, welding process, microstructure analysis and mechanical testing techniques used throughout the study are summarised in this chapter.

### **Chapter 4: Refill Friction Stir Welding of Al-Al Similar Welding (Results and Discussion)**

In this chapter, the material interaction when joining Aluminium to Aluminium using the RFSSW process was investigated using systematic variation of the parameters that could affect the weld quality. This analysis was conducted so that a sound fundamental basis could be developed to optimise the process for more rapid welding cycles.

### **Chapter 5: Refill Friction Stir Welding of Mg-Al Dissimilar and Mg-Mg Similar Welding (Results and Discussion)**

Based on the understanding of the material flow section in Chapter 4, the RFSSW process was modified and then optimised to improve the quality of the Mg-Al joints. These joints were assessed to locate and determine the thickness of intermetallic compounds. The effect of these IMCs on the quality of the joints was then defined.

### **Chapter 6: FE Modelling of the Mechanical Behaviour of Refill Friction Stir Spot Welds (Al-Al and Mg-Al)**

An FE model of the failure of RFSSW joints was developed in order to better understand the mechanical behaviour of the joints when subjected to lap shear testing.



## **Chapter 2: Literature Review**

---

### **2.1 Introduction**

This chapter contains a review of the literature related to the present study. Firstly, the different joining techniques that can be used in automotive spot joining are briefly reviewed, focusing on the friction stir spot welding techniques as a specific solid-state welding technique. The following sections then review information related to the FSSW and RFSSW processes, including heat generation, and the effects of welding parameters on microstructure formation, weld defects, and material flow. The latter two main sections include information about the materials used in this study. Finally, the last section includes a review of FE-modelling of the mechanical behaviour of spot welds.

### **2.2 Joining Overview**

Developments in the field of materials science and engineering in recent years have led to the availability of a wide range of new materials. As a result, designers have become more creative with structural design (Kumar, et al., 2015). The demand for using lightweight materials, such as aluminium and magnesium, in manufacturing construction has also increased, particularly in the automotive and aerospace industries, in order to achieve improved performance and make energy savings. Consequently, new challenges have emerged, represented by the need to find new methods appropriate to join different types of materials in a single structure (Tozaki, et al., 2007; Uematsu, et al., 2008; Uematsu, et al., 2009; Badarinarayan, et al., 2009; Kumar, et al., 2015). Many engineering solutions are available to join structures, but the selection of a specific technique for a certain application depends on a number of factors, including cost, availability, and the performance expected from the structure (Kumar, et al., 2015). Figure 2-1 summarises the classes of common joining methods used for similar and dissimilar materials.

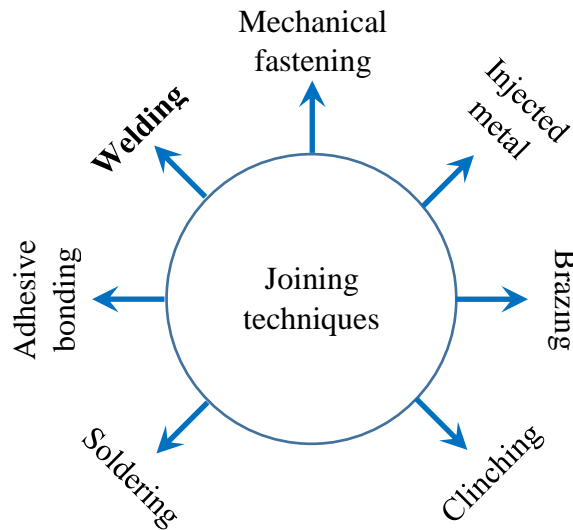


Figure 2-1: Classes of methods used to join similar and dissimilar materials (Kumar, et al., 2015).

Mechanical fastening is a suitable choice for the majority of cases when joining dissimilar materials. Nonetheless, attention has shifted from mechanical joining methods, such as bolting and riveting, to welding, due to the requirements of high-performance structures. This benefit of welding is in addition to the other advantages of this method, such as more cost effective and faster integration time, weight saving, flexibility in design, high joint efficiency, higher structural stiffness, air and water tightness, and no limitation on the width of the part which can be joined together (Kumar, et al., 2015). Attempts have been made with both types of welding techniques (fusion and solid-state welding) to join dissimilar materials. Solid-state welding methods include friction stir welding (FSW) and its subdivisions, ultrasonic welding, diffusion welding, and explosive welding (Tozaki, et al., 2007; Uematsu, et al., 2008; Uematsu, et al., 2009; Badarinarayan, et al., 2009; Kumar, et al., 2015). However, the following sections include a brief review of some of the spot joining methods that can be used in the automotive industry, which are the most relevant processes to the subject of this project.

## 2.3 Fusion Spot Welding

There are a large number of techniques that are classified as fusion welding methods, and they include all methods that required metal to be transformed into a liquid state for the purpose of completing the bonding process. The main difference between these methods is the source, or method, of generating the necessary heat required for melting. Resistance spot welding (RSW) and laser welding are well-known examples of welding methods that are classified under this category; both of these techniques will be discussed briefly in the following sections.

### 2.3.1 Resistance Spot Welding (RSW)

Resistance spot welding (RSW) has been the most popular joining method used for the manufacture of steel body structures by the automotive industry since the 1950s (Han, et al., 2010; Gould, 2012). A typical vehicle's body-in-white contains about 6000 resistance spot welds (Gould, 2012). RSW is normally used to join overlapping metal sheets in separate spots through fusion at the interface (Khan, 2007; Pereira, et al., 2010). To achieve a sound joint, the joining process requires a good combination of the main welding parameters: heat, pressure and time. (Mathers, 2002; Kulekci, et al., 2011). The schematic diagram shown in Figure 2-2 represents the RSW process, which essentially includes the use of two water-cooled copper electrodes and an externally applied force to clamp two or more overlapping sheets. An electric current is then passed through the sheets between the two electrodes, which is designed to generate sufficient heat for melting at the interface due to the resistance of the interface to the flow of current. As a result, a weld nugget is formed and a joint is made between the sheets (Mathers, 2002; Khan, 2007).

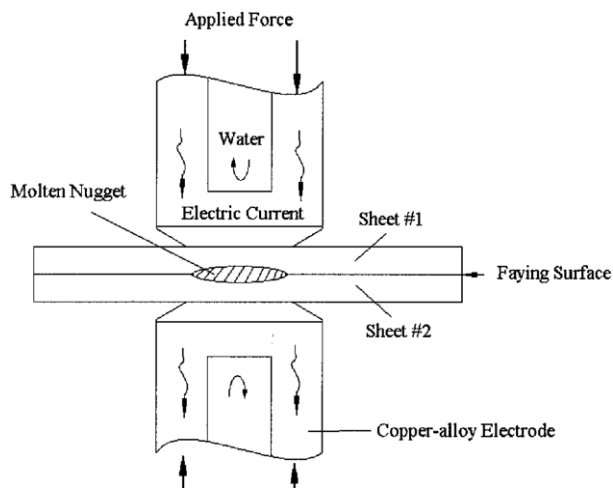


Figure 2-2: Schematic illustration of the resistance spot welding (RSW) process (Khan, et al., 2000).

The heat generated in this technique is due to the Joule effect and depends on the electric current, the time the current is passed between the electrodes and the contact resistance at the joint interface (Mathers, 2002; Uematsu & Tokaji, 2009). This heat generation can be expressed by (Khan, et al., 2000):

$$H = I^2 R t \quad \text{Equation 2-1}$$

Where  $H$  = heat generated, in Joules (watt. seconds);

$I$  = current, in amperes;

$R$  = resistance, in ohms;

$t$  = time, in seconds.

The RSW technique is mainly used to join low carbon steel sheets (Abe, et al., 2009 a; Uematsu & Tokaji, 2009; Pereira, et al., 2010; Gould, 2012), stainless steel, nickel, and titanium alloy components (Pereira, et al., 2010). Due to the advantages of using RSW for steels, like the ease of automation (high speed and flexibility), high reliability, low costs and considerable manufacturing robustness (Pereira, et al., 2010; Gould, 2012), this welding method has been used in a wide range of industrial applications, such as the joining of the bodies and chassis of automobiles, trucks, buses, trailers, railroad and many other products (Pereira, et al., 2010).

In spite of the RSW process being well established for steel using this welding method for aluminium is more difficult because of the difference in the physical properties of the two materials (Han, et al., 2010; Kulekci, et al., 2011; Gould, 2012). As shown in Table 2-1, aluminium has approximately three times the thermal conductivity and less than one-fifth the electrical resistivity of steel at their respective melting points (Han, et al., 2010; Gould, 2012; Liu, et al., 2014). Consequently, to produce a sound aluminium weld using RSW, the welding machines generally require much higher welding currents and more exact pressures, in order to provide the heat necessary to melt the aluminium compared to the heat required for steel welds (Mathers, 2002; Qiu, et al., 2009; Kulekci, et al., 2011; Gould, 2012).

Table 2-1: Properties of pure aluminium, magnesium and iron at their melting points (Liu, et al., 2014).

Properties	Aluminium	Magnesium	Iron
Ionisation energy (eV)	6	7.6	7.8
Specific heat ( $\text{J}\cdot\text{kg}^{-1}\cdot\text{K}^{-1}$ )	$1.08 \times 10^3$	$1.36 \times 10^3$	795
Specific heat of fusion ( $\text{J}\cdot\text{kg}^{-1}$ )	$4 \times 10^5$	$3.7 \times 10^5$	$2.7 \times 10^5$
Melting point ( $^{\circ}\text{C}$ )	660	650	$1.536 \times 10^3$
Viscosity ( $\text{kg}\cdot\text{m}^{-1}\cdot\text{s}^{-1}$ )	$1.3 \times 10^{-3}$	$1.25 \times 10^{-3}$	$5.5 \times 10^{-3}$
Surface tension ( $\text{N}\cdot\text{m}^{-1}$ )	0.914	0.559	1.872
Thermal conductivity ( $\text{W}\cdot\text{m}^{-1}\cdot\text{K}^{-1}$ )	94.03	78	38
Coefficient of thermal expansion (1/K)	$24 \times 10^{-6}$	$2.5 \times 10^{-5}$	$1 \times 10^{-5}$
Density ( $\text{kg}\cdot\text{m}^{-3}$ )	$2.385 \times 10^3$	$1.59 \times 10^3$	$7.015 \times 10^3$
Elastic modulus ( $\text{N}/\text{m}^2$ )	$7.06 \times 10^{10}$	$4.47 \times 10^{10}$	$2.1 \times 10^{11}$
Electrical resistivity ( $\mu\Omega\cdot\text{m}$ )	0.2425	0.274	1.386

Aluminium carries additional limitations that increase the difficulty of resistance welding it compared to when welding steel. The reaction of aluminium with oxygen in the atmosphere leads to the formation of a highly resistive oxide layer (Han, et al., 2010). Irregularity in the oxide film thickness will affect the resistance at the interface between plates and between the electrodes and the plates (Mathers, 2002). This oxide layer should be broken down homogeneously to keep the weld-nugget formation under control, and this generally requires a higher electrode force (Barnes & Pashby, 2000a; Abe, et al., 2009 b; Han, et al., 2010). Moreover, the electrodes used in RSW are made from copper which easily alloys with aluminium (Mathers, 2002); if the contact resistance at the electrode-sheet interface increases for any reason, this will raise the temperature of the copper electrodes by increasing ohmic heating. As a result, the diffusion of aluminium into copper will increase, leading to the formation of brittle intermetallic phases which degrade the electrode surfaces (Mathers, 2002; Han, et al., 2010). Therefore, fast wear, a short life of the welding electrodes and a reduction in weld quality (associated with electrode degradation) present important challenges to using RSW in automotive applications (Mathers, 2002; Han, et al., 2010; Gould, 2012). Furthermore, poor weld microstructures (Gould, 2012; Pouranvari & Marashi, 2013) and inconsistencies in joint strength (Fukumoto, et al., 2003; Uematsu & Tokaji, 2009) have been reported as other limitations of this technique.

Dissimilar welding of magnesium to aluminium alloys using RSW is very challenging due to the low electrical resistivity and high thermal conductivity of both materials (Table 2-1), which mean that high welding currents are required (Czerwinski, 2011; Hayat, 2011). Furthermore, the difference between the two metals in electrical resistivity causes a larger nugget to form on the aluminium side due to the difference in heating rates (Hayat, 2011). Nevertheless, the main issue with using RSW to weld magnesium to aluminium is the very rapid formation of a brittle layer (up to 40µm thick) of intermetallic compounds (IMCs), such as  $Mg_{17}Al_{12}$  and  $Mg_2Al_3$ , in the weld region (Hayat, 2011; Manladan, et al., 2016). The formation of these brittle IMCs negatively influences the weld strength (Hayat, 2011; Liu, et al., 2014). Therefore, to improve the strength of dissimilar joints between magnesium and aluminium, the formation of IMCs should be restricted or controlled. This can be done by using interlayers, such as pure nickel, gold-coated nickel and zinc-coated steel, as barrier materials to suppress the magnesium and aluminium interaction and as a result restrict IMC formation (Manladan, et al., 2016).

### **2.3.2 Laser Welding**

Laser welding, shown schematically in Figure 2-3, is a method which uses a laser beam to heat and melt metals in order to accomplish the bonding process. There are two main types of laser, depending on the system by which the laser beam is produced: solid-state lasers and gas lasers. A progressive expansion of the efficiency and range of the commercially available laser systems (e.g. CO<sub>2</sub> and Nd: YAG laser, fibre lasers, etc.) is taking place for industrial applications in automotive manufacturing (Barnes & Pashby, 2000a).

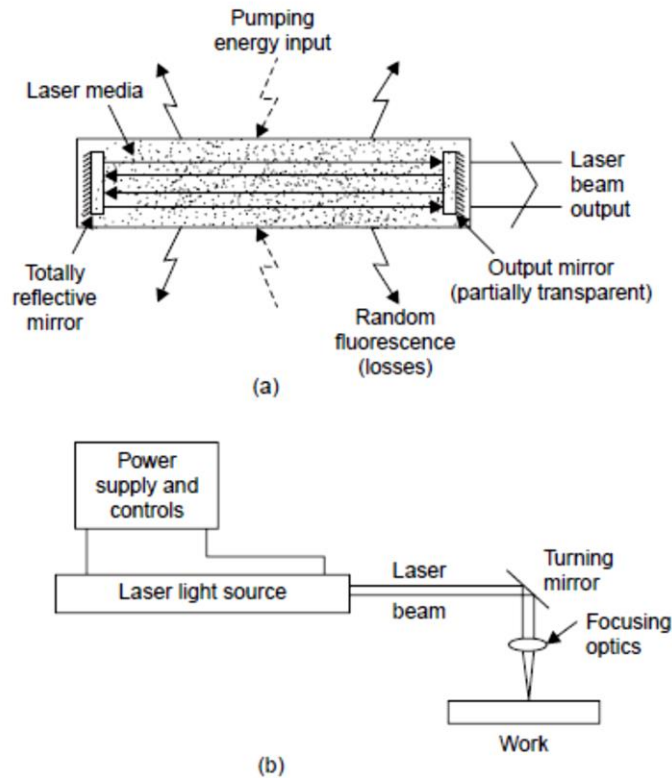


Figure 2-3: Schematic illustration of laser welding: (a) laser source, (b) welding set up (Khan, 2007).

After generating the laser beam, optical systems (such as mirrors and lenses) are used to focus and direct it to achieve high power densities (Kou, 2003). This process heats a very small area on the workpiece, leading to a low net heat input. Laser welding has many advantages, including a high welding speed, a narrow heat-affected zone (HAZ), low thermal distortion, flexibility, and welding in an exact and reproducible manner (Yang & Lee, 1999; Zhao, et al., 1999; Barnes & Pashby, 2000a; Khan, 2007). The developments of new laser technology, such as high-power Nd: YAG and CO<sub>2</sub> lasers and fibre-optic delivery, have improved the ability to use them in high-volume automation (Yang & Lee, 1999; Zhao, et al., 1999).

Laser welding can be used to join aluminium alloys, but it requires a higher power due to the very high reflectivity of the metal surface (Kou, 2003), as well as the high thermal conductivity and low boiling point of the alloying elements, which limits the penetration and efficiency of the process (Barnes & Pashby, 2000a; Mathers, 2002). Moreover, as laser welding is a liquid-state welding process, defects found in joints made by this method are similar to those encountered in other fusion welding processes (Mathers, 2002) such as porosity (Mathers, 2002) and solidification cracking (Barnes & Pashby, 2000a). Porosity is caused by contamination from gases in the environment near the

weld pool, such as oxygen, nitrogen, and hydrogen. Different amounts of  $H_2$  may be absorbed by the molten aluminium alloy in the weld pool (Mathers, 2002). During subsequent cooling, this gas can nucleate as bubbles in the melt pool because of the decrease in solubility during solidification. If the gas bubbles cannot escape from the molten zone before solidification they may become trapped, resulting in porosity. This type of porosity arises because the gas solubility greatly decreases in solid aluminium alloys (Zhao, et al., 1999).

The temperature distribution on the surface of the weld pool can also affect the vaporisation of alloying elements such as magnesium and zinc (Zhao, et al., 1999). The thermal cycle, which refers to temperature variation with time, also affects the microstructure, residual stress, and distortion formed in a welded joint (Zhao, et al., 1999). The high-temperature gradients between the weld zone and the parent metal seen in laser welding promote high residual stresses; as a result, the integrity of the joints will be affected (Mai & Spowage, 2004).

In the case of using laser welding to join dissimilar alloys such as aluminium to steel and aluminium to titanium, a liquid-solid state reaction takes place only at the interface between the two metals. In this situation, it is mainly the metal with a lower melting temperature (aluminium, in these examples) is melted. Nevertheless, even though there is a small difference in melting point between aluminium and magnesium, it is still difficult to apply this method to join this combination due to the resultant intermetallic reaction. Consequently, other methods must be developed to try to control the formation of intermetallic compounds when joining aluminium and magnesium alloys (Borrisutthekul, et al., 2005).

Laser-weld bonding technology is a hybrid joining technology, which combines both welding and adhesive bonding. This process is useful as it can offer the advantages of both welding and adhesive bonding. Laser-weld bonding (Figure 2-4) is a promising method for joining Al alloys and Mg alloys. This process involves the following four stages: (1) spreading adhesive material on the surface of the lower sheet; (2) assembling and applying pressure; (3) laser (seam) spot welding and (4) curing. During the welding process, the adhesive is decomposed. This occurrence results in the partial dispersal of the intermetallic particles generated, which have a negative influence on the properties of the Mg-Al joints (Liu, et al., 2014).



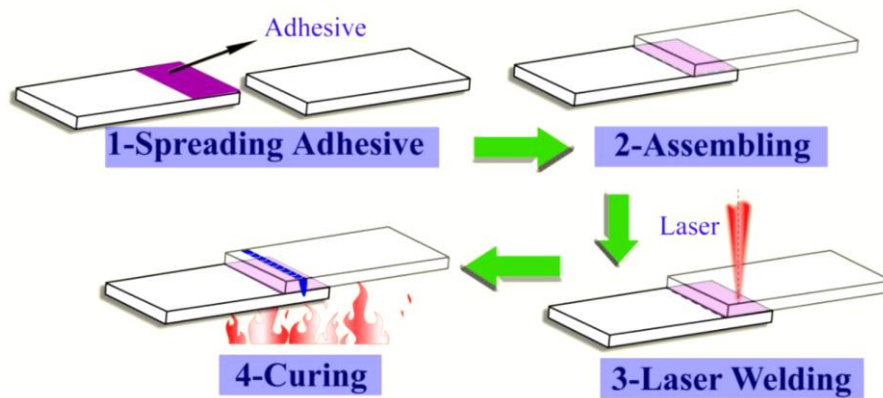


Figure 2-4: Laser weld bonding process (Liu, et al., 2014).

## 2.4 Mechanical Fastening

Mechanical fastening is one of the oldest joining techniques. This technology includes the completion of a connection by mechanical interference, instead of metallurgical bonding. There are several methods of fastening, which are classified under this title, including screwing, folding, clamping, riveting, and clinching (Gould, 2012).

Self-piercing rivets and clinch joints are cold forming processes, which are used for the mechanical fastening of two or more pieces of material. They are well-known methods of joining widely used in automotive body manufacturing (Barnes & Pashby, 2000b).

### 2.4.1 Self-Piercing Riveting

In the self-piercing riveting (SPR) process a hollow rivet is used to connect two or more pieces of sheet metal without a pre-drilled hole. In this process, as shown in Figure 2-5, the hollow rivet is inserted through the sheets and penetrates the upper sheet without fully penetrating the lower sheet, due to the presence of a mandrel or die. The mandrel geometry has two functions; the upsetting of the hollow rivet in the lower sheet and control of the penetration of the rivet inside the lower sheet (Porcaro, et al., 2004; Porcaro, et al., 2006; Abe, et al., 2006; Abe, et al., 2009 b; Gould, 2012).

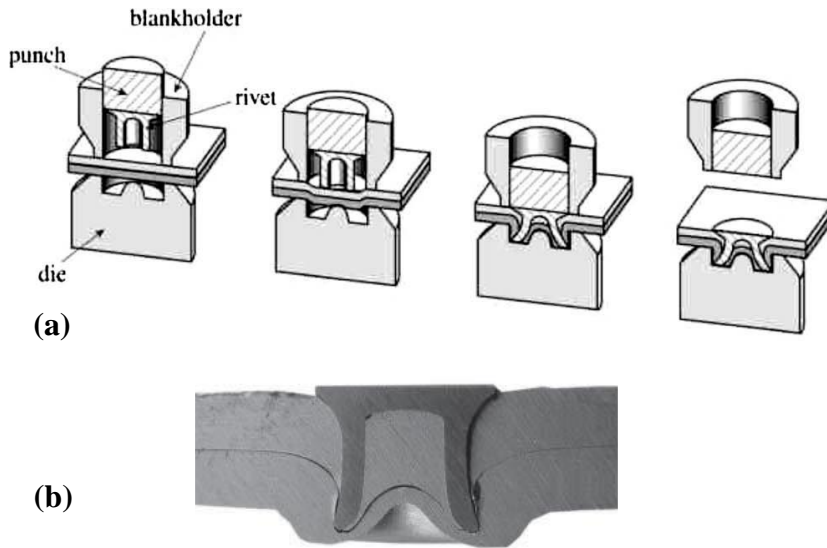


Figure 2-5: a) Schematic illustration of the self-piercing riveting process (Hoang, et al., 2010) b) Cross-section of two sheets joined by a self-piercing rivet (Porcaro, et al., 2004).

#### 2.4.2 Clinching

Clinch joining is very similar to the self-piercing riveting process, as it also involves joining materials by applying a plastic deformation to obtain a mechanical interlock. However, this process does not involve the use of a rivet (Barnes & Pashby, 2000b). The clinching process, shown schematically in Figure 2-6, basically uses two dies. The upper die (or punch) extrudes both of the upper and lower sheets inside the lower die, leading to the generation of an interlock type connection by forming a part of the upper sheet with a larger diameter inside a smaller hole in the lower sheet (Barnes & Pashby, 2000a; Abe, et al., 2007; Gould, 2012).

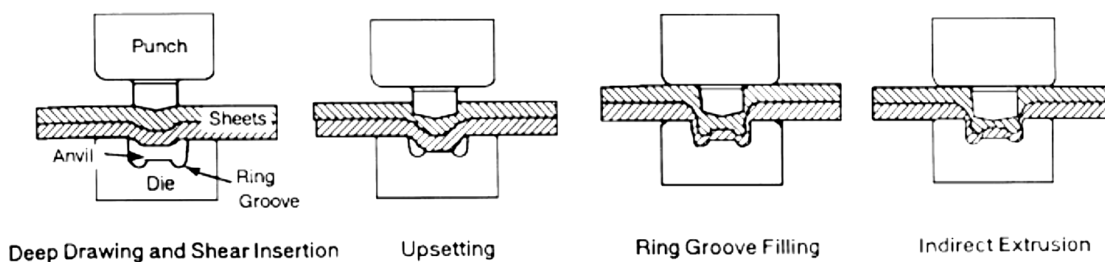


Figure 2-6: Schematic illustration of the clinching process (Barnes & Pashby, 2000b).

The main advantages of SPR and clinching are the ability to join dissimilar metal sheets of different melting points, and they have the same production speed as resistance spot welding (Barnes & Pashby, 2000a; Abe, et al., 2006; He, et al., 2008; Abe, et al., 2009).

a; Abe, et al., 2009 b). These advantages are in addition to a high ease of automation, good tool life, and low energy consumption (Barnes & Pashby, 2000b). On the other hand, these techniques have some important limitations. For example, when using the SPR technique the weight is increased by introducing additional consumable substances (rivets) (Barnes & Pashby, 2000b). In addition, recyclability problems arise because the steel rivets must be removed from the aluminium alloy sheets before the material can be recycled (Abe, et al., 2009 b; Uematsu, et al., 2009). In comparison, the low joint strength is the main problem that limits the application of the clinching technique (Abe, et al., 2006; Abe, et al., 2009 a).

## **2.5 Solid State Spot Welding**

Solid state welding encompasses methods capable of joining materials through the use of heat below their melting temperatures. The parts are heated to allow plastic deformation and pressure to be used to bring the two weld members into intimate contact, without using a filler material. There are several welding processes which are classified under this group including friction stir spot welding and ultrasonic welding, among others (Khan, 2007). Only ultrasonic welding and friction stir welding will be discussed here because of their relevance to the project; as FSSW is the focus of this project, it will be discussed in more detail in the following sections.

### **2.5.1 Ultrasonic welding (USW)**

Ultrasonic welding (USW) has been used to join thin foils since the 1950s; however, more recently this technique has also been applied to join thicker sheets, as a result of the increasing availability of systems with higher power (Bakavos & Prangnel, 2010; Sooriyamoorthy, et al., 2011; Panteli, et al., 2012). In the USW technique, shown schematically in Figure 2-7, ultrasonic vibration produces transitional movements (by shear) parallel to the interface between the metal sheets. The rapid linear shear oscillation across the sheet interface, in combination with the application of a moderate pressure (normal force), generate the necessary heat and deformation to join the opposing sheet workpieces (Sooriyamoorthy, et al., 2011; Gould, 2012).

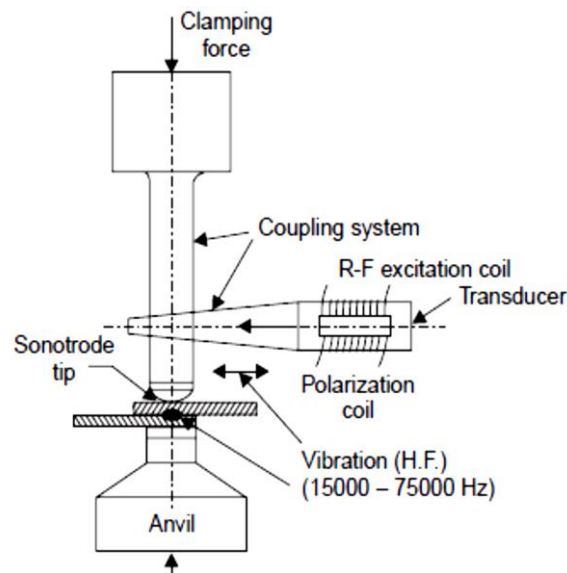


Figure 2-7: Schematic illustration of the ultrasonic welding (USW) process (Khan, 2007).

For a given material combination, USW has several variables, including vibration frequency, power delivery, welding time/energy, clamping pressure and sonotrode tip geometries (Panteli, 2012). In principle, USW is an attractive method for spot joining light alloy structures, like aluminium car body panels, as it can produce joints with good mechanical properties, has a short weld cycle (typically <0.5 s) and is more energy efficient than RSW (using only 0.6–1.3 kJ per weld) (Bakavos & Prangnel, 2010; Patel, et al., 2011; Chen, et al., 2012b). For example, it takes approximately 0.8 kJ of electrical energy to weld two 0.9 mm-thick sheets of AA6111-T4 by using single-transducer wedge-reed welders. This is significantly lower than the 50 to 100 kJ required for the same combination when using resistance spot welding (Jahn, et al., 2007). Additionally, ultrasonic joints are made without consumables, such as filler materials which are normally used in conventional joining processes (Elangovan, et al., 2009 ).

USW can be used to join dissimilar material combinations. It is especially useful for metals with substantially different melting points, metals that form brittle IMCs at the weld joint, and joints which are located close to heat sensitive components (Elangovan, et al., 2009 ). Several researchers have used this technique to join dissimilar materials. For instance, Patel et al. significantly improved the joint strength and failure energy of dissimilar joints between the 5754-O aluminium alloy and AZ31B-H24 magnesium alloy by adding a tin interlayer, which successfully eliminated the brittle  $\text{Al}_{12}\text{Mg}_{17}$  IMCs (Patel, et al., 2012 a). Haddadi et al. investigated the weldability of the AA6111-T4 aluminium alloy to different zinc-coated steels using the USW method. The results

showed that the weldability was affected by the properties of the zinc coating, its melting speed and how much it inhibited intermetallic formation (Haddadi, et al., 2012). Zhang et al. successfully joined the aluminium alloy AA6111 to a titanium alloy TiAl6V4 by high-power ultrasonic spot welding, without detection of a visible IMC layer in the as-welded condition (Zhang, et al., 2014). Finally, the USW technique has been successfully used by Matsuoka and Imai to join aluminium to copper (Matsuoka & Imai, 2009). Nonetheless, in spite of the ability to join dissimilar material combinations by using this method, reaction products (such as brittle IMCs) can still be produced if the weld cycle is sufficiently long or the reaction rate is high enough, such as in Al to Mg welds (Panteli, 2012).

The ability of the ultrasonic power source to deliver sufficient power appears to be the major limitation of ultrasonic welding. Heavy components require high energy to vibrate at a high frequency. Advanced power supplies are limited to about 5500 W. With these power levels; the use of USW is limited to comparatively thin sheets, small components and wires (Elangovan, et al., 2009 ; Gould, 2012).

Normally, it is advantageous to use higher energies in USW (expressed mainly by longer times and larger amplitudes). However, the amount of energy that can be used is limited, because high weld energies can cause excessive indentation and softening, which reduces the strength of the joints (Gould, 2012). For example, Figure 2-8 shows the effect of increasing weld energy (or weld time) on the cross-sectional dimensions of a joint.

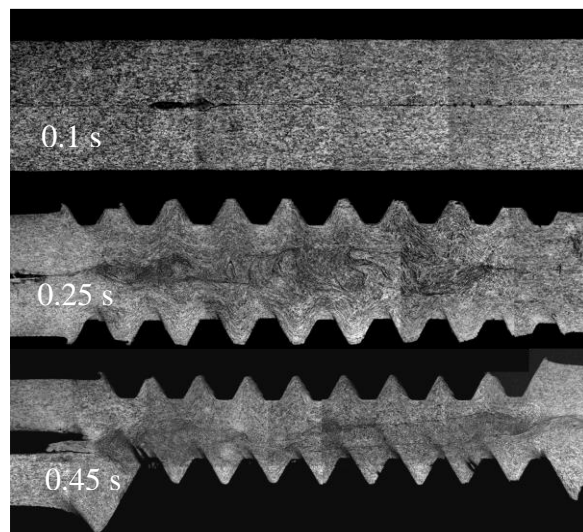


Figure 2-8: The effect of welding time on the cross-sectional appearance of USWs of Al-Al (Prangnell & Bakavos, 2010).

## 2.6 Friction Stir Spot Welding (FSSW) Techniques.

### 2.6.1 Background: Friction Stir Welding (FSW)

Friction stir welding (FSW), a relatively modern welding technology, was invented by Thomas et al. (1991) at the Institute of Welding (TWI), Cambridge, United Kingdom (Shivaraj, et al., 2011; Campanelli, et al., 2011; Chowdhury, et al., 2013). The FSW technique (shown in Figure 2-9) uses a non-consumable rotating tool to generate heat through friction and mechanical deformation in the welding area, resulting in the joining of weld members without them reaching their melting point (Shivaraj, et al., 2011). FSW can be classified as one of the most important innovations in solid state welding, as it has considerable advantages compared to traditional welding processes. It can also produce significant differences, compared to fusion welding, in terms of the weld zone microstructures, the size of the heat-affected zone (HAZ) and residual stresses (Hatamleh, 2008; Badarinarayan, et al., 2009).

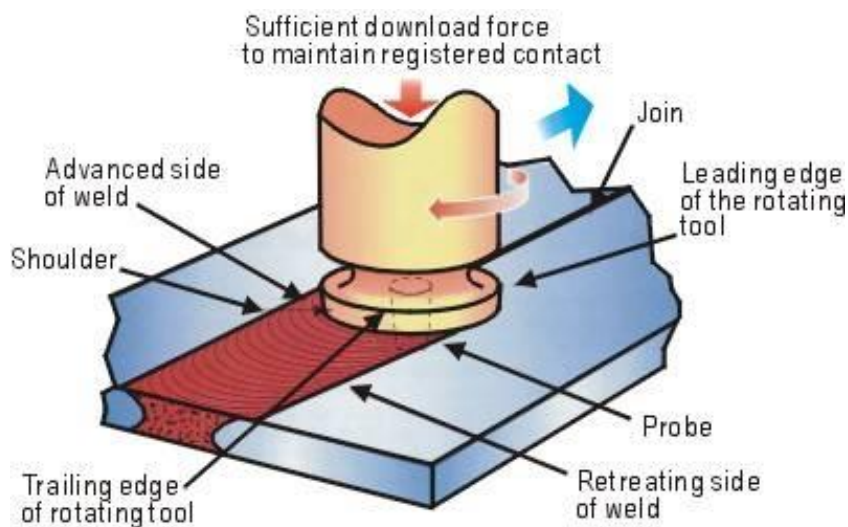


Figure 2-9: Schematic diagram of the friction stir welding (FSW) process (Johnson & Kallee, 2013).

The FSW process consists of three main stages: a plunge, dwell and welding stage. Firstly, in the plunging stage, a rotating non-consumable hard tool is inserted into the join line between the pieces to be welded. When the tool reaches a predefined plunge depth, rotation is continued without any forward movement for a certain time (dwell time), so that the friction and plastic deformation heat up the stir zone and parent metal. Then, during the welding stage, the tool moves forward to form the weld seam (Thomas, et al., 1991; Mishra & Ma., 2005; Mandal, et al., 2008; Buffa, et al., 2008 a).

The FSW process has several welding parameters that affect the final quality of the welded joint. The main independent variable parameters are the vertical force, tool rotation rate, travel speed, tool geometry, tilt angle between the tool and welding materials, dwell time, delay time, plunge depth and plunge rate (Nandan, et al., 2008; Rosado, et al., 2010; Rajakumar, et al., 2011; Bilici & Ykler, 2012). The torque during FSW is affected by many variables, including the applied vertical pressure, tool geometry, tilt angle, the coefficient of friction and material properties, in addition to the amount of slip at the tool-material interface (Nandan, et al., 2008).

The performance of an FSW welded joint is affected strongly by the tool geometry and welding parameters, which have a significant influence on the heat generation and the material flow as a result of the friction forces (Buffa, et al., 2008 a). The FSW tool (shown in Figure 2-10) consists of two parts: the pin and the shoulder. During rotation, the tool generates heat by friction and plastic work as it stirs the material around it. It has been found that the pin size, the angle of the pin, the orientation of the pin thread, the length of the pin and its profile can all have a significant effect on the formation of the welded joint (Bilici & Ykler, 2012).

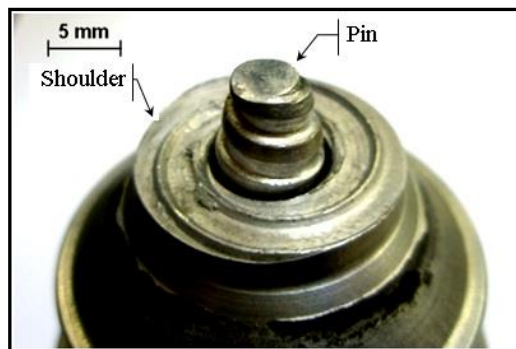


Figure 2-10: Friction stir welding tool (Santos, et al., 2011).

Many new characteristics have been incorporated into welding tool designs. Some tools designed at TWI are shown in Figure 2-11 (Nandan, et al., 2008). Most of these changes were made to the pin; some of them included the redesign of the shape to add threads of various shapes, as well as changing the angle of inclination of the pin in some designs. The shoulder's concavity and its size are also important. Most of the heat generated during the process comes from the friction of the tool shoulder with the workpiece and the deformation this causes below the surface of the workpiece. Moreover, the shoulder prevents the expulsion of material, forges the plasticised material and assists the material flow around the tool (Bilici & Ykler, 2012).



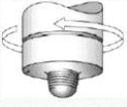


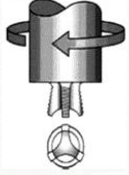
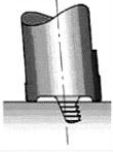
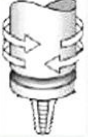
Tool	Cylindrical	Whorl™	MX triflute™	Flared triflute™	A-skew™	Re-stir™
Schematics						
Tool pin shape	Cylindrical with threads	Tapered with threads	Threaded, tapered with three flutes	Tri-flute with flute ends flared out	Inclined cylindrical with threads	Tapered with threads

Figure 2-11: Some selected tools designed at TWI (Nandan, et al., 2008).

Since FSW of metals is a solid-state process, it has many advantages. The first of these benefits is the ability to weld materials which are difficult to weld using conventional welding techniques like fusion welding (Sanderson, et al., 2000). Many authors (Sanderson, et al., 2000; Kallee & Nicholas, 2003; Meran, 2006; TWI Ltd., 2016) have mentioned the following advantages of FSW:

- Avoidance of solidification/ liquation cracking.
- Low weld distortion.
- Excellent mechanical properties, established by mechanical tests like tensile, fatigue and bend tests.
- No generation of fumes, or weld porosity and no splash or spatter.
- High efficiency in energy consumption and the ability to operate in all positions.
- No requirement for consumables (for example filler wire) or protective gases.
- Aluminium and copper of a thickness >75mm can be welded in one pass.
- Relatively few weld parameters to optimise.

Kallee and Nicholas (2003) point out that the FSW process also has many other advantages that make it appropriate to use with automation and robotic control, in addition to the ability to be used with existing conventional equipment. Some of these additional benefits are:

- The tool is non-consumable. For instance, one tool can normally be used to weld about 1000 m in length of 6000-series aluminium alloys.
- The process is not very demanding in terms of the surface preparations of the pieces to be welded; for example, the presence of a thin layer of oxide on the surfaces of metals to be welded can be accepted.



- In mass production there is no need for grinding, brushing or cleaning using chemicals.

In spite of all the advantages mentioned above, FSW also has some limitations (Kallee & Nicholas, 2003):

- FSW has welding speeds somewhat slower than those yielded by fusion welding technologies (about 75cm/min in the welding of 6000 series aluminium alloy plates, 5mm in thickness, by commercially existing machines).
- The pieces being welded must be strongly clamped and the jigging must resist high reaction loads.
- A backing plate is required to support the welded pieces during the process.
- Each weld contains a keyhole at its end.
- Weld geometries are limited to butt or lap joints.

FSW technology is suitable for joining metal sheets, plates, pipes and hollow sections (Michael, et al., 2006). Therefore, it is used to produce a wide range of structural components in application areas like aerospace (aircraft – beams), railways, shipbuilding, the automotive industry and others (Michael, et al., 2006; Nandan, et al., 2008; Singh, et al., 2011; Yazdanian, et al., 2012).

In recent years, it has been shown that several materials that are excessively difficult to weld using conventional fusion welding techniques can be welded using FSW. However, because of tool wear issues, FSW is mainly used to weld materials which have low melting temperatures (Zhang, et al., 2005; Ghosh, et al., 2010), such as aluminium and its alloys (Gopalakrishnan & Murugan, 2011), copper (Meran, 2006), magnesium and other soft metals (Wei, et al., 2012), in addition to some metal matrix composites (MMCs) (Nami, et al., 2011; Gopalakrishnan & Murugan, 2011). However, recently this technique has been successfully used to weld materials with higher melting temperatures, like titanium alloys, nickel alloys and steels (Lee, et al., 2005; Hovanski, et al., 2007). With high strength aluminium alloys, many problems caused by fusion welding such as porosity, hot cracking, residual stresses and distortions, and softening of the heat affected zone, that can be improved using FSW (Ghosh, et al., 2010).

## **2.6.2 Friction Stir Spot Welding (FSSW)**

Friction stir spot welding (FSSW) is a relatively new technique derived from conventional “linear” friction stir welding (FSW) (Badarinarayan, et al., 2009; Lee, et al., 2011; Chowdhury, et al., 2013). This technology was first developed by the German research centre GKSS and has since been applied industrially by Mazda Motor Corporation and Kawasaki Heavy Industry (Thoppu & Gibson, 2009; Bozzi, et al., 2010; Shen, et al., 2011; Yuan, et al., 2011).

FSSW shares the same advantages of FSW in that they are both solid state processes, and can join dissimilar materials and materials that are difficult to fusion weld (Shen, et al., 2011), with low distortion (Tozaki, et al., 2007; Uematsu, et al., 2009; Lee, et al., 2011). The only difference from conventional FSW is that in FSSW the tool only plunges into the overlapped sheets and there is no tool movement along the weld joint line (Bozzi, et al., 2010).

To date, FSSW has been applied successfully in the production of the hood and rear doors of a sports vehicle (Chowdhury, et al., 2013). The FSSW process, shown schematically in Figure 2-12, is used to join two lapped metal sheets (Tran, et al., 2009). It basically consists of three stages: plunging, stirring and retraction (Malafaia, et al., 2010; Bilici & Ykler, 2012). The process starts with a rotating tool, normally consisting of a shoulder with a pin (Malafaia, et al., 2010; Bakavos, et al., 2011) plunging into the workpiece of a lap joint. When the tool shoulder contacts the upper surface of the upper sheet, the downward force is applied, while a supporting tool (backing plate or anvil ) underneath the lower sheet supports this down force (Bakavos, et al., 2011; Fanelli, et al., 2012). The tool rotation and the downward force are continued for an appropriate time (dwell time) to generate heat from friction and plastic deformation. This heat softens the metal and the rotation of the tool causes flow of the plasticised metal in both the circumferential and axial directions (Lathabai, et al., 2006; Tran, et al., 2009; Yuan, et al., 2011; Fanelli, et al., 2012; Bilici & Ykler, 2012). The tool shoulder applies the forging pressure resulting in the formation of a solid-state bond region between the surfaces of the upper and lower sheet around the pin (Tran, et al., 2009; Prangnell & Bakavos, 2010). Finally, the tool is retracted from the sheets and the result is a weld with a characteristic central hole (key hole) left by the pin after the tool has been removed (Bozzi, et al., 2010; Bilici & Ykler, 2012).

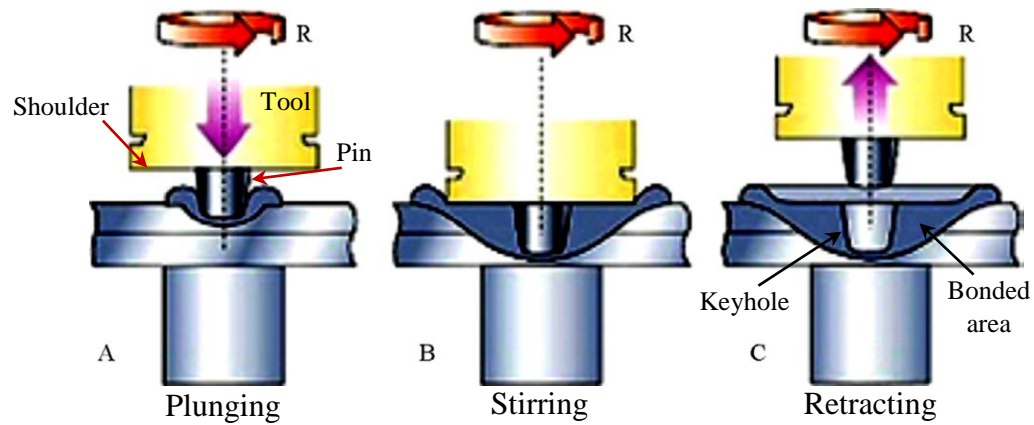


Figure 2-12: Schematic illustration of the friction stir spot welding (FSSW) process (Buffa, et al., 2008 b).

In the FSSW process, the weld quality is affected by fewer parameters than in the case of the friction stir welding because there is no traverse stage. Therefore, the success of the weld depends only on the rotational speed, plunge depth, plunge rate, dwell time and tool geometry (Panteli, 2012).

As with other welding techniques, FSSW has some limitations. The first is its relatively long weld cycle (typically 2 to 5 seconds), which should be less than 1.0 second in order to be adequate for mass automotive production (Bakavos, et al., 2011). The second disadvantage is the keyhole resulting from the pin of the tool, which is undesirable as it almost penetrates the lower sheet (Prangnell & Bakavos, 2010; Bozzi, et al., 2010; Bilici & Ykler, 2012) and can affect the corrosion resistance of the material during service (Bakavos, et al., 2011). Furthermore, it is not easy to achieve a full metallurgical bond using this joining method, which results in low failure energies by cleavage of the joint along the weld line (Prangnell & Bakavos, 2010; Bakavos, et al., 2011). Generally, there is a tendency for the failure path to follow the weld line through the interface between the sheets, which bends upwards near the pin (Bakavos, et al., 2011). This phenomenon is sometimes referred to as a ‘hook’ as shown in Figure 2-13. The formation of the hook, which represents a partial metallurgical bond, is found to be significantly affected by the tool geometry (Badarinarayan, et al., 2009; Yuan, et al., 2011).

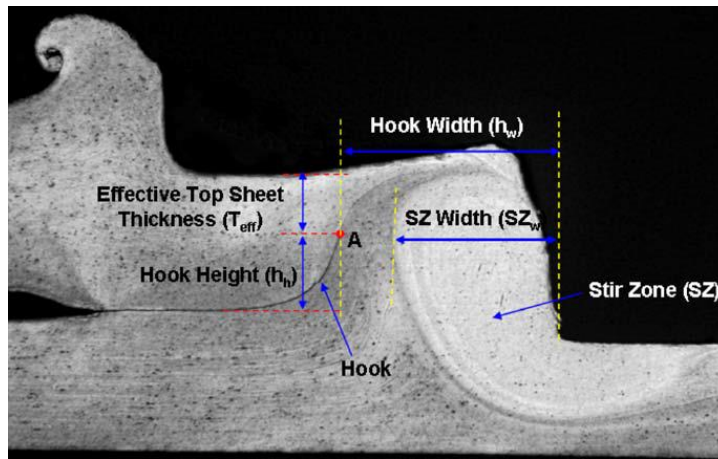


Figure 2-13: The typical macrostructure of a cross-section of a friction stir spot weld showing the different geometrical features of the weld (Badarinarayan, et al., 2009).

The fast growth in the use of FSSW technology in recent years has led to the development of several variations that modify this technique in an attempt to eliminate the exit hole (Babu, et al., 2012) and increase the welded area, which results in an increase in the weld shear strength. Some of these modifications involve the addition of a compound tool motion: for example, the FSSW-stitch, the FSSW-squircle, the FSSW-swing, and the FSSW-octopod (Tier, et al., 2013). A similar technique has also been developed which involves using a tool without a pin (or pinless tool) with or without a scroll-grooved shoulder surface (scroll tool). This tool modification aimed to eliminate the undesirable keyhole and “hooking”, which results from the probe (or the pin) in friction stir spot welding (FSSW). Using this tool resulted in tensile - shear strengths in welded joints with performance that was either comparable or superior to a conventional probe tool (Tozaki, et al., 2007; Bakavos & Prangnell, 2009; Bakavos, et al., 2011) as shown in Figure 2-14. Another process has been modified to refill the hole left by the probe by using an additional welding stage, as shown in Figure 2-15. The tensile shear strength and joint efficiency are consequently increased, due to the act of refilling the hole and the resultant increase in the nugget’s effective cross-sectional area (Prakash & Muthukumaran, 2011).

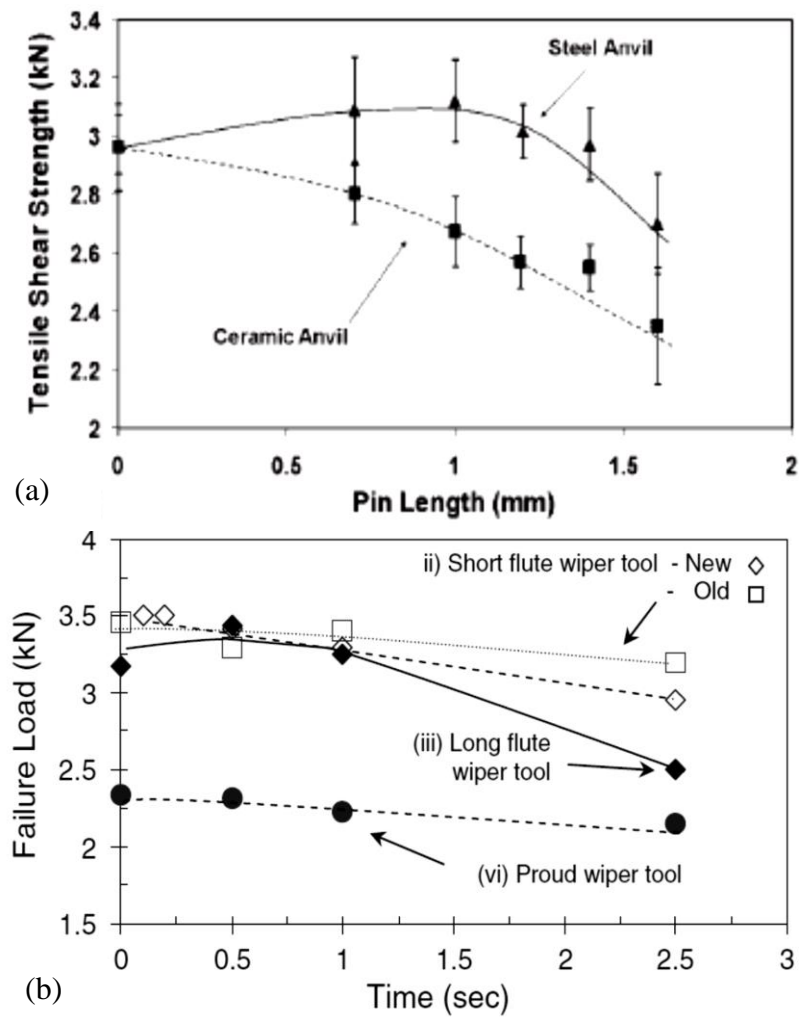


Figure 2-14: Failure loads of AA6111-T4 alloy sheets joined using FSSW (a) effect of pin length and anvil insulation (Bakavos & Prangnell, 2009) and (b) effect of weld dwell time for comparing the performance of the different wiper (pinless) tools (Bakavos, et al., 2011).

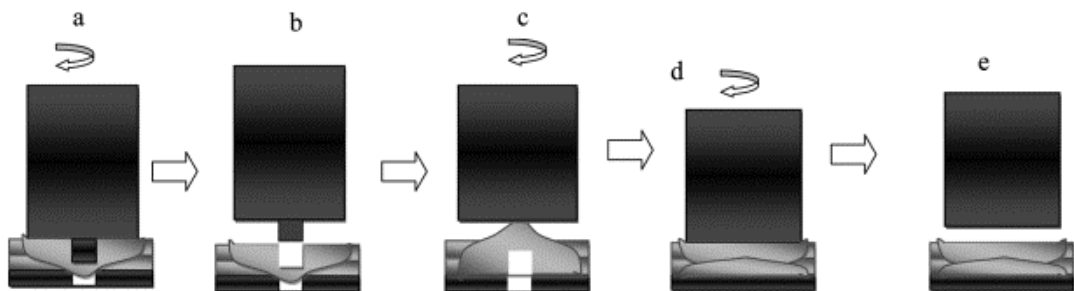


Figure 2-15: Schematic illustration of the friction stir spot welding refilling process developed by Prakash & Muthukumaran (2011).

### **2.6.3 Refill Friction Stir Spot Welding (RFSSW)**

Refill friction stir spot welding (RFSSW) (also known as FSpW) is a new solid state joining technology developed and patented by the Helmholtz-Zentrum Geesthacht (previously known as GKSS Forschungszentrum) in Germany (Parra, et al., 2011; Campanelli, et al., 2012a; Campanelli, et al., 2013a; Shen, et al., 2013). The technique is suitable for joining similar and dissimilar overlapping sheets (Parra, et al., 2011; Amancio-Filho, et al., 2011 a), particularly lightweight materials with low melting points (Campanelli, et al., 2012a) such as aluminium alloys, magnesium alloys (Parra, et al., 2011; Rosendo, et al., 2011) and thermoplastics (Oliveira, et al., 2010; Amancio-Filho, et al., 2011 b). This welding method is expected to have wide applications for joining body parts in the automotive industry (Uematsu, et al., 2008).

RFSSW was developed to eliminate, or reduce, one of the main disadvantages experienced by conventional FSSW (Campanelli, et al., 2012a; Campanelli, et al., 2013a): the formation of a keyhole in the FSSW which almost penetrates the lower sheet (Bozzi, et al., 2010; Bilici & Yüklér, 2012; Campanelli, et al., 2012a). The residual key hole is undesirable because it affects the mechanical properties (Prangnell & Bakavos, 2010; Bakavos, et al., 2011), reduces the effective area of the spot connection (Shen, et al., 2013), and decreases the corrosion resistance during service (Bakavos, et al., 2011).

The RFSSW process is accomplished using a non-consumable welding tool (Figure 2-16) consisting of three parts: a clamping ring, sleeve and pin (Amancio-Filho, et al., 2011 a; Parra, et al., 2011; Campanelli, et al., 2013a; Shen, et al., 2013). Two separate actuators move the pin and the sleeve up and down independently. A third actuator is used to move the clamping ring and welding head to clamp the work pieces. The clamping ring is important for two main purposes: (a) to hold the sheets together in the correct position during welding and (b) prevent flash formation by the plasticised material by working as a barrier (Rosendo, et al., 2011).

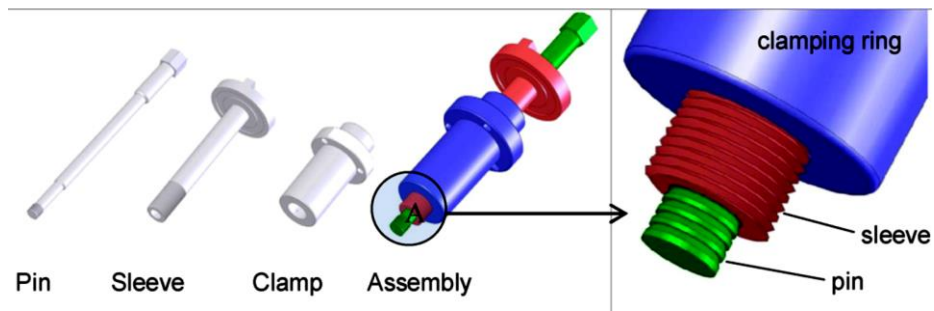


Figure 2-16: Schematic illustration of the RFSSW tool system showing a detailed view of the three parts: pin, sleeve and clamping ring (Tier, et al., 2013).

The RFSSW process is illustrated schematically in Figure 2-17, and can be operated with two different variants depending on the tool element which plunges into the metal sheet: these are the sleeve-plunge (SP) variant and the pin-plunge (PP) variant (Amancio-Filho, et al., 2011 a; Rosendo, et al., 2011; Tier, et al., 2013; Campanelli, et al., 2013a). However, the SP variant is the most logical approach, as most of the heat is generated by the sleeve. Regardless of which variant is used, the process consists of four stages and will be described here for the SP case:

- 1) In the first stage, the initial rotation of the sleeve and the pin begins and the welding head moves against the sheets to be joined with all of the tool faces aligned. As a result, the sheets are clamped between the welding head and a backing anvil to keep them tightly secured during the welding process (Rosendo, et al., 2011; Shen, et al., 2013).
- 2) In the second stage, both of the rotating tool parts (the sleeve and the pin) start moving either up or down in opposite directions to each other (Parra, et al., 2011; Campanelli, et al., 2013a) depending on the variant used. In the sleeve-plunge variant, the rotating sleeve moves downwards and is forced into the upper surface of the sheets to be joined. This action generates frictional heat (Amancio-Filho, et al., 2011 a; Campanelli, et al., 2012a) and deforms the material plastically. At the same time the pin is retracted and moves upwards to create a cylindrical space which accommodates the displaced plasticised material (Oliveira, et al., 2010; Tier, et al., 2013; Shen, et al., 2013).
- 3) When the plunged sleeve reaches a predetermined depth, the motion of the sleeve and pin is reversed and both of them retract to their original position in the upper sheet's surface (the third stage) (Mazzaferro, et al., 2009; Rosendo, et al., 2011). The plunged sleeve is sometimes kept rotating for a predetermined time (called the "Dwell time") in its deepest location to help increase the

material intermixing. The downward movement of the pin at this stage will force the plasticised material from the cylindrical cavity back into the keyhole left by the sleeve and refill it (Amancio-Filho, et al., 2011 b; Campanelli, et al., 2013a).

- 4) In the final stage, the tool is raised and the welding head removed. The result is a completely refilled hole with minimal material loss and a flat surface (Parra, et al., 2011; Campanelli, et al., 2012a; Campanelli, et al., 2013a; Shen, et al., 2013).

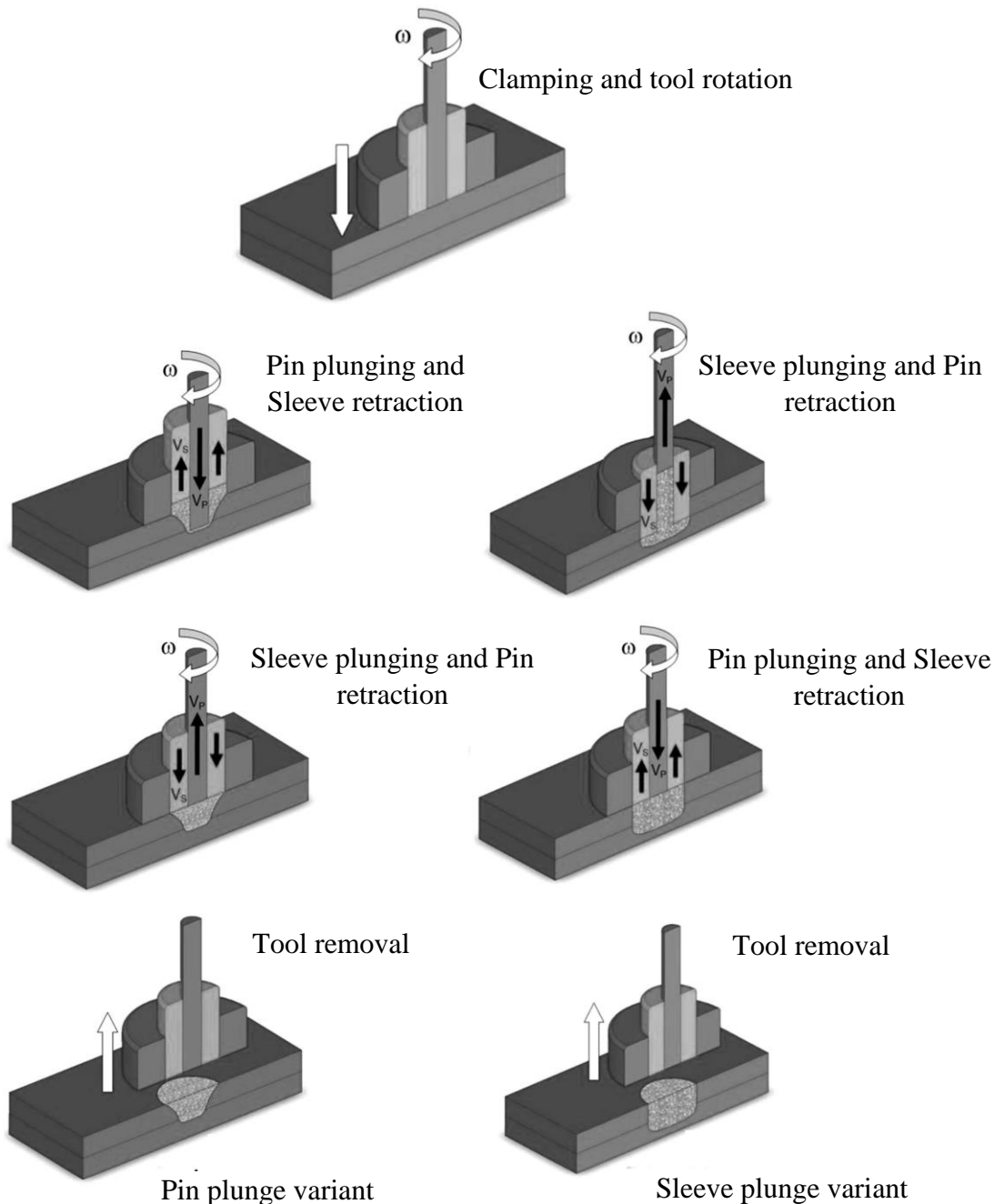


Figure 2-17: Schematic illustration of the two RFSSW process variants (Mazzaferro, et al., 2009).



## 2.7 Heat Generation in FSSW and RFSSW

Heat is generated in FSSW by two sources: the friction between the rotated tool and the workpiece, and the plastic deformation in the region of the welding (Commin, et al., 2009). During the FSSW process, several variables can affect the energy generation, such as the axial force, penetration depth, tool rotation rate, and tool design. The tool rotation has the greatest influence on the heat generation which is about 200 times the energy dissipated by the tool penetration. Therefore, the energy generated due to the downward motion of the tool can be ignored (Su, et al., 2006a). The total energy generated during friction stir spot welding ( $Q_{total}$ ) can be determined using the relation (2-2) (Schmidt & Hattel, 2008):

$$Q_{total} = \delta Q_{sticking} + (1 - \delta) Q_{sliding}$$
$$Q_{total} = \frac{2}{3} \pi \omega [\delta \tau_{yield} + (1 - \delta) \mu p] [(R_{shoulder}^3 - R_{probe}^3)(1 - \tan \alpha) + R_{probe}^3 + 3R_{probe}^2 H_{probe}]$$

Equation 2-2

Where:  $\delta$  is the contact state variable (dimensionless slip rate),  
 $\tau_{yield}$  is the material yield stress at the welding temperature,  
 $\mu$  is the friction coefficient,  
 $p$  is the uniform pressure at the contact interface,  
 $\omega$  is the angular rotation speed,  
 $\alpha$  is the cone angle,  
 $R_{shoulder}$  is the shoulder radius,  
 $R_{probe}$  is the probe radius, and  
 $H_{probe}$  is the probe height.

This equation is conceptually very useful, but it has some problems related in particular to the values of slip rate ( $\delta$ ) and the material yield stress ( $\tau_{yield}$ ), which are not constant and are difficult to calculate. With FSSW in particular, the tool contact area and the slip rate ( $\delta$ ) are not constant and change during the steps of the welding process due to the tool plunging. Meanwhile, the material yield stress (or flow stress) ( $\tau_{yield}$ ) is not constant either, and it changes with changing temperature and strain rate (as seen in Figure 2-18)

which in turn changes in line with the progress of the welding process (Colegrove, et al., 2007).

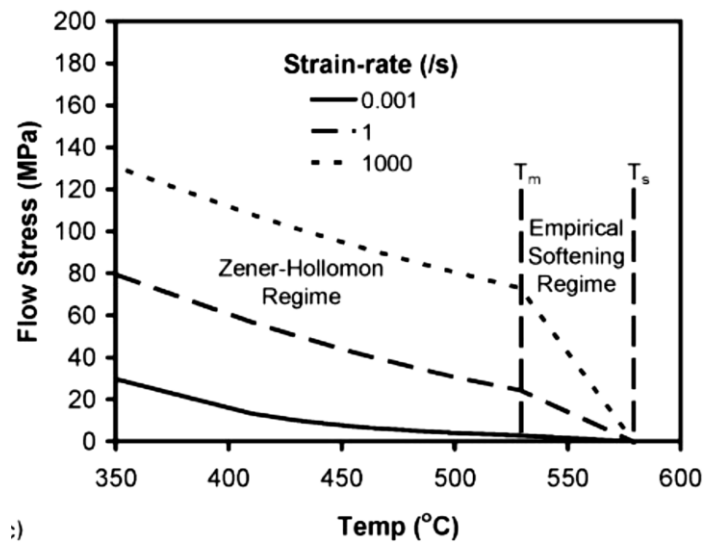


Figure 2-18: Constitutive behaviour of an AA6056 aluminium alloy during FSW ( $T_m=530^\circ\text{C}$  and  $T_s=579^\circ\text{C}$ ) ( $T_m$ : the softening temperature  $T_s$ : the solidus temperature) (Colegrove, et al., 2007).

During a conventional friction spot welding operation, a larger percentage of the energy generated (about 70%) is produced by the rotating pin. This situation is completely different from that generally shown during long seam friction stir welding. For instance, 80–99% of the energy is generated by the tool shoulder if the frictional heating is assumed to be the main heat source. The critical difference is that in FSW the tool shoulder remains in contact with the material of the stir zone during the entire welding operation. In contrast, the tool shoulder in FSSW only comes into contact with the workpiece near the end of the welding process (Su, et al., 2006a). This is one of the reasons why Bakavos and Prangnell (Bakavos & Prangnell, 2009; Bakavos, et al., 2011), developed the concept of ‘pinless tool’ FSSW for welding thin sheets.

In FSSW, the temperature profiles and cooling rates are affected by the material properties and welding variables. The maximum temperature in the weld zone should be high enough to soften the metal and reduce the resistance to the pin, but low enough to prevent melting of the metal. On the other hand, the amount of heat transferred to the tool affects its lifespan, besides if the heat generated is insufficient, this can cause pin breakage due to insufficient material softening (Chao, et al., 2003; Nandan, et al., 2008).

It has been found that only a small amount of the energy generated during FSSW is consumed to create the stir zone (Awang & Mucino, 2010). Su et al. have also reported that a small percentage (about 4.03%) of the total energy generated during the FSSW process is involved in the stir zone formation in Al 6061-T6 welds, and most of the remainder dissipates into the clamp, anvil support, tool assembly and the aluminium sheets (Su, et al., 2006a).

Cooling rates in welding processes can be more important than the heating rates (Singh, 2016) because they determine the sequence of precipitation in age-hardenable alloys. They also affect the grain-size, welded joint distortions, residual stresses, and hot crack initiation. The low cooling rate in FSW results from the diffuse heat source in the process and the relatively low welding speed (Nandan, et al., 2008). Increasing the heat input leads to slower cooling rates if other factors remain constant. Generally, the cooling rate is mostly affected by four weld features (Singh, 2016):

- 1) The size of the weld nugget which reflects the effective heat source volume.
- 2) The mass of the base metal and clamping which act as a heat sink.
- 3) The welding speed.
- 4) Material thermal conductivity.

There are several methods that can be used to measure the temperature during the welding process, the most common of which is using embedded thermocouples (Nandan, et al., 2008). Temperature has also been measured using an in-situ neutron diffraction technique, based on measuring changes in the lattice spacing to deconvolute the temperature and residual stresses (Woo, et al., 2007).

To date, no model in the published literature has been presented to determine the total energy generated during the RFSSW process, and very few papers have been written about temperature measurement and the simulation of the temperature distribution during this process. Shen et al. 2015 measured the temperature during the RFSSW cycle using thermocouples located between the sheets at different distances (2.66, 4.32, 6.07 and 7.56) from the nugget edge of a refill friction stir spot welded 7075-T6 aluminium alloy. The maximum temperatures observed at distances of 2.66 and 4.32 mm outside of the SZ were 470.9°C and 446.4°C respectively (Figure 2-19 a). The thermal profile (Figure 2-19 b) shows a very rapid increase in temperature before the start of the sleeve plunge, because both of the pin and sleeve were first kept in contact with the sheet

surface for 0.25 s while rotating (marked as  $t_1$  in the Figure 2-19 b). This step was carried out to generate frictional heat in order to reduce the force required for plunging (this represents the first stage in the RFSSW process explained in section 2.6.3). The temperature increases significantly from 280 °C to 470.9 °C with a heating rate of 40°C s<sup>-1</sup> during the plunging and retracting of the sleeve (marked as  $t_2$  and  $t_3$  in Figure 2-19 b), these events represent the second and third stages defined in section 2.6.3 respectively. The temperature then drops to 325°C with a cooling rate of 58°C s<sup>-1</sup> after the sleeve retracts to its original position (marked as  $t_4$  in Figure 2-19 b) and represents the fourth stage defined in section 2.6.3. The maximum temperature reached at the boundary of the nugget was estimated to be 501°C (Shen, et al., 2015). This peak temperature is close to the temperature of 527°C measured by Gerlich et al. when they used the standard FSSW process for joining an AA7075 aluminium alloy (Gerlich, et al., 2006).

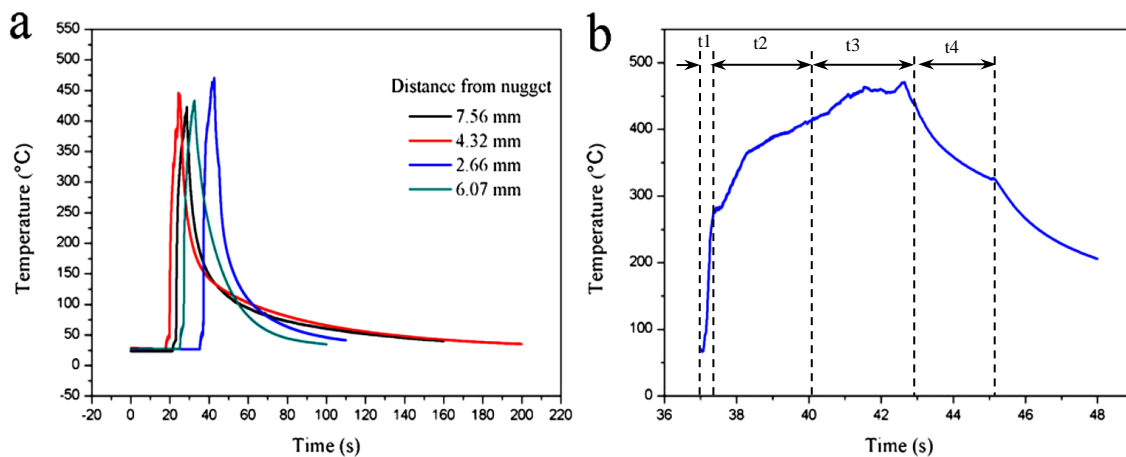


Figure 2-19: Temperature cycle during the complete welding process (a) in different distances from the SZ and (b) at a distance of 2.66 mm (Shen, et al., 2015).

In one of the few published simulations of the RFSSW process Zhao, et al., (Zhao, et al., 2016) used a computer FE method to model the temperature distribution during the plunge stage, as shown in Figure 2-20 a. This work predicted that the material near the bottom of the sleeve cavity and that flowed inside the sleeve cavity during the welding process would have a higher temperature compared with other regions in the weld, including the material near the outer edge of the sleeve. Three factors represent the reasons behind this temperature distribution:

- 1- A higher effective strain rate is experienced by the material stirred near the bottom of the sleeve cavity (see Figure 2-21), therefore, the heat generated due to plastic deformation is higher.
- 2- A relatively poor cooling condition was observed near the bottom of the sleeve cavity. This is because this area is generally cooled by the back anvil, which had a lower interfacial heat transfer compared to the surrounding base material.
- 3- In this location, the material was affected by the heat generated at both the inner and bottom surfaces of the sleeve.

However, it should be noted that in this work the peak temperature in the stir zone (530 °C) was higher than the eutectic melting temperature of the 7B04 aluminium alloy used in the simulation (475 °C), while the thermo-mechanically affected zone and the heat affected zone, showed peak temperatures (368 and 302 °C respectively; see Figure 2-20 b) that were lower than the solution temperature (465 °C) but higher than the base metal artificial ageing temperature (180 °C) (Zhao, et al., 2016).

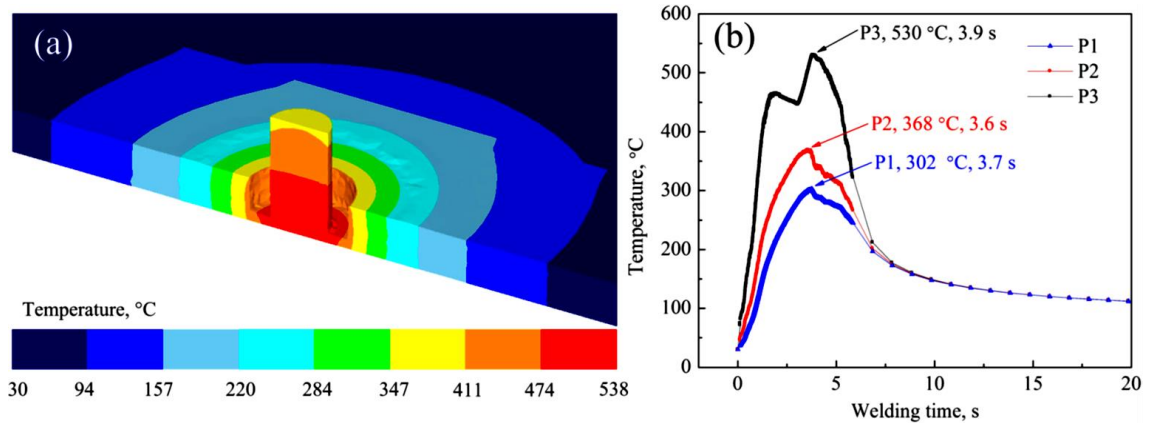


Figure 2-20: (a) Results of the simulated temperature distribution in the RFSSW process for a half weld at the welding time of 3 s and (b) thermal cycles in different tracked positions (where P1, P2 and P3 located at a distance of 9, 6 and 0 mm from the weld centre) (Zhao, et al., 2016).

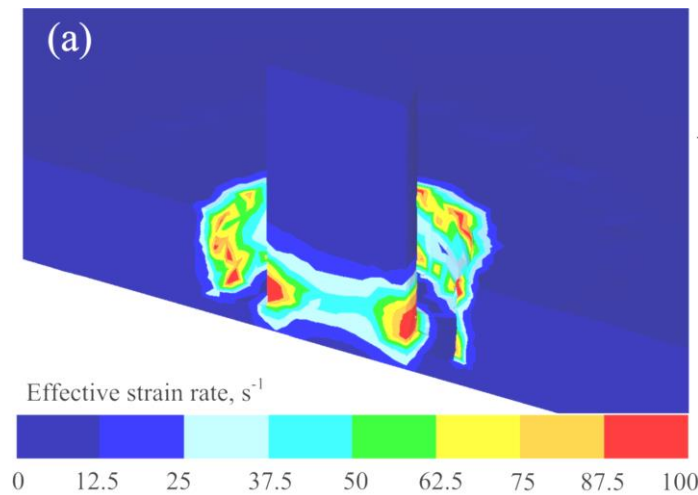


Figure 2-21: Results of the simulated strain rate distribution in an RFSSW process for a welding time of 3 s (Zhao, et al., 2016).

A significant problem with this research is that the temperatures were measured in locations far away from the stir zone (SZ). Moreover, the temperature measurements did not cover a wide range of welding parameters (such as tool rotation rate, dwell time, plunge depth and plunge rate) to clarify the effect of these parameters on the thermal distribution.

More published information is available on the temperature distribution and thermal cycle in Al-Mg dissimilar RFSSW, although the results are more complicated and have a different profile than for welding similar Al alloys, due to liquid formation at the weld interface. For example, a peak temperature of 437 °C was measured by Gerlich et al. which corresponds to the eutectic reaction temperature in the Al-Mg system (Gerlich, et al., 2005).

A typical thermal cycle for dissimilar RFSSW of Al-Mg from this work is shown in Figure 2-23. The temperature was measured by thermocouples embedded in the weld region with the configuration illustrated in Figure 2-22. During the first stage of the welding process (sleeve plunging), the temperature increased rapidly to a peak temperature of about 450 °C and then decreased to 370 °C. This decrease in temperature occurs due to the local melting of the material, which results in a decrease of the plasticised material viscosity. This process in turn leads to a reduction in the generation of frictional heating and has a significant effect on the heating rate. Later the temperature increases again to about 432 °C, because of the solidification of the local molten material. This temperature increase enhances the viscosity of the plasticised

material, leading to a greater plastic work rate, before decreasing to about 412 °C. The temperature shows a slight increase to 440 °C during the following two stages (the dwell and sleeve retraction periods). In these results (Figure 2-23), in spite of the difference in the material flow during the dwell and sleeve retraction stages, the temperature level in both stages remains relatively constant. A possible reason for this behaviour is an increase in the amount of the eutectic liquid, which might have resulted in temperature stabilisation. Finally, the temperature decreases to room temperature after the fourth welding stage (the surface dwell period) (Suhuddin, et al., 2013 a).

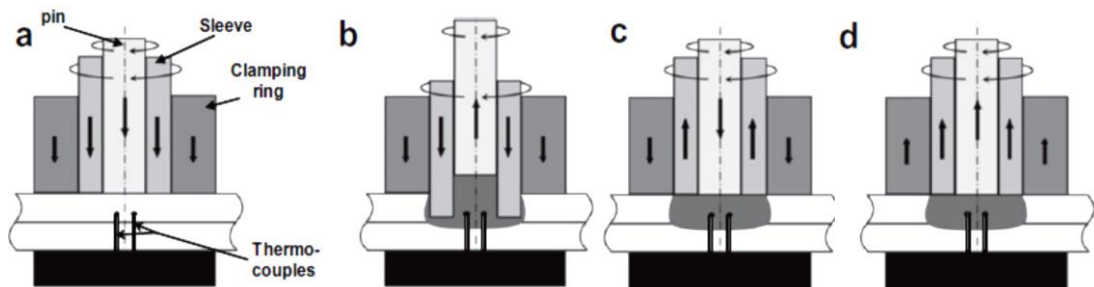


Figure 2-22: A schematic illustration of the RFSSW process with the placement of the thermocouples during the temperature measurements (Suhuddin, et al., 2013 a).

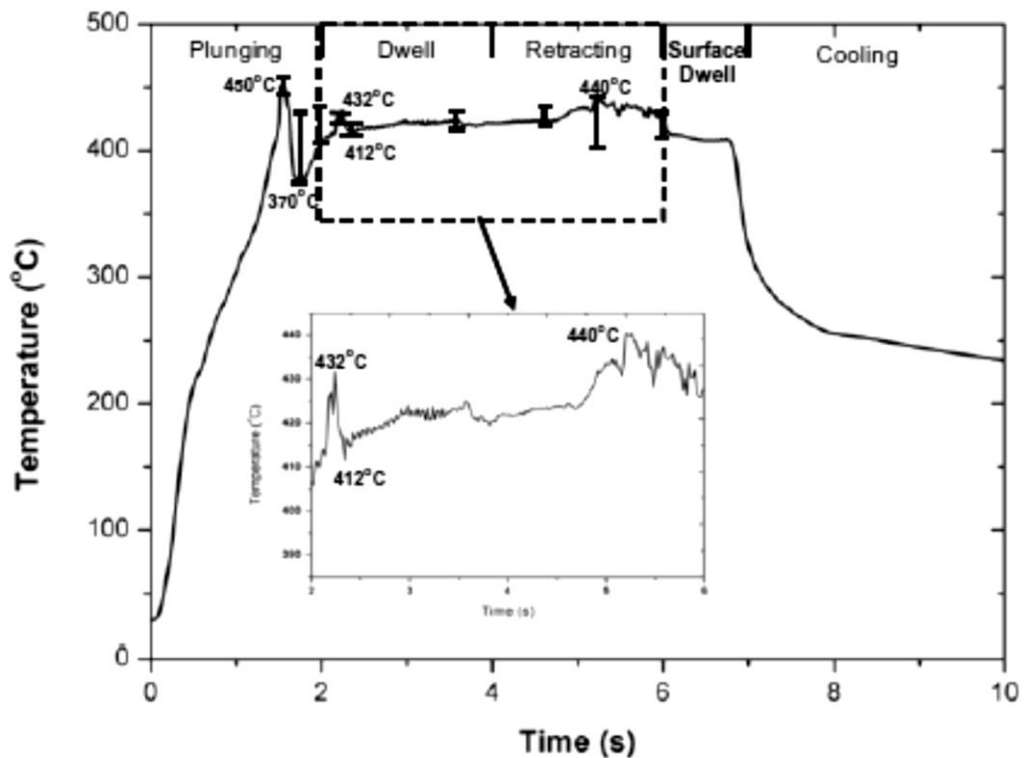


Figure 2-23: The temperature profile during RFSSW of an Al-Mg dissimilar joint. The diagram also shows the scattering of the key temperatures (Suhuddin, et al., 2013 a).

## **2.8 Effects of Welding Parameters on the RFSSW process**

In spite of the significant differences between refill friction stir spot welding (RFSSW) and traditional friction stir spot welding (FSSW), the two processes still have the same key welding parameters, which have a great effect on the properties of the welded joints. In terms of the joint performance produced by the two techniques, the key welding parameters are (Rosendo, et al., 2011; Parra, et al., 2011; Bilici & Yüklér, 2012; Shen, et al., 2013):

- 1- Tool rotational rate.
- 2- Plunge depth.
- 3- Plunge rate.
- 4- Dwell time.

A longer dwell time leads to greater heat generation from the tool in the weld. Indeed, a long dwell time in FSSW induces a larger weld area, which can increase strength, but at the same time this leads to a larger HAZ and, in dissimilar material welding, induces the production of a larger amount of intermetallic compounds (Jambhale, et al., 2015). It should be noted that the term ‘welding time’ or sometimes ‘total welding time’ refers to the period that results from the summation of the plunging, dwell and retraction times.

When the tool is plunged into the workpiece, both the tool and weld members are heated up. A greater plunge rate results in a greater heating rate and a more rapid effect on the microstructure at an earlier stage of the weld cycle. On the other hand, a fast plunge rate can adversely affect the tool life by increasing wear because the workpiece material is less softened during the initial plunging stage (Jambhale, et al., 2015).

There is no full agreement among researchers on which one of the welding parameters has the most influence on the quality of the welds implemented on Al alloys using the RFSSW method. Figure 2-24 shows that the tensile-shear strength of the RFSSW joints generally increases with increasing welding time, plunge depth and rotating rate, but it is noticeable that the welding time is the key factor which affects the quality of the welds (Amancio-Filho, et al., 2011 a; Yang & Yang, 2013). This conclusion agrees with the findings of other researchers (Parra, et al., 2011; Rosendo, et al., 2011; Shen, et al., 2015), because the welding time is a major parameter that controls the energy generated by the tool at a given tool rotation rate, which is required for material mixing to produce



a good joint between the welded sheets (Parra, et al., 2011; Yang & Yang, 2013). Moreover, increasing the plunge depth in combination with increasing welding time is generally found to result in an increase in the lap shear strength, as shown in Figure 2-25, due to the increase in nugget diameter that results from increasing these two parameters (Shen, et al., 2015).

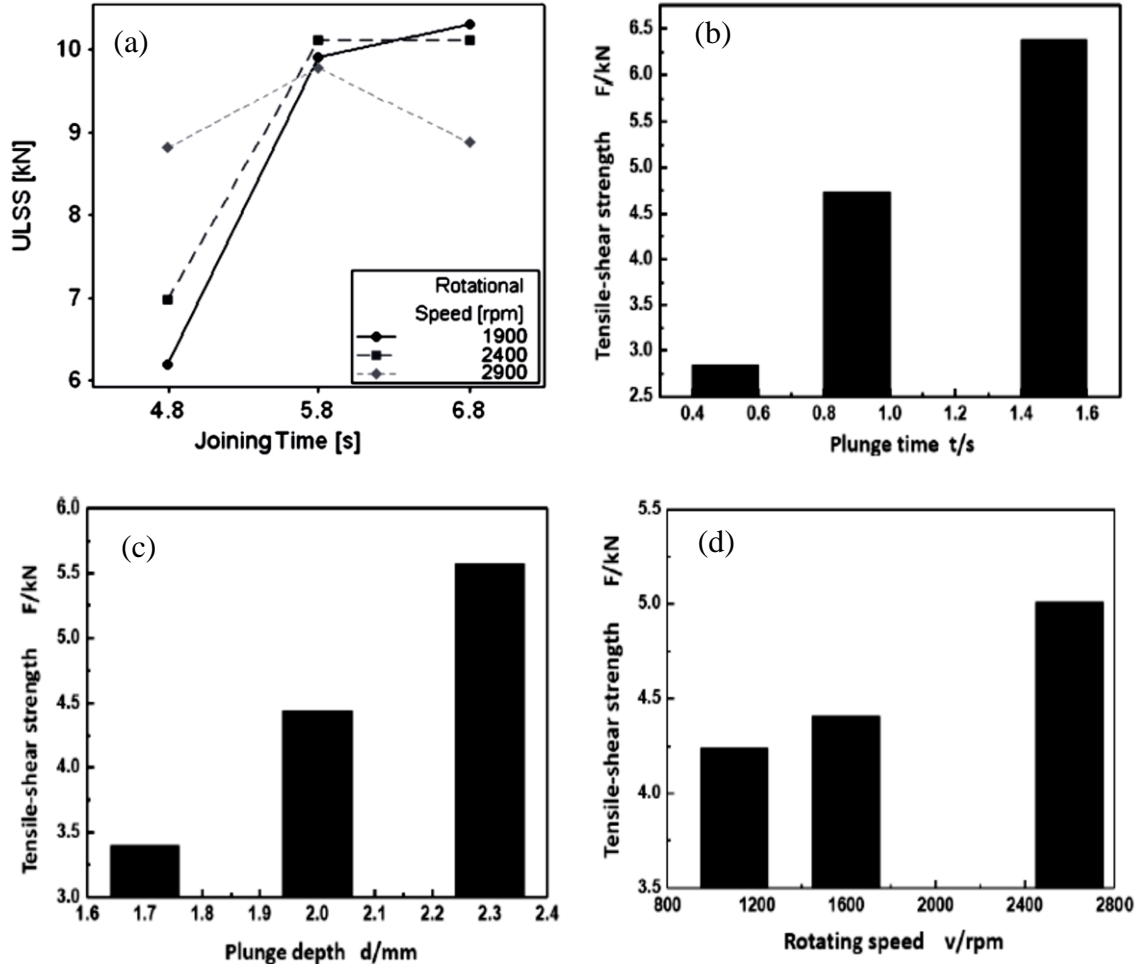


Figure 2-24: The effect of key welding parameters on the tensile shear strength of RFSSW joints: (a) the rotational rate and welding time (Amancio-Filho, et al., 2011 a), (b) plunge time, (c) plunge depth and (d) tool rotation rate (Yang & Yang, 2013).

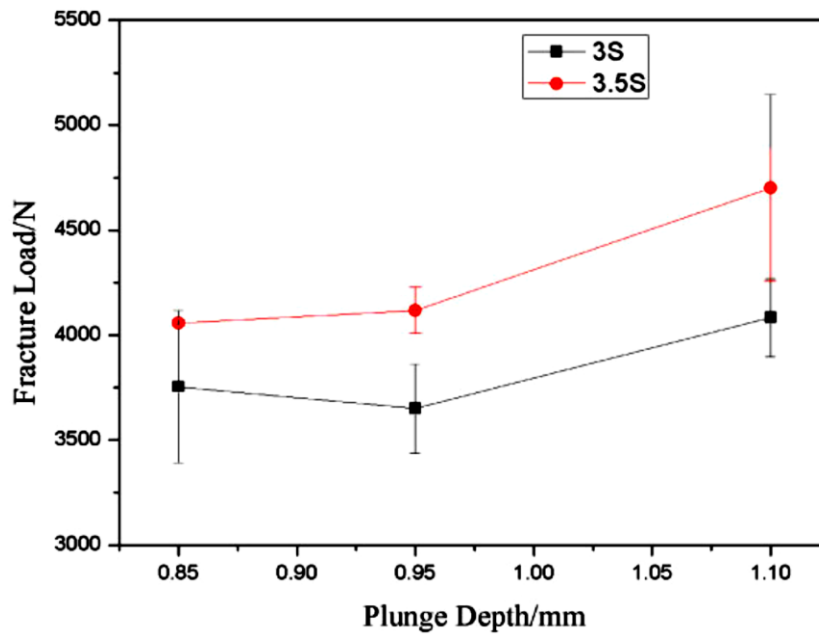


Figure 2-25: The effect of plunge depth and welding time on the lap shear strength of RFSSW joints (Shen, et al., 2015).

Some studies have shown conflicting results with those found by the first group of researchers summarised above. For example, Rosendo et al. (Rosendo, et al., 2015) found that welds produced using slower tool rotation rates (1900 rpm) and longer welding times ( $\geq 3$  s) showed higher strengths and higher fracture energies (Rosendo, et al., 2015). These results are similar to the findings of Tier et al. (Tier, et al., 2013) with a difference in tool rotation rate because of the use of a different material. In contrast, Cao et al. (Cao, et al., 2016) found that the most important parameter that affects the weld strength is the plunge depth, followed by the welding time and the tool rotational rate. This claim was based on the findings that an increase in the plunge depth, joining time or rotational rate increased the height of the hooking defect and this resulted in a decrease in the weld strength (Cao, et al., 2016).

By combining all the results of the above research, it can be seen that the performance of the welded joint depends on all the parameters together, as well as the material, and not on any of these parameters individually.

The effects of welding parameters on the performance of Al-Mg dissimilar RFSSWs are different to those observed when welding similar Al alloys. As shown in Figure 2-26, the effect of the tool rotation rate, plunge depth and dwell time on the lap shear strength (LSS) has large data scatter, due to the effect of the size of the IMCs and their distribution in the interfacial area between the weld members. This is caused by the

brittleness of the IMCs, which causes the joints to show a through-weld fracture mode, where the tip of the bonding area represents a location for crack initiation, which then propagates through the brittle IMC layers (Suhuddin, et al., 2014).

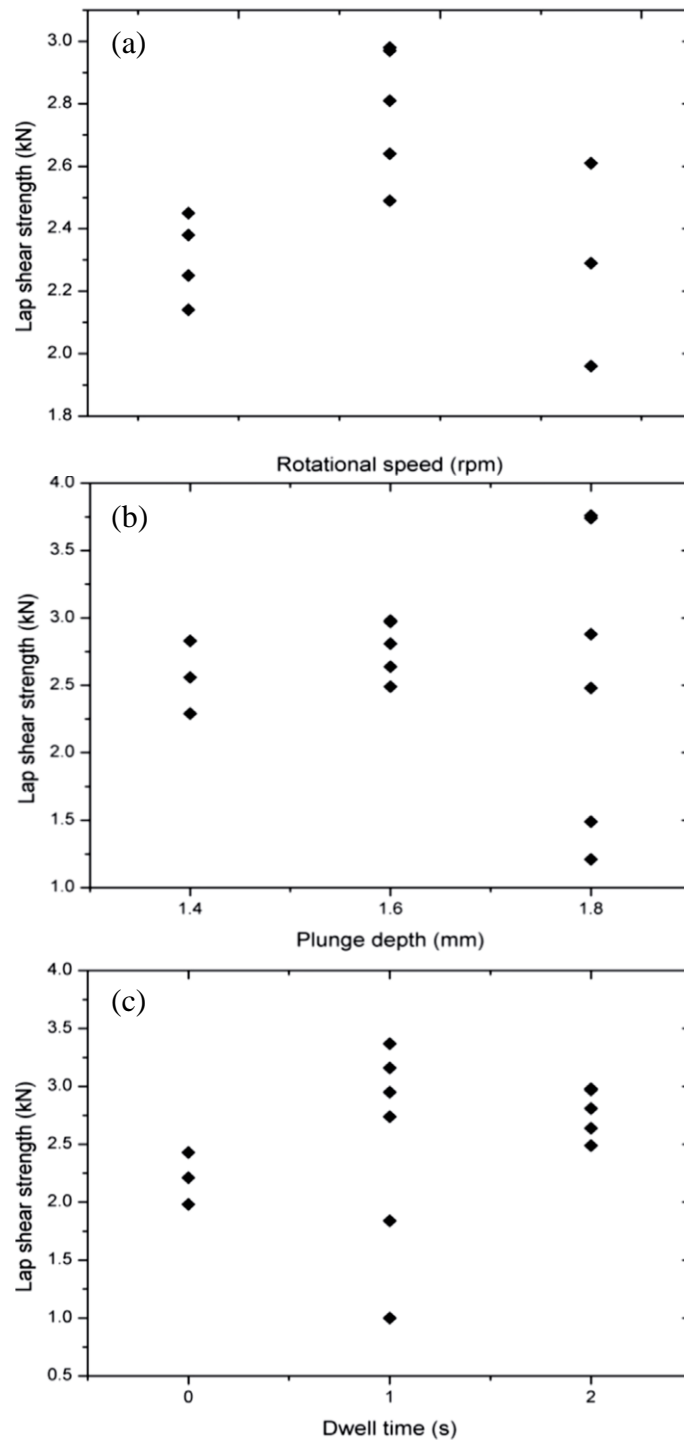


Figure 2-26: Effect of the RFSSW process parameters on the lap shear strength of AA5754 to AZ31 joints (Suhuddin, et al., 2014).

## **2.9 Material Flow in FSSW and RFSSW**

The material flow during the RFSSW process has an important effect in determining the weld quality; consequently, understanding the material movement is important for parameters optimisation and for the validation of numerical simulations (Kalagara & Muci-Küchler, 2010).

There are several techniques that can be used to visualise the material flow and highlight the material movement in different regions of the joint. These techniques include:

- 1- Using sheets of different materials (or sometimes different alloys of the same metal) in a lap, butt or butt-lap configuration. The material flow can then be visualised by etching the welded samples (Su, et al., 2006 b; Bakavos, et al., 2011).
- 2- Using marker particles of a second material, such as  $\text{Al}_2\text{O}_3$  or Cu, placed in holes drilled in the sheets before welding. To visualise the material flow, etching can also be used in this method (Su, et al., 2006 b; Kalagara & Muci-Küchler, 2010).
- 3- Use of marker material with a very high difference in density from the welded material; for instance, using gold or tungsten with aluminium welds. The material flow in this method can then be visualised using computed x-ray tomography (Bakavos, et al., 2011).

Currently, only a partial understanding of the material flow during FSSW has been achieved due to the high complexity of the process. Investigations in this field have shown that variables that affect the material flow pattern significantly include the tool geometry, welding parameters and the material to be welded (Yuan, et al., 2012).

The most widely accepted model for the material flow in the conventional FSSW process is shown in Figure 2-28, which is based on the findings of experimental investigations conducted by Su et al. and Su et al. (Su, et al., 2006 b; Su, et al., 2007) shown in Figure 2-27. The model suggests that during the dwell period, a ribbon of contiguous lamella of the two materials being welded (AA5754 and AA6111 in this situation) is moved downwards by the thread of the pin as the tool rotates. When the lamellae are discharged from the bottom of the pin thread it moves outwards and

upwards in a helical vertical rotational flow, before moving back towards the tool periphery and downwards again (Su, et al., 2006 b; Su, et al., 2007; Gerlich, et al., 2008). These results are consistent with the findings of Yang et al. on the material flow during FSSW of AZ31 Mg sheets, using Cu foil in the interface between the two sheets as a tracer material (Yang, et al., 2010).

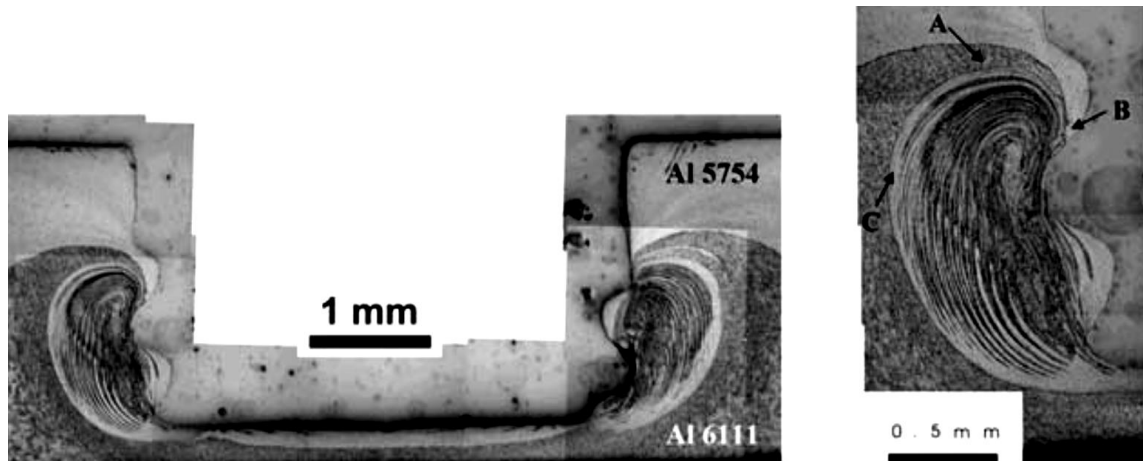


Figure 2-27: Interlamellar regions produced during dissimilar Al 5754-Al 6111 FSSW using a threaded pin tool (Su, et al., 2007).

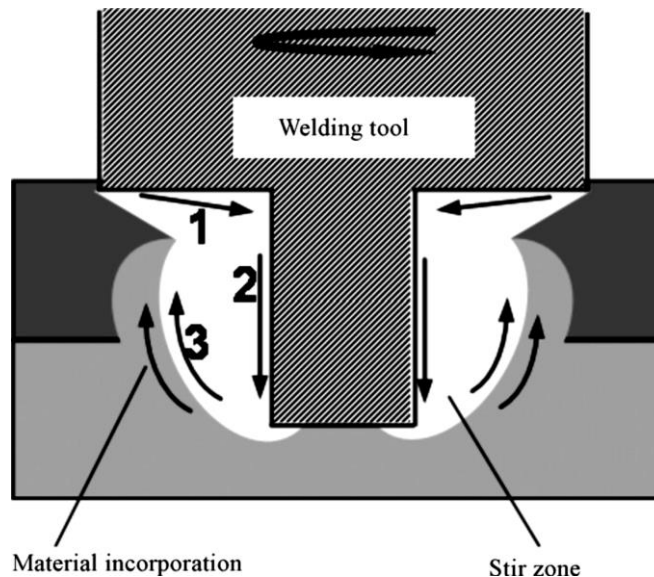


Figure 2-28: Schematic illustration of a material flow model during FSSW: (1) the material underneath the shoulder moves towards the root of the pin, (2) the material spirals downwards along the pin surface, (3) the plasticised material follows a helical rotational path upwards (Yang, et al., 2010).

In spite of the “simple” design of a pinless tool, it has been found that the material flow in the weld still exhibited the complexity indicated in Figure 2-29. The tool surface features exerted a strong influence significantly increasing the penetration of the plastic zone into the lower sheet. In addition, the increased dwell time caused the material flow to develop multiple layers of the two alloys (Figures 2-29 a and c). Surface features on the tool also caused the more complex flow pattern shown in Figures 2-29 b and d, described by the material flow model shown in Figure 2-29 e (Bakavos, et al., 2011).

By using high-resolution X-ray tomography with a gold layer as tracer material, Bakavos et al. showed that the weld interface, which was marked by a uniform sputter-deposited gold layer, developed a dished nature as a function of dwell time, as seen in Figure 2-30 (Bakavos, et al., 2011).

To understand the material flow behaviour in an FSSW joint implemented by a pinless tool Reilly et al. (2015) conducted an experimental investigation and developed a simulated kinematic model. Their experiments revealed that the distinctive shape of the metal flow occurs because material in the welding area under the tool is separated into two regions. One region in the centre of the joint sticks to the tool, and a second annular slip region towards the outer periphery of the joint provides a transition for the material from the sticking velocity ( $\omega r$ ) at some radius in the central region and the stationary surrounding material. Their interpretation of the material flow has been confirmed by kinematic modelling (Figure 2-31). The layering of material is achieved with purely circumferential flow and the horizontal layers in a cross-section view are related to the material sticking to the tool. The upward bend of the layers in a vertical direction at the edge of the weld zone satisfies the model boundary condition of zero velocity in the surrounding material (Reilly, et al., 2015).

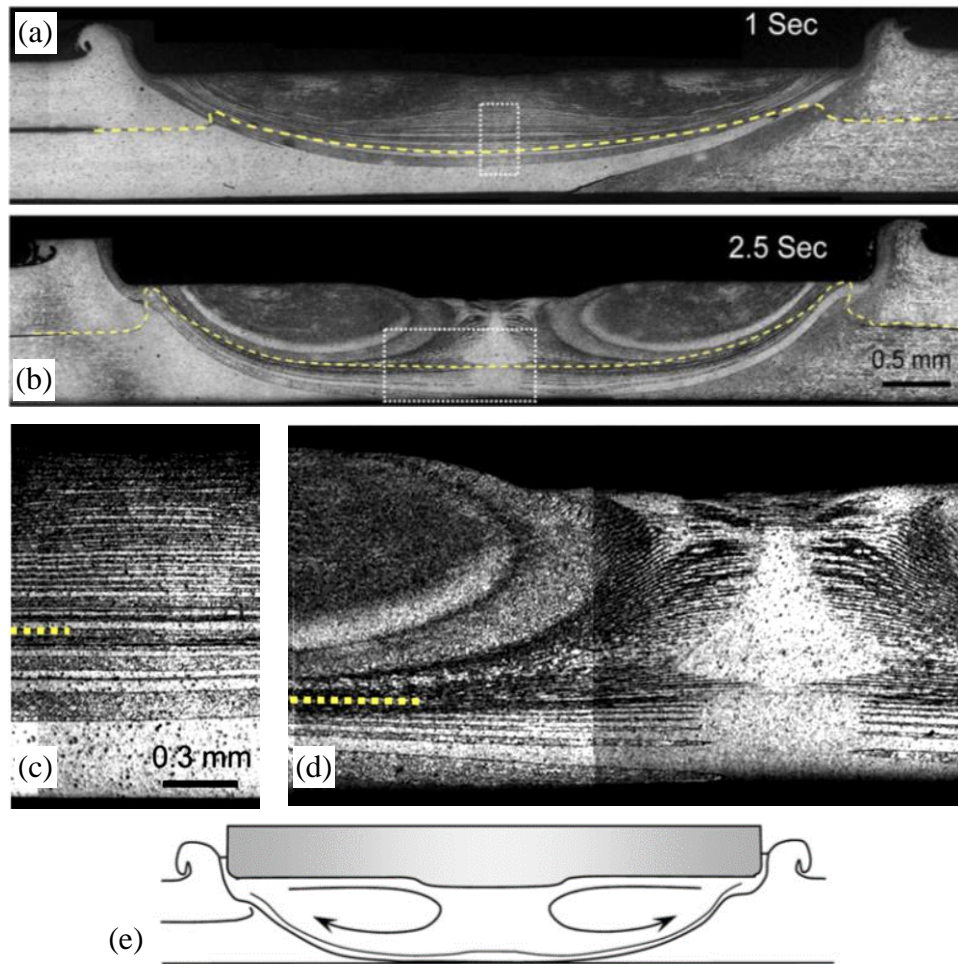


Figure 2-29: Material flow observed with a pinless tool from welds produced with the upper and lower sheets split through the weld centre into dissimilar copper content alloys; cross-section views weld formation with a 0.2-mm plunge and a dwell time of: (a) 1.0 s and (b) 2.5 s. (c) and (d) show magnified views from regions highlighted with white rectangles in (a) and (b) respectively, and (e) provides schematic diagram indicating the material flow. The dashed lines indicate the position of the weld line determined by X-ray tomography (Bakavos, et al., 2011).

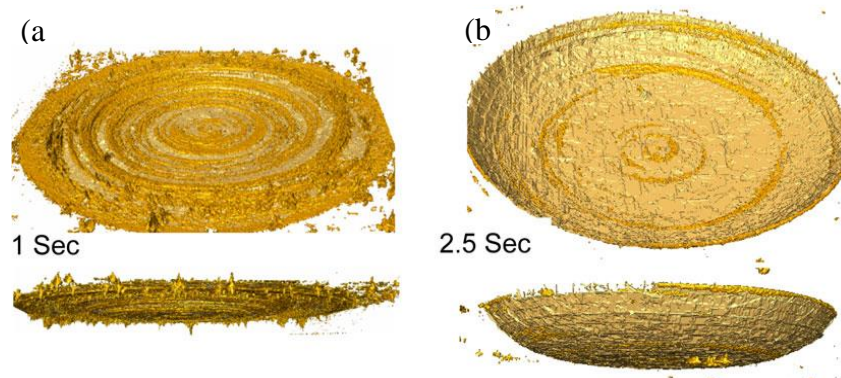


Figure 2-30: X-ray tomography results showing the dished nature developed by the weld interface (marked by an original uniform sputter deposited gold layer) for welds produced with the pinless tool, as a function of dwell time (Bakavos, et al., 2011).

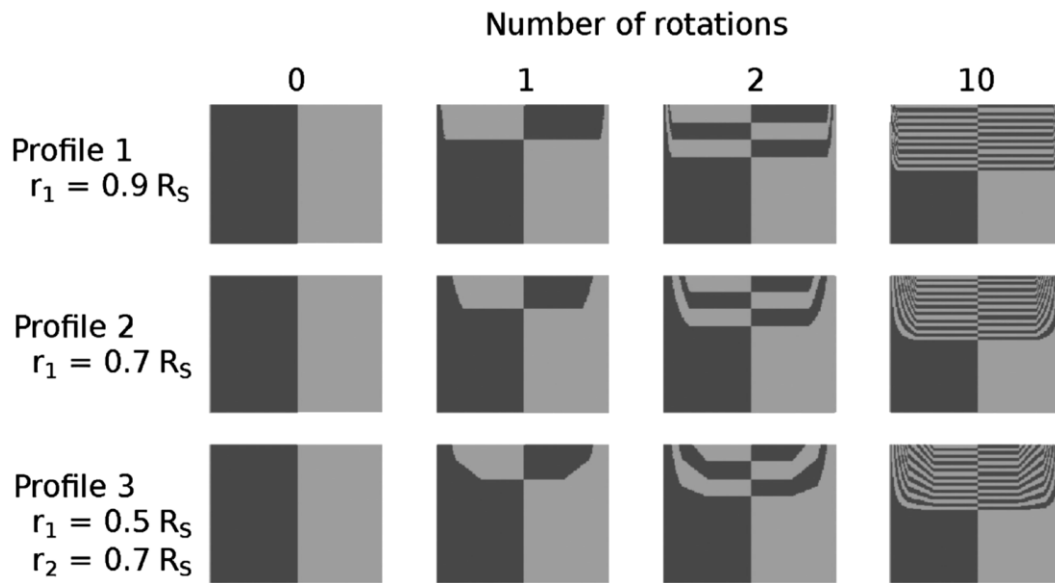


Figure 2-31: Cross-sectional views of a kinematic model after different numbers of tool rotations, for three surface stick-slip conditions (velocity profiles 1, 2 and 3 respectively; where  $r_1$  is the radius at which slipping first occurs, and  $r_2$  refers to the radius from which slipping starts to decrease linearly to zero at the tool periphery radius ( $R_s$ )) (Reilly, et al., 2015).

A very limited number of papers have been published concerning material flow in refill friction spot welding (RFSSW). The RFSSW process is also a double-acting process, meaning that the material flow is more complicated than in FSSW.

Figure 2-32 shows the results of the numerical simulation for the material flow behaviour during RFSSW of the Alclad 7B04-T74 aluminium alloy carried out by Zhao et al. (2016). The results reveal that the material flows rotationally and symmetrically with respect to the centre of the weld, driven by the rotation of the welding tool. As seen in Figure 2-32a, the flow velocity of the material in the sleeve cavity is much higher than that of the material near the outer edge of the sleeve. During the sleeve plunging stage, the material flows from the bottom and the periphery of the sleeve into the sleeve cavity (as marked by a red arrow in Figure 2-32b). However, during the sleeve retracting stage, the pin extrudes this material and forces it to flow downwards out of the cavity, then it continues flowing horizontally and upwards to fill the gap left by the sleeve retracting (as marked by a red arrow in Figure 2-32c). This path of the material flow results in upward curving of the hook, the bonding ligament with a “U-shaped” morphology, and upward distortion of the grains in the thermomechanically-affected zone (TMAZ) (Zhao, et al., 2016).



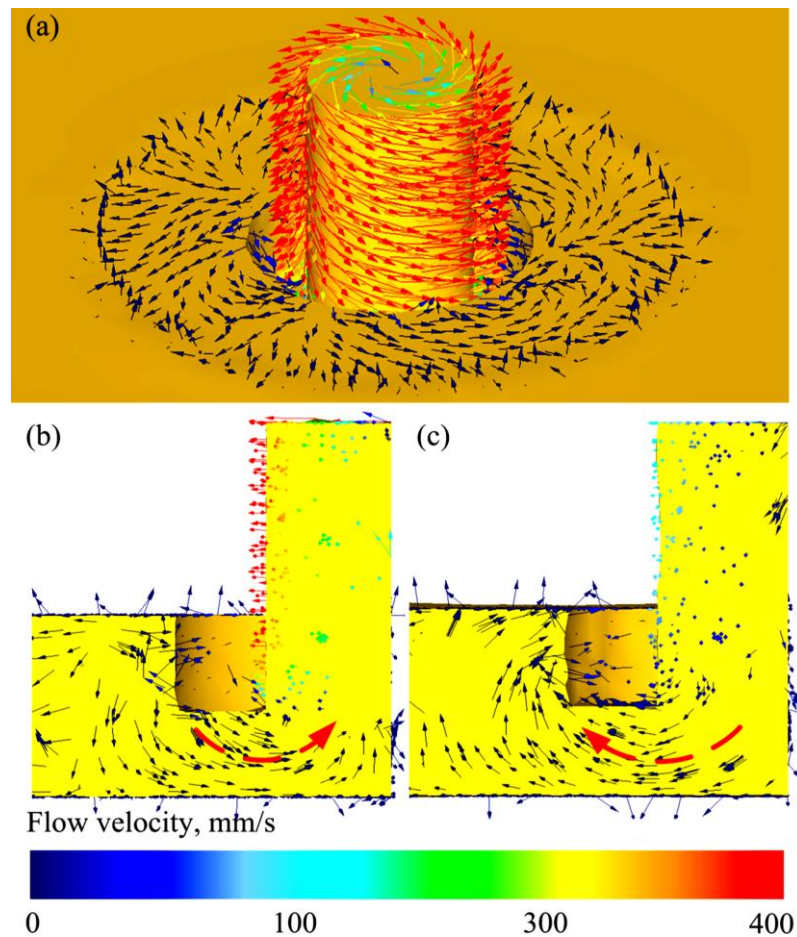


Figure 2-32: Simulation results of material flow during RFSSW (a) velocity distribution of material flow on the weld surface at a welding time of 3 s (during the sleeve retracting stage), and velocity distribution for material flow in the weld half-cross-section during sleeve, (b) plunging and (c) retracting (Zhao, et al., 2016).

Suhuddin, et al., (2011) proposed a pattern for vertical material flow during the RFSSW of dissimilar welds between AA5754 aluminium and AZ31 magnesium alloys, which is shown schematically in Figure 2-33. The plasticised material is forced into the cylindrical cavity generated by the pin retraction by the sleeve plunging (step a) and then the pin forces the plasticised material back to its original location (step b). This material flow pattern is important because it explains the shape and the distribution of the intermetallic compound IMC (grey areas) seen throughout the cross-section of the weld (Suhuddin, et al., 2011).

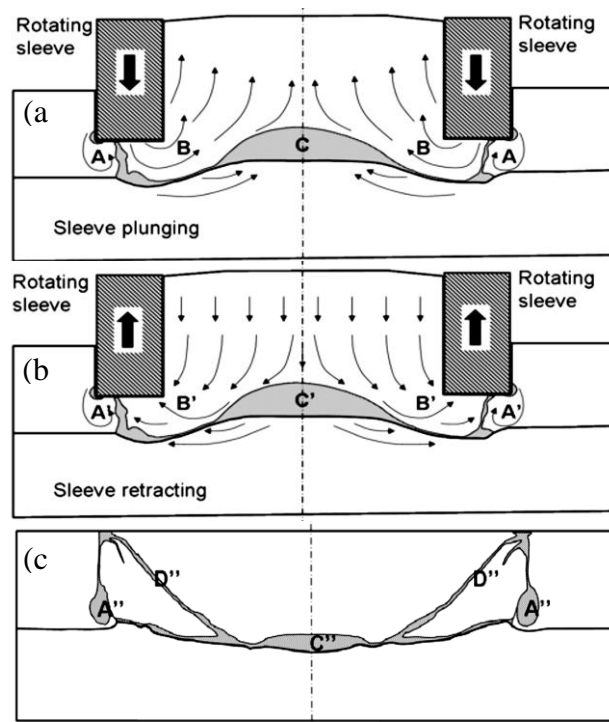


Figure 2-33: Material flow in RFSSW during sleeve-plunging (a), sleeve-retracting (b) and the final intermetallic compound distribution (c) (Suhuddin, et al., 2011).

## 2.10 Microstructure Formation and Weld Defects in Al-Al Similar Friction Stir Spot Welds

### 2.10.1 Microstructure Formation in Al-Al Similar Welds

Heat-treatable aluminium alloys can be strengthened using precipitation hardening through ageing, naturally or artificially, from the solution-heat-treated condition. In welding, the microstructure of such materials changes as a result of the heat allied with welding processes (Nandan, et al., 2008). Heat generation and plastic deformation resulting from the tool rotation can cause notable changes in the microstructure, which modify the mechanical characteristics of the material locally around the joint (Fanelli, et al., 2012). In RFSSW, the microstructures of the welded joint show variations in the grain sizes across both the width and the thickness (Shen, et al., 2013). In general, the microstructures of an RFSSW joint can be classified into four regions, when moving from the far edge towards the centre of the joint. The first region is the base metal (BM), where there are no metallurgical changes as a result of the welding process (Fanelli, et al., 2012). The heat-affected zone (HAZ) is the second region, in which both the microstructure and mechanical properties change only because of the welding thermal cycle (Mazzaferro, et al., 2009). The third region is the thermo-mechanically

affected zone (TMAZ). This region can be detected from the distortion of the grains compared with the base material. This grain structure is the result of two factors: the heat transferred from the stir zone and plastic deformation due to the rotated and plunged tool (Parra, et al., 2011; Rosendo, et al., 2011; Fanelli, et al., 2012). The last region is the nugget (sometimes called the stir zone (SZ)); in this region the grains are very refined and equiaxed (Parra, et al., 2011). The appearance of the microstructure in this zone is associated with dynamic recrystallisation, which results from the very high strain experienced during the plunging stage and the thermal cycle imposed by the process (Gerlich, et al., 2007; Gerlich & Shibayanagi, 2009; Parra, et al., 2011).

The investigation of the cross-section of RFSSW of AA6181 welded joints using optical microscopy (OM) in Figure 2-34, shows only two distinct weld regions in addition to the base metal, the SZ and TMAZ, because in this sample the HAZ cannot be easily distinguished from the base metal. However, it can be located using microhardness profiles of the joint cross-section, as shown in Figure 2-35, where it shows a lower hardness level compared with the base metal and the stir zone. Further to this observation, it can be distinguished from the TMAZ because it does not contain distorted grains (Parra, et al., 2011; Rosendo, et al., 2011). The HAZ is caused primarily by overageing of the parent alloy. In the weld centre, with heat-treatable aluminium alloys, the temperature increase is usually sufficient to solution-treat the material, which leads to post-weld natural ageing of the material. This effect, combined with overageing in the HAZ, leads to the ‘W’ shaped hardness profile typically seen across the weld zone in FSSWs (Bakavos & Prangnell, 2009). More details on the behaviour of specific alloys during welding is provided in section 2.12.4.

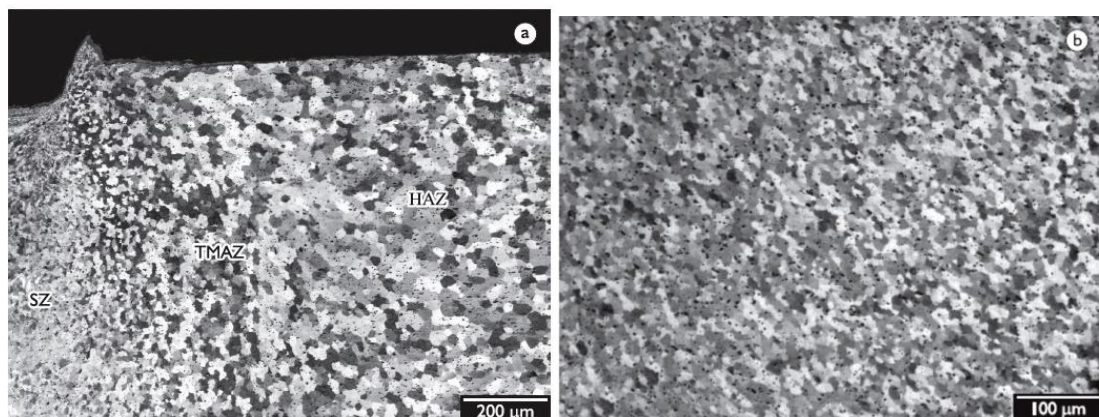


Figure 2-34: Optical micrograph of the cross-section of an RFSSW joint, of AA6181-T4 aluminium alloy, showing (a) the three weld regions SZ, TMAZ and HAZ, and (b) refined microstructure in the SZ (Parra, et al., 2011).

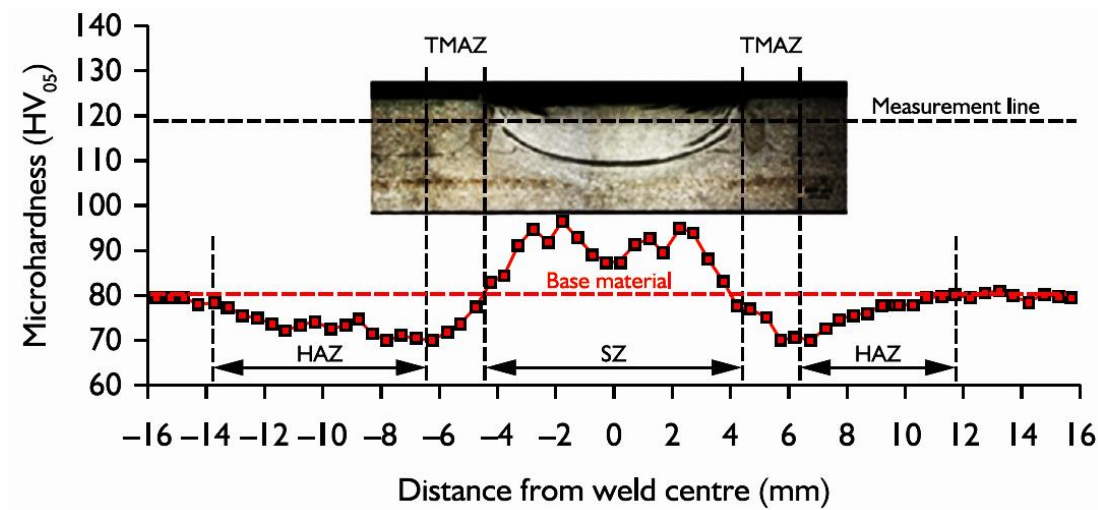


Figure 2-35: Microhardness profile measured in the middle of the upper sheet at the cross-section of an RFSSW joint of AA6181-T4 aluminium alloy (Parra, et al., 2011).

### 2.10.2 Weld Defects in Al-Al Similar Welds

Three geometric and metallurgical features that can be classified as defects can be seen in RFSSW joint cross-sections: hooking, partial bonding and bonding ligaments (shown in Figure 2-36). These defects have been found to have a significant effect on the joint failure strength under tensile shear loading by affecting the fracture mechanism (Rosendo, et al., 2011; Rosendo, et al., 2015).

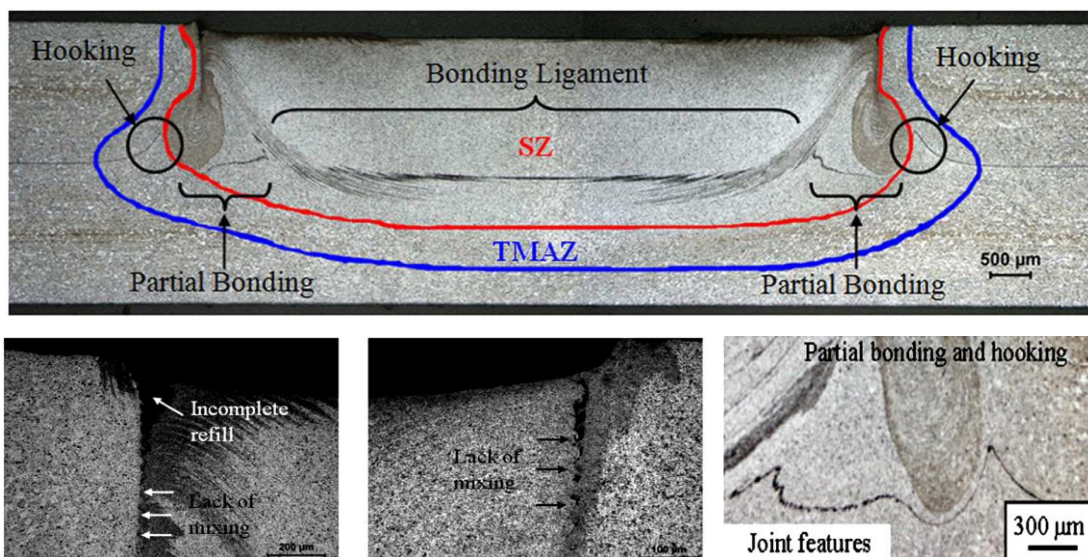


Figure 2-36: Macrographs of RFSSW joint cross-section showing detrimental weld zone, geometric/metallurgical features and weld defects (Rosendo, et al., 2011; Rosendo, et al., 2015).



Hooking is a geometric feature that arises from the displacement of the weld interface creating a ‘V’ shape with a sharpened edge pointing to the upper surface. A possible reason for this hook formation is deformation of the lower sheet during the final stages of the welding process, when the pin of the tool pushes the material, which was previously displaced, back to its initial position, leading to bending of the sheet interface. However, two different types of hook defect have been detected (Cao, et al., 2016) based on their location. They have been found to be closely related to the sleeve plunge depth (see Figure 2-37) and their height increases with increasing plunge depth, welding time, and tool rotational rate, as seen in Figure 2-38 (Cao, et al., 2016).

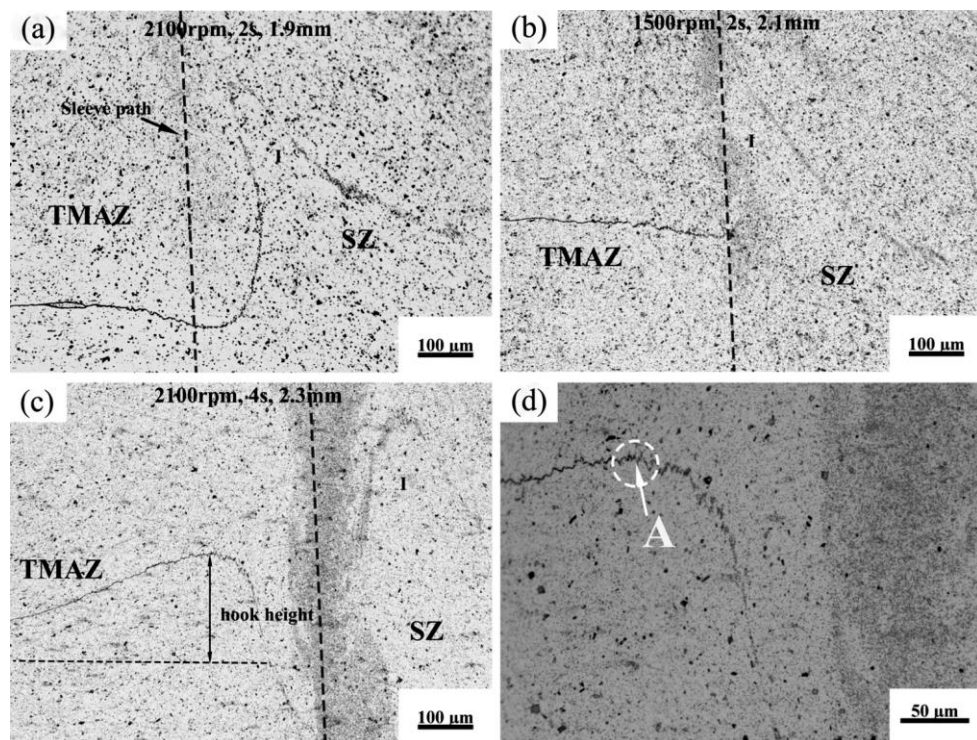


Figure 2-37: Different types of hook defect in RFSSW welds made at (a) 2100 rpm, 2.0 s and 1.9 mm; (b) 1500 rpm, 2.0 s and 2.1 mm; (c) 2100 rpm, 4 s and 2.3 mm; and (d) magnified view of a hook defect in (c) (Cao, et al., 2016).

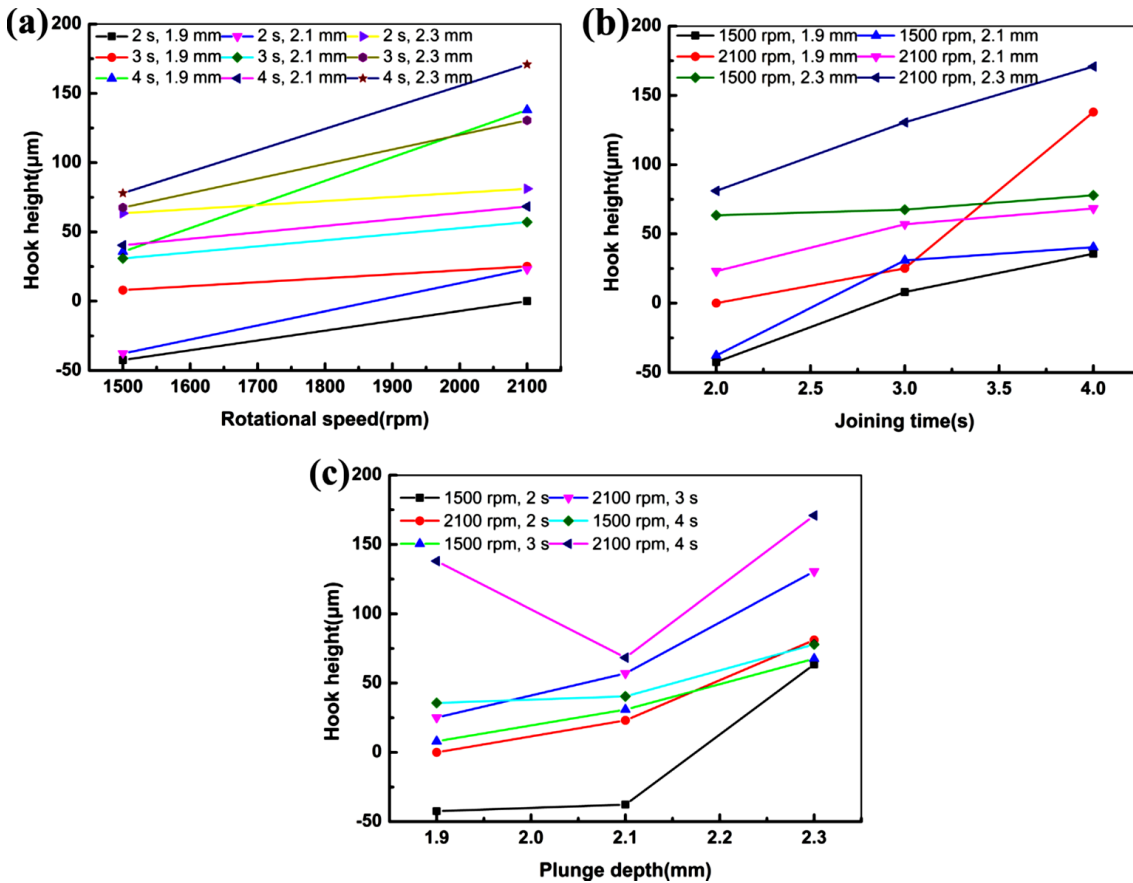


Figure 2-38: The effect of welding parameters on the hook height: (a) rotational rate, (b) joining time, (c) plunge depth (Cao, et al., 2016).

Partial bonding is a transition region in which the connection between the joined sheets is discontinuous and not very strong. The appearance of partial bonding in joint cross-sections usually looks like an uneven short line (Parra, et al., 2011; Rosendo, et al., 2011; Rosendo, et al., 2015), where a ‘bonding ligament’ is a high strength region of good adhesion between the joined sheets. The ends have a characteristic shape resulting from the material flow during the process, particularly when the plasticised material is pushed back to its original position by the pin in the third stage of the welding process (Parra, et al., 2011; Rosendo, et al., 2011; Rosendo, et al., 2015).

The combination of welding time and rotational rate have a significant effect on the generation of these features. In addition to these three features, a number of other weld defects have been detected in the cross-sections of some of the welds, including incomplete refilling, voids, and lack of mixing between metals (Parra, et al., 2011; Rosendo, et al., 2011; Shen, et al., 2013; Rosendo, et al., 2015). The presence of these defects in the welds is related to the material flow during the welding process (Shen, et al., 2013), and they are only seen in welds that are produced using welding times that

are too short, perhaps because of an excessively low-energy input. (Rosendo, et al., 2015).

## **2.11 Microstructure Formation of Dissimilar Al-Mg Spot Welds**

An interfacial reaction in dissimilar metal welding is the main metallurgical factor that affects the performance of the joints, especially if the dissimilar materials produce brittle intermetallic phases.

In RFSSW of Al to Mg, IMCs are generally found to be distributed at the interface between the base materials and in the Al upper sheet, as shown in Figure 2-39 (a) (Suhuddin, et al., 2013 b). The IMC distribution is affected by the material flow induced by the tool movement (Suhuddin, et al., 2013 b; Suhuddin, et al., 2014). In Al to Mg welds microstructure examination and EDS chemical composition analysis of the weld interface at a location under the sleeve commonly shows chemical compositions corresponding to two intermetallic compounds:  $\text{Al}_{12}\text{Mg}_{17}$  and  $\text{Al}_3\text{Mg}_2$ , as seen in Figure 2-40 (Suhuddin, et al., 2014). The total thickness of the phases in the weld centre shown in Figure 2-39a is about 500  $\mu\text{m}$ , and the microstructure consists of two phases, as shown in Figure 2-39b, a grey structure with a Mg content of 48-65 at.% and a mixed grey and black structure (a eutectic structure ) with a higher Mg content of 65-80 at.%. According to the equilibrium Al-Mg phase diagram (see Figure 2-58), the grey phase corresponds to  $\gamma\text{-Al}_{12}\text{Mg}_{17}$  and the eutectic structure (the mixed grey and black structure) contains  $\gamma\text{-Al}_{12}\text{Mg}_{17}$  and  $\delta\text{-Mg}$  (Suhuddin, et al., 2013 a; Suhuddin, et al., 2013 b).

The presence of a eutectic structure in the microstructure of Al-Mg RFSSW has also been reported by Suhuddin et al. in two separate studies and provides evidence of the formation of a liquid phase during the welding process (Figure 2-41) (Suhuddin, et al., 2013 b; Suhuddin, et al., 2014). This occurs because of the low-melting-point eutectic reactions found in the Al-Mg system (about 437 °C).

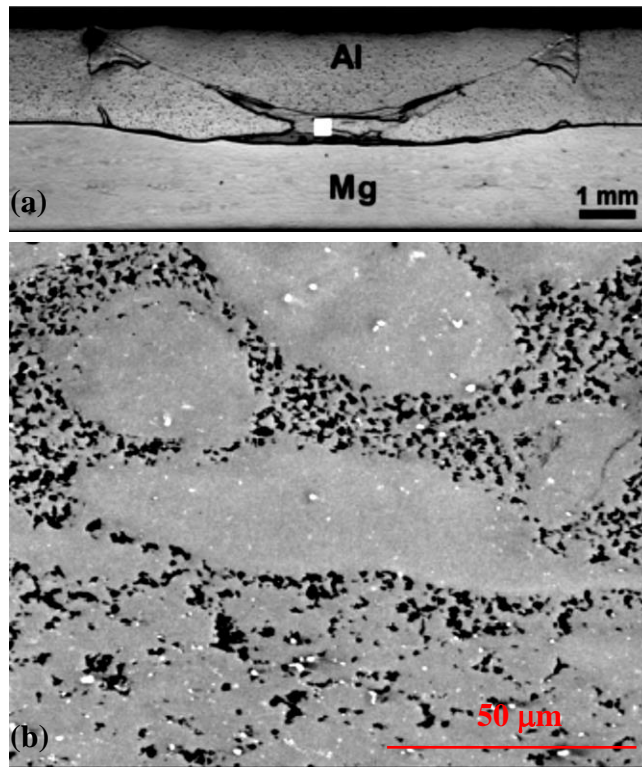


Figure 2-39: Cross-section of an Al5754-AZ31 RFSSW joint: (a) as-welded sample, (b) micrographs of the eutectic structure in the IMC layer taken from the weld centre as marked in (a) (Suhuddin, et al., 2013 b).

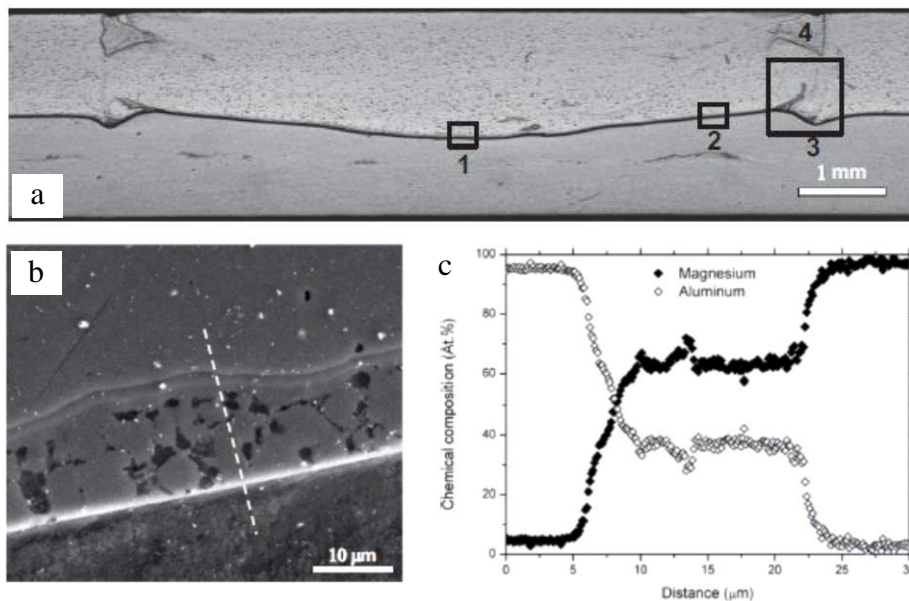


Figure 2-40: (a) Macrograph of an RFSSW joint between AA5754 Al and AZ31 Mg, (b) enlarged microstructures from region 2, and (c) the chemical composition distribution across the interface (Suhuddin, et al., 2014).



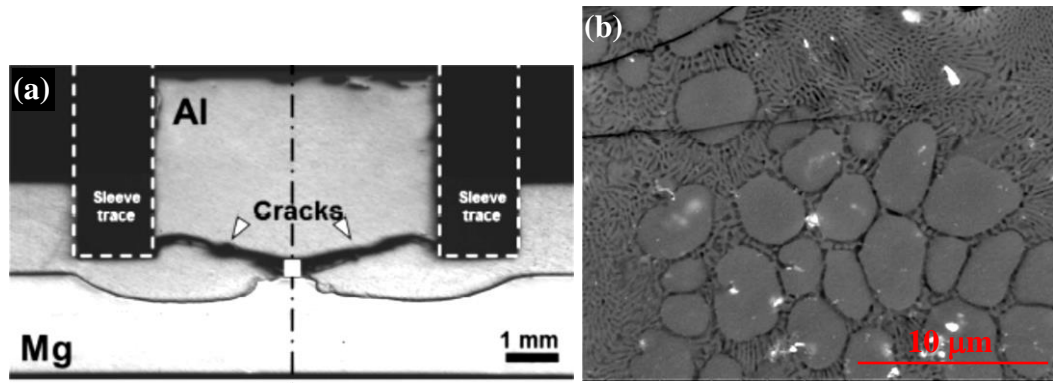


Figure 2-41: Cross-section of an Al5754-AZ31 RFSSW joint: (a) a quenched sample with the process stopped before the sleeve retraction stage, (b) micrographs of the eutectic structure in the IMC layer taken from the weld centre as marked in (a) (Suhuddin, et al., 2013 b).

Most previous studies on the dissimilar FSSW process of Al to Mg joints report the presence of a thick IMC layer at the weld interface (Figure 2-42), which is mainly composed of  $\text{Al}_3\text{Mg}_2$  and  $\text{Al}_{12}\text{Mg}_{17}$ , in addition to a eutectic structure of Mg and  $\text{Al}_{12}\text{Mg}_{17}$ . Cracks easily propagate through this layer, resulting in low fracture energy during lap-shear tests (Sato, et al., 2010). The thickness of the IMC layer (Choi, et al., 2011) and the distribution of the IMC particles in the interface are found to be the main factors affecting the lap shear strength of Al-Mg dissimilar FSSW joints (Sato, et al., 2010).

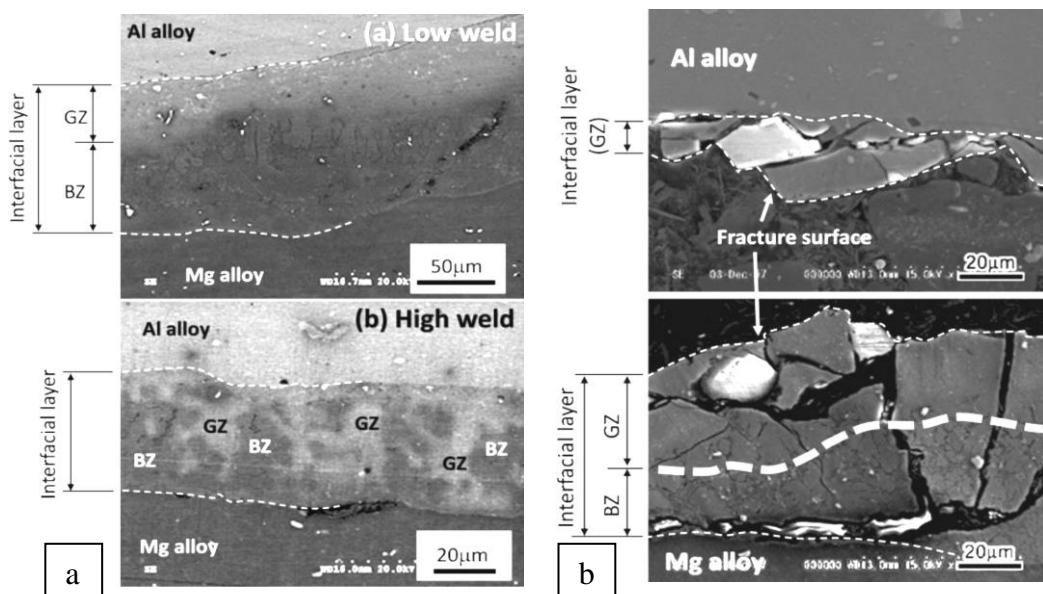


Figure 2-42: Typical SEM images of (a) the interfacial layers in low- and high- rotational-rate welds (1500 and 2250 rpm respectively); (b) the corresponding interfacial layer in the fractured welds (GZ is composed of  $\text{Al}_3\text{Mg}_2$  and  $\text{Al}_{12}\text{Mg}_{17}$ , BZ is made up of the (Mg and  $\text{Al}_{12}\text{Mg}_{17}$ ) eutectic structure) (Sato, et al., 2010).

To summarise, RFSSW is an attractive joining method of growing interest and investigations are being conducted into the use of this process for joining similar and dissimilar materials combinations. However, there are still several areas for which there is limited data that required further understanding or improvement, such as reducing the long welding time (found to be more than 1.0 s in most of the literature) and controlling the material flow during the process, which is the main factor affecting the formation of the weld defects. Other factors to be investigated include, increasing the weld joint strength during the lap-shear test, and controlling, or reducing, the effect of the interfacial brittle intermetallic phases formed in the joining of dissimilar material combinations. To date, there is insufficient literature available to fully understand how to optimise the process to improve such issues.

## **2.12 Al Alloys**

### **2.12.1 Overview and Classification of Al Alloys**

One of the most attractive properties of aluminium is its low density ( $2.69 \text{ g/cm}^3$ ), which is about 1/3 that of steel. Aluminium can achieve high strength, and so can achieve high strength-to-weight ratio, through alloying and strengthening by cold-working and/or heat-treatment. Nevertheless, the modulus of elasticity of aluminium (69 GPa) is about 1/3 that of steel (210 GPa) and is slightly affected by alloying. A wide range of production processes can be used for aluminium, so that its alloys are available in many semi-finished forms, such as extrusions, castings, forgings, pressings, and machined components (Benedyk, 2010). These abilities make aluminium the ideal engineering solution that satisfies the requirements of a material for use in the automotive industry. However, its higher cost compared to steel represents the most important obstacle to the use of aluminium (by weight aluminium is about five times more expensive than steel). In spite of the high cost, the amount of aluminium in automobiles has increased steadily in the past three decades from 37 kg in 1973 to about 161 kg in 2010 as seen in Figure 2-43 (Kelkar, et al., 2001; Benedyk, 2010). Many vehicle manufacturers have shifted towards replacing much of the overall vehicle structure with aluminium by increasing its use in three main application areas (Lutsey, 2010; Hirsch, 2011; Ghassemieh, 2011):

- (1) The powertrain in engine cylinder heads and blocks, transmission housings, fuel system, radiators and liquid lines;
- (2) The chassis and suspension in the axle, cradle, wheels, steering systems and suspension arms;
- (3) The car body (BIW), doors, hoods/bonnets, front structure, wings, bumpers and crash elements and various interiors,

These changes are in addition to the application of aluminium in air-conditioning systems (Ghassemieh, 2011).

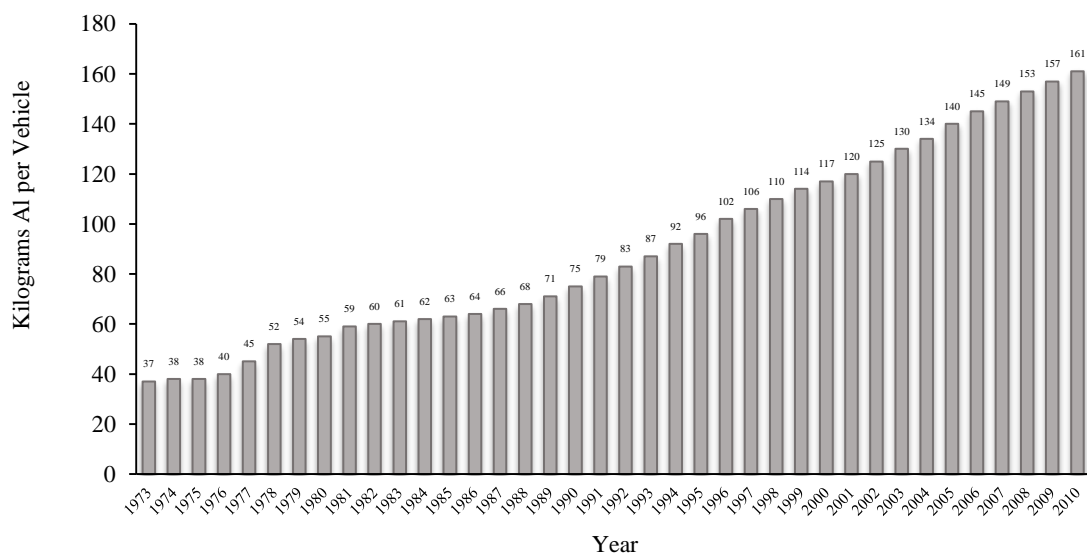


Figure 2-43: The increase in aluminium content in North American small vehicles over the last three decades (Benedyk, 2010).

The number of aluminium alloys used in automotive applications is far greater than the number of ferrous alloys used in the same field. It is important to identify the major differences between cast and wrought aluminium alloys and, in the wrought group, between heat-treatable and non-heat-treatable alloys. According to the wrought alloy designation system of the Aluminium Association, which is recognised as the international standard, aluminium alloys are identified by a four-digit system based on the main alloying element. This system is summarised in Table 2.2. The first digit for wrought alloys identifies the group of the alloy and the last two digits identify the original alloy, while, the second digit represents any modification to the alloy. For casting alloys, the system is slightly different. The group is again identified by the first digit, the alloy is identified by the second two digits, whereas the last digit, which is

separated from the other digits by a decimal point, indicates the product form (for example 0 for cast and 1 for ingot) (Benedyk, 2010; Smallman & Ngan, 2014).

Table 2-2: Aluminium Alloy Designation Systems (Smallman & Ngan, 2014)

<b>Wrought Alloys</b>	<b>Designation</b>	<b>Casting Alloys</b>	<b>Designation</b>
99.00% (minimum) aluminium	1xxx	99.00% (minimum) aluminium	1xx.x
Copper	2xxx	Copper	2xx.x
Manganese	3xxx	Silicon with added copper and/or manganese	3xx.x
Silicon	4xxx	Silicon	4xx.x
Magnesium	5xxx	Magnesium	5xx.x
Magnesium and Silicon	6xxx	Zinc	6xx.x
Zinc	7xxx	Tin	7xx.x
Others	8xxx	Others	8xx.x

The temper designations in the European Committee for Standardisation (CEN) member countries (EN standards) are largely the same as those used in the US by the Aluminium Association for wrought and cast aluminium alloys and are summarised in Table 2.3 (Benedyk, 2010).

Table 2-3: Aluminium Association and European Union (EN) Aluminium Alloy Temper Designation System (Benedyk, 2010)

F – As fabricated.
O – Annealed.
H – Strain-hardened (wrought products only).
W – Solution heat-treated.
T – Thermally treated to produce tempers other than F, O, H (typically solution heat-treated, quenched, and precipitation-hardened).
Numeric additions indicate specific variations:
H14 – Strain-hardened, ½ hard.
T4 – Solution heat-treated and naturally aged.
T6 – Solution heat-treated and artificially aged.
T65 – Solution heat-treated, stress relieved by stretching a specified amount, and artificially aged.

Aluminium alloys used in the manufacturing of most automotive applications, including both sheet and casting grades, are mainly dominated by three material classes (Hirsch, 2011; Gould, 2012).

- (1) Sheet materials consist of two alloy classes: 5XXX and 6XXX.
  - (a) The 5XXX (Al-Mg-(Mn)) alloys are non-heat-treatable and can be strengthened using solid solution strengthening or work hardening. These alloy grades are normally alloyed with 2–5% of magnesium. In automobile manufacturing, these materials are mainly applied in under-body applications and are used where high corrosion resistance is required. The most common in this class are 5754, 5182, and 5083.
  - (b) The 6XXX (Al Mg Si) alloys, with a combination of Mg (0.5 to 1%) and Si (0.5 to 1.5%), are precipitation-hardenable alloys. The well-known alloys in this group are 6111 and 6022. Normally, these materials are supplied in the T4 (naturally-aged) condition, for manufacturing by forming and subsequent welding. This grade of alloys is attractive for skin panel applications because of their ability to obtain high tensile strengths (<300 MPa) as a part of the paint bake ageing cycle.
- (2) The A3XX alloys represent the typical casting aluminium alloys used in automotive applications. These are aluminium-magnesium-silicon alloys with a high silicon content for the promotion of castability. Aluminium alloy castings offer the possibility of lower-cost nodal connections.

Figure 2-44 shows some applications of aluminium alloys in a typical automobile. To optimise the properties in the finished component and tailor them to the requirements of the automotive performance, modifications can be made to these alloys by way of minor alloying additions, but within the chemical specifications required by the individual standards, and their processing parameters (e.g. rolling, extrusion, casting, forging, heat treatment, surface finishing, welding, etc.) (Benedyk, 2010).

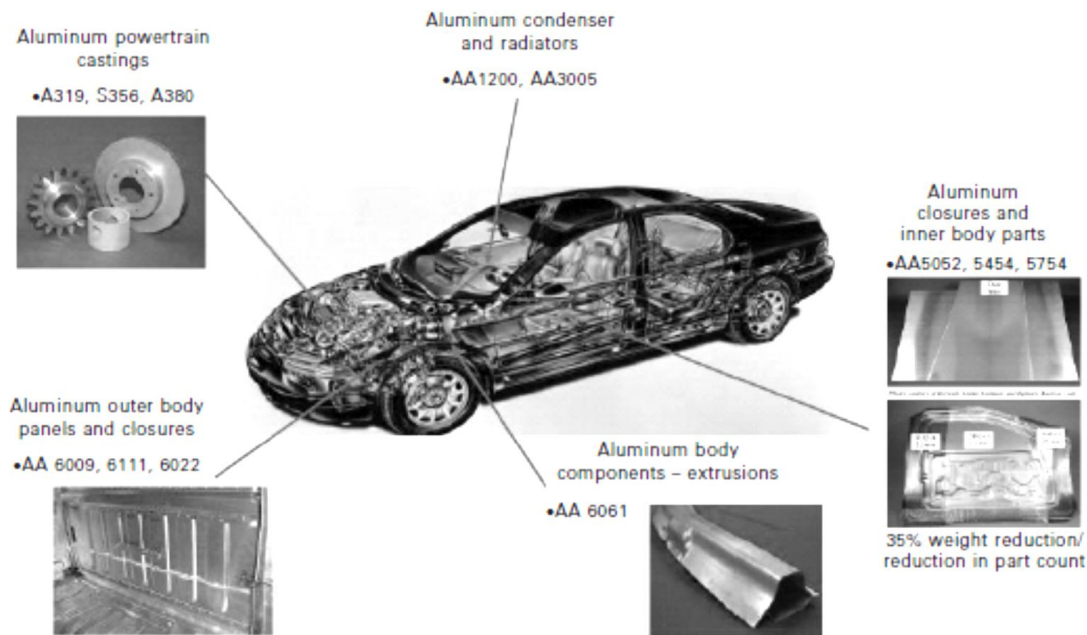


Figure 2-44: Typical aluminium alloy applications in an automobile (Benedyk, 2010).

### 2.12.2 Precipitation Hardening of Al Alloys

The discovery of the precipitation hardening phenomenon in aluminium alloys dates back to the early twentieth century, specifically the year 1906 (Nie, 2014). Considerable progress has been made in subsequent years in terms of improving the response of aluminium alloys to age-hardening by the addition of microalloying elements. Age-hardening represents one of the most important strengthening mechanisms for the design and improvement of medium and high strength wrought aluminium alloys for a wide range of automotive, aerospace engineering and architectural applications. By the addition of certain alloying elements, wrought Al alloys 2xxx, 6xxx, and 7xxx series have been developed using precipitation-strengthening (Sha, et al., 2011). The simple requirement that should be met by a system in order for precipitation hardening to occur is a strong decrease in the solid solubility limit with decreasing temperature, as shown in Figure 2-45 for the Al-Cu system (Smallman & Ngan, 2014; Nie, 2014).

In order to control the precipitation process and increase alloy strength, a series of heat treatments are applied. Firstly, the alloy is subjected to solution treatment at a high temperature (above 450°C) in order to dissolve the major alloying elements into the aluminium matrix. This process is then followed by rapid cooling by quenching in water or another cooling medium. The rapid cooling prevents the precipitation of the equilibrium phase; as a result, the alloy consists of an unstable supersaturated solid solution at room temperature (Sha, et al., 2011; Smallman & Ngan, 2014). Finally, after

quenching, if the alloy is allowed to ‘age’ for enough time at room temperature, or as a pre-selected elevated temperature, the solid solution decomposes by first forming solute clusters and GP zones and then following a sequence of transformation phases, which depend on the specific alloy system. Precipitation takes place through nucleation and growth processes, where initial fluctuations in the concentration of the solute (atoms of the alloying elements) provide small clusters of atoms in the lattice that grow to act as nuclei for the precipitates. The size of the precipitates is time-temperature-dependent. If precipitation occurs at a lower temperature the precipitate becomes finer. On the other hand, if the ageing process is allowed to continue for a long time, at any given temperature, the particles will transform to a more stable phase and become coarser (i.e. the small particles tend to redissolve, while the large ones tend to grow more). The finely dispersed small particles are progressively substituted by coarser particles with a smaller number and wider dispersion. As a result, the alloy becomes softer; this situation is known as an over-aged condition (Figure 2-47) (Smallman & Ngan, 2014; Nie, 2014).

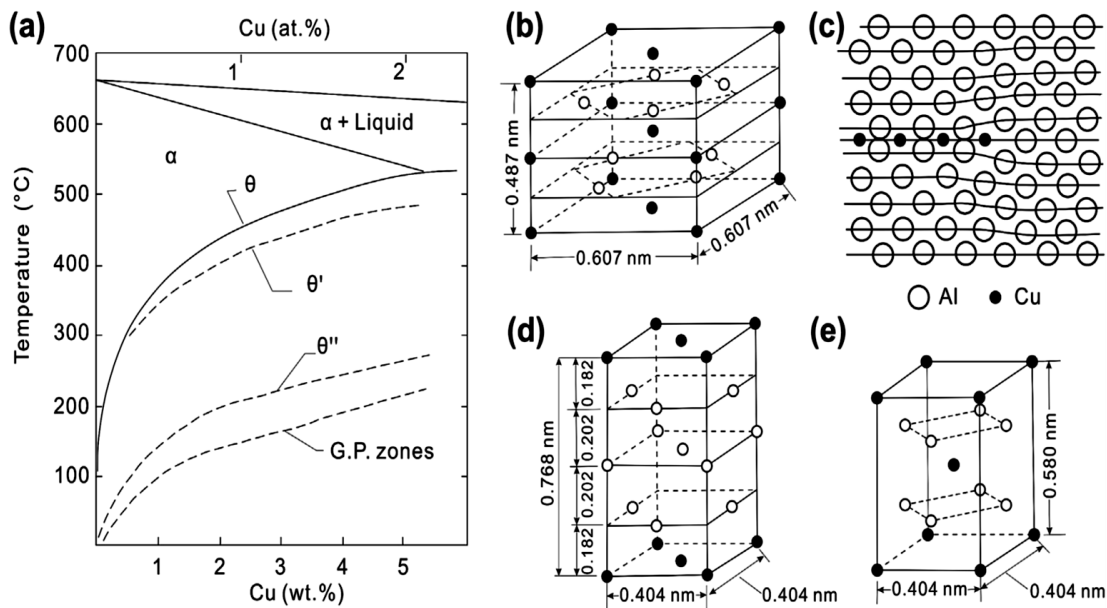


Figure 2-45: (a) The Al-rich side of an Al-Cu binary diagram showing GP zone,  $\theta''$  and  $\theta'$  solvus lines (dotted lines), (b)  $\theta$  unit cell, (c) GP zone, (d)  $\theta''$  unit cell and (e)  $\theta'$  unit cell (Nie, 2014).

The solutionisation and quenching treatment results in the retention of both solute atoms and point defects in excess of their equilibrium concentrations in a supersaturated solid solution as well as residual stresses produced by the quench itself. In the subsequent ageing treatment, the development of fine precipitates usually results in a large increase in strength. For instance, the tensile strength of Duralumin (Al- 4% Cu alloy containing

Mg, Si, and Mn) may be increased from 210 to 410 MPa by solution treatment and artificial ageing (Smallman & Ngan, 2014).

Electron microscopy and X-ray techniques show that in almost all age-hardening systems, the initial precipitates do not have the same structure as that for the equilibrium phase (Smallman & Ngan, 2014; Nie, 2014) some of the common aluminium precipitation hardening systems are shown in Table 2-4. Generally, the precipitation in aluminium follows the general ageing sequence (Smallman & Ngan, 2014; Nie, 2014):

$\alpha_0$  (Supersaturated Solid Solution (SSSS))  $\rightarrow \alpha_1$  + Solute Clusters  $\rightarrow \alpha_2$  + GP Zones  $\rightarrow \alpha_3$  + Intermediate Precipitates  $\rightarrow \alpha_4$  + Equilibrium Precipitates.

This sequence takes place because the equilibrium precipitates are incoherent with the matrix, while the transition structures (intermediate precipitates) are either fully coherent, or at least semi-coherent. The system thus follows this sequence because the coherent metastable phases present the lowest energy barrier to nucleation and thus yield a higher nucleation rate (Nie, 2014; Smallman & Ngan, 2014). A well-known example of this type of precipitation sequence is Al–4wt%Cu alloys which are solution heat-treated and water-quenched, with subsequent natural or artificial ageing being carried out below about 180 °C. In this system, metastable GP zone precipitates (Figure 2-45c) are nucleated first, rather than the equilibrium  $\theta$  phase (Figure 2-45b). This is because the GP zones have the smallest activation energy barrier for nucleation because they have low interfacial energy and are fully coherent with the Al matrix. Moreover, the strain energy of these zones is minimised by choosing a disc shape perpendicular to the elastically soft  $\langle 100 \rangle_\alpha$  directions in the Al matrix. Therefore, the GP zones nucleate much more easily in spite of the fact that the driving force for their precipitation is less than for the equilibrium  $\theta$  phase (see Figure 2-46) (Nie, 2014).

The precipitates surface energy controls the nucleation process when the interfacial energy is large, (i.e. when there is a discontinuity in the atomic structure at the nucleus-matrix interface); this dominates the energy barrier to nucleation. However, the coherence condition also usually requires straining the equilibrium lattice by the precipitate in order to fit the matrix lattice, or the adoption of a metastable lattice. In spite of the higher strain and volume-free energies in the early stages of precipitation,



nucleation is still more rapid due to the lower interfacial energy (Smallman & Ngan, 2014).

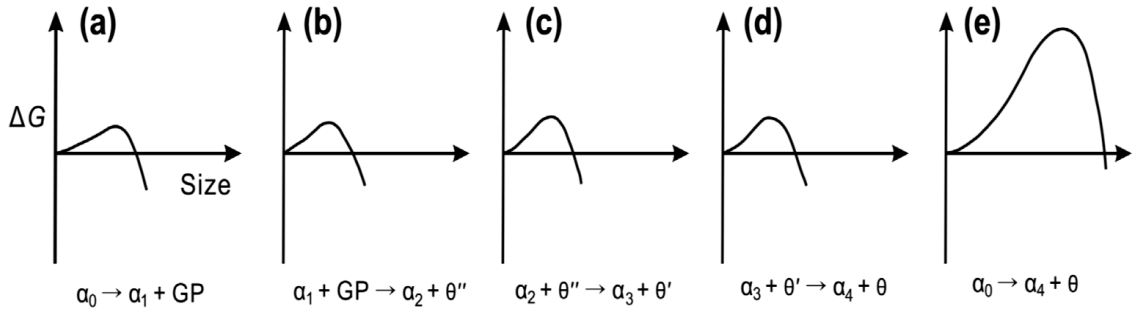


Figure 2-46: Activation energy barriers to the nucleation of precipitate phases in Al-Cu binary alloys.  $\alpha_0$  is the original SSSS, and  $\alpha_1$ ,  $\alpha_2$ ,  $\alpha_3$  and  $\alpha_4$  are the matrix compositions in equilibrium with GP zones,  $\theta''$ ,  $\theta'$  and  $\theta$ , respectively (Nie, 2014).

Table 2-4: Some of the common aluminium precipitation hardening systems (Smallman & Ngan, 2014).

Base Metal	Solute	Transition Structure	Equilibrium Precipitate
Al	Cu	(i) Plate-like solute-rich GP[1] zones on $\{100\}_{Al}$ ; (ii) ordered zones of GP [2]; (iii) $\theta'$ -phase (plates).	$\theta$ -CuAl <sub>2</sub>
	Ag	(i) Spherical solute-rich zones; (ii) platelets of hexagonal $\gamma'$ on $\{111\}_{Al}$	$\gamma$ -Ag <sub>2</sub> Al
	Mg, Si	(i) GP zones rich in Mg and Si atoms on $\{100\}_{Al}$ planes; (ii) ordered zones of $\beta'$ .	$\beta$ -Mg <sub>2</sub> Si (plates)
	Mg, Cu	(i) GP zones rich in Mg and Cu atoms on $\{100\}_{Al}$ planes; (ii) $S'$ platelets on $\{021\}_{Al}$ planes .	S-Al <sub>2</sub> CuMg (laths)
	Mg, Zn	(i) Spherical zones rich in Mg and Zn; (ii) platelets of $\eta'$ on $\{111\}_{Al}$	$\eta$ -MgZn <sub>2</sub> (plates)

Figure 2-47 shows ageing curves for Al–Cu alloys with different concentrations of Cu. The solution treatment for the Al–Cu binary alloys can be conducted by heating them to the region of the single-phase  $\alpha$ , shown in the phase diagram in Figure 2-45a. This process is followed by water-quenching to room temperature, and artificial ageing at 130 °C or 190 °C. As the main resistance to the movement of the dislocations is the solid solution hardening, therefore, the strength, or hardness, is comparatively low in

the as-quenched condition. The hardness increases as a result of the formation of GP zones and/or precipitates during isothermal ageing, because extra stress is required to force the dislocations through the coherent zones or precipitates. In each curve, the peak hardness is linked with the optimum precipitate size distribution which in this system is associated with the presence of  $\theta''$  and  $\theta'$  precipitates. Figure 2-47 shows clearly that the maximum hardness in the ageing curves is significantly affected by the composition of the Al-Cu alloy and ageing temperature (Nie, 2014).

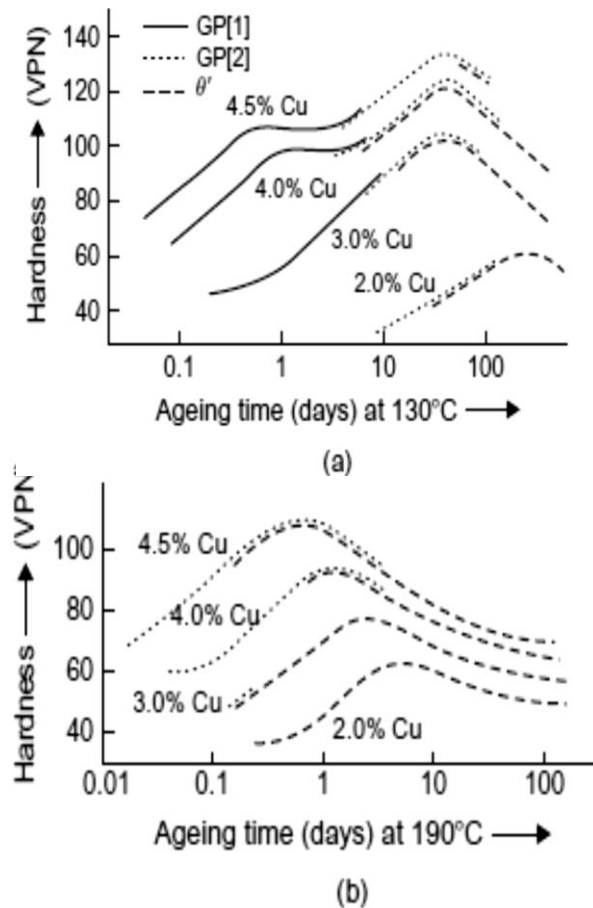
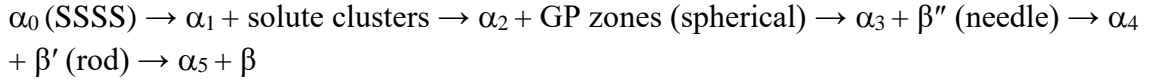


Figure 2-47: The effect of copper percentage and ageing time on the hardness of Al-Cu binary alloys on ageing at (a) 130°C and (b) 190°C (Silcock, et al., 1954).

### 2.12.3 Aluminium Alloy AA6111

The 6xxx series aluminium alloys are commonly used as structural alloys with medium strength for automotive and construction applications (Sha, et al., 2011). Aluminium alloys in this series are precipitation-hardenable with main alloying elements of magnesium and silicon, as seen in Table 2-5. This group of alloys is generally used in a naturally aged condition (T4) and then formed and welded. A higher tensile strength

(<300 MPa) can be obtained after ageing this class of alloys, making them attractive for use in automotive skin panel applications (Gould, 2012). The sequence of precipitation in Al-Mg-Si ternary alloys is usually considered to be (Sha, et al., 2011):



However, the actual sequence is frequently significantly more complex than the above and includes additional metastable phases that are influenced by various parameters including alloy compositions, ageing temperature and ageing time (Sha, et al., 2011).

Table 2-5: Composition of some of the 6xxx series aluminium alloys used for automotive panel applications (Burger, et al., 1995).

Alloy	Mg wt%	Si wt%	Cu wt%	Fe wt%	Mn wt%	Zn wt%	Cr wt%	Ti wt%
6009	0.4-0.8	0.6-1.0	0.15-0.6	≤ 0.50	0.2-0.8	≤ 0.25	≤ 0.10	≤ 0.10
6010	0.6-1.0	0.8-1.2	0.15-0.6	≤ 0.50	0.2-0.8	≤ 0.25	≤ 0.10	≤ 0.10
6111	0.5-1.0	0.6-1.1	0.5-0.9	≤ 0.40	≤ 0.40	-	≤ 0.10	≤ 0.10
6016	0.3-0.6	1.0-1.5	≤ 0.20	≤ 0.50	≤ 0.20	-	0.10	-
6xxx	0.5-1.4	0.6-1.5	≤ 0.10	≤ 0.30	≤ 0.10	-	≤ 0.10	≤ 0.10

The AA6111 aluminium alloy is one of the most important alloys in the 6xxx series. This alloy has become one of the preferred choices among aluminium alloys in the automotive industry, because of its good combination of formability and high strengthening potential (Esmaeili, et al., 2003; Wang, et al., 2003). Like the other alloys in the 6xxx series, the AA6111 alloy is based on a pseudo-binary composition of Al-Mg<sub>2</sub>Si, where the intermetallic compound Mg<sub>2</sub>Si is the equilibrium precipitate. As shown in Figure 2-48, the maximum solubility of this intermetallic compound is 1.85 wt% at 595 °C and the solubility decreases rapidly with reducing temperature (Polmear, 2007).

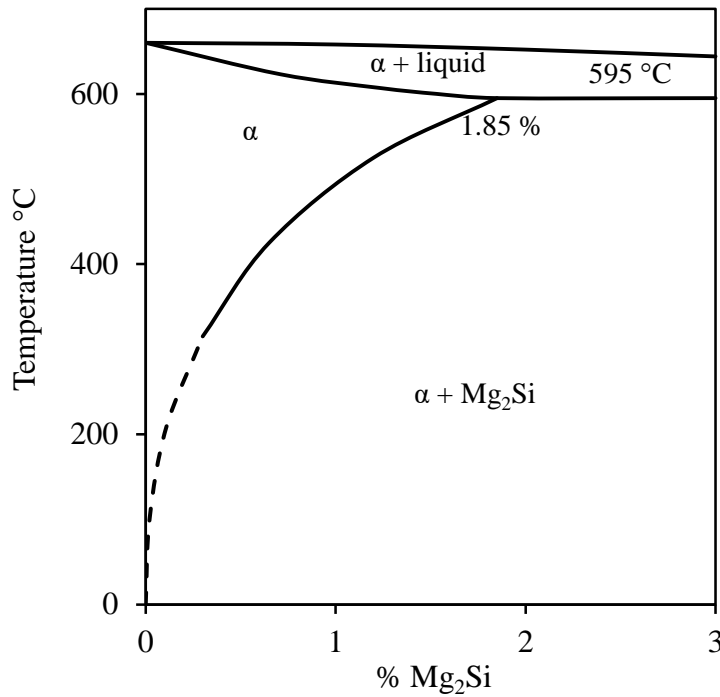
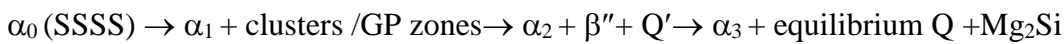


Figure 2-48: The pseudo-binary Al-Mg<sub>2</sub>Si system (Polmear, 2007).

The AA6111 alloy can be strengthened using artificial ageing (such as the paint baking treatment at about 180°C for 30 minutes) where several metastable phases appear in the microstructure. The sequence of precipitation in this alloy can be described as (Wang, et al., 2003):



Where SSS refers to the supersaturated solid solution. The structure of the GP zones has a needle-like morphology in Al-Mg-Si alloys (Wang, et al., 2003). The  $\beta''$  precipitates also have a needle-shaped morphology with a composition of  $\text{Mg}_5\text{Si}_6$  and lie along the  $\langle 100 \rangle$  direction in the aluminium matrix (Wang, et al., 2003). The  $Q'$  and  $Q$  phases are present in the precipitation sequence because the AA6111 alloy contains Cu in its composition (Polmear, 2007). Numerous commercial aluminium alloys from the 6xxx series contain varying amounts of Cu. These Cu additions convert these alloys into the quaternary Al-Mg-Si-Cu system and the precipitation sequences become more complicated. This process, results in the coexistence of several other equilibrium phases, which can precipitate during the ageing treatment along with  $\beta$ . These phases include  $\theta$  ( $\text{Al}_2\text{Cu}$ ), the S-phase ( $\text{Al}_2\text{CuMg}$ ) and the T-phase as well as the quaternary intermediate Q-phase (Sha, et al., 2011). The metastable form of Q is  $Q'$ , but this is

disputed as both have the same crystal structure and lattice parameters. Q' has a lath morphology and is coherent with the aluminium matrix along its long axis, which is parallel to  $\langle 100 \rangle_{\alpha\text{-Al}}$  and  $\{150\}_{\alpha\text{-Al}}$  of the aluminium matrix habit planes (Wang, et al., 2003; Sha, et al., 2011) and has compositions ranging from  $\text{Al}_4\text{CuMg}_5\text{Si}_4$  to  $\text{Al}_4\text{Cu}_2\text{Mg}_8\text{Si}_7$  (Weatherly, et al., 2001). However, the  $\beta''$  precipitate is still the most effective strengthening phase because of its higher volume fraction (Polmear, 2007). The ageing process highly influences the degree of strengthening because it controls the precipitates' nature, the volume fraction, the average size, and size distribution, which affects the interaction between the precipitates and dislocations (Wang, et al., 2003).

#### **2.12.4 The Microstructures of AA6111 FSSWs**

The typical structure of the FSSW joints produced in heat-treatable aluminium alloys consist of three regions: the stir zone (SZ), thermomechanically affected zone (TMAZ), and heat affected zone (HAZ), as well as the base metal (BM) described in earlier section (2.10.1). Because AA6111 is a heat-treatable alloy, it is to be expected that it will undergo microstructural changes as a result of the welding process. This alloy is normally used in automotive manufacturing in the form of sheets in a T4 condition. After welding, the sheets are subjected to a paint-bake thermal cycle (in the range of 150-180 °C to cure the paint). After this treatment, the yield strength of this alloy will be increased by artificial ageing due to the formation of more clusters of solute in addition to the increasing density of the fine  $\beta''$  precipitates (Chen, et al., 2013).

As mentioned earlier (section 2.10.1), the hardness distribution across FSSW joints of heat-treatable Al alloys exhibit 'W'-shape profiles (Figure 2-35). This occurs because the metal in the SZ of the AA6111 FSSW joint partially recovers its strength due to the increase in temperature to levels high enough for solution treatment, which thus encourages post-weld natural ageing. To achieve a considerable natural ageing response, the temperature in this location must have approached the solvus of the  $\beta$  phase, which means peak temperatures of about 540°C must be reached. A large decrease in hardness (about 30%) can usually also be seen at the periphery of the joints, with the lowest hardness level located approximately at the TMAZ/HAZ border, caused by rapid overageing, which usually occurs in the temperature range 300-400 °C. In general, two types of precipitates can be seen at different locations in the weld, depending on the local temperature reached; incoherent coarse spherodised precipitates

and finer semicoherent laths. The precipitates with lath morphology most likely are the Q phase and appear in locations with a relatively low temperature, because their solvus temperature is 440 °C, while the precipitates which have a coarse spheroidised shape are the  $\beta$  phase (Figure 2-49) (Bakavos & Prangnell, 2009).

Figure 2-50 shows TEM micrographs for an AA6111 FSSW joint in different conditions and locations in the welded joint. GP zones cannot be resolved in the T4 parent material (Figure 2-50 a) by conventional microscopy. By comparing Figure 2-50 (b) with Figure 2-50 (d), it can be noted that the parent sheet and weld centre showed different precipitation behaviour after the post-weld heat treatment. Fine  $\beta''$  needles can be observed in both regions, but they exhibited different size and density. A much greater volume fraction of  $\beta''$  precipitates can be seen in the paint baked weld sample in Figure 2-50 (d). The heat-treated parent material shows another type of precipitate with rectangular cross-sections, which is the Q' phase. This phase did not appear in the paint baked welds (Chen, et al., 2013).

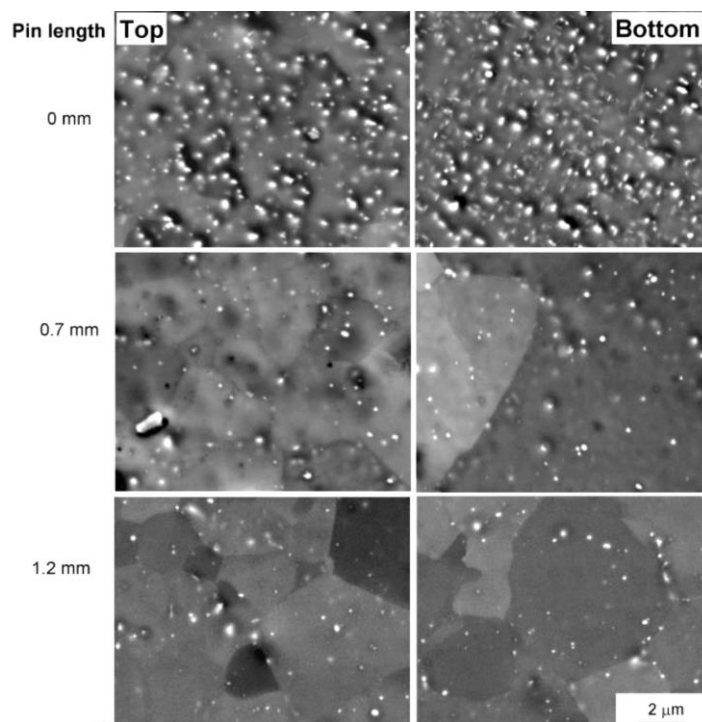


Figure 2-49: SEM images showing coarse precipitates of the second phase present in weld zones of the AA6111 FSSW joints, as a function of pin length, at 0.2 mm below the top and above the bottom surface of joints at a radial distance of 3.5 mm from the weld centre (Bakavos & Prangnell, 2009).

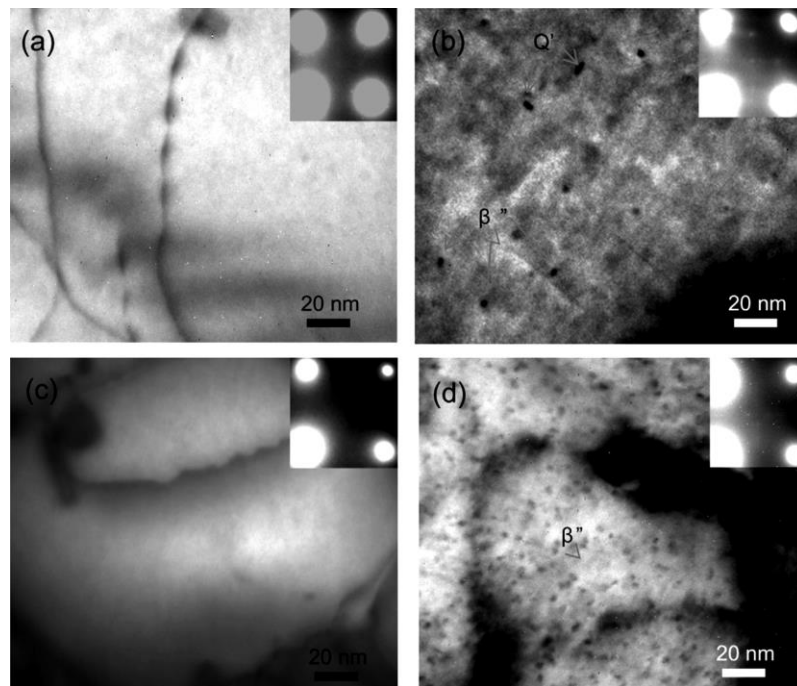


Figure 2-50: TEM micrographs for: the AA6111 parent material (a) in the T4 condition and (b) after the paint-bake treatment, and from the pinless FSSW joint centre of a 0.5 second dwell-time weld (c) in the as-welded condition, and (d) after the paint-bake treatment (Chen, et al., 2013).

## 2.13 Magnesium Alloys

### 2.13.1 Overview and Classification of Mg Alloys

Magnesium is the least dense metal used in the automotive industry. It represents a promising possible metal substitute for lightweighting purposes, because it has a density which is about 30% and 75% lower than aluminium and steel, respectively (Lutsey, 2010; CAR, 2011). By comparing the specific strength and specific stiffness of magnesium with aluminium and iron (Figure 2-51) it can be noted that there is little difference in specific stiffness between Mg, Al, and iron, with the specific stiffness higher than Mg by only 0.69% and 3.7% for Al and iron, respectively. In contrast, Mg has a specific strength significantly higher than that of Al and iron, with a ratio of about 14.1% and 67.7%, respectively (Ghassemieh, 2011).

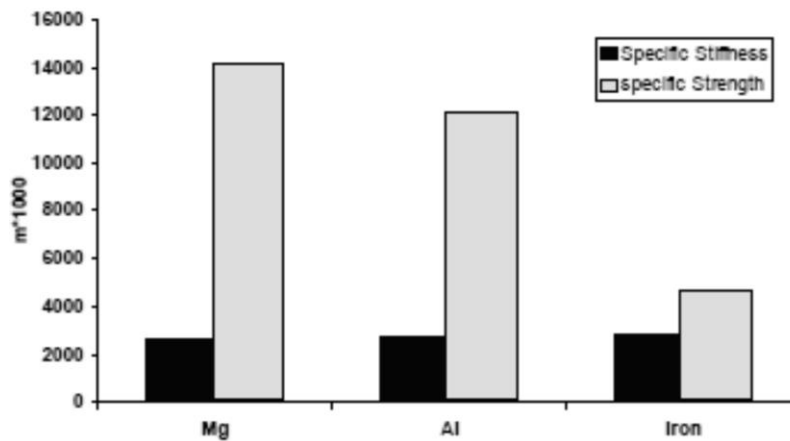


Figure 2-51: Comparison of the specific stiffness and specific strength of pure Mg with Al and iron (Ghassemieh, 2011).

Production of magnesium has seen a significant upward trend from the 1940s, as shown in Figure 2-52, with just over 700,000 metric tons produced in 2008, and production has doubled within the last ten years alone (Powell, et al., 2010). This rapid increase in production reflects the large growth in demand for this metal in various applications.

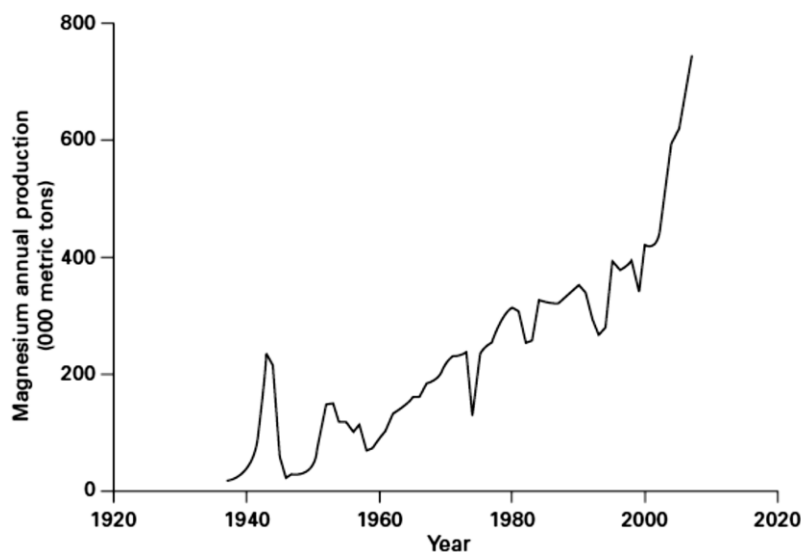


Figure 2-52: Magnesium production data in the period 1938–2008 (Powell, et al., 2010).

Some of the key advantages that make magnesium attractive as a structural material for automotive applications, in addition to its high specific strength, include its high fluidity, hot formability, and damping capacities. The use of magnesium in the automotive industry dates back the to 1930s when it was used in the Volkswagen Beetle as an engine block (Powell, et al., 2010). Figure 2-53 shows a timeline summarising the growth in automotive applications of magnesium. Curently the drivetrain and the



interior represent the main focus of magnesium applications owing to concerns over its corrosion performance (Schumann & Friedrich, 2006). Due to the ability to die-cast magnesium into thin-walled parts (Jambor & Beyer, 1997; CAR, 2011), it is possible to use magnesium in instrument panels and cross car beams (CAR, 2011). Applications also include body construction (Schumann & Friedrich, 2006), doors (Jambor & Beyer, 1997) and closures. For instance, the use of magnesium to make the inner structure of the lift gate of the Lincoln MKT resulted in a total mass reduction of about 10 kg (CAR, 2011).

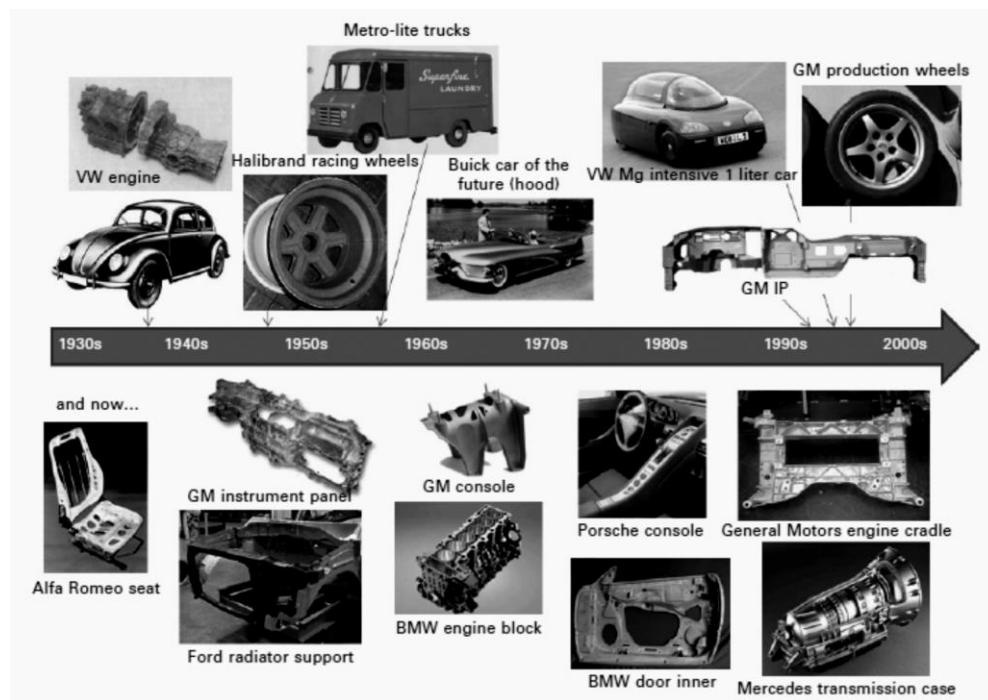


Figure 2-53: Timeline summarising magnesium automotive applications (Powell, et al., 2010).

Magnesium is commonly alloyed with other metals to improve its strength, corrosion resistance, formability, etc. for engineering applications (Polmear, 2007; Powell, et al., 2010). The hexagonal lattice structure of magnesium (Figure 2-54), together with favourable size factors with a diverse range of solute elements, due to its atomic diameter of 0.320 nm, represent the main features that control the physical metallurgy of Mg alloys (Polmear, 2007). Common examples of alloying elements that are widely present in commercial magnesium alloys include aluminium, zinc, cerium, silver, thorium, yttrium and zirconium (Polmear, 2007; Mordike & Lukác, 2006).

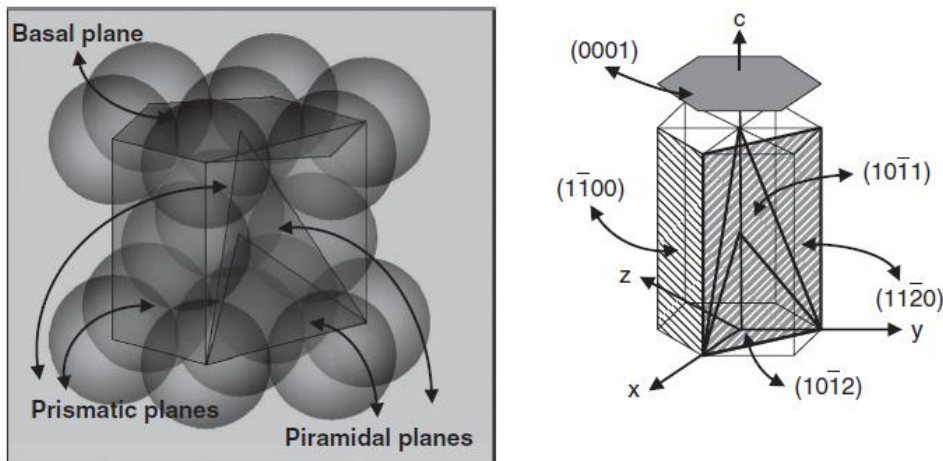


Figure 2-54: Schematic of magnesium's hexagonal close-packed (HCP) crystal lattice and major planes (Kaya, 2013).

Magnesium alloys are classified using a system that combines letters and numbers (normally two letters and two numbers). The two letters specify the main alloying elements outlined in Table 2-6 (Powell, et al., 2010). The letters are arranged so that the code of the element that represents the highest percentage in the alloy is used first (Polmear, 2007). These two letters are followed by numbers which show the nominal weight percentage of the two principal alloying elements. A well-known example is the alloy AZ91; the code indicates that the magnesium alloy contains 9% (by weight) Al and 1 % (by weight) Zn (Polmear, 2007; Powell, et al., 2010).

Table 2-6: Literal symbols for alloying elements in magnesium alloys (Powell, et al., 2010).

Letter	Element	Letter	Element	Letter	Element
A	Aluminium	J	Strontium	R	Chromium
B	Bismuth	K	Zirconium	S	Silicon
C	Copper	L	Lithium	T	Tin
D	Cadmium	M	Manganese	V	Gadolinium
E	Rare earth	N	Nickle	W	Yttrium
F	Iron	P	Lead	X	Calcium
H	Thorium	Q	Silver	Y	antimony
		Z	Zinc		

Like aluminium alloys, magnesium alloys also have designations for their heat treatments, which are shown in Table 2-7. The ‘H’ and ‘T’ treatments are normally followed by one or more digit which represents a subdivision of a particular treatment.

Table 2-7: General divisions of the temper designations for magnesium alloys (Mordike & Lukác, 2006).

F	As fabricated
O	Annealed recrystallised (wrought products only)
H	Strain-hardened
T	Thermally treated to produce stable tempers. Other than F, O or H
W	Solution-heat-treated (unstable temper)

### **2.13.2 Magnesium Alloy AZ31**

The number of wrought magnesium sheet alloys, which are commercially available, is relatively limited (Powell, et al., 2010). AZ31 (Mg-3Al-1Zn-0.3Mn) represents one of the oldest sheet alloys (Table 2-8 shows the composition of magnesium wrought alloys used for sheets and plates), which is still the most common magnesium alloy used at room temperature or for moderately elevated temperature applications. The strength of this alloy can be increased by strain-hardening and it is weldable, even though the welded joints should be treated to relieve the thermal stress and reduce susceptibility to stress-corrosion cracking (Polmear, 2007). Typically this alloy is available in either a partially hard H-24 temper, or in an annealed O temper. Figure 2-55 shows typical microstructures of AZ31 in these two temper conditions. It is difficult to distinguish individual grains in the H24 temper material 'as rolled condition', due to the high deformation. In comparesion, the grains in the annealed O temper material are homogeneously distributed with clearly visible boundaries. The AZ31 material in the O temper has a lower strength compared with age-hardenable aluminium sheet alloys, such as AA6111, but it offers comparable yield strength to those of the work-hardenable alloys, such as AA5754 or AA5182 (Powell, et al., 2010). The mechanical properties of the AZ31 alloy in both of these temper treatments are shown in Table 2-9.

Table 2-8: Composition of magnesium wrought alloys used for sheets and plates (Kammer, 2006).

Alloy	Al	Mn	Zn	Th	Si	Cu	Ni	Fe	Special	Other (total)
AZ31B	2.5 - 3.5	0.20 - 1.0	0.6 - 1.4	-	0.10	0.05	0.005	0.005	0.04 Ca	0.30
AZ31C	2.4 - 3.6	0.15 - 1.0	0.50 - 1.5	-	0.10	0.10	0.03	-	-	0.30
HK31A	-	-	0.30	2.5 - 4.0	-	0.10	0.01	-	0.40-1.0 Zr	0.30
HM21A	-	0.45-1.1	-	1.5 - 2.5	-	-	-	-	-	0.30
ZE10A	-	-	1.0 - 1.5	-	-	-	-	-	0.12-0.22 RE	0.30
LA141A	1.0-1.5	0.15	-	-	0.004	0.005	0.005	0.005	0.005 Na 13.0-15.0 Li	0.30

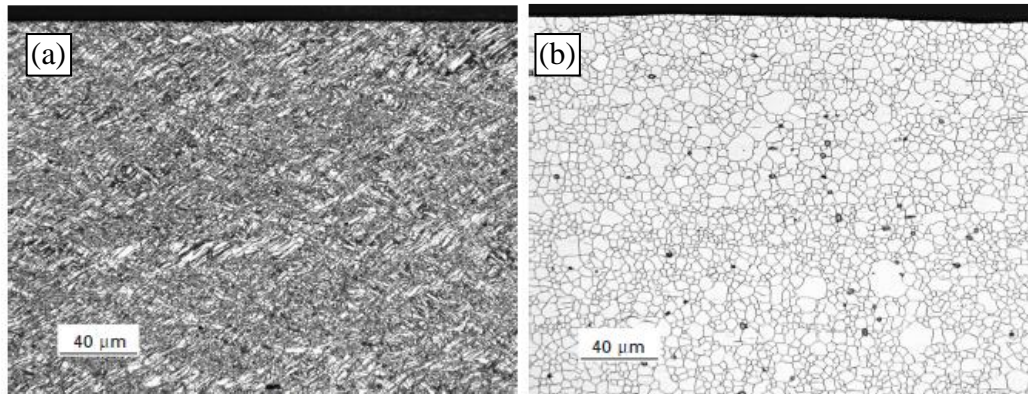


Figure 2-55: Typical microstructures for an AZ31 magnesium alloy sheet, showing (a) as-rolled H-24 temper and (b) annealed O temper (Powell, et al., 2010).

Table 2-9: Mechanical properties of an AZ31 sheet at room temperature (Juchmann, 2006).

Properties	Unit	AZ31 "O"	AZ31 "H24"	AZ31 experiment.	AZ31 commercial
Tensile strength	MPa	221-275	269- ...	230-280	220-290
Yield strength	MPa	...	200- ...	130-200	125-220
Uniform elongation	%	...	...	10-18	...
Elongation at rupture	%	12	6- ...	10-23	8-21
Anisotropy		/	/	1.2-2.0	/
Consolidation index		/	/	0.15-0.2	/

Aluminium is considered an ideal choice as an alloying element for magnesium (Kammer, 2006). Several Mg alloys systems contain up to 10 mass % of Al, such as AZ, AE, AM and AS (Mordike & Lukác, 2006). The optimum combination of ductility and strength for structural applications can be obtained when using about 5–6% of aluminium, as seen in figure 2-56 (Powell, et al., 2010). The limit of solubility of aluminium in magnesium at eutectic temperature is about 12.7 mass % and this decreases to about 2% at room temperature (Mordike & Lukác, 2006). Therefore, the microstructure of these alloys normally contains intermetallic precipitates of  $Mg_{17}Al_{12}$  in a matrix of primary Mg. These intermetallic precipitates play an important role in determining the properties (Mordike & Lukác, 2006; Pekguleryuz, 2013). For example, the presence of the  $Mg_{17}Al_{12}$  phase in the microstructure results in limited creep resistance because of the poor thermal stability of this phase (Mordike & Lukác, 2006).

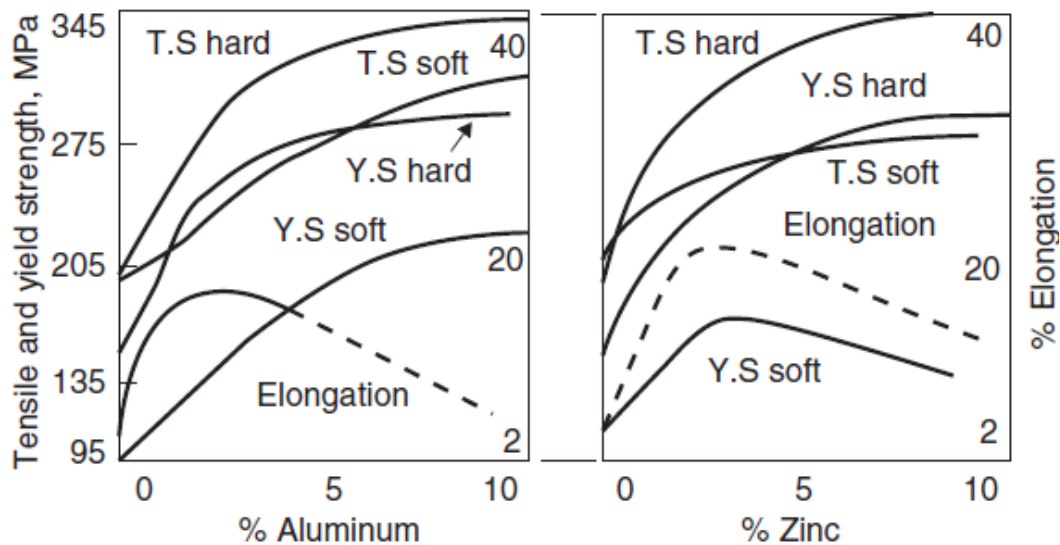


Figure 2-56: The effects of Al and Zn additions on the mechanical properties of Mg in annealed (soft) and hard rolled conditions (Pekguleryuz, 2013).

The addition of zinc to the AZ31 alloy also improves the strength, especially if the content is higher than 3 % (Figure 2-56) (Kammer, 2006). Solid-solution strengthening with zinc is more efficient than aluminium if an equal atomic percentage is used, but the solubility of zinc in magnesium is only 6.2%, which is much lower than that of aluminium (Polmear, 2007). The addition of zinc to Mg-Al alloys also improves the die casting characteristics due to the improvement of metal flow, although, it decreases ductility and increases hot-shortness (Powell, et al., 2010).

Manganese was also one of the first alloying elements to be used commercially with magnesium. Mn has a maximum solid solubility of 2.2 % in magnesium, but it is added to the Mg-Al-Zn system in lower concentrations (about 0.2-0.3 %). Its main role is to remove the impurities of certain heavy metals (such as iron) by reacting with them to result in the formation of comparatively less harmful intermetallic compounds, which improves overall corrosion resistance (Polmear, 2007).

## 2.14 Aluminium and Magnesium Intermetallic Compounds

### 2.14.1 Al-Mg Binary Phase Diagram

Due to the importance of the Al-Mg system to the aluminium industry, this binary system has been the subject of numerous studies (Saunders, 1990). These include experimental investigations and theoretical calculations (Schurmann & Voss, 1981; Murray, 1982; Su, et al., 1997; Okamoto, 1998). There is a general consensus that two intermetallic compounds exist in the Al-Mg phase diagram: (1) the  $\beta$ -Al<sub>3</sub>Mg<sub>2</sub> phase, with a range of compositions of 37-40 at % Mg and (2) the  $\gamma$ -Al<sub>12</sub>Mg<sub>17</sub> phase with a wider range of solid solubility (Saunders, 1990). Figure 2-57 shows the two most commonly cited forms of the Al-Mg phase diagram, where Figure 2-57a represents the phase diagram calculated by Murray (Murray, 1982) while Figure 2-57b shows the phase diagram experimentally determined by Schurmann and Voss (Schurmann & Voss, 1981). It can be seen that there is still some uncertainty about the nature of the phases types and structure in the composition range of 40-60 at %Mg (Saunders, 1990).

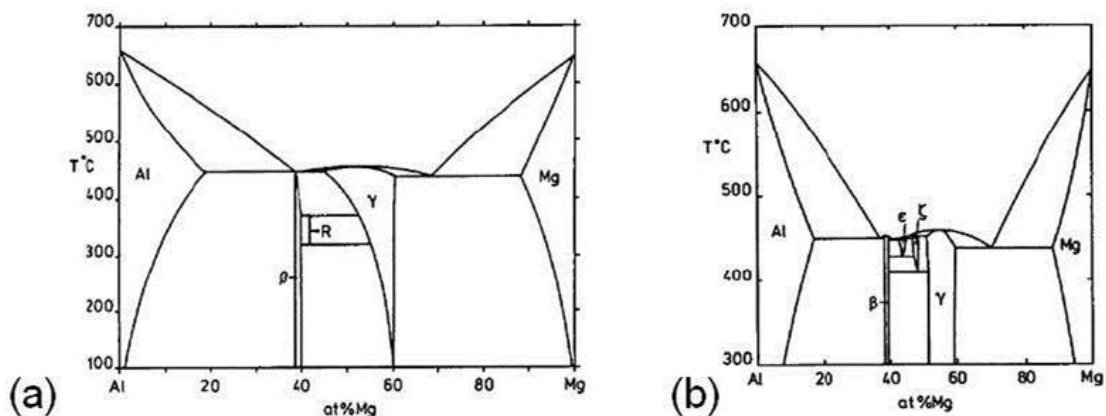


Figure 2-57: Al-Mg equilibrium phase diagrams a) calculated by Murray (Murray, 1982), and b) experimentally determined by Schurmann and Voss (Schurmann & Voss, 1981).

Okamoto (1998) combined of the experimentally determined phase diagram of Su et al. (Su, et al., 1997) and the calculated phase diagram of Murray (Murray, 1982) to produce a newer version of the Al-Mg phase diagram, shown in Figure 2.58 (Okamoto, 1998). This Figure shows another two phases: the  $\epsilon$ -Al<sub>30</sub>Mg<sub>23</sub> phase, which forms at 410 °C as a result of a peritectoid reaction ( $\beta + \gamma \rightarrow \epsilon$ ), and the  $\lambda$  phase, which forms following the reaction  $\beta + \gamma \rightarrow \lambda$  at 430 °C; however, the structure of  $\lambda$  remains to be determined (Su, et al., 1997).

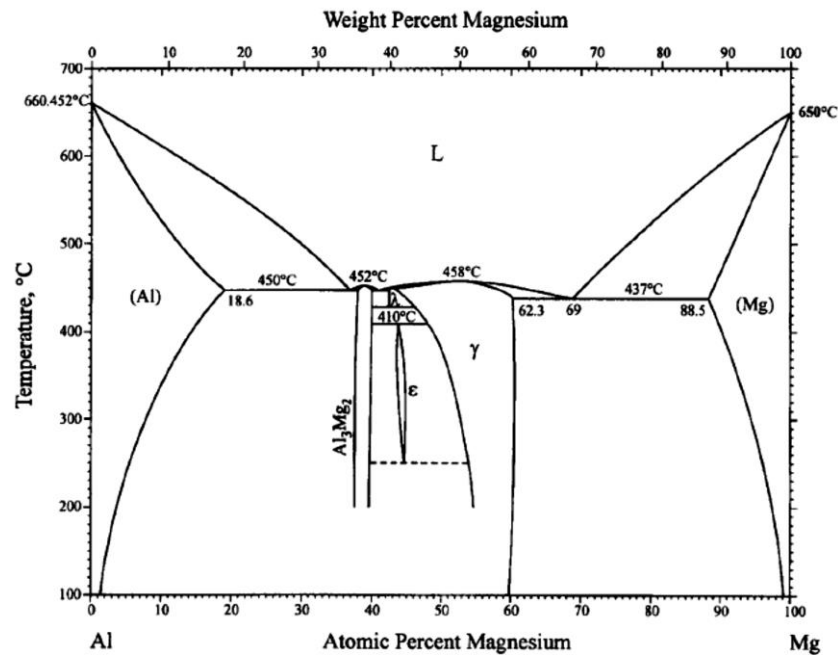


Figure 2-58: The Al-Mg binary phase diagram drawn by Okamoto using calculated data from Murray and experimental results from Su et al. (Okamoto, 1998).

### 2.14.2 Gamma Phase

The gamma intermetallic phase (Al<sub>12</sub>Mg<sub>17</sub>) has a cubic A12 crystal structure, as shown in Figure 2-59. The  $\gamma$  phase has a melting point of 450 °C and represents the second main phase that forms eutectically in Mg-Al binary alloys and in Mg-Al-Zn ternary alloys, which have a high Al:Zn ratio. It is found that this phase suffers from softening at high temperatures, because of its partial metallic bonding; and this results in adverse effects on the creep resistance and strength at elevated temperatures (Pekguleryuz, 2013). The Al<sub>12</sub>Mg<sub>17</sub> phase is found to have a very high nanohardness of about 4.35 nHV (GPa) compared to 0.90 nHV (GPa) for pure magnesium (Zhang, et al., 2010).

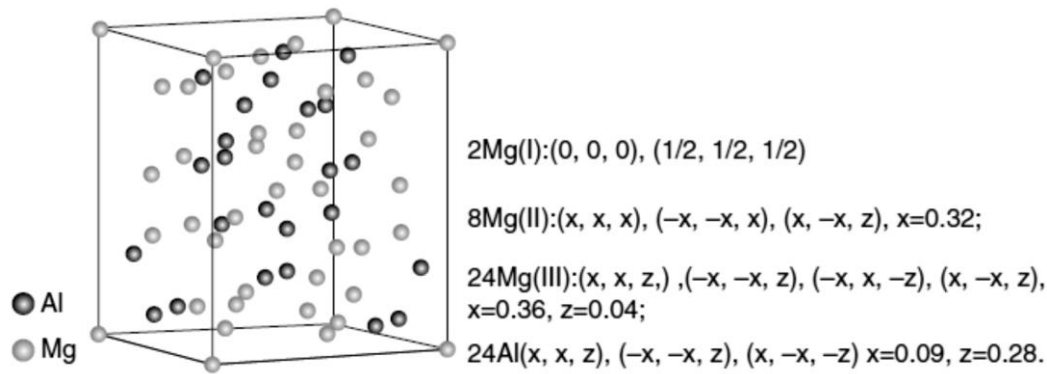


Figure 2-59: Crystal structure of the gamma phase ( $\text{Al}_{12}\text{Mg}_{17}$ ) (Pekguleryuz, 2013).

### 2.14.3 Beta Phase

The  $\beta$  phase ( $\text{Mg}_2\text{Al}_3$ ) was originally studied by Sten Samson (Samson, 1965); as a result, it is frequently referred to as the Samson structure. More recently this structure has attracted considerable interest among crystallographers due to its complex nature and the possibility of new technical applications (Wolnya, et al., 2008).

The actual composition of the  $\beta$  phase is  $\text{Al}_{61.5}\text{Mg}_{38.5}$ , which represents the average of the lowest and highest possible percentages of Mg (37 and 40 at % respectively) in this compound. This phase has a cubic crystal structure shown in Figure 2-60, with approximately 1168 atoms, which are distributed over 1832 atomic positions in the unit cell and lattice spacings of  $28.239 \pm 0.001 \text{ \AA}$  (Samson, 1965; Jeglič, et al., 2007; Wolnya, et al., 2008). The nanohardness of  $\text{Al}_3\text{Mg}_2$  is found to be 4.40 nHV (GPa) compared to 0.90 nHV and 4.35 nHV (GPa) for pure magnesium and  $\text{Al}_{12}\text{Mg}_{17}$  respectively (Zhang, et al., 2010).



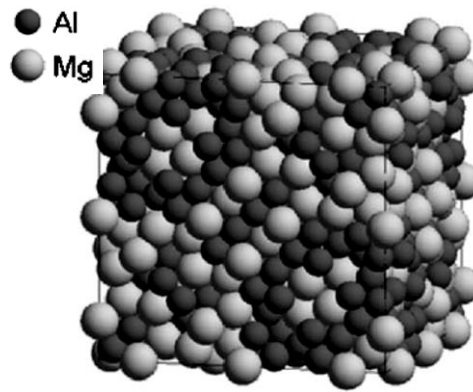


Figure 2-60: Complete unit cell of  $\beta$ - $\text{Al}_3\text{Mg}_2$  phase (Jeglić, et al., 2007).

The  $\beta$  phase melts at 452 °C and undergoes a phase transformation from a cubic structure ( $\beta$ -phase) to a rhombohedral  $\beta'$  phase. This phase has 293 atoms per unit cell (Feuerbacher, et al., 2007), at a range of temperatures extending from -3 to 237 °C for Mg contents of 39.7 and 38.2 at.%, respectively (De Noirfontaine, et al., 2010).

#### 2.14.4 Other Phases

A side from the  $\beta$  ( $\text{Mg}_2\text{Al}_3$ ) and  $\gamma$  ( $\text{Al}_{12}\text{Mg}_{17}$ ) phases, aluminium and magnesium have been found to form other compounds when they react, such as  $\epsilon$  (sometimes known as R) and  $\lambda$ . These compounds particularly tend to form in the range of composition from about 45 to 60 at% Al, as shown in the section of the Mg-Al phase diagram in Figure 2-61 (Su, et al., 1997).

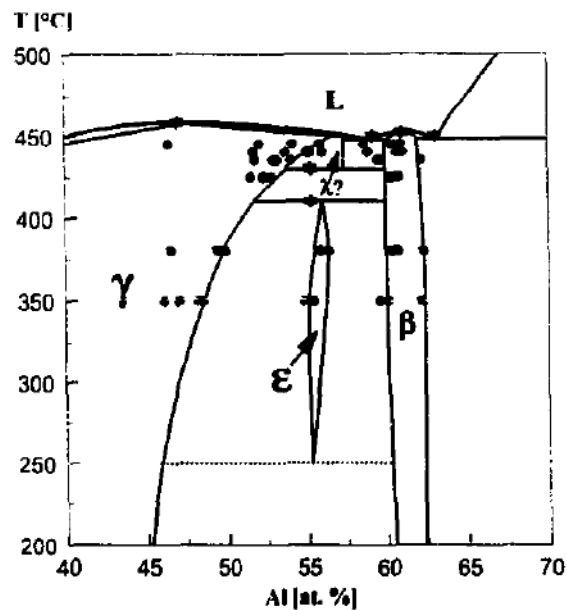


Figure 2-61: The middle section of the Mg-Al phase diagram proposed by Su et al. (Su, et al., 1997).

The  $\epsilon$  ( $\text{Al}_{30}\text{Mg}_{23}$ ) phase has a rhombohedral structure with the large unit cell shown in Figure 2-62 and a composition of  $55.9 \pm 0.5$  at% aluminium. Su et al. (Su, et al., 1997) found that this phase can be observed in alloys annealed for 260 h and 170 h at  $350^\circ\text{C}$  and  $380^\circ\text{C}$  respectively, but it could not be detected after annealing for 50 h. Therefore, they concluded that the formation of this phase is very sluggish (Su, et al., 1997).

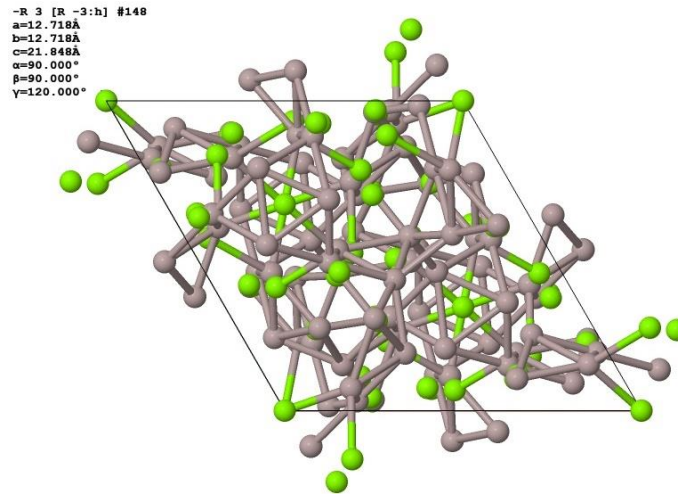


Figure 2-62:  $\epsilon$ - $\text{Al}_{30}\text{Mg}_{23}$  phase crystal structure (Villars, 2014).

In their work, Su, et al., (Su, et al., 1997) detected a stable  $\lambda$  phase in samples annealed in the range of  $435$  to  $445^\circ\text{C}$ , which indicates the occurrence of a peritectic reaction ( $\text{L} + \gamma \leftrightarrow \lambda$ ) at  $450^\circ\text{C}$ . The  $\lambda$  phase is transformed by a eutectoid reaction into  $\beta + \gamma$  in a temperature range of  $435$  to  $425^\circ\text{C}$  (Su, et al., 1997). Conversely, the temperature of the  $\epsilon$  phase peritectoid reaction ( $\beta + \gamma \rightarrow \epsilon$ ) calculated by Zhong et al. (Zhong, et al., 2005) was  $700\text{ K}$  ( $427^\circ\text{C}$ ), which is higher than that proposed by Su et al. by about  $17^\circ\text{C}$ . Moreover, the  $\lambda$  phase was not detected in this study (Zhong, et al., 2005).

## 2.15 FE Modelling of the Mechanical Behaviour of RFSSW Joints

Finite element (FE) analysis is a suitable method for the study of the mechanical behaviour of spot joints due to the complexity of their geometry and the considerable differences in the mechanical properties of the interacting materials. Quantitative clarification of the tensile-shear tests for lap joint samples represents an important application of FE analysis, as it is difficult to estimate the critical values of stress and strain directly from these laboratory measurements, unless the very nonuniform fields of stress and strain in the joints are understood (Mitchell, et al., 1975).

Since the RFSSW process is still a new technique, little research has been published on the topic of simulation of the tensile-shear tests. In general, the most significant problems faced by researchers in the field of simulation of tensile-shear tests for RFSSW joints are two issues: firstly, the question of how to represent the geometry of the joint shape and, secondly, the distribution of the material properties in the various regions of the joint.

To simplify the geometric shape of the joint most researchers assume that the SZ has a disc shape (Mazzaferro, et al., 2009; Campanelli, et al., 2013b; Rosendo, et al., 2015). Two approaches can be used to represent the material properties. The first approach involves the use of non-heat-treatable alloys, which reduces the differences in material properties between the joint regions. In their work Campanelli et al. (Campanelli, et al., 2013a; Campanelli, et al., 2013b) modelled the typical lap-shear test of the RFSSW joints for AZ31 magnesium alloy sheets, by using non-heat-treatable alloys to reduce the variables in the simulation and to focus on the weld geometry. They proposed four different models to represent different specific weld defects, shown in Figure 2-63 (Campanelli, et al., 2013a; Campanelli, et al., 2013b). The main problem with such models is that they show the effect of one variable, the geometric variable, on the joint performance, while they neglect the influence of other variables, especially the use of materials with properties that can be changed as a result of the welding process.

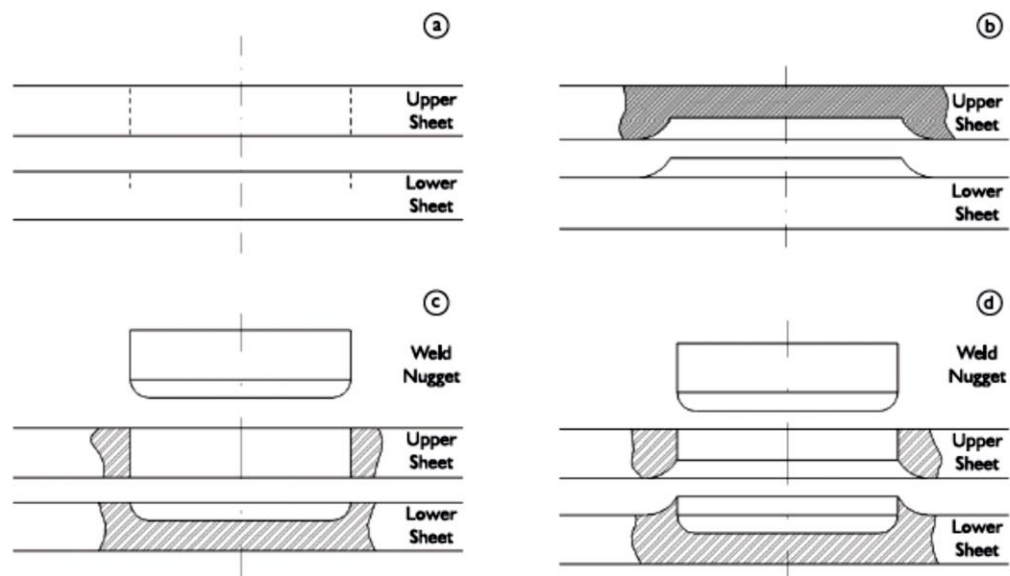


Figure 2-63: The geometric features of the welded joint: (a) indistinct weld nugget without a hook, (b) indistinct weld nugget with a hook, (c) distinct weld nugget without a hook and (d) distinct weld nugget with a hook (Campanelli, et al., 2013b).

The second approach for the simplification of material properties involves dividing the joint into different divisions depending on the material properties in these regions (i.e. base metal (BM), heat-affected zone (HAZ), thermomechanically-affected zone (TMAZ) and stir zone (SZ)), with the assumption that the material properties are homogeneous in each of these regions individually. Mazzaferro et al. (Mazzaferro, et al., 2009) used a numerical model for predicting the mechanical properties of RFSSW joints from an AA2024-T3 aluminium alloy. The joint in their model consisted of three regions SZ, TMAZ, and BM, the properties of which were assumed based on the hardness profile shown in Figure 2-64. They assumed that the SZ region and the TMAZ had a mechanical strength of 5% greater and less than that in the base metal respectively. They found that the stresses reached the ultimate tensile strength of the material in an annular region around the contact area between the sheets. This region then extended towards the top surface of the upper sheet, due to the increase in load, producing a situation where a plug pull-out fracture mode should occur (Figure 2-65) (Mazzaferro, et al., 2009). In spite of the results they obtained, assuming a uniform distribution of material properties is still problematic and leads to inaccuracy in the stress distribution that results from the model because the large difference in material properties between neighbouring regions will result in a high stress concentration on the borders between these regions, especially for joints that have a HAZ with material properties that are very different from the BM and SZ (for example, in as-welded condition). To solve this problem and to reduce the effect of sharp differences in the levels of the material properties in the finite-element model of an FSSW joint, Nguyen, et al., (Nguyen, et al., 2011) divided the TMAZ and HAZ into four and five sub-regions, respectively, as shown in Figure 2-66a. The researchers achieved this using hardness measurements to first evaluate the field strength of the weld zones (Figure 2-66b).

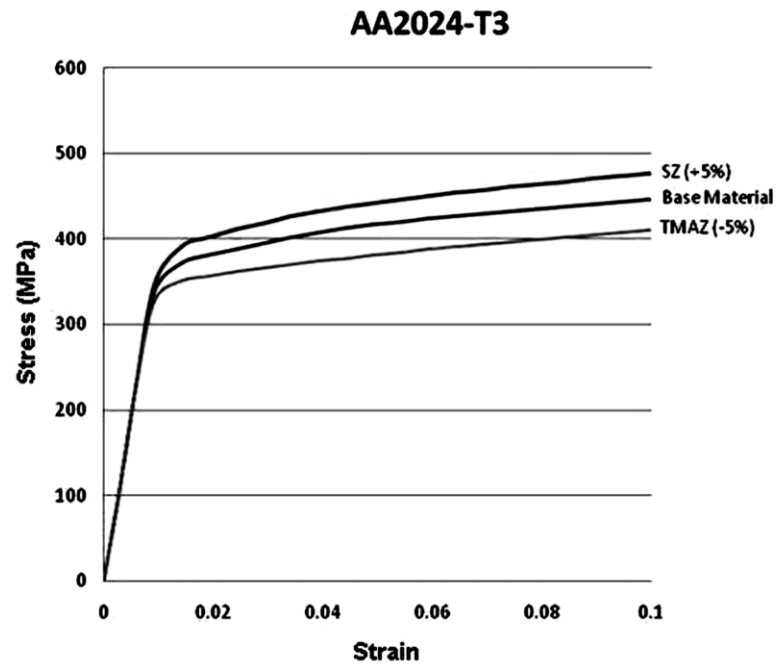


Figure 2-64: The engineering stress-strain curves assumed for the BM, SZ, and TMAZ (Mazzaferro, et al., 2009). Note the lack of difference in the assumed work-hardening behaviour.

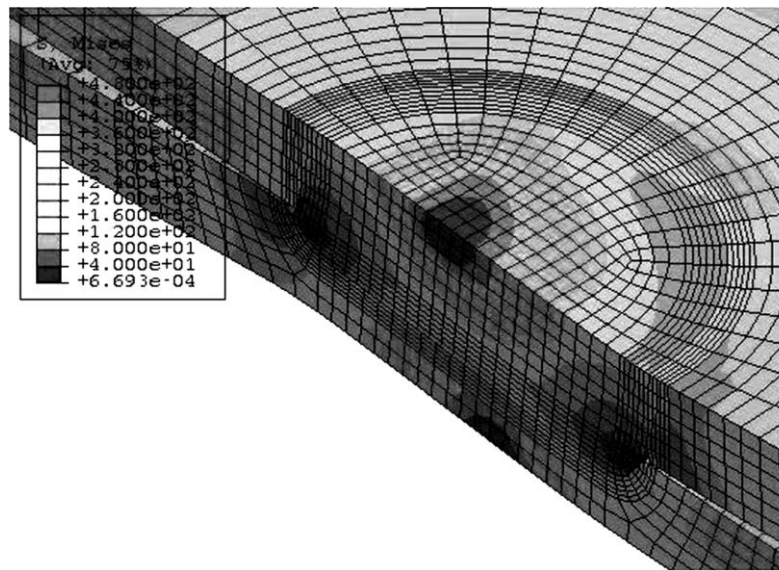


Figure 2-65: Stress distribution in the RFSSW joint under loading (Mazzaferro, et al., 2009).

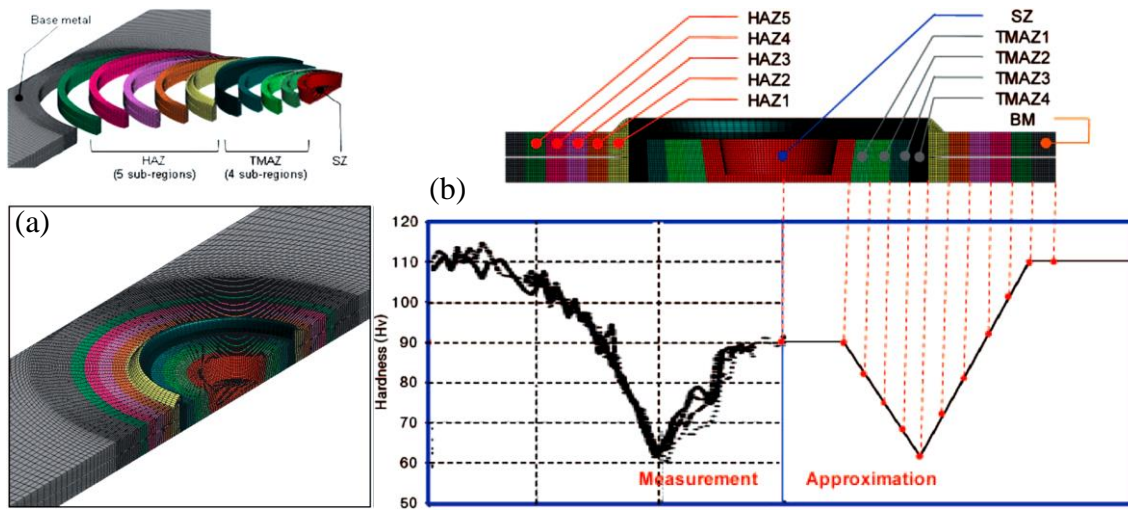


Figure 2-66: Finite-element model of a FSSW joint with 5 different material property regions (a) and (b) the hardness profile of these regions (Nguyen, et al., 2011).

## **Chapter 3: Experimental Methods**

---

### **3.1 Introduction**

To achieve the objectives of this study, three alloys were used: a well-known automotive aluminium alloy AA6111-T4, 6082-T6 and the magnesium alloy AZ31-H24. These materials were joined using refill friction stir spot welding (RFSSW) with the sleeve plunge variant. The standard RFSSW process was subsequently modified to improve the observed tendency for defect formation. The lap-shear test was predominantly used to analyse the mechanical properties of the joints. To understand the mechanical performance of these welds, the cross-sections of the welded joints, in the as-welded and heat-treated conditions, were subjected to several tests, such as hardness testing, metallographic analysis using scanning electron microscopy (SEM), energy dispersive X-ray (EDX) analysis, electron-backscatter diffraction (EBSD) analysis, and transmission electron microscopy (TEM), as well as optical microscopy (OM). To further clarify the welding mechanisms, thermal measurements were carried out during the weld cycle. In addition, special samples were made using marker materials, combined with the X-ray tomography technique to monitor the material flow. Finally, an FE model was developed to simulate the deformation behaviour of the similar and dissimilar joints in lap shear tests. An explanation for each of these methods will be presented in this chapter.

### **3.2 Materials**

The materials used in this study were the aluminium alloys AA6111-T4 and AA6082-T6 and the magnesium alloy AZ31-H24, the nominal compositions of which are shown in Table 3.1. The uniform thickness of the as-received AA6111-T4, AA6082-T6, and AZ31-H24 sheets were 0.94 mm, 0.86 mm and 1.05 mm, respectively.

Table 3-1: Nominal chemical compositions of the alloys used in this study.

Alloy	wt% Mg	wt% Si	wt% Cu	wt% Fe	wt% Mn	wt% Zn	wt% Al
AA6111	0.8	0.7	0.7	0.25	-	-	Balance
AA6082	0.9	0.8	0.1	0.25	-	-	Balance
AZ31	Balance	-	-	-	0.5	1	3

The hardness of the as-received materials was measured using the micro-hardness test procedure (Section 3.6), with an average of 10 measurements performed on each sheet of each material. The average hardnesses of the AA6111-T4, AA6082-T6 and AZ31-H24 were  $89 \pm 2$  HV,  $114 \pm 3$  HV, and  $55 \pm 2$  HV respectively.

### 3.2.1 Surface Preparation for Welding

After cutting the samples to the required dimensions for each test, the surfaces were prepared for the welding process by grinding them using 1200 grit silicon carbide papers to remove the oxides. The samples were then cleaned with ethanol to remove the grease and dust from the surface.

### 3.3 Welding Method: Refill Friction Stir Spot Welding (RFSSW) and Modified FSSW

In this work the RFSSW process was used to study the effects of different welding parameters on the mechanical performance and microstructural features of AA6111-T4 similar aluminium alloy joints and AA6111-T4 to AZ31-H24 dissimilar joints. Welds were performed using a RFSSW machine model RPS100, manufactured by HARMS+WENDE HWH shown in Figure 3.1. The machine has computerised control with a touch screen used to input the welding parameters and to set alarms for the user in the event of any problems occur.

The machine contains an electrical motor used to rotate the sleeve and the pin to the required tool rotation rate, and two actuators, which are used to move the pin and the sleeve up and down during the welding process, while pressurised air is used to move the clamping ring. The welding process is controlled by a computerised control unit connected to the machine and a desktop computer.





Figure 3-1: The refill friction stir spot welding machine.

A monitoring system on the computer recorded the rotational rate, pin and sleeve position, axial load, welding time and electrical current. A typical monitoring chart for a welding cycle is shown in Figure 3.2.

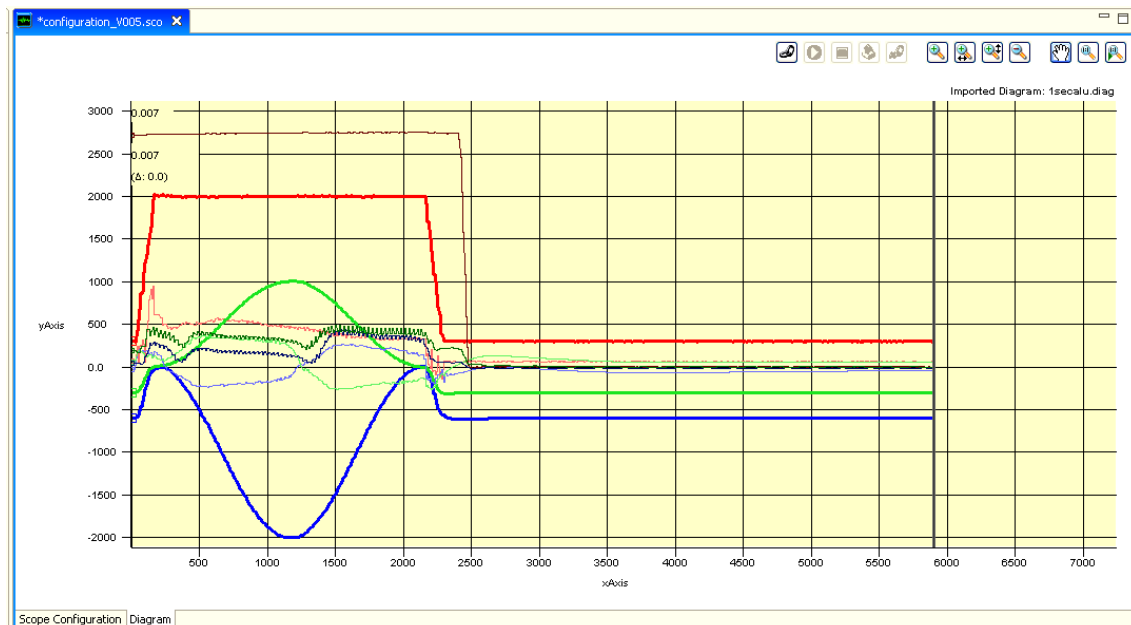


Figure 3-2: Typical monitoring chart for the RFSSW process.

The welding head shown in Figure 3.3 carries the welding tool which consists of a pin, sleeve and clamping ring (further details are shown in Figure 3.4). The dimensions of each tool component were as follows: the pin measured 5.2 mm in diameter, the sleeve had an outer diameter of 9 mm and the clamping ring had an 18 mm outer diameter.

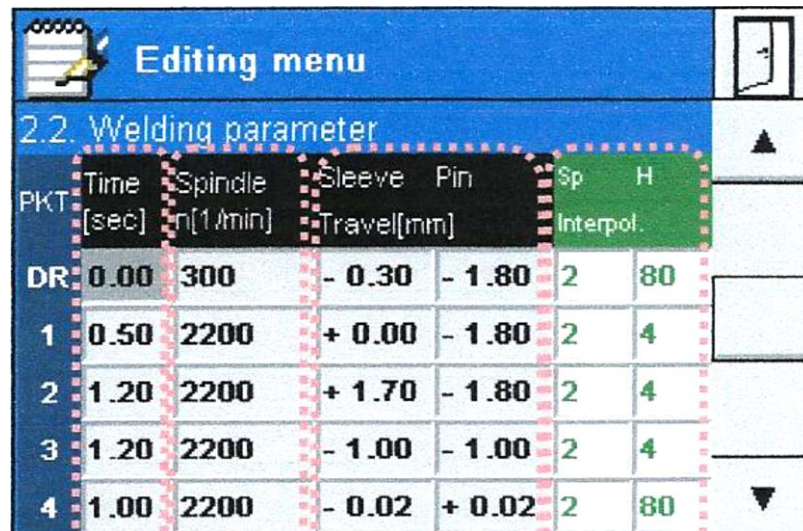


Figure 3-3: Welding head for the RFSSW process.



Figure 3-4: The RFSSW tool parts.

The main parameters in the welding process that can be controlled by the machine's software are: time (for each step of the process, i.e. plunging time, dwell time and retracting time); tool rotation rate (also for each welding step); and the sleeve and pin travel (plunge depth). Figure 3.5 shows the control table for the machine variables.



The image shows a software interface titled "Editing menu" with a sub-header "2.2. Welding parameter". Below this is a table with columns: PKT, Time [sec], Spindle n[1/min], Sleeve Travel[mm], Pin Travel[mm], Sp Interpol., and H. The table contains five rows of data, with the first row labeled "DR" and the others numbered 1 through 4. The values for Time, Spindle, Sleeve, Pin, Sp, and H are specified for each step.

PKT	Time [sec]	Spindle n[1/min]	Sleeve Travel[mm]	Pin Travel[mm]	Sp Interpol.	H
DR	0.00	300	- 0.30	- 1.80	2	80
1	0.50	2200	+ 0.00	- 1.80	2	4
2	1.20	2200	+ 1.70	- 1.80	2	4
3	1.20	2200	- 1.00	- 1.00	2	4
4	1.00	2200	- 0.02	+ 0.02	2	80

Figure 3-5: The RFSSW machine variable control table.

Different combinations of welding parameters were used in this study. The effect of welding time (including the change in the time of each welding step), the tool rotation rate and the plunge depth, in addition to modification of the process by adding additional steps, especially for welding Mg to Al, will be discussed in Chapter 5.

Table 3-2: Range of welding parameters used in this study.

Material Combination	Welding Parameter			
	Tool-rotation Rate (rpm)	Sleeve-plunging Depth (mm)	Pin-plunging Depth (mm)	Welding Time (s)
AA6111 to AA6111	1500 - 2500	0.2 – 1.0	-	0.3 – 2.0
AZ31 to AA6111	1300 - 2800	0.8-1.6	0.2	0.7-2.0

As described in section 2.6.3, the conventional RFSSW process consists of four stages. After clamping and beginning tool rotation, the rotating sleeve is plunged into the top sheet and penetrates the joint line, while simultaneously the pin is retracted to allow the plasticised material to be pushed upwards into the sleeve tube (Figure 3-6, step b). In the following stage, the sleeve retracts and the pin then pushes back the displaced material to the surface level of the joint to form a weld (Figure 3-6, step c). However, the preliminary results when welding Mg to Al showed that with the conventional RFSSW process, void defects were normally detected in the weld edges near the position where the sleeve plunged, due to insufficient material refilling. A modified RFSSW process was thus used in this study, in which the conventional refill weld cycle

was followed by another plunge step with a shallower pin depth (Figure 3-6, step d) and a very short additional time. By using this new modified method with a two-stage refill action, voids and defects were successfully avoided during dissimilar joining of Mg to Al alloys.

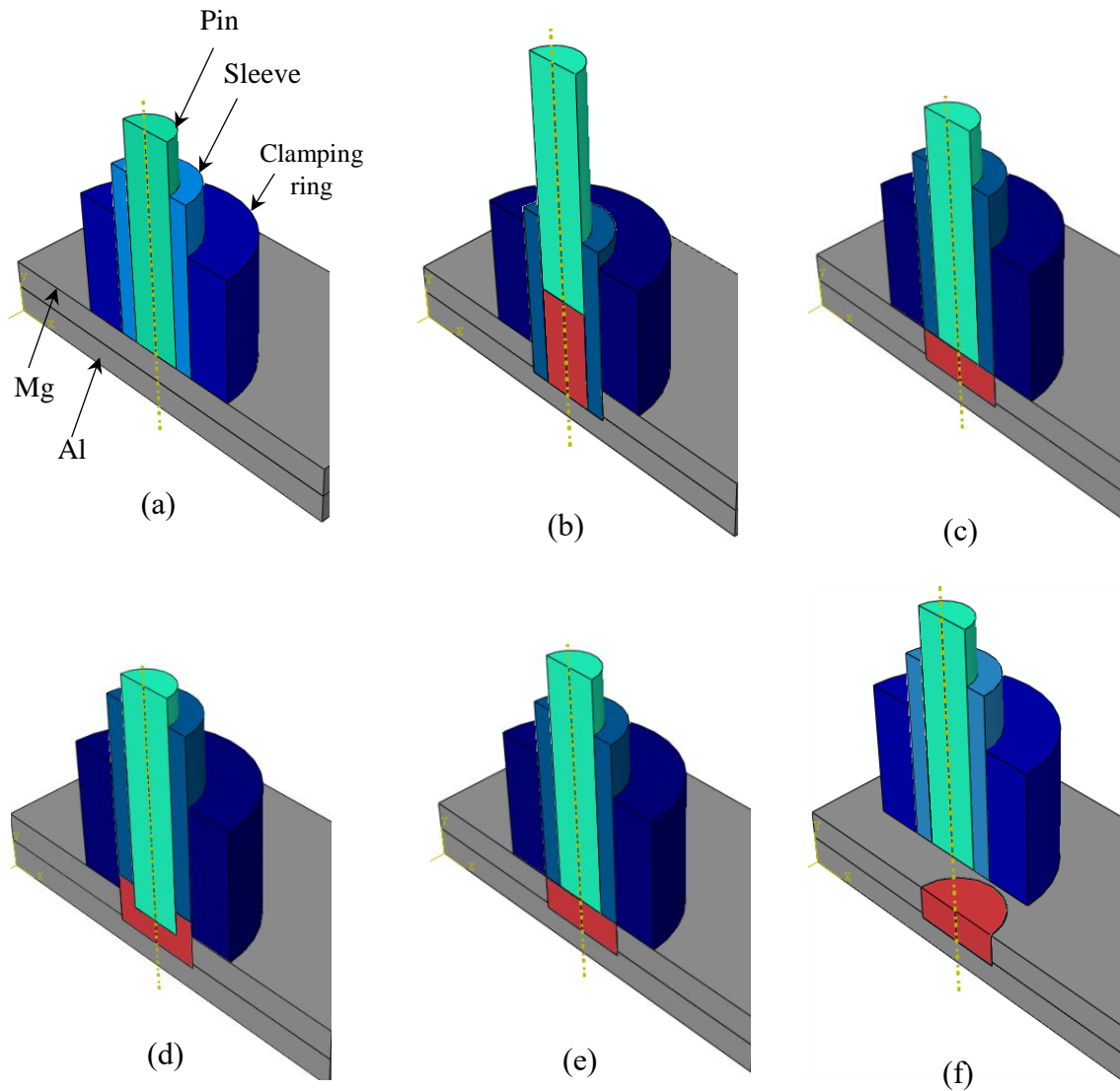


Figure 3-6: Schematic illustration of the modified RFSSW process: (a) to (c) the conventional refill process with the sleeve plunging first; (d) and (e) the second refill stage with slight pin-plunging, as developed in this project.

### **3.4 Heat Treatments**

After welding the similar AA6111 aluminium alloy samples the welds were directly artificially aged at 180 °C for 30 minutes in order to simulate the paint-bake thermal cycle (or PBC, as it is known in the automotive industry). After this heat treatment, the samples were mechanically tested (using lap-shear test) and some other samples were sectioned for hardness and metallographic investigations.

Other heat treatments were also carried out for special purposes, such as heat treatment of the AA6082-T6 alloy. The AA6082 aluminium alloy was used as a marker material because it has a similar response to deformation but with a lower copper content than AA6111, leading to different etching characteristics compared to AA6111 (Bakavos, et al., 2011; Reilly, et al., 2015). The AA6082 alloy was heat treated before welding to balance its hardness with the hardness of the AA6111-T4 alloy, so that the two alloys would have as similar flow properties as possible. The heat treatment consisted of: solution heat-treatment at 520 °C for 45 minutes then quenching in water. The samples were then naturally aged for 120 hrs.

To simulate the material properties in the stir zone and heat affected zone, which were required for the FE modelling of the lap-shear test in as-welded and artificially aged conditions, several samples of AA6111 were subjected to different heat-treatments, including:

1. Solution-heat treatment only at 500° C for 20 min.
2. Solution-heat treatment at 500° C for 20 min, followed by artificial ageing at 140° C for 25, 45, and 53 min.
3. Solution-heat treatment at 500° C for 20 min, followed by artificial ageing at 180° C for 15 and 30 min.
4. Artificial ageing only at 180° C for 30 min.

### **3.5 Thermal Measurements**

To measure the weld temperature during RFSSW, 0.5 mm k-type thermocouples were used with a National Instruments datalogger, which recorded the temperature measurements at a frequency of 100 Hz. The thermocouples were located in two

different configurations, depending on the material combination being welded. For AA6111 similar aluminium alloy welding, to prevent damage during the welding process, the thermocouples were located in five different locations underneath and in very tight contact with the lower sheet (0, 3, 6, 9, and 12 mm from the centre of the weld), as shown in Figure 3.7. Conversely, only one site was chosen for the location of the thermocouple during temperature measurement for the AZ31-H24 magnesium alloy to AA6111-T4 aluminium alloy dissimilar welds. In this situation the thermocouple was located between the two sheets 3 mm from the weld center (as seen in Figure 3-8), which corresponds to the location at the weld interface where the highest temperature was recorded in the AA6111 similar welding.

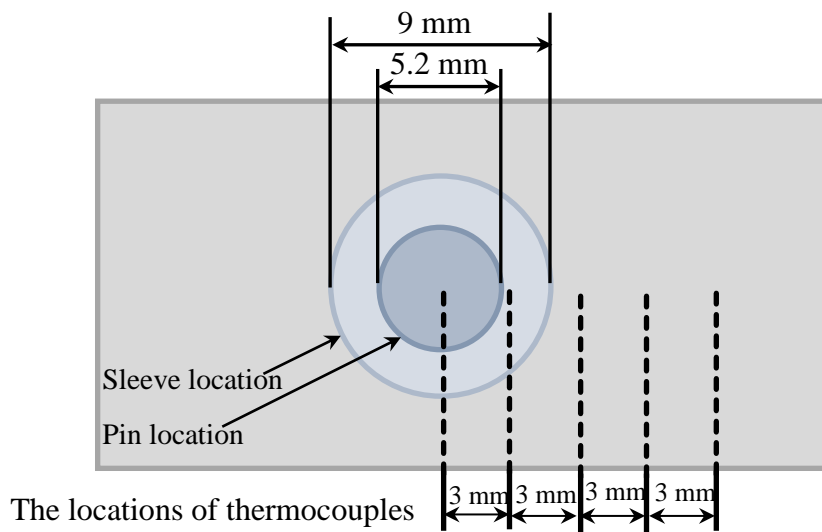


Figure 3-7: Schematic illustration of the different thermocouple locations for AA6111 similar aluminium alloy welding.

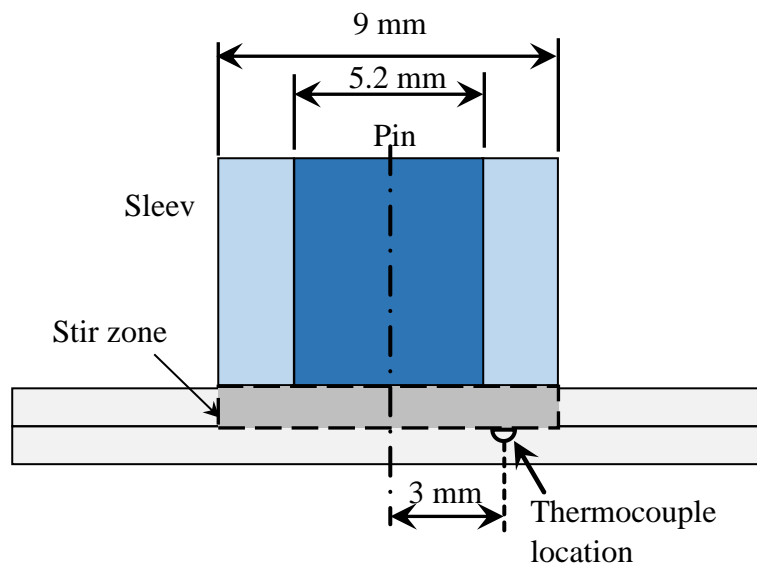


Figure 3-8: Schematic illustration of the thermocouple location for the dissimilar AZ31-H24 magnesium alloy to AA6111-T4 aluminium alloy welding.

### 3.6 Hardness Test

Microhardness testing was implemented to identify the effect of the welding process and the heat treatments on the local mechanical properties of the weld cross-section. After cutting the welded samples through the weld centre, they were mounted and polished.

Due to the significant change in the microhardness when moving from one point to another through the weld cross-section a step distance of 0.5 mm was used between every two points. This adaption led to the need to use a load of 200 g to keep the proper distance of no less than 5 times of the indentation diameter between the measured points,. Measurements were made in the form of two parallel lines of points. The first line was located in the mid thickness of the upper sheet and extended from one edge to the other through all the areas of the welded joint. The second line was the same as the first line, but located in the mid-thickness of the lower sheet, as shown in Figure 3-9.

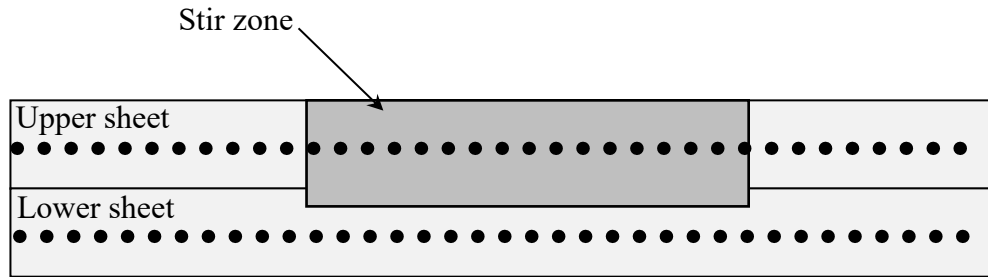


Figure 3-9: Schematic illustration of the locations of the microhardness measurements.

The hardness tester used for the measurements was an Instron Wilson Tukon 2100, with a pyramid shaped indenter. The dimensions of the two diagonals of the resulting shape ( $d_1$  and  $d_2$ ) (see Figure 3.10) were measured using the measuring facility integrated into the machine. Vickers Microhardness (HV) values were then calculated by the machine using the equation:

$$HV = 1.854 \left( \frac{P}{d^2} \right) \quad (3 - 1)$$

where  $P$  is the applied load and  $d = (d_1 + d_2)/2$

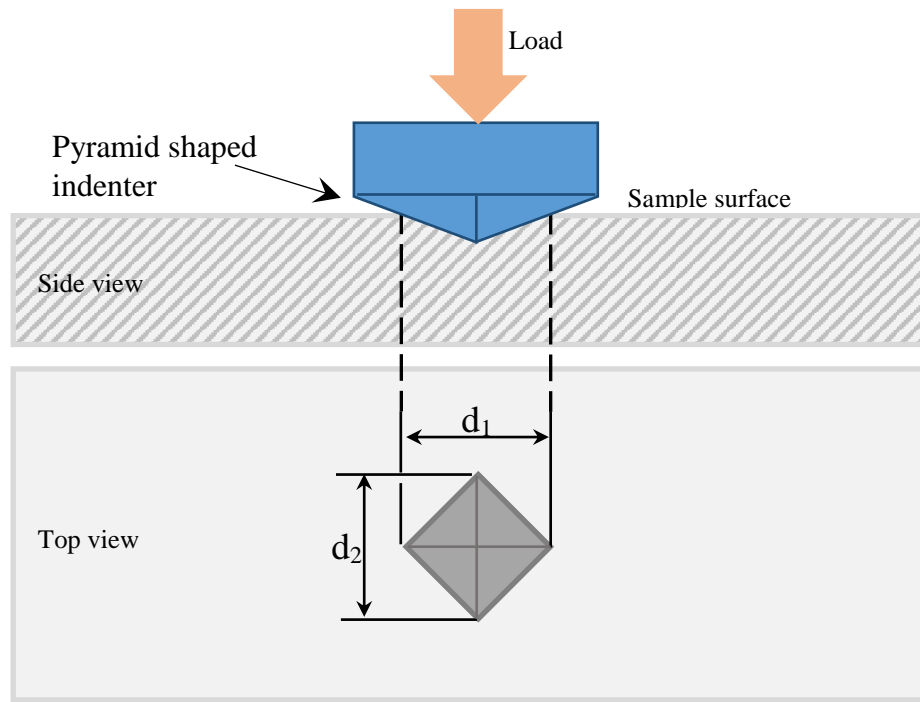


Figure 3-10: Schematic of the Vickers Microhardness indentation test.

### 3.7 Mechanical Testing

To evaluate the performance of the welded joints, lap tensile-shear tests were performed using an Instron (50 kN) mechanical testing machine with a 5 kN load cell. A 1.0 mm/min crosshead travel speed was used and the data was collected at 50 Hz. The samples were prepared so that the rolling direction was parallel to the longitudinal axis; as shown in Figure 3-11, the dimensions measured 100 mm in length and 25 mm in width (samples of 50 mm width were used for aluminium to aluminium welds). For the AZ31 magnesium to AA6111 aluminium dissimilar welds the samples were arranged so that magnesium was the upper sheet. The joint was located in the centre of the 25 mm overlap length between the upper and lower sheets (an overlap of 50 mm was used for aluminium to aluminium welds). Two spacers with a length of 25 mm were used at each end of the samples for the purpose of preventing misalignment of the sheets during testing. During each test the load-displacement data was recorded to identify the peak load and to calculate the fracture energy from the area under the load displacement curve.



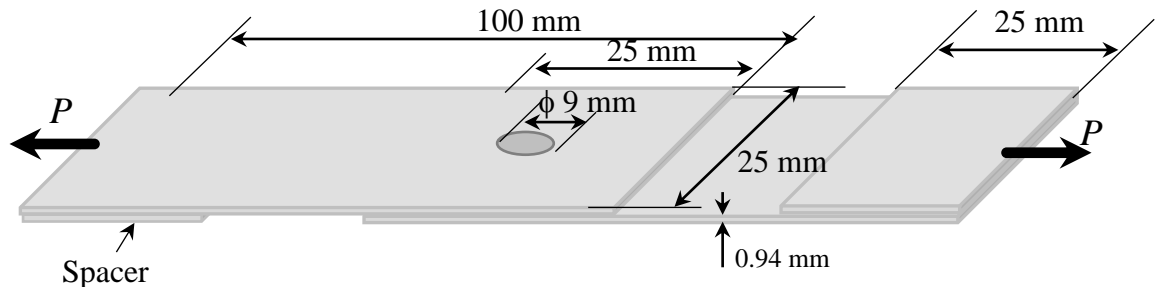


Figure 3-11: Schematic illustration of lap-shear test specimens. The bold arrows represent the applied force  $P$ .

To measure the mechanical properties of different weld zones in the as-welded and artificially aged conditions, which were required for FE modelling of the lap shear test, several standard tensile test samples of AA6111 aluminium alloy and AZ31 magnesium alloy were tested with the same machine and parameters used to test the welded samples in different heat-treatment conditions (section 3.4), in addition to the as-received (T4 for AA6111 and H24 for AZ31). More details about the results of these tests and how this data was used in the FE modelling will be discussed in chapter 6.

## 3.8 Metallographic Examination

### 3.8.1 Sample Preparation

For metallographic analysis, the welded joints were sectioned across their centre using a Struers Accutom-5 cutting machine with a Struers 30A13 blade (with dimensions of 125 mm diameter and 0.5 mm thickness). The samples were then either cold-mounted or mounted in a brass holder, then ground using a Struers Tegra Pol-31 automatic machine with silicon carbide papers of 600, 800, 1200 and 4000 grades, respectively, using water as a lubricant and allowing grinding time of 2 min for each step. The samples were then polished using diamond spray with a particle size of 6  $\mu\text{m}$ , 3  $\mu\text{m}$  and 1  $\mu\text{m}$ , with a water-based lubrication solution for the similar AA6111 welds and oil-based lubrication solution for the AZ31 to AA6111 dissimilar welds. The final polishing step was completed using 0.2  $\mu\text{m}$  colloidal silica (O.P.S) solution for 7 minutes for all samples except those on which EBSD was performed, where the final polishing time for them was 1 hour. Between each stage, the samples were thoroughly washed with ethanol. The samples were carefully washed with ethanol after each polishing stage.

### **3.8.2 Optical Microscopy**

An OLYMPUS BH-2 Optical microscope was used to determine the microstructure of the welded joint cross-sections, material flow, and the failure behavior of the tensile-shear samples. A Kellers reagent (95 ml H<sub>2</sub>O, 2.5 ml HNO<sub>3</sub>, 1.0 ml HCl, and 1.5 ml HF) was used to complete the etching process with an etching time of 15 sec.

### **3.8.3 Scanning Electron Microscopy (SEM)**

Scanning electron microscopy (SEM) uses a focused electron beam to collect information from the surface of a sample via interaction between the beam and atoms in the sample. Because of the shorter wavelength of electrons compared with light, SEM images have a higher resolution in comparison with optical microscopy. In this study, two types of microscope were used to perform SEM analysis: an FEI Quanta 650, and an FEI Magellan. To obtain high resolution images, these microscopes were equipped with a Field Emission Gun (FEG-SEM).

The FEG consists of a sharply pointed tungsten tip with several kilovolts negative potential relative to the sample surface, so that the electrons are emitted from the tip and accelerated to the surface of the sample (Voutou & Stefanaki, 2008). Several lenses are used to control the diameter and focus the beam. These include the condenser lenses and objective lens. When an electron beam collides with a sample, it interacts with the atoms in the surface; some of the incident electrons then displace electrons from their orbits around nuclei of the sample atoms. As a result, these atoms become unstable; to return to stability, they emit different types of radiation (as shown in Figure 3-12), which are captured by various detectors and give different information (Voutou & Stefanaki, 2008). The interaction between the electron beam and the atoms of the sample surface results in two types of electrons being emitted: secondary electrons (SE) and backscattered electrons (BSE) (Figure 3-12b). These two types of electrons provide different and valuable information about the nature of the sample material (Watt., 1997).

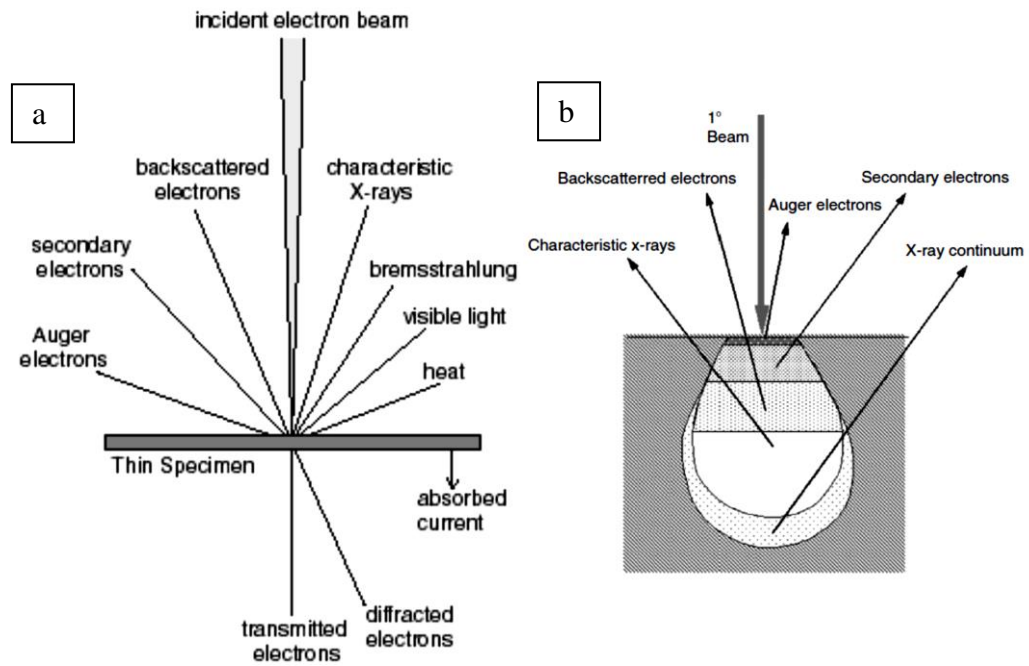


Figure 3-12: Effects produced by the electron beam–specimen interaction: (a) general effects (Voutou & Stefanaki, 2008), and (b) regions from which signals can be detected in the scanning electron microscope (Zhou, et al., 2007).

Secondary electrons (SE) represent the strongest region of the electron energy spectrum emitted from the surface; they result from interaction between the incident electrons and the electrons in the lower-energy electron shells of the sample material, which excites them. These excited electrons move towards the sample surface experiencing elastic and inelastic collisions, then these electrons are emitted from the surface if they still have sufficient energy when they reach it (Watt., 1997; Voutou & Stefanaki, 2008). Production of SE is closely related to the sample topography. Because they have low energy (5eV), only secondary electrons, which are very near the surface (<10 nm) can leave the sample and be observed. Any changes in the sample topography greater than this depth will change the yield of secondary electrons because of collection efficiencies (Voutou & Stefanaki, 2008). Consequently, the SE imaging mode provides high resolution topographical images.

Backscattered electrons (BSEs) consist of high-energy electrons from the electron beam which are backscattered, or reflected, out of the sample interaction volume. The behaviour of a backscattered electron directly depends on the atomic number of the sample and how close it gets to the nucleus. Because of this difference in production rates, elements with higher atomic number result in more backscattering and will appear

brighter than elements with lower atomic number. This difference in interaction is used to distinguish parts of the sample, which have different elements (Watt., 1997; Voutou & Stefanaki, 2008). The BSE imaging mode was used in the present study to recognise areas with dissimilar chemical compositions, and especially to differentiate between the IMC layer and base metals.

#### **3.8.4 Energy Dispersive X-ray (EDX)**

An energy dispersive X-ray (EDX; also called EDS) is most often used to determine the distribution and content of elements in a certain region of material (Voutou & Stefanaki, 2008). In the EDX technique, a characteristic X-ray spectrum is emitted due to the interaction of the high-energy electrons in the incident beam with electrons in the sample atoms. As a result, the electrons are ejected from the atoms' inner shells, which forces the electrons to drop down from higher shells to fill the gap. The energy difference due to this electron movement from higher to lower shells is emitted in the form of an X-ray. Because each element has its own characteristic energy differences, it is possible to use the EDX method to analyse the sample composition, in terms of the quantity and distribution of the elements (Watt., 1997).

#### **3.8.5 Electron Backscatter Diffraction (EBSD)**

The “electron backscatter diffraction” (EBSD) technique provides quantitative microstructural information about the local crystallographic nature of a sample such as the grain boundary character, grain size, grain orientation, texture, and phase identity (Maitland & Sitzman, 2006). In this study, an FEI Magellan microscope was used to perform EBSD with an accelerating voltage of 20 kV. This machine is equipped with Oxford Instruments Xmax80 SDD system, EBSD detector and an AZTEC integrated analysis system. The results were analysed using Channel5 EBSD acquisition software provided by HKL Technology ApS., Denmark.

EBSD works by positioning a sample with a flat and highly polished surface at a shallow angle, typically  $20^\circ$ , with the incident electron beam (because the stage in the SEM machine is usually used to tilt the sample plane to this shallow angle, the stage tilt value is often referred to as  $70^\circ$ ). Electrons are diffracted from the incident beam position on the surface of the sample. With the stationary of the beam, an EBSD pattern (EBSDP) emanates spherically from this point. When the primary electron beam

interacts with the crystal lattice, the backscattered electrons, which have low energy loss, are channelled and exposed to path differences, resulting in constructive and destructive interference. If a phosphor screen is located a short distance from the surface of the sample in the path of the diffracted electrons, a diffraction pattern can appear, which can be used to identify the phase and observe its orientation from the material in the interaction volume (Maitland & Sitzman, 2006).

### **3.8.6 Focused Ion Beam (FIB) Milling**

The basic principle of operation of a focused ion beam (FIB) device is the removal of atoms from the material of the target by bombarding it with accelerated heavy ions (gallium ( $\text{Ga}^+$ ) is usually used for this purpose) (Wirth, 2009). A FIB device can be used for imaging by using low beam currents, milling specific locations with high beam currents, or to deposit material like Pt or W. The deposition and milling modes were used in the current study to prepare TEM samples using an FEI Quanta 3D dual-beam FIB.

To prepare a TEM sample using the FIB technique, the steps shown schematically in Figure 3-13 were used. Firstly, Pt was deposited on the area of interest in order to protect it (Figure 3-13a). The second step consisted of the cutting of trenches in both sides of the region to be studied (Figure 3-13b). This was followed by cutting a ‘U’ shape in the selected region, as shown in Figure 3-13c. In the next step, a probe was attached to the sample, by deposition of Pt, and used to lift out the sample (Figure 3-13d). A Pt deposition was then used again to attach the sample to a specific holder (Figure 3-13d). In the final step, the attachment between the sample and the probe was cut. These steps were followed by several thinning stages, achieved by milling the surface. As a result, the sample was thinned to less than 300 nm. The final stage involved cleaning to remove impurities from the sample surface deposited during the process (Figure 3-13f) (FEI, 2007).

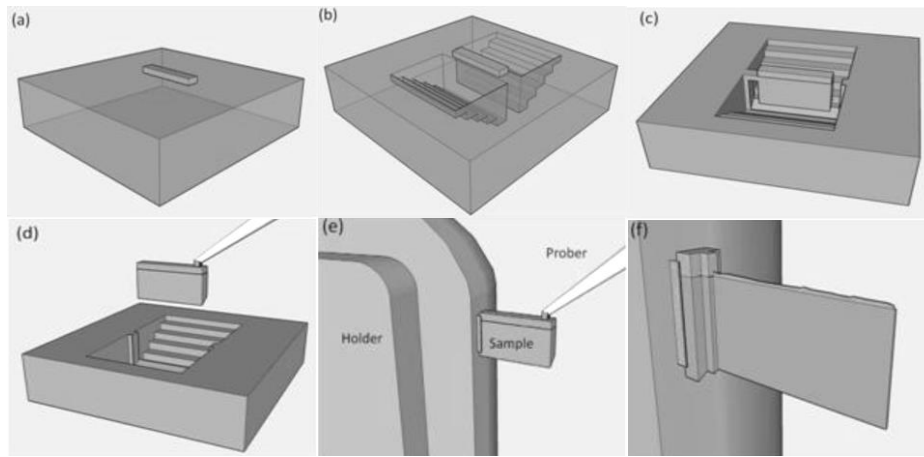


Figure 3-13: Schematic diagram illustrating the FIB procedure of TEM sample preparation: (a) deposition of Pt, (b) bulk-out, (c) U-cut, (d) lift-out, (e) mounting, (f) thinning and cleaning (FEI, 2007).

### 3.8.7 Transmission Electron Microscopy (TEM)

Transmission electron microscopy (TEM) is a technique in which an electron beam interacts and passes through an ultra-thin specimen. In the TEM method shown schematically in Figure 3-14, the electron beam is emitted from a source and then focused and magnified using a system of electromagnetic lenses. When the electron beam hits the sample, many types of electrons can be generated, as shown in Figure 3-12a. Diffracted electrons and transmitted electrons are the two types of electrons used to collect the information in conventional TEM. The objective lens forms the primary image, the objective lens and objective aperture are used to control the image type (either the microstructure image or diffraction pattern) by choosing from the elastically scattered electrons. After its generation, the image passes through a magnifying system which consists of three lenses, the first and second of which are used to control the image magnification and the third is the projector lens. Finally, the image can be seen either on a fluorescent screen or a monitor or both (Voutou & Stefanaki, 2008). By proper use of the apertures and the tilt coils, different types of images can be obtained. A Bright Field Image is obtained if an unscattered electron beam is selected by the objective aperture. Alternatively, if diffracted beams are selected the result will be a Dark Field Image (Voutou & Stefanaki, 2008).

In this study, TEM analysis was performed using an FEI Tecnai TF20 microscope operating at 200 kV with two modes: the conventional imaging mode, which was used to observe the microstructure at the interface of the dissimilar joints, and the diffraction mode to identify the existing phases.

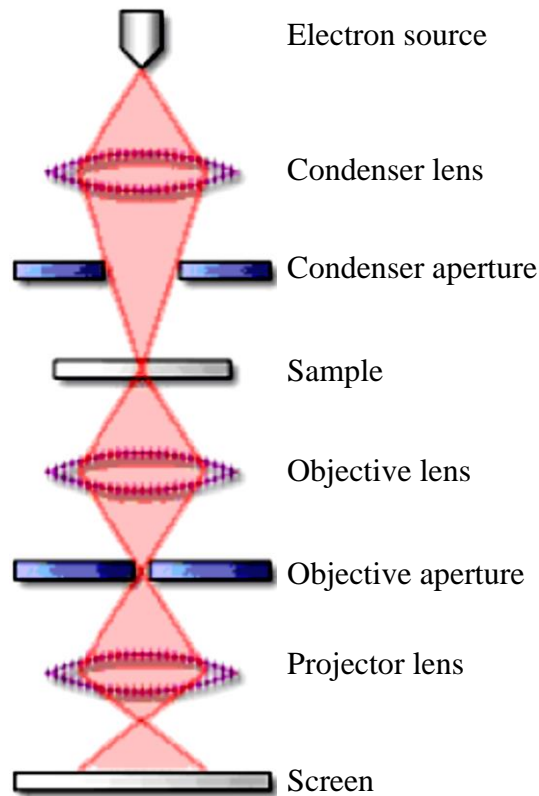


Figure 3-14: Schematic diagram illustrating the TEM optical system (Voutou & Stefanaki, 2008).

### 3.9 Material Flow during RFSSW

#### 3.9.1 Sample Preparation for Dissimilar Aluminium Alloy Flow Experiments

To monitor the material flow in the stir zone during the RFSSW process, some welds were made using two aluminium alloys, AA6111 and AA6082 (of the same thickness). The AA6082 aluminium alloy was used as a marker material because it has a similar response to deformation but with a lower copper content than AA6111, leading to different etching characteristics compared to AA6111.

Before welding, the AA6082-T6 alloy was heat-treated, following the procedure explained in section 3.4. Heat treatment was used to balance its hardness with the hardness of the AA6111-T4 alloy, so that the two alloys would have as similar flow properties as possible.

Several welds were produced with lapped and butted dissimilar alloy sheets, where both of the upper and lower sheets of the sample were changed using two pieces of the different alloy, as shown schematically in Figure 3-15. The sheet alignment was carried

out carefully to ensure that the boundary between the two alloys passed through the centre of the weld.

To visualise the material flow during the early stages of welding, the process was interrupted when the sleeve reached a certain plunge depth (0.2, 0.6 and 1.0 mm).

After welding, the samples were then sectioned through the welded joint centre in a line perpendicular to the original border between the two alloys, and characterised using optical microscopy.

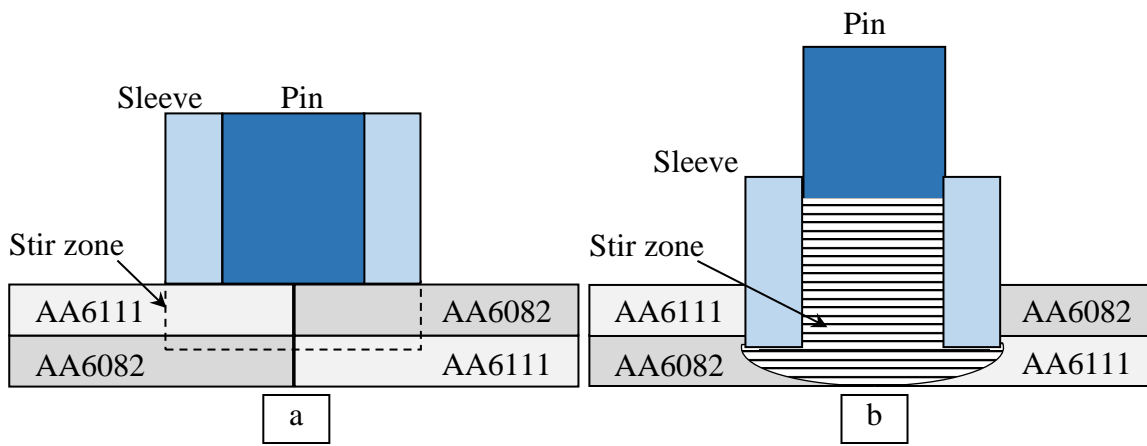


Figure 3-15: Schematic illustration of one of the material flow sample alignments (a) before welding and (b) after interruption of the process.

### 3.9.2 Sample Preparation for X-Ray Tomography

To monitor the weld interface and the location of the weld defects during the welding process, several welds with different plunge depths (0.2 to 1.2 mm) were performed using two AA6111 aluminium alloy sheets sputter-coated with a thin gold layer (measuring approximately about 100 nm). The two coated sheets were placed so that the two layers of gold formed a single layer at the interface between the sheets, as seen in Figure 3-16a. Process interruption was also used on these samples with a range of plunge depths (0.2 to 1.0 mm) to visualise the interface during the early stages of the welding process and to understand how some weld defects were generated.



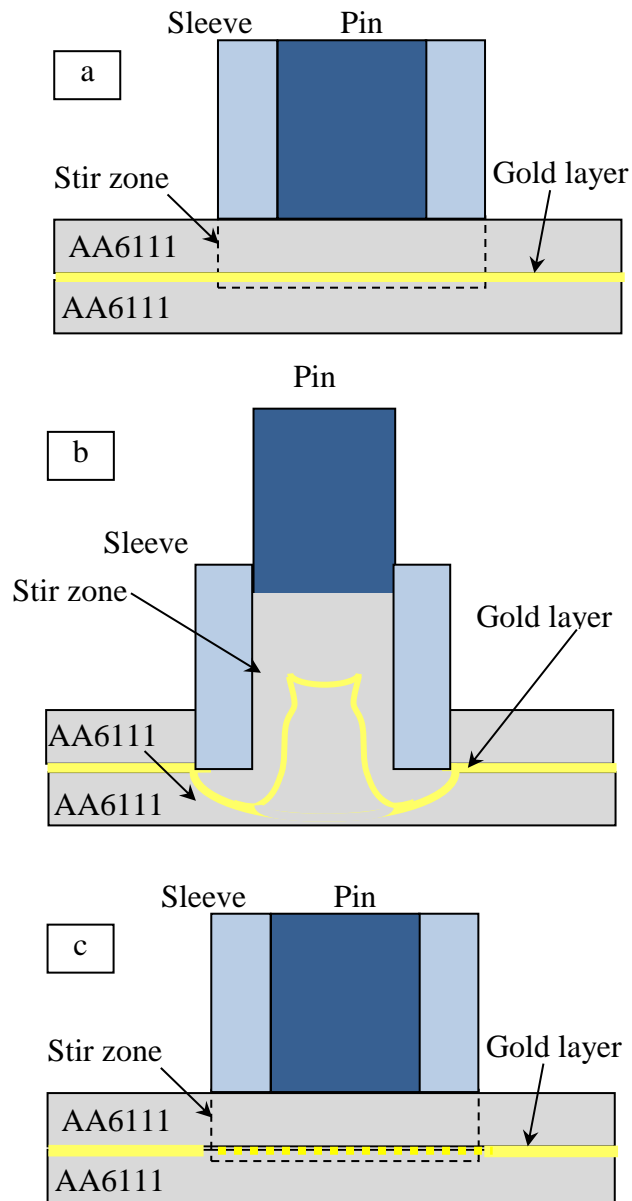


Figure 3-16: Schematic illustration of the alignment for the X-ray Tomography sample; (a) before welding and (b) after interruption of the process (c) for the completed process.

### 3.9.3 Description of the X-Ray Computational Tomography Technique (XCT)

X-ray computational tomography (XCT) is a non-destructive method that can be used to obtain three-dimensional (3D) images of the internal parts of a material. It can show all microstructural features, such as different phases, inclusions, cracks, and pores, which lead to attenuation or modifying the optical phase along the path of the X-ray beam (Maire, et al., 2001). The tomography technique was developed to overcome the drawback in radiography where a high amount of information is projected on a single plane, resulting in an image that can be difficult to interpret if the complexity of the microstructural features along the sample thickness is important. In tomography, the

information of a series of many radiographs is combined, taken with each sample orientation in front of the detector (Maire, et al., 2001).

Different set-ups can be used to perform a tomographic scan, but in general three elements must be present to complete the process: an X-ray source, a rotation stage on which the sample is fixed and an X-ray detector, as shown in Figure 3-17a (Maire, et al., 2001; Babout, 2006). Two different types of X-ray sources are commonly used as shown in Figure 3-17b: a cone source (laboratory tomography) where the beam of the X-ray is divergent, and a polychromatic parallel source (synchrotron tomography), where the X-ray beam is polychromatic or monochromatic (Babout, 2006; Salvo, et al., 2010).

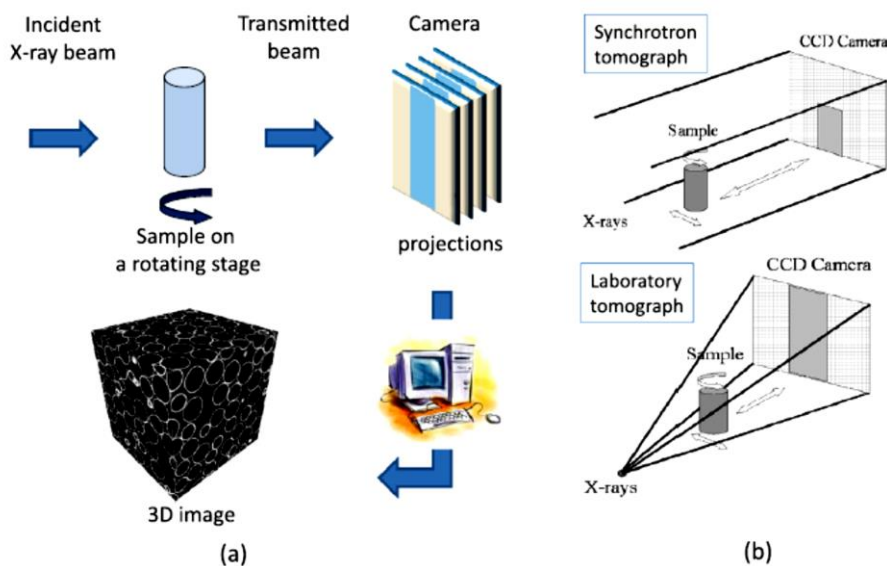


Figure 3-17: (a) Principle of X-ray tomography; (b) synchrotron and laboratory tomography (Salvo, et al., 2010).

The specimen to be imaged is placed on a rotating stage in the path of an X-ray beam. Part of the X-ray is absorbed by the sample material whereas the other part is transmitted. In order to obtain high-quality 3D images, it is necessary for the transmission ratio (the ratio of the transmitted intensity to the initial intensity) to be large enough (above 20%). This ratio is generally related to the X-ray's energy, nature of the material and the sample thickness (Salvo, et al., 2010). The transmitted X-ray's are converted into visible light using a fluorescent screen. This light then passes through the appropriate optic lenses and is recorded by a CCD, or CMOS, camera. The result is an image that corresponds to a projection of the sample (Maire, et al., 2001; Salvo, et al., 2010). The sample is then rotated over 180° or 360° and an appropriate

number of projections are recorded during this rotation, usually several hundreds. This set of projections is then used to reconstruct a 3D image of the sample (Salvo, et al., 2010). To reconstruct 3D images from 2D projections, special imaging software packages have been developed, like Avizo, VGStudiomax, and ImageJ. The image-processing toolbox in Matlab also offers some 3D image-processing possibilities (Babout, 2006).

The results presented in this study have been obtained on a laboratory XCT system in the Manchester X-ray-Imaging Facility. The tomography device used was a Nikon Metrology 225/320 kV Custom Bay, which uses an X-ray beam with a maximum energy of 225 kV (multi-metal) or 320 kV (tungsten), with a linear resolution range (voxel size) of 3  $\mu\text{m}$  – 160  $\mu\text{m}$ . This machine is usually operated with a 225 kV source and a choice of tungsten, copper, molybdenum, and silver targets. The voltage used in this study was 95 kV, with a current of 105  $\mu\text{A}$ . In spite of the limited resolution (20  $\mu\text{m}$ ), this device was still able to identify the position of the thin gold marker used in the experiments due to its high absorption (as gold has a higher density than aluminium) and was able to scan the whole weld area in one data set. After finishing the 360° scan for each sample, the 5000 recorded frames were processed and the 3D images were reconstructed using Avizo 3D software, which was developed by the FEI Visualization Sciences Group.

### **3.10 FE Modelling of the Lap Tensile-Shear Test of RFSSW Joints**

In order to simulate the mechanical behaviour of the RFSSW joint, an FE model of the specimen of the lap-shear test was developed using Abaqus-CAE software. The modelled sample of similar Al-Al joint consisted of an upper sheet, lower sheet, upper HAZ, lower HAZ, and SZ, depending on the variation of the local mechanical properties in these regions. On the other hand, for the dissimilar joints of Mg to Al the magnesium side (upper sheet) was assumed to have only two regions the upper sheet and SZ because the AZ31 magnesium alloy is a non-heat-treatable.

To simulate the gripping in the lap tensile-shear test, one of the ends of the modelled sample was assumed to be fixed and the other pulled by an applied force. Only one-half of the actual sample was modelled, so as to reduce the computing time and a third

boundary condition was assumed on the plane of symmetry to restrict the movement perpendicular to this plane and simulate the presence of the other half of the sample.

Due to the difficulty of evaluation of the material strength of each region in the sample, the microhardness level was taken as an initial reference for the local mechanical properties. Several heat treatments were applied to standard tensile test samples to simulate the hardness levels of the regions of the welded joint in the as-welded and artificially aged conditions (as discussed in section 3.4). The stress-strain curves obtained from the tensile test for these samples were then transformed into the true stress-strain plastic response curves that were required for the model.

A tetrahedral structured mesh with ten-node C3D10M elements was used in all regions of the welded joint with greater mesh density SZ and HAZ due to the highest stresses are developed in these regions.

The procedures used in the model simulations are discussed further in chapter 6.

## **Chapter 4: Refill Friction Stir Welding of Al-Al Similar Welding (Results and Discussion)**

---

### **4.1 Introduction**

This chapter presents the results of the investigation and optimisation of similar aluminium joints produced with short weld times using the refill friction stir spot welding (RFSSW) process. The study aimed to assess the effect of a range of welding parameters and material conditions on the mechanical properties of the joints. These included the three main welding parameters: sleeve plunge depth, tool rotation rate, and welding time (the ranges of these welding parameters are summarised in Table 3-2). The main focus of the research was on developing the understanding required to optimise the process for rapid welding with a weld cycle of less than 1.0 second. In terms of the materials used, in this part of the study, an AA6111-T4 aluminium alloy was used in addition to the AA6082-T6 alloy as a marker material in the investigation of the material flow (more details are described in Chapter 3).

To increase understanding of the performance of the welded joints and the possible reasons for their behaviour, several experiments were conducted, including: investigating the effect of the welding parameters on the material flow and material intermixing in the stir zone, as well as analysing the thermal profile and thermal history. In addition, the consequential influence of the thermal profile and thermal history on the microstructure and the hardness profiles of weld cross-sections was investigated and, in turn, their effect on the weld strength and fracture mode. The chapter also shows the effect of the process parameters on defects in the welded joints and the influence of the natural and artificial ageing heat treatments on joint performance.

### **4.2 Welding Optimisation**

To optimise the welding parameters and reduce the welding time as much as possible, an initial matrix of welds with different welding parameters were produced. At the beginning of the tests, the tool rotation rate and plunge depth were maintained at the level of 2000 rpm and 1.0 mm respectively. The welding time (which consists of three

parts: plunge time, dwell time and retraction time) was varied in numerous ways. The first approach involved reducing the plunge time from 0.7 s down to 0.242 s, which represents the shortest possible plunge time and corresponds to the highest plunge rate of the machine (4.1 mm/s); the dwell time was also lowered from 1.5 s to 0.05 s. However, the plunge time and retraction time for a 1.0 mm plunge depth used later in this study were both fixed at 0.25 s to prevent damage to the tool and the machine. The second step involved changing the rotation rate to 2500, 1500 and 1000 rpm by repeating the same procedure of changing the plunge rate and dwell time as used with the 2000 rpm welds. The final step was to reduce the sleeve plunge depth from 1.0 mm to 0.8, 0.5 and 0.2 mm. This reduction in plunge depth allowed for a reduction in plunge time and, in turn, the total welding time to 0.125 and 0.3 s, respectively, when using a plunge depth of 0.2 mm.

The results of the experiments using the matrix of variables detailed above are summarised in Figure 4.1, following completion of the welded joints. The quality of the welds was first assessed depending on the appearance of the weld surface and the completeness of the refilling process. It can be noted that the weld surface appeared flat and the refilling process was completed successfully in welds which were performed using rotational rates of 1500 and above, as shown in Figure 4.1. These results provided evidence of the success of the welding process and refilling the keyhole left by the tool plunge. Using a tool rotation rate of 1000 rpm or less led to welds with rough surfaces being obtained, even when increasing the plunging time, or the total welding time, as shown in Figure 4.1, in some cases, refilling in the final step was found to be incomplete. The increase in tool rotation rate increased the heat generated which affected the flow of plasticised metal, leading to an improvement in the refilling step, in addition to improving the appearance of the weld surface.

In contrast, a satisfactory weld appearance was obtained irrespective of the weld duration for all rotation rates of 1500 rpm and above.

Based on the above results, a range of welding variables suitable for producing similar AA6111 aluminium alloy joints with a good appearance and complete refilling of the hole were selected for the purpose of conducting the following tests and evaluating the performance of the welding process. These welding parameters are surmised in Table 4.1.

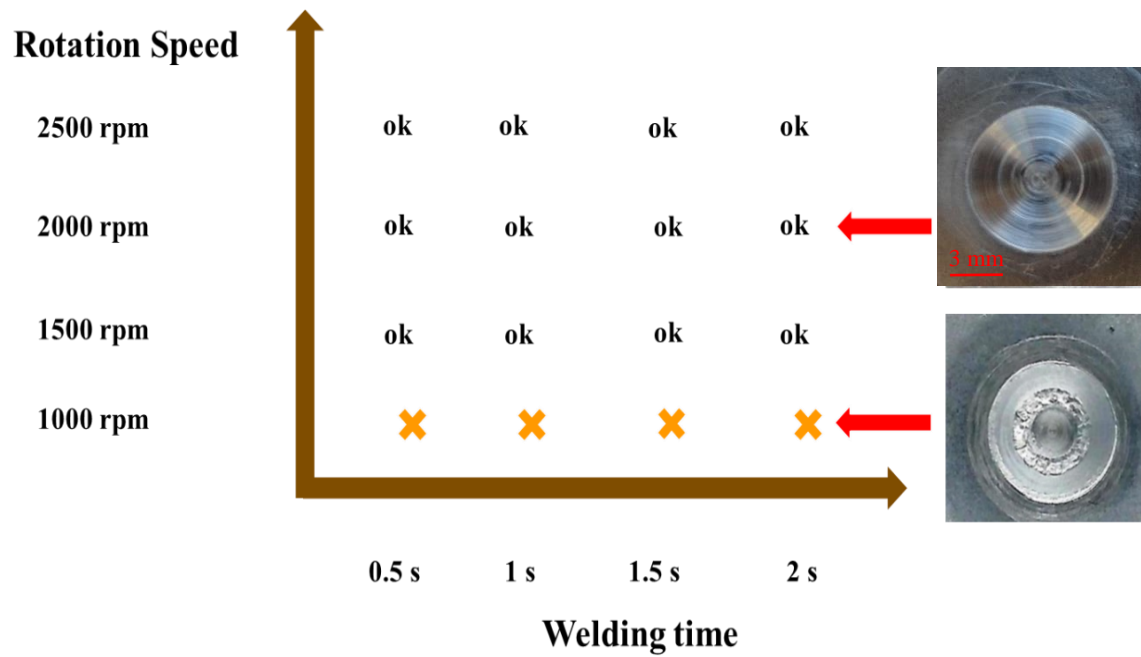


Figure 4-1: The effect of plunge time and tool rotation rate on the weld surface appearance and the completeness of the refilling process.

Table 4-1: The range of welding parameters used in RFSSW of AA6111 similar joints.

Welding Parameters					
Tool rotation rate (rpm)	Sleeve plunge depth (mm)	Welding Time (s)			
		Plunge	Dwell	Retraction	Total
1500,2000, 2500	0.2, 0.5, 0.8, 1.0	0.125-0.25	0.05-1.75	0.125-0.25	0.3- 2.0

### 4.3 Effect of the Process Parameters on Material Flow in Refill Friction Stir Spot Welding and Weld Defects

Material flow was studied for welds produced using a range of process parameters. In addition, incomplete welds were produced by implementing a process of interruption during the dwell stage. The main aim of this study was to understand how the material flow influenced the mechanism of joint formation and its quality. Two techniques were used to reveal the metal flow in the stir zone. The first was the contrast technique, where strips of two aluminium alloys, AA6111 and AA6082, were used with different configurations (either replacing the lower sheet with AA6082, or by using a butt configuration and replacing the upper, or lower, sheet or both with the two Al alloys)

(see section 3.9.1). This method has been found to be helpful in order to understand the level of coupling with the tool and the development of the deformation zone in friction spot welding (Bakavos, et al., 2011). According to the experimental results provided in this work based on contrast technique, Reilly et al. (2015) have developed a kinematic model to understand the material flow and the formation of layering in the stir zone for pinless FSSW. One of the model assumptions needed to replicate the actual weld behaviour is that the upper and lower surfaces are stuck to the tool and backing plate respectively. According to this assumption, the top of the stir zone rotates with the tool relative to the stationary lower surface. Figure 4-2 shows the output of the model in a series of three-dimensional views for the butted interface. These results show that the continuous twisting of the top surface as a result of the tool rotation converts the interface between the dissimilar alloys, which was originally a vertical plane, into a spiral ‘corkscrew’. In order to make the model consistent with the experimental results of material flow, the researchers found that the material in the welding area under the tool is separated into two regions: the first is a central region in which the material sticks to the tool and the second is an annular slip region that provides a transition from the sticking velocity at the central region to the stationary surrounding material (Reilly, et al., 2015).

The AA6082 alloy was selected for the purposes of this study because it has a similar response to deformation but with a lower copper content than AA6111. This difference in copper contents provides different etching responses, which results in a contrast in optical microscopy. To balance the mechanical properties of the two alloys, the AA6082 was first heat-treated (solution heat-treated and naturally aged) before welding, using the procedure outlined in section 3.4.

The second technique used was 3D imaging by X-ray tomography. Special samples were prepared to use with this technique: AA6111 sheets were first sputter-coated with a thin layer of gold. Two of the coated sheets were then placed so that the gold formed a single layer at the interface between the two sheets, as seen in section 3.9.2. This method was found to be suitable for detecting the location of the original interface after pinless FSSW had been performed (Bakavos, et al., 2011). Monitoring of the gold layer revealed the location of the joint interface during and after the completion of the RFSSW process.



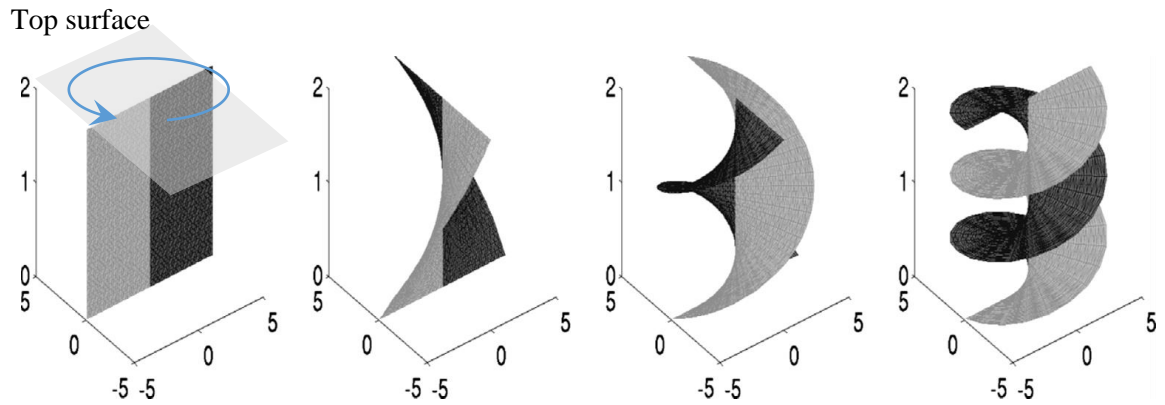


Figure 4-2: The output of the kinematic model, showing the surface velocity profile by assuming complete sticking for 0, 1/4, 3/4 and 1.5 revolutions. All dimensions are in mm (for clarity, the vertical scale has been stretched) (Reilly, et al., 2015).

Figure 4-3 shows examples of the information that can be obtained from this contrast method. The two alloys AA6111 and AA6082 were arranged in the double-butt configuration shown in Figure 3-15 to produce the welds. The welding process was interrupted when the sleeve reached plunge depths of 0.2, 0.6, and 1.0 mm to visualise the material flow during the plunging stage of the process. Figure 4-3a shows that when using a 0.2 mm plunge depth a weld has been partially formed, and there is little deformation of the lower sheet surface, where one layer can be seen at this early stage. The stir zone (SZ) has an onion-like structure composed of multiple-layers of the two alloys. The formation of these layers in RFSSW follows the same procedure suggested by Reilly et al. (Reilly, et al., 2015) for layer formation in conventional pinless FSSW.

The situation is somewhat different when the sleeve plunge occurs. In the centre of the weld, the addition of more layers to the upper part of the SZ stops when this material enters the sleeve cavity (Figure 4-3b and c) because it will stick to the pin and inner surface of the sleeve and rotate with them. However, numerous very thin layers can be seen to continue to be created in the region of the higher strain near the tip of the sleeve, which is the area of transition between material that is coupled with the rotating tool and the stationary material under the clamp. The layer formation is directly connected to the circumferential flow and the horizontal layers are associated with the material sticking to the tool. Conversely, the layers in the transition region, especially near the edge of the weld zone, show an upward bend, satisfying the transition condition from the tool rotation rate of the material stuck to the tool, to zero speed in the surrounding material (Reilly, et al., 2015). The slight effect of the stirring on the lower sheets when using a 0.2 mm plunge depth can also be seen and this results in a small metallurgically bonded

area 6.4 mm in diameter. This compares to a tool diameter of 9 mm, which gives a metallurgically bonded area of about 51 % of the tool area.

By increasing the plunge depth to 0.6 mm (Figure 4-3b), the SZ clearly penetrates into the lower sheet and reaches the lower surface. As a result, the metallurgically bonded area becomes larger with approximately an 8.4 mm diameter, or about 87 % of the tool area. From comparison of Figure 4-3a and Figure 4-3b it can be noted that although there is a large difference in the metallurgically bonded area, in general there are similarities between the two cases, in that the layers near the tip of the sleeve are much thinner than the layers in other areas and, when moving away from the sleeve surface location, upwards or downwards, the layers become thicker. It also can be seen that the centre of the weld contains a “dead zone”, where lower material flow from the shear occurs due to the rotating tool.

A highly deformed area can also be seen near the internal edge of the sleeve in Figures 4-3b and d. This high strain results from material flow from three different directions: the up-down movement of the material flowing into the inner surface of the sleeve, the horizontal movement of the material under the sleeve from the outer edge to the sleeve cavity, and the down-up movement from the lower sheet. The material flow in this region is fully compliant with the findings of the strain distribution model suggested in Figure 2-21 by Zhao et al. (Zhao, et al., 2016).

With a further increase in the plunge depth to 1.0 mm (Figure 4-3c), intercalation of the layers near the tip of the sleeve has become so fine that the layers themselves become indistinguishable. The resultant metallurgically bonded area from this plunge depth is even larger than the tool area, at approximately 9.4 mm in diameter or about 109 % of the tool area. Although the layering in this sample cannot be counted except at the top of the weld (inside the sleeve cavity), it can be noted that the deformation is concentrated near the internal edge of the sleeve.

Characteristic weld defects can also be observed at the interfaces that are affected by the material flow. An example of such a defect includes the hook feature that starts to develop strongly with plunge depths of 0.6 mm or above, which can be clearly seen when using a plunge depth of 1.0 mm, as shown in Figures 4-3c and 4-3e.

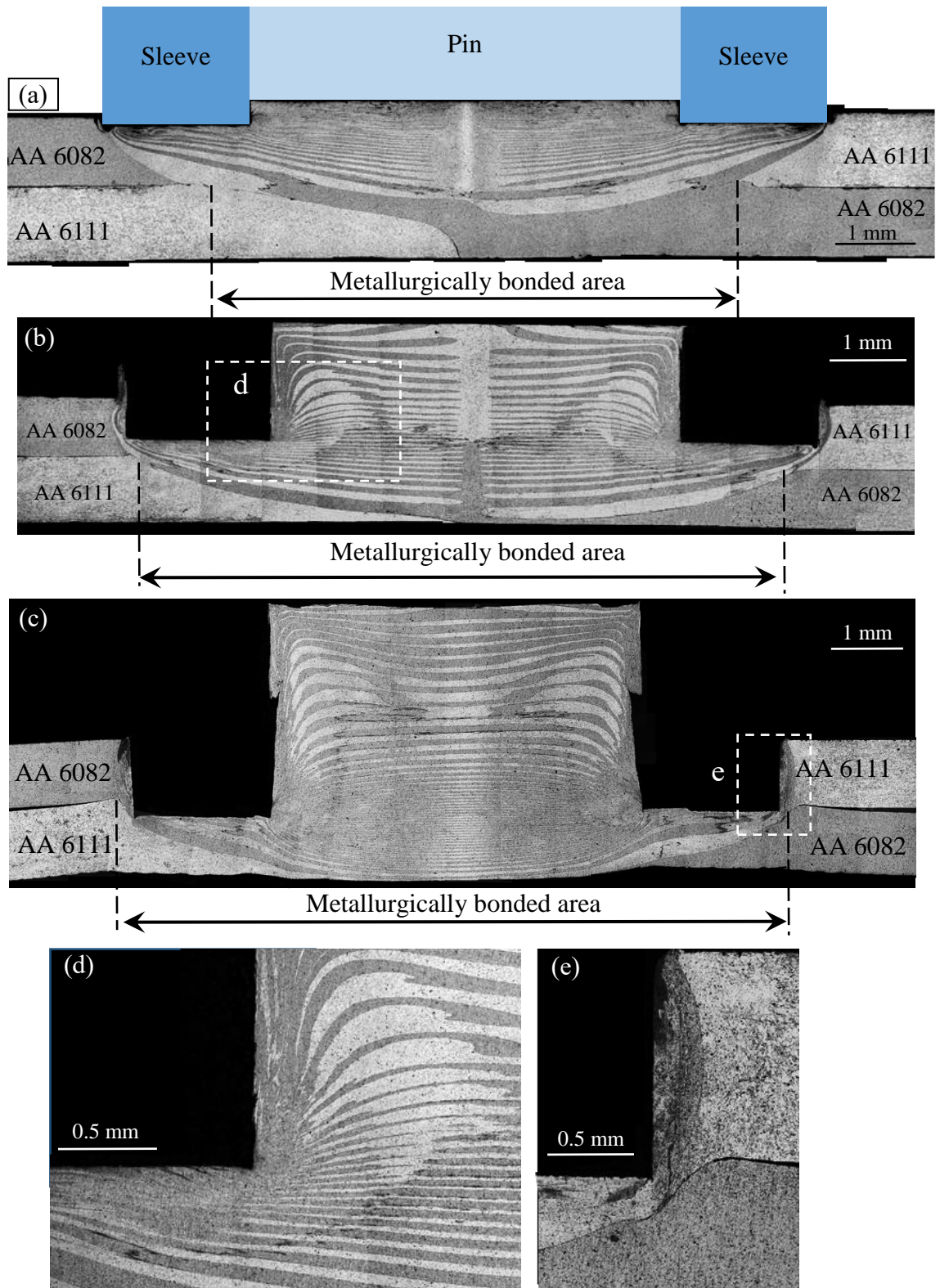


Figure 4-3: Effect of weld plunge depth and process interruption on the material flow for a tool rotation rate of 2500 rpm and plunge rate of 2.0 mm/s: (a) 0.2 mm plunge depth, 1.1 s total weld time; (b) 0.6 mm plunge depth, 0.9 s total weld time; (c) 1.0 mm, 1.35 s total weld time; (d) a higher mag. view of the region near the internal edge of the sleeve as marked in (b) ; and (e) a higher mag. view of the hooking and the region near the external edge of the sleeve as marked in (c).

To clarify the effect of plunge depth on intermixing of the lower sheet during the plunging stage, some interrupted welds were also produced using a split lower sheet with the AA6111 and AA6082 alloys in a butt configuration. As can be seen from Figure 4-4, the lower sheet and the interface between the two sheets are highly affected when the sleeve penetrates the upper sheet. The phenomena occurring here can be separated into two effects. The first is layering of the lower sheet as a result of the stirring which was discussed in the previous section. On the other hand, a second effect can be seen at the edges of the stir zone where the joint line is pushed down into the lower sheet. This process displaces material from the lower sheet to the centre of the weld and upwards forming a nearly conical shape in the layers (as shown in Figure 4-4 a). A further increase in plunge depth to 0.8 or 1.0 mm increases the downward thrust on the weld interface, leading to displacement of more material from the lower sheet upwards into the sleeve cavity. The shape of this displaced material was found to become almost cylindrical with thinner layers (Figure 4-4b and c).

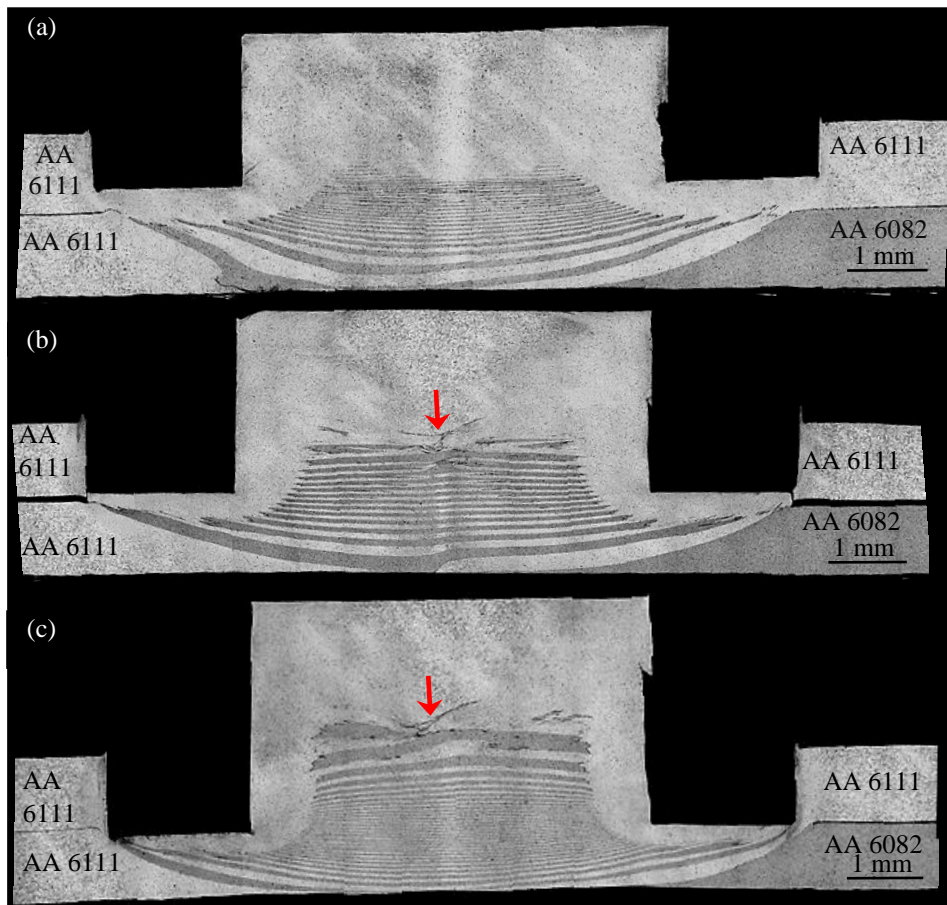


Figure 4-4: Effect of sleeve plunge depth and process interruption on material flow in the lower sheet for a tool rotation rate of 2000 rpm: (a) 0.6 mm plunge depth, 0.24 s plunge time, 1.25 s total time; (b) 0.8 mm plunge depth, 0.237 s plunge time, 0.75 s total time; and (c) 1.0 mm plunge depth, 0.25 s plunge time, 1.2 s total time. A weld defect in the centre, consisting of an unbonded interface region, is indicated with an arrow.



A few weld defects could be observed at the interface that can be related to the material flow, such as the non-bonded area in a “dead zone”, which can be seen in the centre of the welded joint (Figures 4-4b and 4-4c).

To determine the position of the interface between the upper and lower sheets in the joint centre, which represents the future join line, an interrupted weld was produced using similar sheets of an AA6111 alloy. As can be seen from Figure 4-5, the central part of the upper sheet and the interface between the sheets were only slightly deformed when the sleeve penetrated the upper sheet, while the material in the upper sheet was pushed down from the edges by the sleeve and towards the centre of the weld (marked by a red arrow in Figure 4-5b) resulting in a distinctive almost circular shape in the cross-section shown in the same figure.

Figure 4-5 also shows the development of the hook feature, which is seen clearly in Figure 4-5c; this image gives evidence that this type of weld defect is formed during the plunging stage of the welding process.

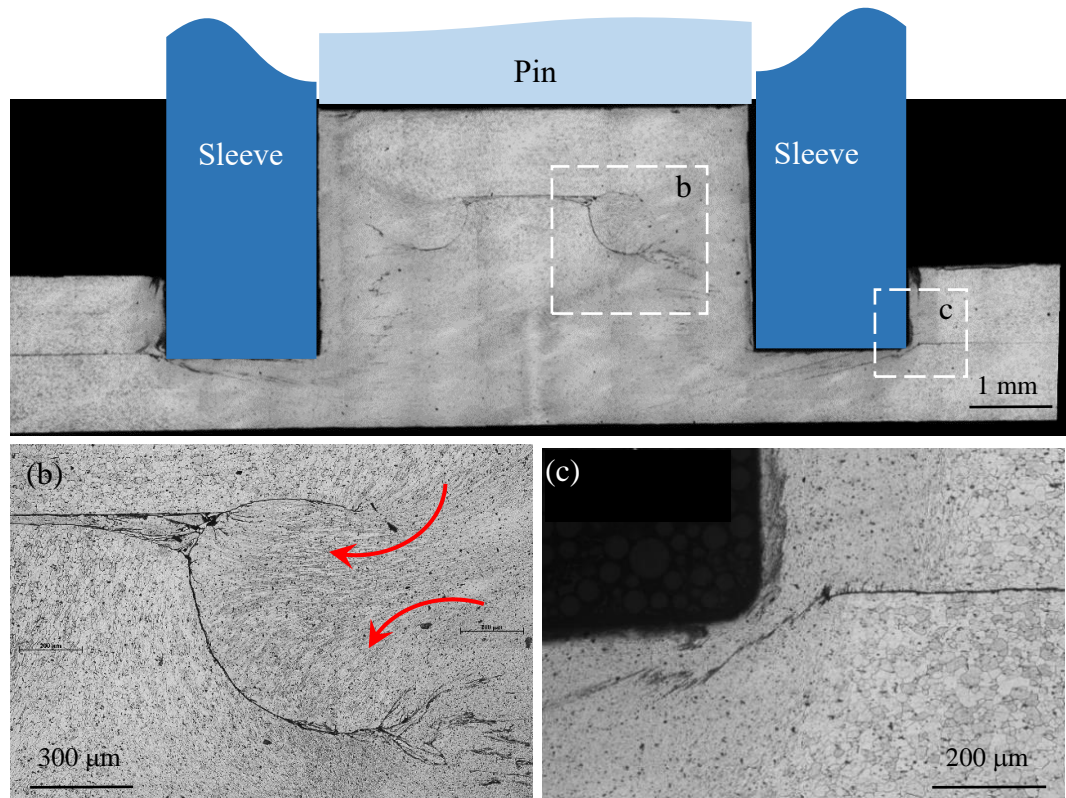


Figure 4-5: Cross-section of an AA6111 similar interrupted RFSSW, showing the joint interface flow in the upper sheet, 2000 rpm tool rotation rate, 1.0 mm plunge depth and 0.25 s plunge time, (a) full cross section showing the location of the sleeve and pin ; (b) a higher mag. view of half of the central region as marked in (a); and (c) a higher mag. view of the hooking and the region near the external edge of the sleeve as marked in (a).

Figure 4-5 does not show the interface between the upper and lower sheet in the area under the sleeve and near the bottom of the sleeve cavity sufficiently clearly. Therefore, some interrupted welds were produced using a gold interfacial layer as a marker material and computed X-ray tomography was employed as a 3D monitoring technique. Figure 4-6 shows the gold interfacial layer after the sleeve plunging step with 0.8 mm plunge depth (Figures 4-6 a and c) and 1.0 mm plunge depth (Figures 4-6 b, d and e). Although this Figure shows the morphology and location of the interface, it also gives an evidence of what happens to the metal above and below the interface. The interface in both plunge depths can be divided into three distinct areas. The first region is located under the sleeve, which has a vortex shape where the material is flowing from the outer edge of the weld zone towards the centre in a helical motion. This phenomenon is due to the combined effect of the vertical movement of the sleeve, which drives material towards the sleeve cavity, and the rotational motion, which is trying to shear material in the direction of rotation. In the second region, located near the internal edge of the sleeve and at the bottom of the sleeve cavity, most of the gold layer has disappeared from this area. This gives an indication of the high amount of plastic deformation that occurs at this location. This region also clearly shows very fine layers can be seen when using the contrast technique (Figures 4-3c and d). The third region is located in the centre of the weld inside the sleeve cavity. This area is more affected by the vertical movement than the rotational movement, where it can be noted that most of the gold layer is retained, but with a change in the shape of the interface due to the vertical movement of the material from the bottom to the top in the centre and from the top downwards at the edges of the region.

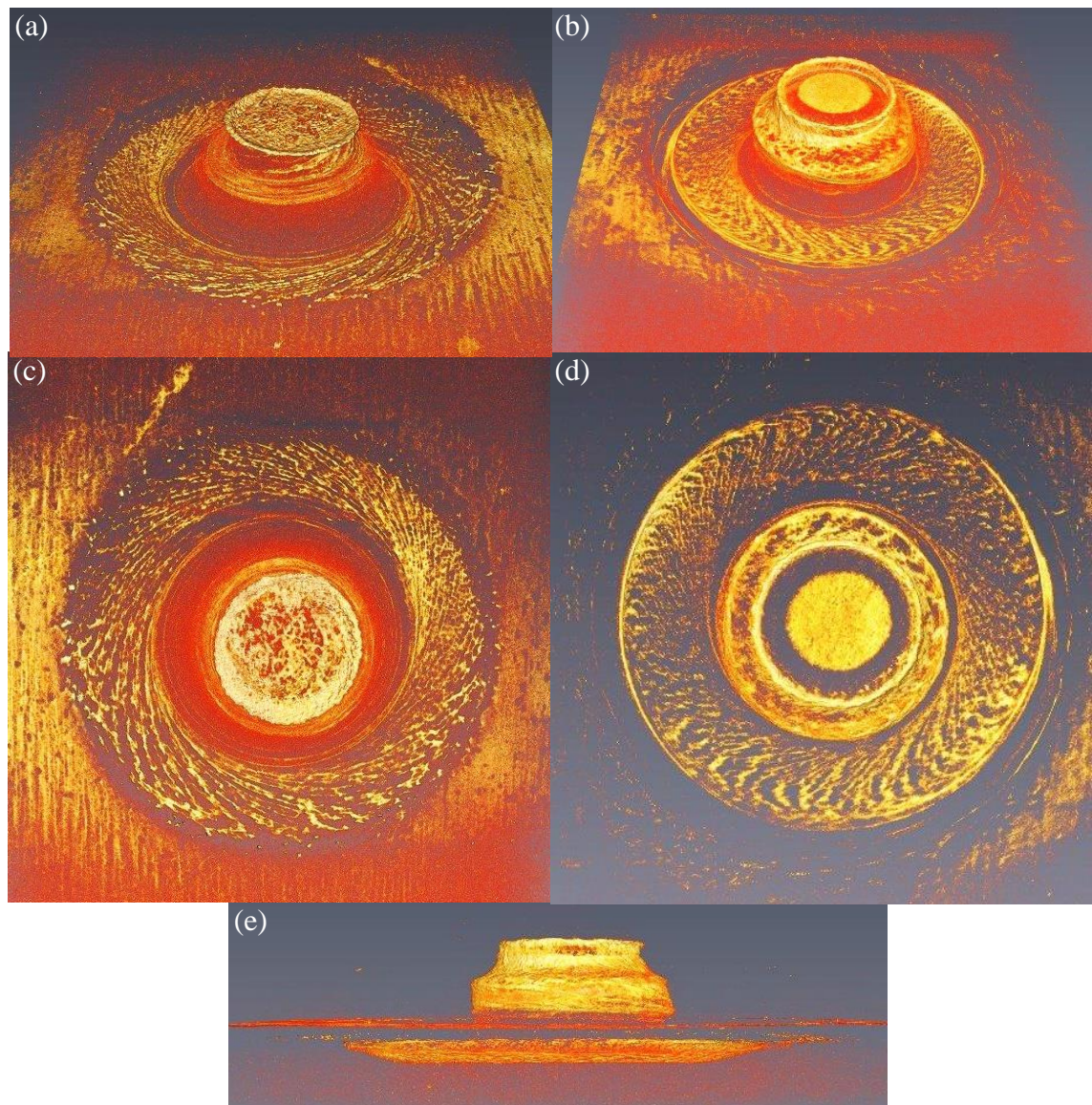


Figure 4-6: The results of X-ray tomography showing the distribution of gold at the weld interface, for interrupted welds produced with 2000 rpm tool rotation rate; (a) and (c) a plunge depth of 0.8 mm; (b) (d) and (e) a plunge depth of 1.0 mm.

The material flow during the plunge and dwell stages can be described by the proposed material flow model shown in Figure 4-7. To clarify, this material flow model is divided into five regions. The first region is located in contact with the periphery of the rotating sleeve and is mainly in the upper sheet. The material in this region is moved downwards in a helical vertical rotational flow due to the combined vertical and rotational shear movement resulting from the penetration of the rotated sleeve into the upper sheet. When this material reaches the bottom of the sleeve, the resistance of the surrounding material forces it to move outwards and upwards with a helical vertical rotational flow



back towards the outer surface of the sleeve. This process occurs because of the resistance of the material near the top surface of the upper sheet, which is constrained by the clamping ring and the surrounding sheet. This motion results in the characteristic semi-elliptical shape of the cross-section of the stir zone and it seems to be the main reason behind the hook formation (see Figures 4-3 b, c, and e). The material in this region continues to move during the plunge and dwell stages, resulting in a region composed of lamellae of AA6111 and AA6082 if they are used in a butt configuration to replace the upper sheet.

The second region is located under the sleeve (see Figures 4-3 b and c, and Figure 4-7 a). The material in both the upper and lower sheets in this region is subjected to vertical and horizontal rotational movement. In this region, the material is pushed down by the sleeve, but it is constrained by the backing plate and clamping ring so that it is displaced to enter the cavity produced when the pin is retracted. The horizontal rotational movement seems to be the dominant factor affecting the material flow in this region; as a result, the material takes the shape of a vortex.

The third region represents the part of the lower sheet located in the centre of the weld. The material in this region is pushed by the material from the second region and forced to enter the cavity produced by retracting the pin in a vertical and rotational movement. This material faces resistance from the upper sheet material, especially where it sticks to the tool near the internal surface of the sleeve, which results in the characteristic shape of the interface marked by the dashed gold line in Figure 4-7 that can be seen in Figure 4-6e.



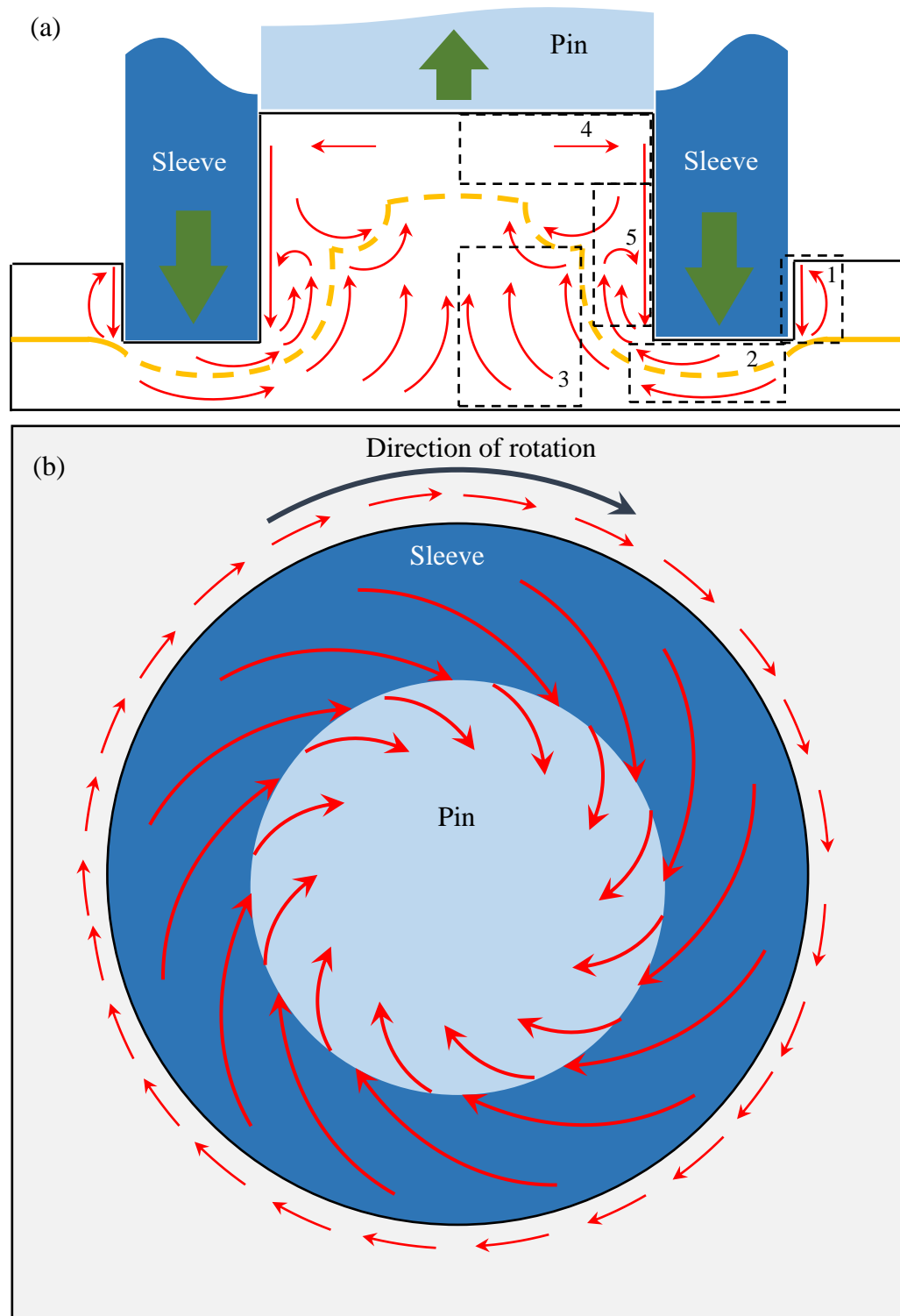


Figure 4-7: A schematic diagram indicating the material flow during the plunging stage: (a) cross-sectional view and (b) top view.

The fourth region is located inside the sleeve cavity and represents the material that came from the upper sheet and was in contact with the pin. This material is mostly stuck to the pin during the early stages of welding; consequently, it is subjected to a circumferential flow leading to the formation of horizontal layers of the marker materials seen in the cross-section view in Figures 4-3 b and c (Reilly, et al., 2015). The

fifth region is located in contact with the inner surface of the sleeve. Material flow in this region is more complicated than in other regions. The material adjacent to the sleeve is moved vertically downwards when the sleeve plunges through the upper sheet. This material is then divided into two parts. The first part moves towards the centre to meet the material that comes from the lower sheet and is then directed upwards, leading to the formation of the circular shape shown in Figure 4-5b. The second region of material continues moving in the same direction until it meets the material from the upper sheet that has been pushed by the sleeve. This conversion of material from different directions results in the material revolving in a loop near the internal edge of the sleeve.

Figure 4-8 shows a series of micrographs from cross-sections through completed RFSSWs with a lower sheet of AA6111 and an upper sheet replaced by AA6111-AA6082 in a butt configuration. The welds were produced using a plunge depth of 1.0 mm and a range of tool rotation rates and welding times. It can be observed that the stir zone is composed of distinct inter-layering of the two alloys, and the number and thickness of the layers depend on the welding parameters (i.e. tool rotation rate and welding time). By comparing the thickness of the layers for each tool rotation rate with different welding times for example, Figure 4-8 a with Figure 4-8 b (welding times were 0.55 and 2.0 s with a constant plunge and retraction times of 0.25 s) it is clear that the number and thickness of the layers in the upper part of the stir zone are comparable, which means that the difference in dwell time between the two welds (0.05 and 1.5 s respectively) did not affect the layering of the upper part of the stir zone, or in other words, the layers in this region mostly formed during the initial plunge stage. In contrast, additional finely spaced layers are formed near the bottom of the cavity produced by retracting the pin during the dwell time as explained previously when discussing the material flow for interrupted welds (see Figure 4-3). Comparison of the number and thickness of the layers in welds produced using different tool rotation rates for instance, in Figure 4-8d with Figure 4-8f reveals that the layers become thinner. Meanwhile, the number of layers increases with increasing tool rotation rate from 2000 to 2500 rpm, due to the increase in number of revolutions during the plunge stage from about 8.3 to 10.4.

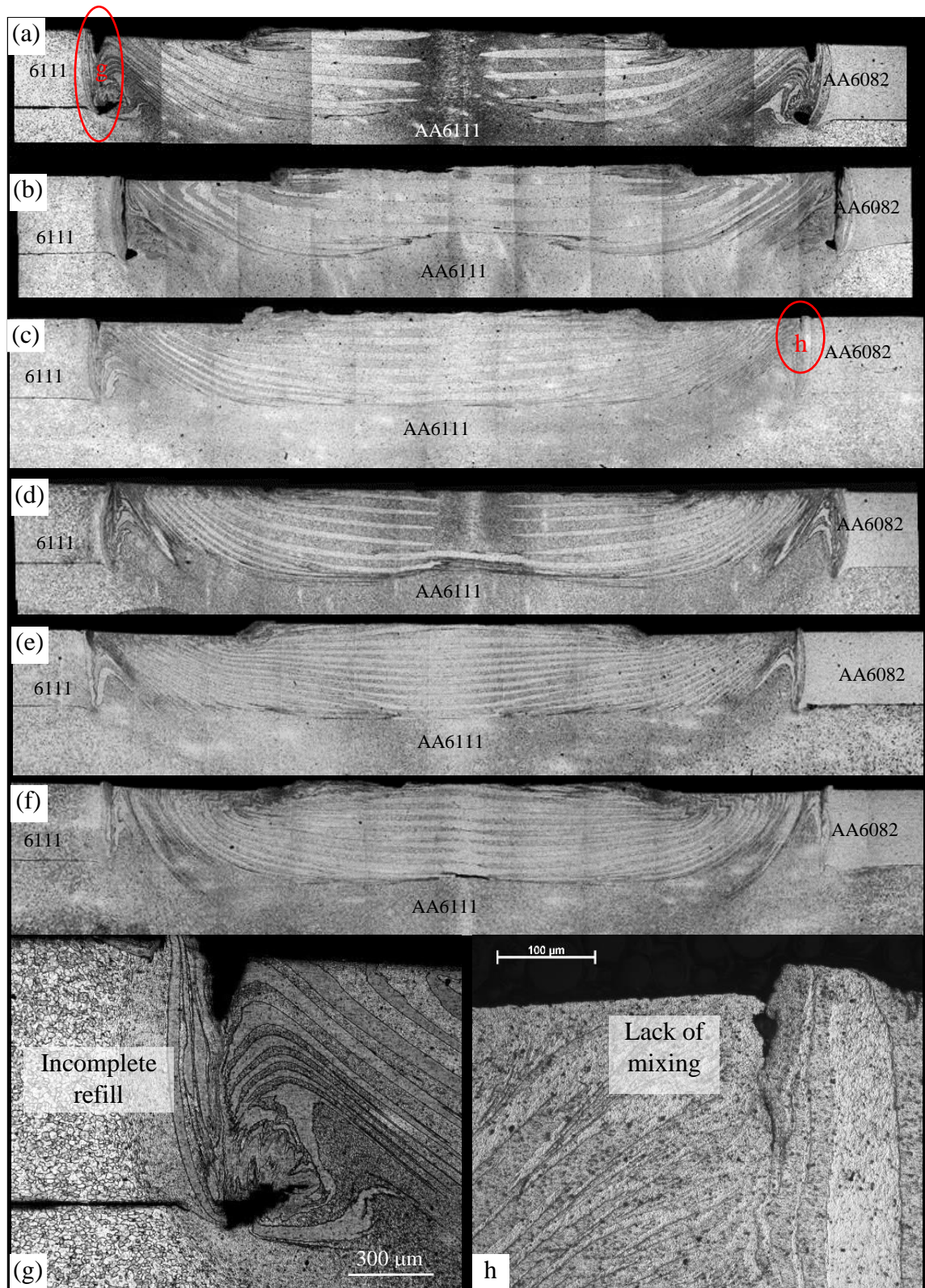


Figure 4-8: Effect of welding parameters on the material flow: welding condition (a) 0.55 s, 1500 rpm; (b) 2.0 s, 1500 rpm; (c) 0.55 s, 2000 rpm; (d) 2.0 s, 2000 rpm; (e) 0.55 s, 2500 rpm; (f) 2.0 s, 2500 rpm. The figure also shows some weld defects in (g) and (h).

The edges of the stir zone have a characteristic shape for all welding parameters. This shape results from the material flow during the retraction of the sleeve and simultaneous downward motion of the pin, where the material from the lower sheet is pushed up by the refilling process to fill the annular cavity from the sleeve plunge. At the same time, material from the inside of the sleeve cavity also flows to fill the sleeve cavity. The material flow in this region is important because it is the main factor affecting the formation of weld defects, such as incomplete refill and a lack of mixing (Rosendo, et al., 2011; Rosendo, et al., 2015) (see Figures 4-8g and h). The most likely reason for the formation of these two types of weld defects is insufficient plasticity of the material that came from the upper region of the sleeve cavity, which is used to refill the annular cavity created when the sleeve retracts. The lack of plasticity of this material results from the lower temperature and lower heat generation in this region compared to the area at the bottom of the sleeve cavity, especially when low tool rotation rate (1500 rpm) or short welding times (0.55 s) are used (see Figure 2-20).

To study the effect of the plunge depth on the morphology of the weld interface for completed RFSSWs, several welds were again produced using the aluminium different alloys AA6111 and AA6082. However, in this occasion the welds were produced in a horizontal lap configuration with a constant tool rotation rate of 2000 rpm, a welding time of 1.0 s, and a range of plunge depths from 0.2-1.2 mm. Figure 4-9 shows a series of micrographs for cross-sections of these welds. It can be noticed that the interface between the two sheets does not remain at the same level with increasing plunge depth, especially when using plunge depths of 0.6 mm or more. Moreover, the interface is pushed down at the weld centre, causing the material from the lower sheet to be pushed up in a region near the weld edge, developing a bowl-shaped deformation zone. This behaviour is identical to that seen in pinless FSSW by Bakavos et al (Bakavos, et al., 2011) (see Figures 2-29 and 2-30). The edges of this deformation zone are coupled with the hooking results in a characteristic “W” shape at the weld edges.



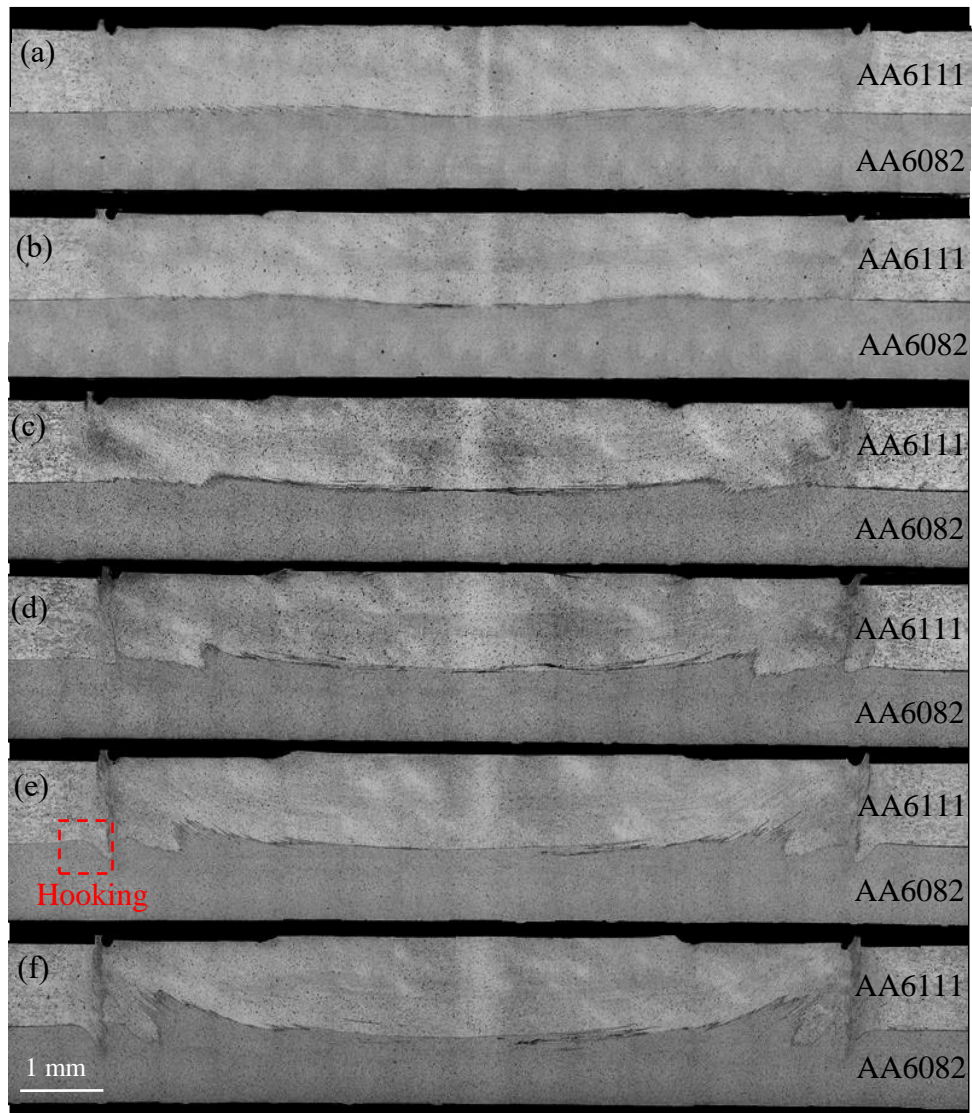


Figure 4-9: Development of the shape of the weld line as a function of plunge depth with 1.0 s welding time and 2000 rpm tool rotation rate: (a) 0.2 mm, (b) 0.4 mm, (c) 0.6 mm, (d) 0.8 mm, (e) 1.0 mm, and (f) 1.2 mm.

Figure 4-10 shows a series of micrographs for the development of the hook defect as a function of sleeve plunge depth. No hook can be detected when using a plunge depth equal to or less than 0.6 mm; the hook only becomes noticeable when using plunge depths of 0.8 mm or more. As seen in Figure 4-11, the height of the hook increases almost linearly with increasing plunge depth. Since the hook is formed by deforming the interface between the two sheets due to the vertical material flow in the region out of the sleeve during the plunge stage, as shown in Figure 4-7a (region 1), a deeper plunge results in more displacement of the interface and leads to a bigger hook. These results are highly compatible with the findings of Cao et al. (Cao, et al., 2016); however, the aforementioned authors suggested that the hook is formed during the final stages of the

welding process. In contrast, the results of the investigation of the material flow in this study prove that the hook is formed during the plunge stage.

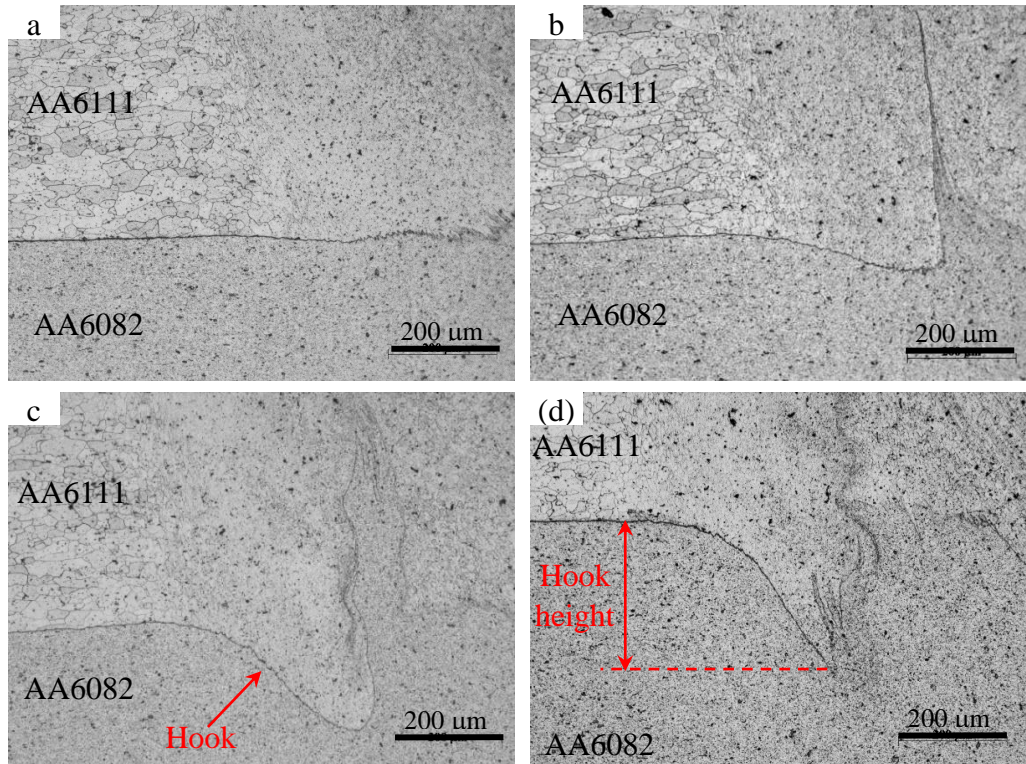


Figure 4-10: Hook development as a function of plunge depth with 1.0 s welding time and 2000 rpm tool rotation rate: (a) 0.6 mm, (b) 0.8 mm, (c) 1.0 mm, and (d) 1.2 mm.

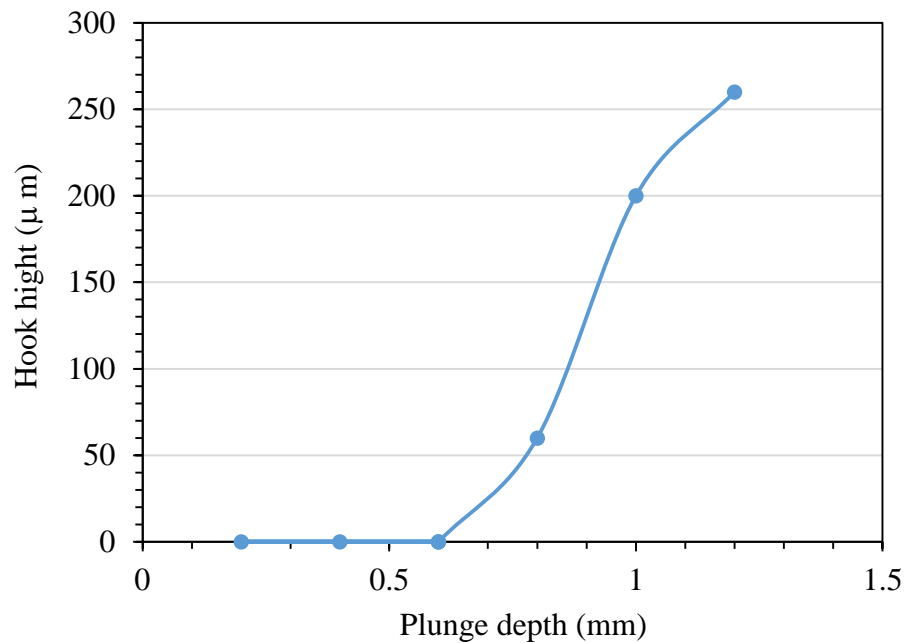


Figure 4-11: The effect of plunge depth on hook height (1.0 s welding time and 2000 rpm rotation rate).



The position of the joint interface for completed RFSSWs, determined using X-ray tomography and a gold interfacial layer as a marker, can be seen in Figure 4-12. These images show that the distribution of the gold layer, which was uniformly distributed in the interface between the two sheets before welding, becomes non-homogenously distributed across the interface, and more concentrated in the centre and the edges of the stir zone. This change have occurred because the sleeve is the only part that plunges through the upper sheet and reaches the interface so that it moves the gold to its internal and external edges. Conversely, the central area, which is located under the pin, appears less affected because the pin does not plunge through the upper sheet during any of the welding stages. As a result, the area under the sleeve represents the main metallurgically joined area. While the area under the pin represents a partial, or non-joined, area.

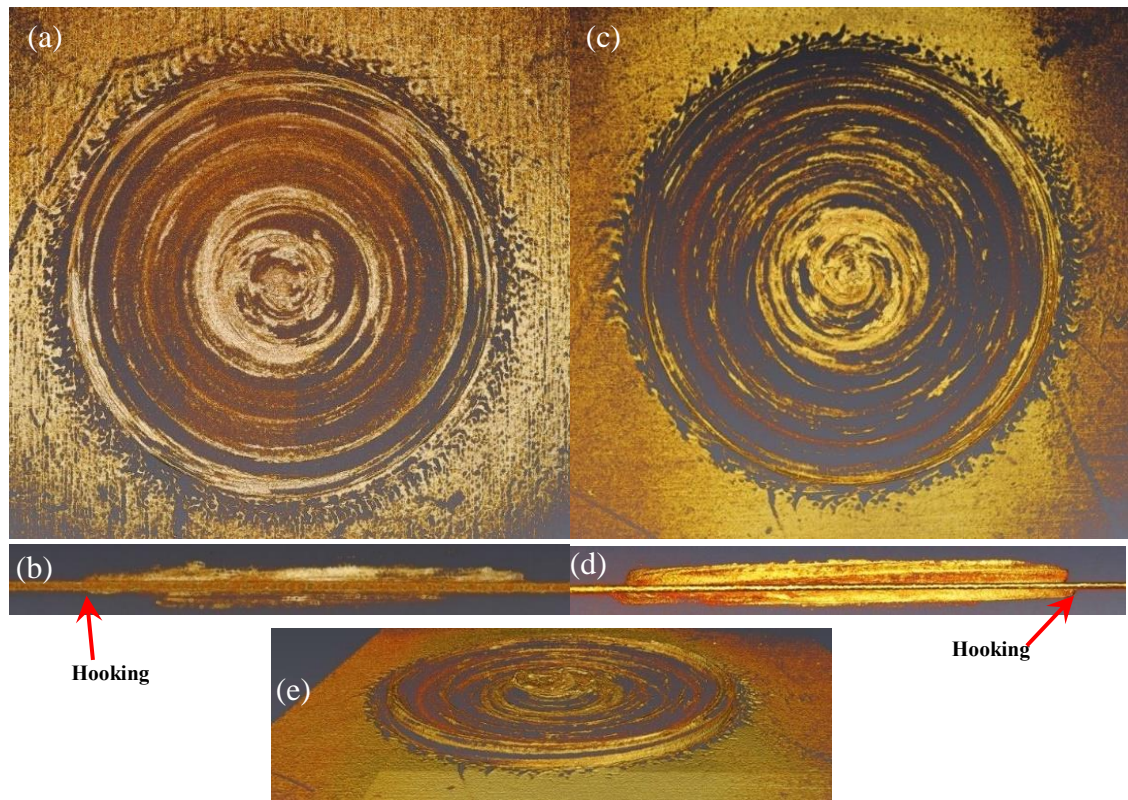


Figure 4-12: The results of X-ray tomography showing the distribution of gold at the weld interface for welds produced with 2000 rpm tool rotation rate: (a) and (b) plunge depth of 0.8 mm, (c) (d) and (e) plunge depth of 1.0 mm.

Material flow during the sleeve retraction and refilling stage can be described by the proposed model shown in Figure 4-13. During this stage, the vertical flow of the material in all regions is reversed, but the rotational flow remains in the same direction as the tool rotation. The material of the upper sheet, which was inside the sleeve cavity during the plunge stage, is now clearly stuck to the tool surface and simply rotates as a

‘plug’, which therefore does not add any additional layers in the contrast marker experiments (Figure 4-8). However, as a result of this, there is a steep velocity gradient between this rotating plug and the base sheet, which continues to develop layers in the lower sheet and an intense shear gradient. Therefore, most of the new layers will be added to this region during the dwell and retraction stages.

To clarify this material flow model in the retraction stage, the same region classification that was used for the plunge stage will again be used. The material in the first region is moved in the same helical vertical rotational flow but in an upward direction due to the retraction of the rotated sleeve and plunge of the pin. When this material reaches the upper surface of the upper sheet, the surrounding material, which is supported by the clamping ring, forces it to move outwards and downwards with a helical vertical rotational flow back towards the interface between the two sheets. The material movement in this adds more lamellae of the contrast markers (AA6111 and AA6082) in Figure 4-8 to those already formed during the plunge and dwell stages.

The material in the second region, which belongs to the upper and lower sheets, is subjected to vertical and rotational horizontal movement and is forced by the material that comes from the central weld region and the sleeve cavity to move up and refill the annular void created by the sleeve retraction (see Figures 4-8 and 4-9). The central weld region (third region) is also subjected to helical movement during this stage, but the vertical movement seems to be more dominant. The material in this region is pushed by the material from the upper sheet plug (region 4), which in turn is pushed down by the plunged rotated pin, and due to the resistance of the backing plate, the material then tends to take a rotational-horizontal path (Figures 4-8 and 4-9).

The material in the fourth region mostly sticks to the pin during the early stage of welding and rotates with it; therefore, it is supposed that this material is subjected mostly to a vertical movement during the final refill stages. In the fifth region, the material flows in two directions in addition to the rotational flow. The material near the centre is moved in a vertical direction and contributes to pushing the material of regions 2 and 3 downwards. On the other hand, the material adjacent to the sleeve is moved in a horizontal direction to refill the annular cavity created by the sleeve retraction. The observation is especially true during the last stage of the welding process, which can be seen schematically in Figure 4-13c.



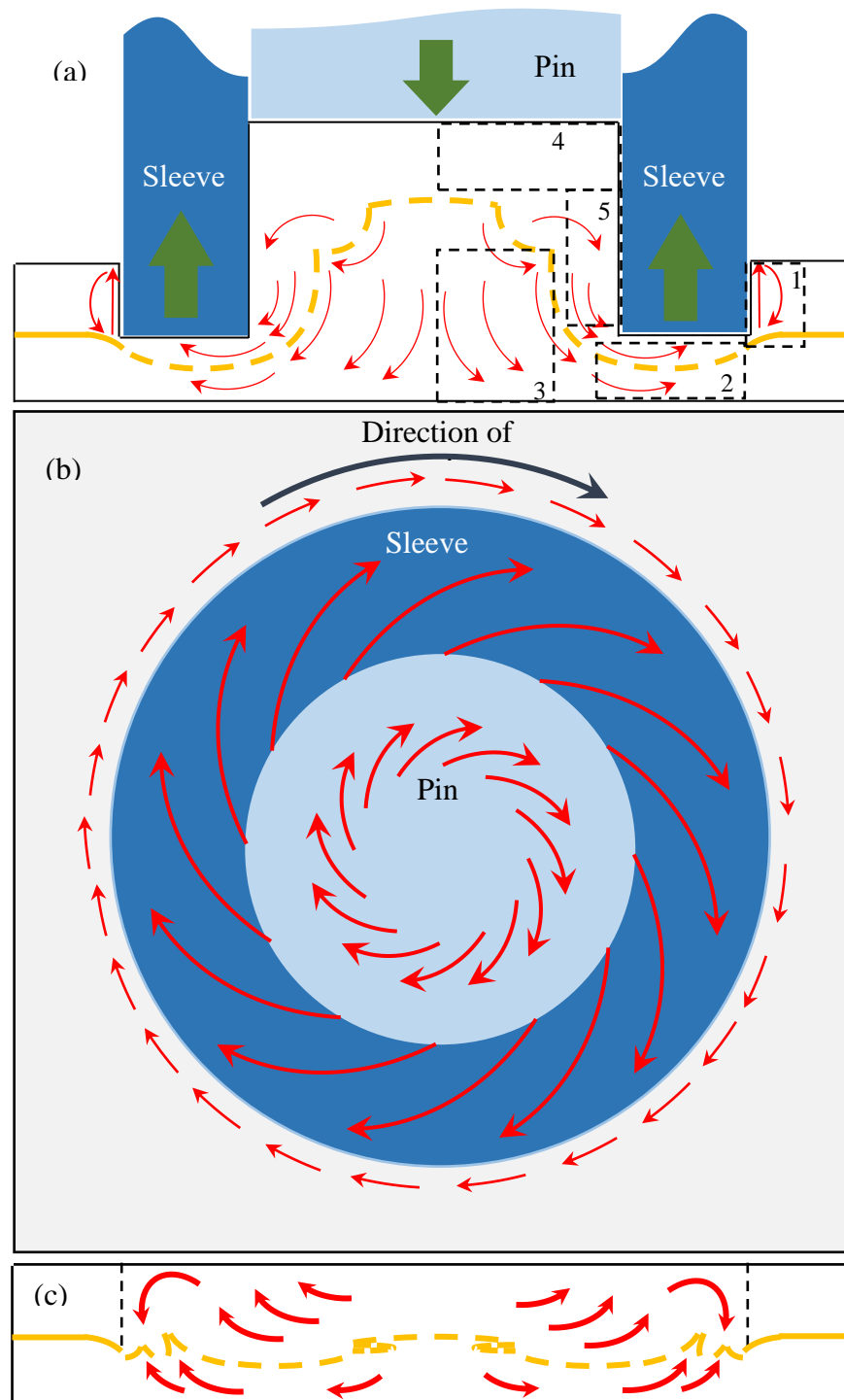


Figure 4-13: A schematic diagram indicating the material flow during the retraction stage: (a) cross-sectional view and (b) top view, and (c) near the end of the refill process (cross-sectional view).

#### **4.4 Effect of Welding Variables on the Weld Thermal Field and Thermal History**

Experiments were performed to measure the temperatures reached in the weld zones during the RFSSW cycle. The dynamic nature of the welding process meant that the thermocouple could be destroyed or moved if it was located at the interface between the two sheets. Therefore, thermocouples were located underneath the lower sheet in the weld centre and at four other locations with a spacing of 3 mm between each, as shown in Figure 3-7.

Figure 4-14 shows a typical temperature history curve at a distance of 3 mm from the centre of an RFSSW, which was obtained using welding parameters of a 2500 rpm rotation rate, 2.0 s welding time, and a 1.0 mm plunge depth. It can be noted that the temperature increases rapidly from room temperature to about 471 °C, with a rate of increase of about 1450 °C/s, during the first stage of the welding process (sleeve plunging stage) marked by  $T_1$ . In the FSSW processes, heat is generated by two sources: friction between the rotated tool and the material being welded, and the plastic deformation in the welding region (Commin, et al., 2009). As sticking occurs between the tool and the material of the workpiece during the early stages of the welding process (Reilly, et al., 2015), plastic deformation becomes the dominant factor in heat generation during the plunge stage and due to the use of a very high plunge rate (4 mm/s), which led to a very high strain rate. The temperature was observed to increase rapidly during this stage.

In the second stage, dwell time (marked by  $T_2$ ), the rate of increase in temperature decreased to about 73 °C/s, but the increase in temperature continued and reached a peak of 580 °C at the end of this stage. The main reason for this decrease in the rate of temperature increase is that during this stage most of the plastic deformation occurs near the bottom of the sleeve (see the material flow section, Figure 4-3) and the high local temperature causes material to soften in this region, which reduces the power dissipation. Meanwhile, the material that enters the sleeve cavity during the plunge stage rotates with the tool, resulting in lower plastic deformation and lower heat generation. As a result, the total heat generated during this stage is lower than that produced in the plunge stage.

In the third and final stage of the welding process, the sleeve retraction (marked by  $T_3$ ), the temperature begins to decline at a rate of about  $160\text{ }^{\circ}\text{C/s}$  and reaches  $539\text{ }^{\circ}\text{C}$  at the end of this stage, which represents the end of the weld cycle. Although the tool rotation continues during this stage, the temperature significantly decreases, for two reasons. The first reason is the refilling of the annular cavity formed by the sleeve plunge with ‘colder’ material that comes from the sleeve cavity (Zhao, et al., 2016), which acts as a heat sink that absorbs some heat and reduces the temperature. The second reason is the movement of the sleeve and progressive reduction of the material-tool contact area, which is the main source of heat generation, away from the thermocouples during this stage. However, the cooling rate still shows a slight increase after completion of the weld cycle suggesting that heat is still generated during the retraction stage.

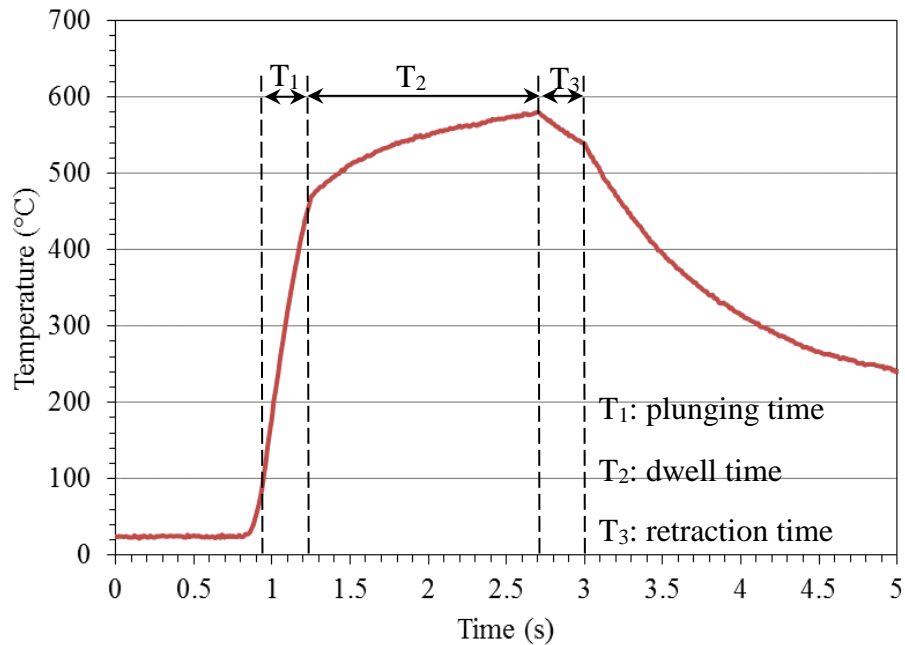


Figure 4-14: Typical temperature history curve recorded for the welding process (2500 rpm tool rotation rate, 2.0 s welding time and 3mm from weld centre).

In order to verify the reliability of any measured thermal cycle for it to be included in the later discussion, the cycles had to satisfy the following criteria:

- The temperature curve should follow the typical shape shown in Figure 4-14.
- The temperature curve should not show any significant random fluctuation.
- The thermocouple should remain in the position in which it was placed before the welding process began.

The results from temperature measurements showing the thermal history for different distances from the weld centre (0, 3, 6, 9, and 12 mm) for an RFSSW produced using a tool rotation rate of 2500 rpm, a welding time of 2.0 s, and a 1.0 mm plunge depth, are shown in Figure 4.15. It can be noted that the thermal history in the stir zone and the region near it (6 mm from the weld centre) followed the typical shape shown in Figure 4-14, where the temperature increased rapidly in a linear relationship during the plunge stage, continued to rise more slowly during the dwell time, and then decreased rapidly after reaching the maximum temperature. In comparison, locations far away from the weld centre (9 and 12 mm) showed slightly different behaviour, where the heating and cooling rates were significantly lower than for thermal histories in the stir zone. Nevertheless, the most important difference between the thermal histories, is that there was a large difference in the maximum temperature reached at each point of the weld in Figure 4.15, depending on the distance from the centre. For example, the peak temperature measured at a point located at a distance of 3 mm from the weld centre was higher than that measured at the exact weld centre, or at a point located at a distance of 6 mm from the weld centre by 56 and 151°C respectively.

The results showed that the highest peak temperatures were measured at a distance of 3 mm from the weld centre. There are three reasons for this. Firstly, at this distance, the thermocouple was located directly under the sleeve, which represents the main source of heat generation. Due to the high strain rate experienced by the material stirred at the bottom of the sleeve cavity (see Figure 2-21 and Figure 4-3) as it plunged, a heat generation increases with increasing tool velocity (see equation 2-2) (Schmidt & Hattel, 2008), the heat generated by plastic deformation in this region is higher. Secondly, in this region, the material flow was complex and subjected to very high plastic deformation (see Figures 2-2, 4-3 d, and 4-7) as it was also affected by the heat generated at both the inner and bottom surfaces of the sleeve (Zhao, et al., 2016). On the other hand, in the centre of the weld, which was completely under the pin, the tool surface velocity was minimal. The temperature was thus less than that measured under the sleeve (at a distance of 3 mm from the weld centre). The pin also had less effect on heat generation because it was retracted and moved upwards during the plunge stage of the welding process. By moving away from the weld edge towards the parent material, the temperature decreases due to heat dissipation into the surrounding material, from the upper sheet to the clamping ring by conduction and the air by convection, and from the lower sheet to the backing plate by conduction. Conduction losses to the backing plate

are also greatest under the tool, where the interfacial heat transfer coefficient is reduced by the clamping pressure (Bakavos & Prangnell, 2009).

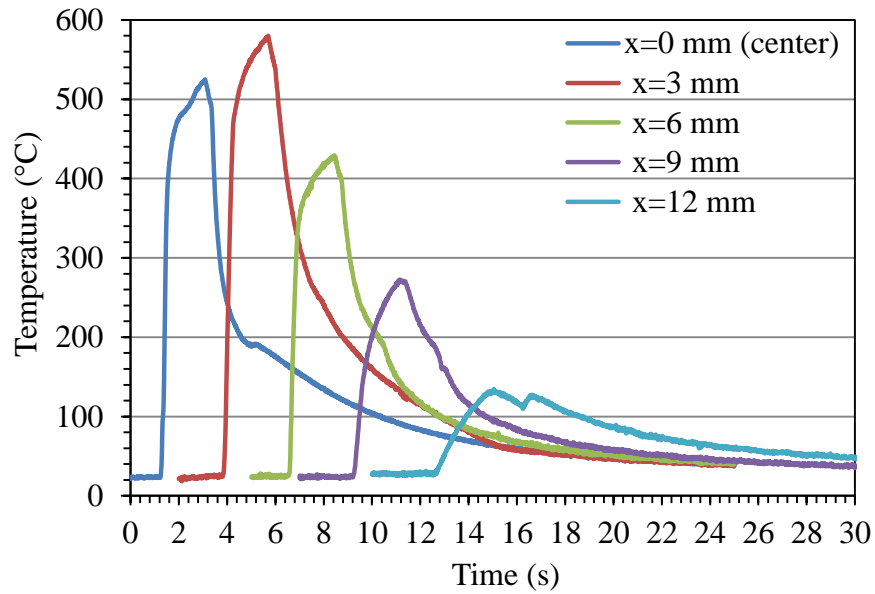


Figure 4-15: Thermal histories at different distances from the weld centre (0, 3, 6, 9 and 12mm) for RFSSW using a tool rotation rate of 2500 rpm, a welding time of 2.0 s and a 1.0 mm plunge depth.

Numerous measurements were made at a variety of tool rotation rates and welding times, using these thermocouple locations. The relationship between the peak temperatures reached in each weld cycle and the distance from the weld centre are plotted in Figure 4-16. This Figure also shows the location of the pin and the sleeve to clarify the effect of each of them on the heat generation. As discussed above, there was a general trend that the highest peak temperature was measured at a distance of 3 mm from the weld centre, with a somewhat lower peak temperature at the weld centre. It was also observed that the measured peak temperatures decreased significantly when moving from the point located at 3 mm from the weld centre to the parent material. Therefore, all of the curves of the peak temperatures show a significant volcano mountain-like shape.

From Figure 4-16a it can be noted that the peak temperature measured at each distance has clearly increased with increasing tool rotation rate, especially in the weld zone. For example, the peak temperatures measured at a point located at a distance of 3 mm from the weld centre are 419.2 °C and 496.5 °C when using a welding time of 0.55 s and tool rotation rate of 1500 and 2500 rpm respectively. These results are evidence of the impact of increasing the tool rotation rate on the amount of heat generated in the weld (see equation 2-2) (Schmidt & Hattel, 2008). However, by moving away from the weld zone, the temperature difference at a given point for different tool rotation rates

decreases significantly. This is likely to be due to the heat loss from the upper surface of the upper sheet and the lower surface of the lower sheet to the backing plate by conduction.

Comparing Figures 4.16 a and 4.16 b shows that an increase in welding time from 0.55 s to 2.0 s increased the levels of the peak temperatures at all points. For instance, when using a tool rotation rate of 2500 rpm and a plunge depth of 1.0 mm to implement RFSSWs, the measured peak temperature for the point located at a distance of 3 mm from the weld centre increased from 496.5 °C to 580°C, when increasing the welding time from 0.55 s to 2.0 s (while using a constant plunge and retraction time of 0.25 s and increasing dwell time from 0.05 s to 1.5 s). This result proves the significant impact of welding time on the temperature levels and the total heat input.

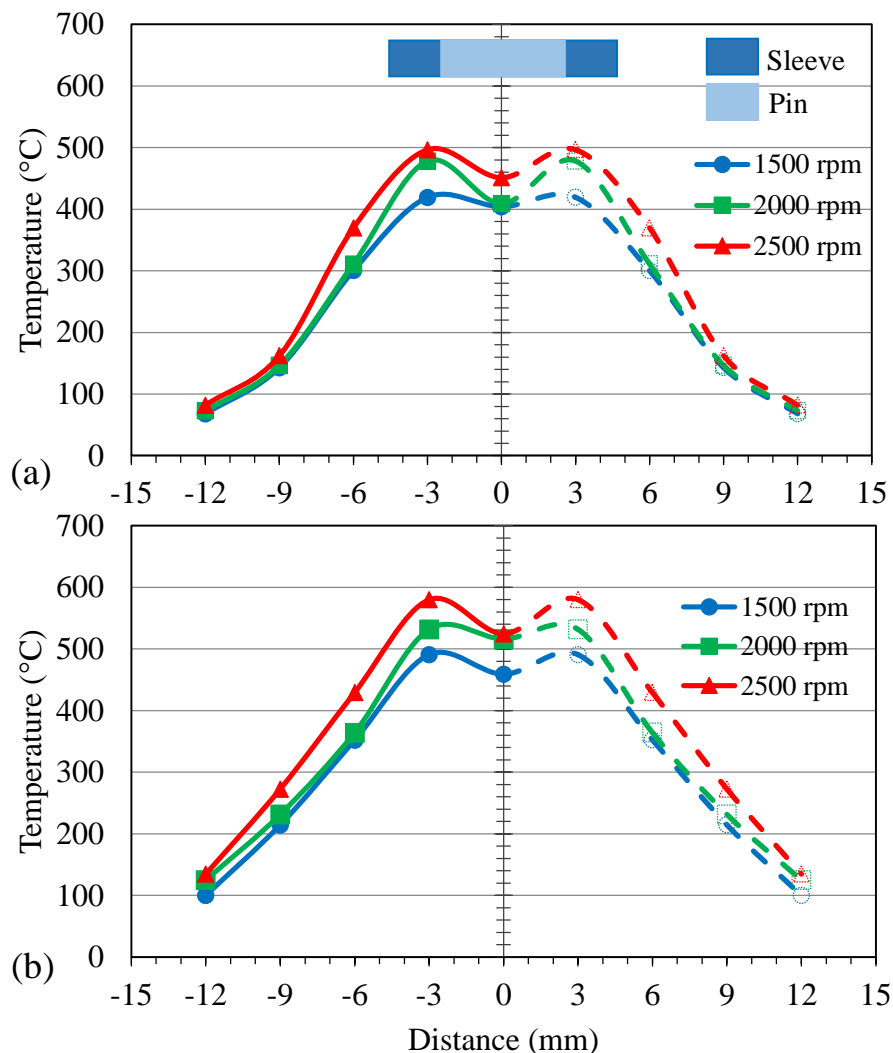


Figure 4-16: The relationship between peak temperature, rotation rate, and distance from the centre of RFSSW. The welds were produced using 1.0 mm plunge depth and a welding time of (a) 0.55 s and (b) 2.0 s.

## **4.5 Weld Microstructure**

Investigation via optical microscopy (OM) of the cross-section of joints produced using RFSSW with the AA6111 aluminium alloy 1.0 mm thick sheet revealed three distinct weld microstructure zones: the stir zone (SZ), the thermo-mechanically affected zone (TMAZ), and the base metal (BM), as shown in Figure 4-17. In FSW, the heat affected zone (HAZ) is generally found to be located between the BM and TMAZ, but because the grain structure (at the optical microscope level) of this region is not affected during the weld cycle, and in fact in most cases only minimal, or no loss of hardness was found (see Figures 4-20 and 4-23), it was not easy to distinguish from the BM using optical microscopy. However, HAZ could be located using scanning electron microscopy (see Figure 4-19).

As shown in Figures 4.17 b and c, the main feature that characterised the SZ was the very refined grains. In general, these grains were equiaxed in most of the SZ regions. This appearance of the microstructure resulted from dynamic recrystallisation, caused by the high strain reached during the sleeve plunging stage, in addition to the high temperature during the welding cycle (Gerlich, et al., 2007; Gerlich & Shibayanagi, 2009; Parra, et al., 2011). In spite of the very high temperature reached in the stir zone (see Figure 4-16), no metallographic evidence was found to confirm any local melting. Nevertheless, the high peak temperatures reached the solvus temperatures of the strengthening phases. AA6111 is known to contain two equilibrium phases:  $\text{Q}$  ( $\text{Al}_5\text{Cu}_2\text{Mg}_8\text{Si}_6$ ), with a solvus temperature of 440 °C, which could be reached when using most of the combinations of welding parameters (see Figure 4-16 a), and  $\beta$  ( $\text{Mg}_2\text{Si}$ ) with a solvus temperature of 540 °C, which could be reached only when using longer welding times (see Figure 4-16 b) (Bakavos, et al., 2011).

The thermo-mechanically affected zone (TMAZ) can be observed from the distortion of the grains compared to the base material (see Figure 4-17 d). Two factors are responsible for the grain structure in this region; the more moderate temperature due to the heat transferred from the stir zone and the more moderate strain caused by the shear gradient from the material that was coupled to the rotated and plunged tool, relative to the surrounding colder constraining material (Parra, et al., 2011; Rosendo, et al., 2011; Fanelli, et al., 2012). The HAZ area and BM had the same microstructure appearance at optical microscopy resolution, and showed a wide range of grain sizes, but in general,

the grain size was much bigger compared to that in SZ and TMAZ (see Figure 4-17 e). In the HAZ, both the microstructure and mechanical properties change, primarily because of the effect of the welding thermal cycle on the state of matrix precipitation. Nonetheless, these changes were found to have no effect on the grain structure (Mazzaferro, et al., 2009).

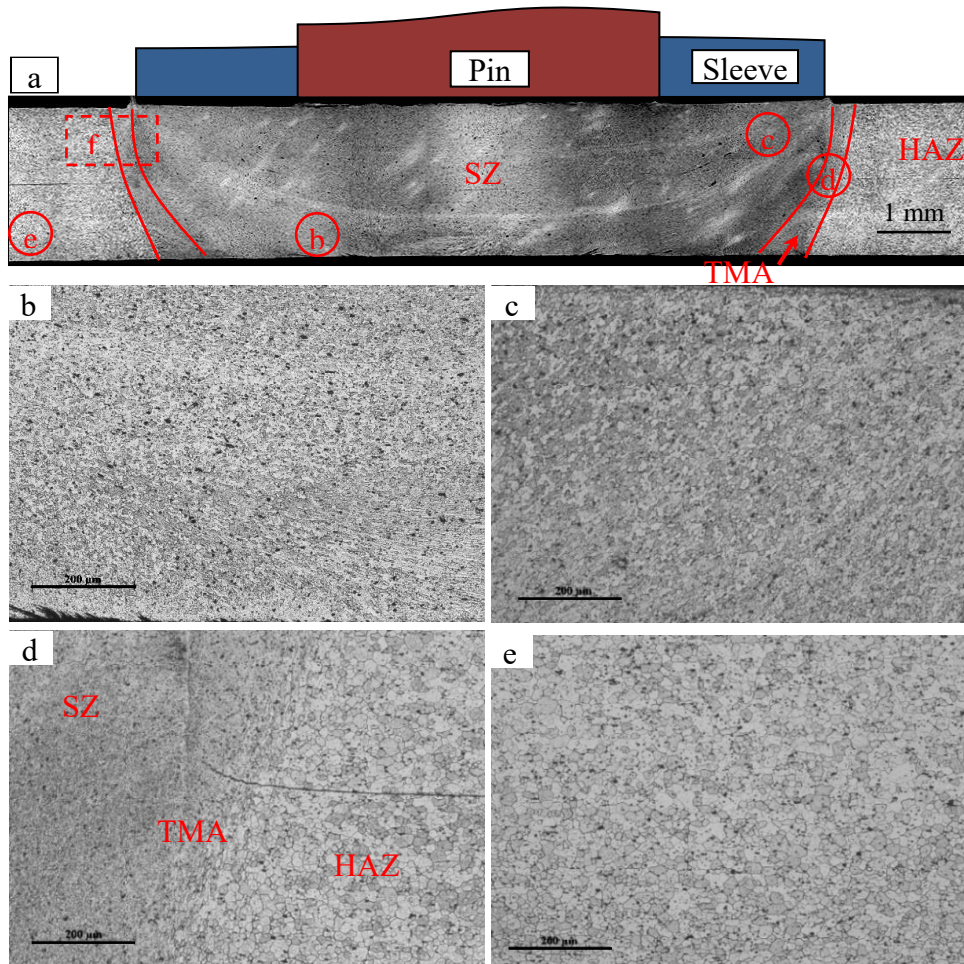


Figure 4-17: (a) Typical macrostructure of a RFSSW joint cross-section (0.55 s welding time, 2000 rpm tool rotation rate, and 1.0 mm plunge depth); (b), (c), (d), and (e) show the microstructure at the locations marked in (a); (f) the weld edge and the adjacent regions in which the band contrast and EBSD maps shown in Figure 4-18 were taken.

The grain structure of the three zones can be seen more clearly at higher resolution in Figure 4-13 c. This figure shows an EBSD map from an area located at the edge of the weld zone and marked by the red rectangle (f), shown in Figure 4-17 a. This figure reveals that in this location mapped across the weld edge, there are five distinct regions: the first region on the right, marked (1), is the SZ, which has very refined equiaxed grains. The grains gain this shape and size for the reasons explained earlier in this section. The second region (marked 2) shows a band of finer grains than in region 1 because this region was located close to the surface of the plunging and retracting



sleeve. Therefore, the material in this region was subjected to the highest strain rate during the welding cycle, which resulted in the highest level of grain refinement. The EDS line scan through this line and other regions of the weld edge shown in Figure 4-18 b revealed that this band of ultra-fine grains does not contain any oxide layer and the dark lines shown in the EBSD map represent only a layer of very fine grains located close to the surface of the former sleeve cavity. The third region (marked with 3) contains bands of grains with two distinct sizes and shapes: very fine grains and much bigger grains, elongated in the direction of the material flow. These curved bands or layers of grains with different sizes result from the material flow induced by the sleeve plunge (see region 1 in Figure 4-7 and Figure 4-13). The fourth region is the TMAZ (marked 4). In this region, grains are affected by plastic deformation, but the deformation is not sufficient for them to be greatly displaced. Therefore, grains in this region also have an elongated shape in the material flow direction. The fifth region contains much bigger grains than those found in the other regions, here, the grains are identical to the parent grain structure with a nearly equiaxed morphology, because the material in this region was only affected by heat and was not subject to any plastic deformation.

As mentioned earlier in this section, it was difficult to differentiate the HAZ from the base metal using an optical microscope. Therefore, SEM was used to investigate the effect of the welding process and post-weld heat treatment on the strengthening precipitate phases. Figure 4-19 b, and c show SEM images from the HAZ in the as-welded and paint baked treatment conditions (to simulate the paint baked treatment the samples were artificially aged at 180 °C for 30 min.). From the comparison between the two figures, it can be seen that the samples in both conditions contain two types of particles the first is big and very bright particles which are containing iron in their composition. These particles were found in the base material in the as-received condition. On the other hand, dark particles can also be seen in both conditions but with different sizes and distribution. In the as-welded condition the sample contained a very low density of very small, widely spaced precipitates (dark precipitates). These spheroidised precipitates are probably  $\beta$  phase, since the temperature reached in this region was much lower than 540 °C, which is the solvus temperature of this phase. However, the maximum temperature was most likely to be high enough to dissolve the Q phase and its intermediate phases, since the solvus temperature of the Q phase in AA6111 is 440 °C (Bakavos & Prangnell, 2009) (see Figure 4-16). A greater volume

fraction of coarser, but still very fine, precipitates can be seen in the artificially aged sample (see Figure 4-16 c). This increase in volume fraction occurred due to the growth of pre-existing precipitates combined with some precipitation during the paint bake cycle.

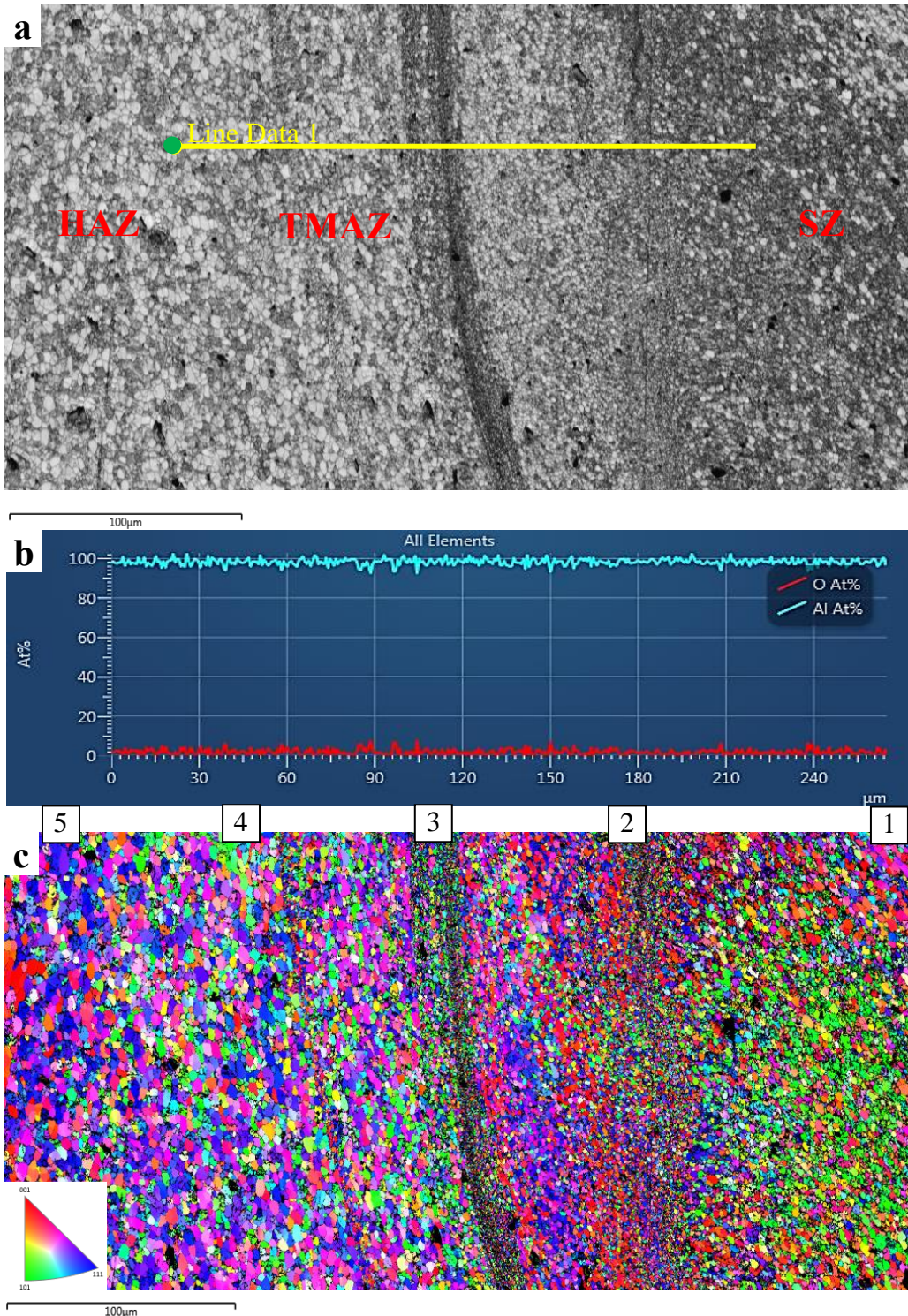


Figure 4-18: (a) Band contrast map at the weld edge (from the red rectangle region marked ‘f’ in Figure 4-17) for a sample welded with a 2500 rpm tool rotation rate and 2.0 s welding time, showing the main three regions SZ, TMAZ, and HAZ; (b) an EDS line scan data for the yellow line shown in (a); and (c) x-direction IPF coloring orientation map from the same region as (a).



Using TEM investigation Chen et al. found that the precipitates in a paint baked nugget in FSSWs consist of two phases: fine  $\beta''$  needles and a  $Q'$  phase. However, it is not possible to discriminate between such phases in SEM. Moreover, Chen et al. showed that the heat-treated base metal (shown in Figure 4-19 d) contained the same two types of precipitates, but with a larger volume fraction. This finding is believed to have occurred because the parent material had experienced a much shorter natural ageing time, which delays artificial ageing in 6000 series alloys (Chen, et al., 2013).

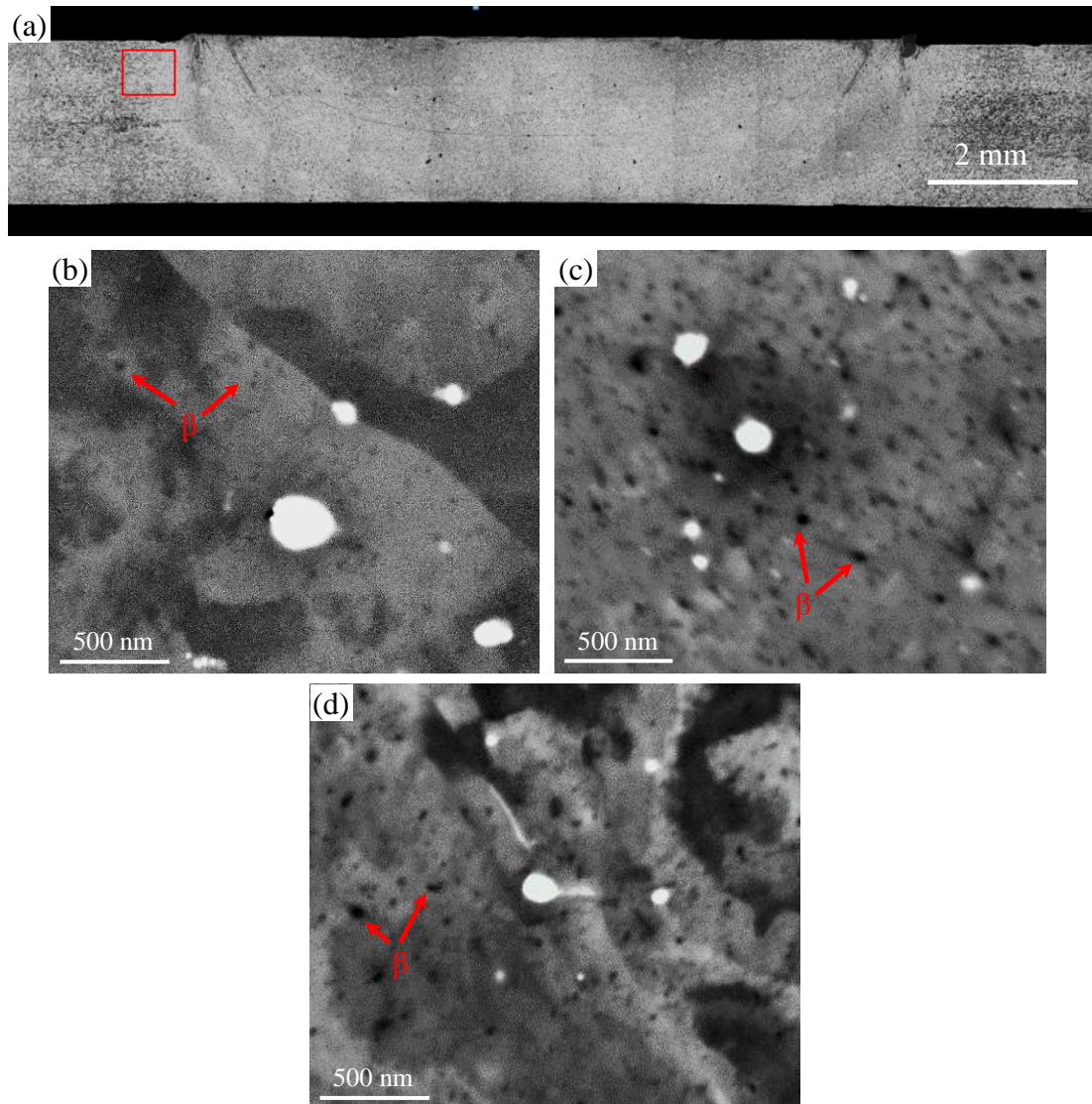


Figure 4-19: SEM (BSE) images for a sample welded with a 2500 rpm tool rotation rate and 2.0 s welding time: (a) OM image for the full joint; (b) HAZ (marked as a red rectangle in (a)) in the as-welded condition; (c) artificially aged at 180 °C for 30 min. at the same location as (b); and (d) the parent material also artificially aged at 180 °C for 30 min., for comparison.

## **4.6 Effect of Welding Variables on Joint Hardness Profiles in the as-Welded, Naturally Aged, and Artificially Aged Conditions**

Microhardness testing was implemented to detect the effect of the welding parameters and natural and artificial ageing on the local mechanical properties of the weld cross-sections. Measurements were made in the form of two parallel lines of points passing through all the areas of the welded joints. The first line was located in the mid-thickness of the upper sheet and the second line was located in the mid-thickness of the lower sheet, as shown in Figure 3-9.

The effect of the RFSSW parameters on the microhardness profiles of the AA6111-T4 aluminium alloy welds in the as-welded condition is shown in Figure 4-20. This figure shows hardness profiles for three different welding conditions, measured immediately after welding (within one hour of welding). In general, the hardness profile across the welds show a typical W-shape, similar to that usually seen in friction stir spot welds in the same alloy and other heat-treatable alloys although the hardness in the nugget region is still quite low owing to the natural ageing time (Bakavos & Prangnell, 2009). For example, in Figure 4-20a, the base material shows an average hardness of about 89 HV. The hardness starts to decrease towards the weld centre in the HAZ reaching a minimum value of about 60 HV at a region near the interface between the heat affected zone (HAZ) and the thermomechanically affected zone (TMAZ). Hardness minima have previously been detected in similar positions in FSSWs of the aluminium alloy AA6111 (Bakavos & Prangnell, 2009). The decrease in hardness level in the outer regions of the HAZ is mainly associated with the over-ageing of the rolled microstructure of the base material, because the maximum temperature reached in this region was not as high during welding (less than 300 °C, see Figure 4-16). The region of the HAZ closer to the weld centre reached a higher peak temperature (more than 300 °C, see Figure 4-16), resulting in greater coarsening combined with partial solutionisation of the naturally aged parent material (Parra, et al., 2011). However, coarsening of precipitates reported to be the predominant phenomenon in this region of the HAZ, which located nearer the weld centre, because the peak temperatures in this region did not reach the  $\beta$  phase solvus (540°C) (Bakavos & Prangnell, 2009; Parra, et al., 2011). The weld nugget in the TMAZ shows a slightly higher hardness level than the reduction that would be expected due to precipitate coarsening, this result is likely because it is affected by the plastic deformation, which can result in some strain hardening. However, this is still not

enough to balance the softening from the coarsening of the matrix precipitates (Parra, et al., 2011). In comparison, the stir zone (SZ) shows a slightly higher hardness level than the HAZ and TMAZ, due to the high strain rate and higher temperature reached in this zone (420 to 580 °C depending on the tool rotation rate and welding time). These high strain rate and temperature lead to dynamic recrystallisation of the stir zone and grain refinement, as well as near complete re-solutionisation, which causes subsequent rapid natural ageing. The grain refinement and rapid post weld natural ageing represent the main factors that result in a slightly higher hardness level for the SZ than for the HAZ in the ‘as-welded’ condition (Bakavos, et al., 2011).

Comparison between the hardness profiles of the upper and lower sheets shows very slight differences, but a more noticeable difference can be seen when using a higher tool rotation rate, or a longer welding time. For these conditions the HAZ of the upper sheet expands sideways and the minimum hardness values decrease slightly. This reduction in hardness occurs because more heat is generated due to the plastic deformation and friction of the tool in the upper sheet. Further to this, there is an increase in the thermal input and expansion of the thermal field when increasing both the welding time and the tool rotation rate (see Figure 4-16).

The effect of welding time on the average hardness at the weld centre of the upper sheet in the as-welded condition is shown in Figure 4-21. The average hardness only slightly decreases with increasing welding time for all tool rotation rates; this means that the temperature level was probably high enough to dissolve most of the strengthening precipitates for all of the welding conditions in the process window (Chen, et al., 2012 a). This occurs because the naturally aged parent sheet mainly only contains clusters and GPZs, which have a relatively low reversion temperature. For example, welds produced using a lower rotation rate (1500 rpm) only showed a slight decrease in the average hardness at their centres. This result is due to the increasing temperature with increasing welding time (see Figure 4-16), which would be expected to cause coarsening of the grain structure, as well as slightly increased dissolution of coarser precipitates (Chen, et al., 2012 a).

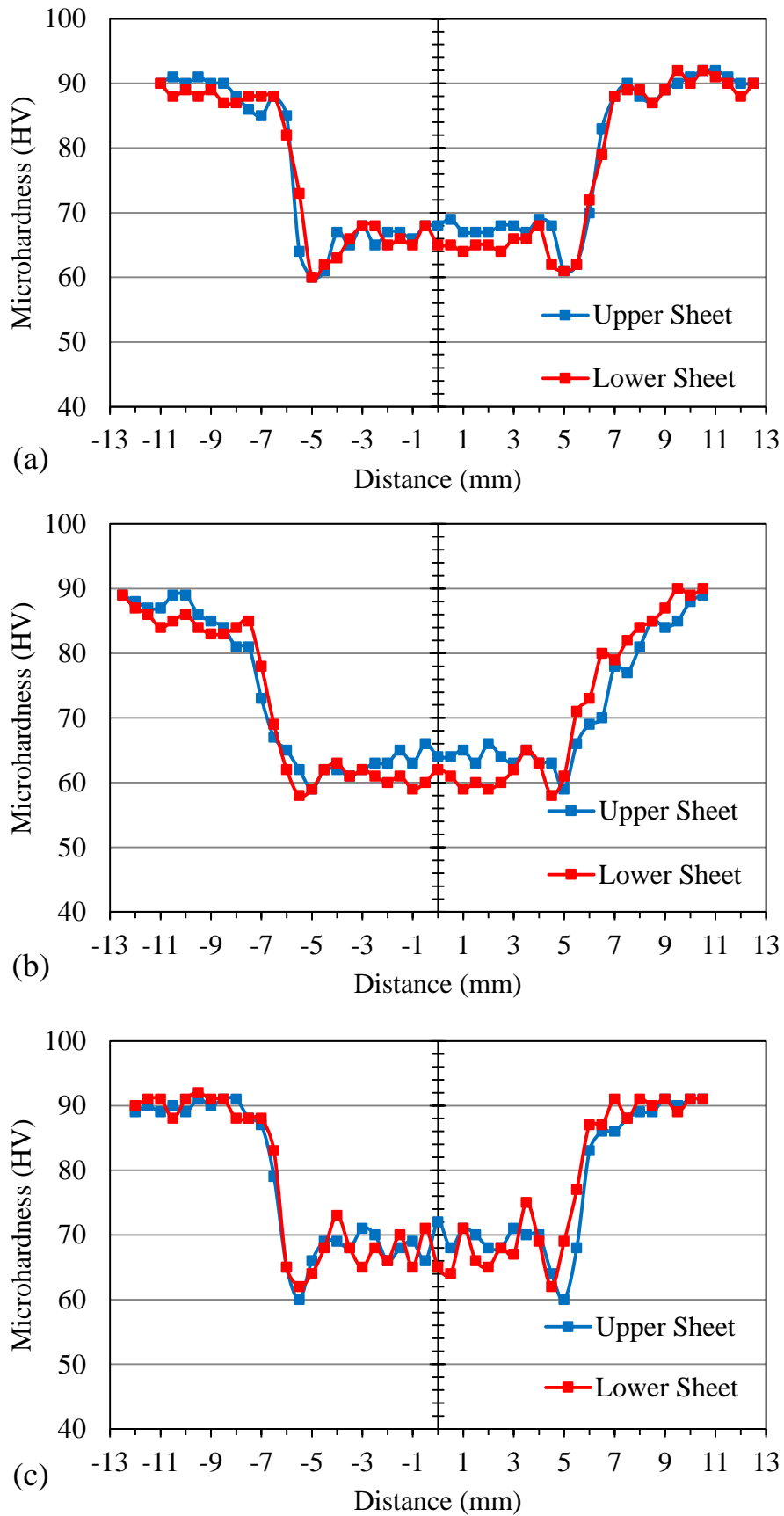


Figure 4-20: Hardness profiles of welds produced with different tool rotation rates and welding times: (a) 1500 rpm , 0.55 s; (b) 1500 rpm, 2.0 s; and (c) 2000 rpm, 0.55 s, measured immediately after welding (within one hour).

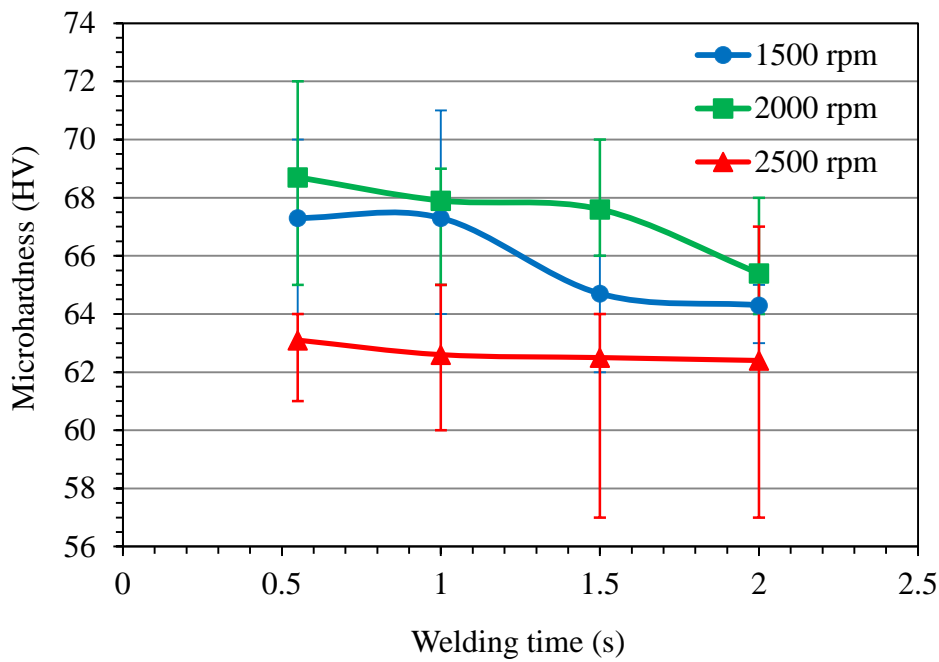


Figure 4-21: The relationship between the welding time and the average hardness at the weld centre after welding with different tool rotation rates, measured immediately after welding (within one hour).

Figure 4.22 shows the effect of welding time on the extent of the HAZ width immediately after welding (within one hour). The width of the HAZ was measured from the point of minimum hardness (near the TMAZ/HAZ interface) to the point where the hardness level became equal to the hardness of the base material (89 HV). The HAZ width shows a clear increase with increasing welding time and tool rotation rate, due to the expansion of the thermal field and increase in peak temperature in regions more distant from the weld centre (see Figure 4.16). This rise in the peak temperatures results in greater coarsening of the strengthening particles or even solutionisation of strengthening precipitates in the regions where the peak temperatures exceed the solvus temperatures, leading to an expansion of these regions with greater heat input (Parra, et al., 2011).

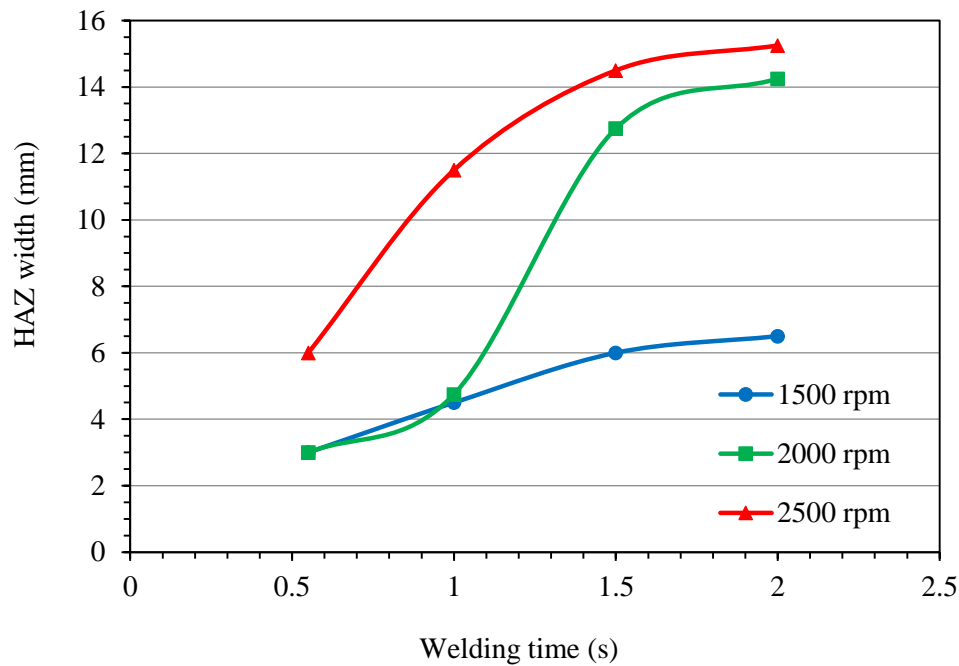


Figure 4-22: The effect of welding time on the width of the HAZ, measured immediately after welding (within one hour).

To study the effect of post weld natural ageing on the local mechanical properties of the RFSSW joints produced in the AA6111-T4 aluminium alloy, several welds were produced with a range of welding parameters. Figure 4-23 shows an example of hardness profiles from naturally aged samples. These three samples were welded with different welding times and tool rotation rates and then left for 30 days at room temperature before their hardness was re-measured. Similar to the hardness measurements for the samples in the as-welded condition, shown in Figure 4-20, the microhardness measurements were made in the form of two parallel lines passing through the mid-thickness of the upper and lower sheets (shown in Figure 3-9).

The hardness level in the stir zone shows a clear increase in natural ageing in comparison to the hardness levels in the as-welded condition (Figures 4-20 and 4-23) for all the samples and all welding conditions. However, the changes in hardness levels were different, both between the upper and lower sheets and between samples produced with different welding parameters. For example, in Figure 4-23a, the hardness level of the upper sheet in the SZ is significantly higher than the hardness level of the lower sheet. A possible reason for this difference is the effect on the response to natural ageing of different levels of solutionisation during the welding, i.e. a higher heat input would have led to more dissolution of strengthening particles during the welding cycle and thus a higher solute supersaturation. In order to achieve the maximum response to



natural ageing, the peak temperature during welding should approach the solvus of the  $\beta$  phase, which is of the order of 540°C, and the maximum temperature measured underneath the lower sheet when using the same welding conditions (1500 rpm, 0.55 s, 1.0 mm plunge depth) was 419.2 °C (see Figure 4-16). This is expected to be lower than the result for the upper sheet because most of the heat is generated in the upper sheet, resulting in a lower level of solutionisation. Thermal losses are also greater from the lower sheet owing to the greater contact area with the base plate compared to the clamping ring. Therefore, the ability of the hardness level to increase by natural ageing was noticeably reduced in the lower sheet (Bakavos & Prangnell, 2009). In natural ageing, the hardness increases as a result of the precipitation of GPZs and solute clustering with ageing time (Chen, et al., 2012 a). After natural ageing, it is still possible to distinguish the HAZ in welds produced using longer welding times (2.0 s), because at this position these welds reach peak temperatures for a sufficient time during the welding cycle that were not high enough to dissolve the strengthening particles, but that were sufficient to result in over-ageing and a decrease in hardness level.

The effect of the welding time and tool rotation rate on the average hardness of the weld centre of the upper sheet, after natural ageing for 30 days, is shown in Figure 4-24. In general, it can be seen that the average hardness of the weld centre increased with increasing welding time and tool rotation rate. This result can be explained by the fact that the temperature at the weld centre increased (Figure 4-16), which led to the dissolution of more strengthening precipitates during the welding cycle and increased the saturation of the solid solution, resulting in a greater thermodynamic driving force for natural ageing.

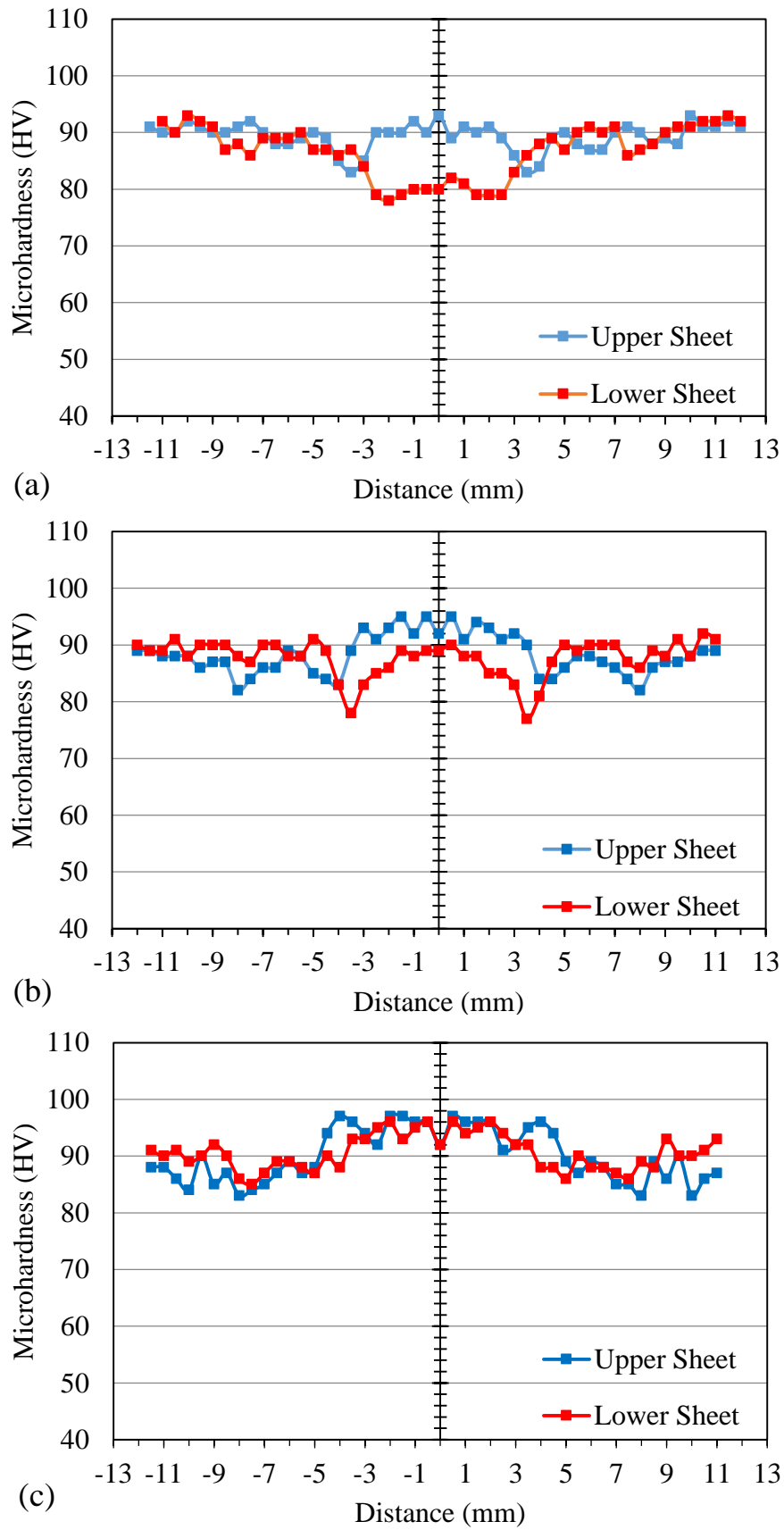


Figure 4-23: Hardness profiles for samples naturally aged for 30 days, welded with different tool rotation rates and welding times: (a) 1500 rpm, 0.55 s; (b) 1500 rpm, 2.0 s; and (c) 2500 rpm, 0.55 s.

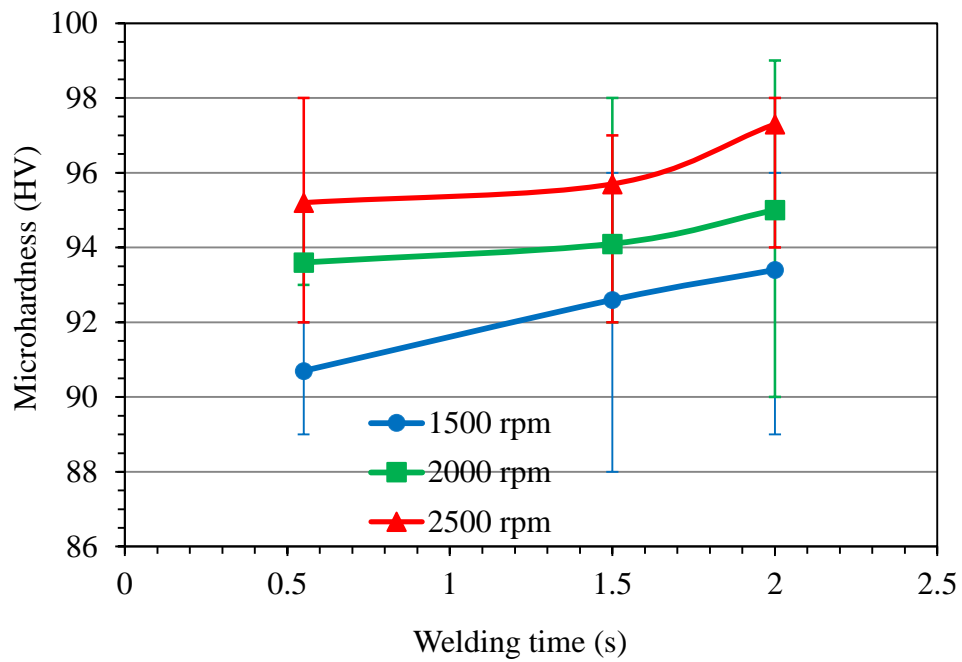


Figure 4-24: The average hardness of the weld zone centre of the upper sheet. The samples were naturally aged for 30 days.

In order to simulate the paint baking (PBC) heat treatment, immediately after welding samples were also artificially aged at 180 °C for 30 min. The effect of artificial ageing on the microhardness of the AA6111-T4 aluminium alloy RFSSWs, produced using a tool rotation rate of 1500 rpm, 1.0 s welding time and 1.0 mm plunge depth, is shown in Figure 4-25. For comparison, this figure also shows the hardness profiles of samples in the as-welded condition. As previously, the microhardness was measured across the mid thickness of the upper and lower sheets. As can be seen, the hardness levels in the stir zone and HAZ significantly increased after artificial ageing, compared with the hardness levels of the samples in the as-welded condition. However, the changes in hardness level were slightly different between the upper and lower sheets. These differences occurs for the same reasons mentioned above in the case of natural ageing, in terms of the differences between the peak weld temperature reached in the upper and lower sheets, which led to some difference in the response to the precipitation process. A higher peak temperature in the weld zone during the welding process would lead to greater dissolution of the strengthening precipitates ( $\alpha$  and  $\beta$  and other metastable intermediate precipitates) and increase the saturation of the solute atoms in the solid solution, which results in a higher response to artificial ageing. The increase in hardness seen is a result of the precipitation of GPZs and  $\beta''$  during paint bake ageing (Wang, et al., 2003; Raeisinha, et al., 2006; Chen, et al., 2012 a).

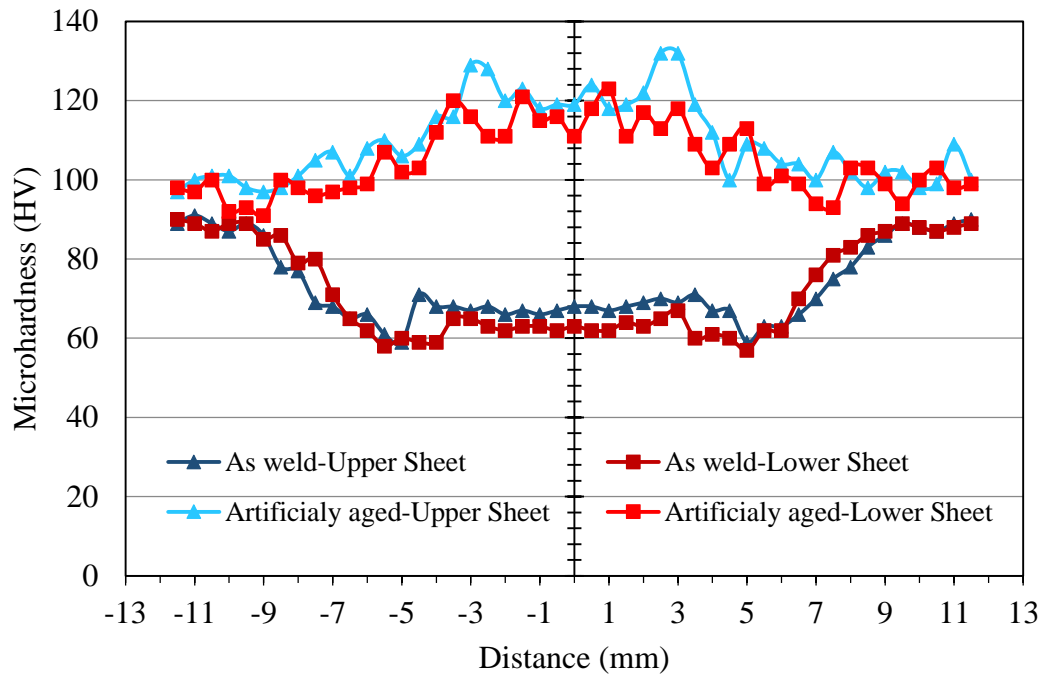


Figure 4-25: Hardness profiles of AA6111 RFSSWs produced with 1500 rpm tool rotation rate, 1.0 s welding time and 1.0 mm plunge depth, immediately after welding and after artificial ageing at 180 °C for 30 min.

#### 4.7 Effect of Welding Variables on Weld Strength

Tensile lap-shear tests were performed to evaluate the performance of the welded lap joints as a function of the welding parameters. Figure 4-26 shows an example of typical load-extension curves for the lap-shear tests of RFSSW joints produced with the AA6111 alloy, in the as-welded condition tested within one hour after welding. The welded joints were produced using different welding parameters. All curves show a ductile behaviour, where the samples deform plastically before the formation of a crack, at the peak load, which subsequently leads to a sudden decrease in the force. After this rapid decrease in load, the rate of decrease begins to decline during crack propagation through the sample until full separation, or final fracture, when the remaining connected area becomes unable to withstand further extension.

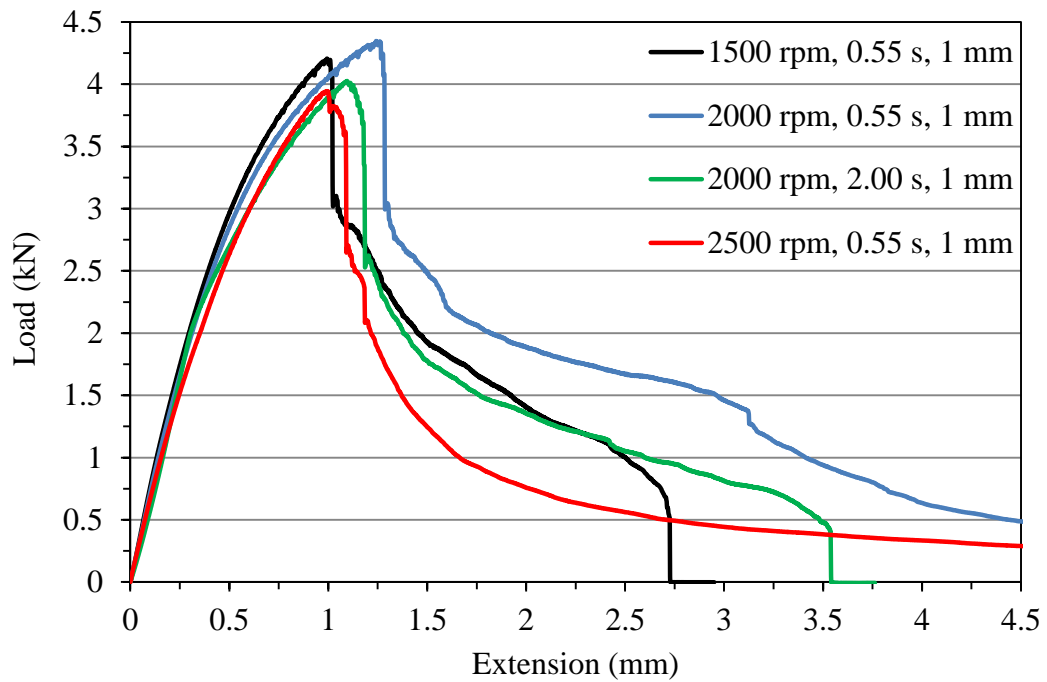


Figure 4-26: Example of load-extension curves for the tensile lap-shear test of RFSSW joints in the as-welded condition, tested within one hour after welding. The welds were produced using different welding parameters.

The effect of the welding parameters (total welding time, sleeve plunge depth, and tool rotation rate) on the average peak load of the similar AA6111 RFSSW joints in the as-welded condition is shown in Figure 4-27. Each point represents the average of the peak load measured for three samples for each welding condition. The welding time varied in the range of 0.3 to 2.0 s, and a range of 0.2 to 1.0 mm was used for the plunge depth, while three tool rotation rates were used: 1500, 2000, and 2500 rpm. Figure 4-27 a shows that the average peak load of the samples recorded from the lap-shear tests, welded using 1500 rpm as a tool rotation rate, increased when increasing both the welding time and plunge depth. But, as can be clearly seen, increasing the plunge depth had a greater effect on increasing joint strength than the welding time. For example, when using a welding time of 0.55 s, on increasing the sleeve plunge depth from 0.2 mm to 1.0 mm the average peak load increased by almost 100 % from 2.13 kN to 4.04 kN. On the other hand, an increase in welding time from 0.3 s to 2.0 s, for the same plunge depth of 0.2 mm, increased the average peak load from only 2.07 kN to 2.89 kN, equivalent to an increase of about 40 %. The main reason for the increase in joint strength with increasing plunge depth and welding time is the increase in the metallurgically bonded area. For example, by increasing the plunge depth from 0.2 to 1.0 mm, the metallurgical join line (spot diameter) in the cross-section is increased from about 6.4 to 9.4 mm (see Figure 4-3). In other words, the metallurgically bonded area

increases from 32.2 mm<sup>2</sup> to 69.4 mm<sup>2</sup>, which means an increase of about 115 % a similar percentage to the change in peak failure load. Moreover, the increase in welding time also increases the nugget diameter and results in improving the lap-shear strength (Shen, et al., 2015). These results are highly compatible with the findings of the other researchers such as Amancio-Filho et al. (2011 a), Parra et al. (2011), Rosendo et al. (2011), Yang & Yang (2013), and Shen et al. (2015) (see Figure 2-24). However, previous research has found that the welding time was the key factor that affected the quality of the welds, while the results of this project show that the most important welding parameter is the sleeve plunge depth. This conclusion is also compatible with the findings of Cao et al. (Cao, et al., 2016).

Comparison of Figures 4-27 a, b, and c shows the effect of tool rotation rate on the average peak failure load. These figures show that increasing tool rotation rate has a more complex effect on the average peak load. For instance, when using a plunge depth of 0.5 mm and a welding time of 0.55 s, increasing the tool rotation rate from 1500 rpm to 2000 rpm increased the average peak load from 2.24 kN to 2.76 kN. On the other hand, increasing the tool rotation rate with the use of deeper plunge depths (0.8 and 1.0 mm) led to a reduction in peak loads for all welding times (the only exception was very short welding times of 0.55 s with a plunge depth of 0.8 mm). For example, on increasing the tool rotation rate from 1500 rpm to 2500 rpm, the average peak load decreased from 4.04 kN to 3.94 kN when using 0.55 s as a welding time, and from 4.2 kN to 3.82 kN, when using a welding time of 2.0 s. The main reason for this decrease in weld strength is the increase in the peak temperature reached in the weld zone in addition to the expansion of the HAZ with increasing tool rotation rate and welding time, which is especially dramatic for high tool rotation rates of around 2500 rpm (see Figure 4-16). The corresponding increase in duration of the local thermal cycle exacerbated the deterioration of the local mechanical properties in the HAZ (see Figures 4-20 and 4-22) due to an increase in the level of over-ageing depending on the welding parameters and the distance from the edge of the SZ. The HAZ is important because, as will be shown below, it is the region in which the crack starts and propagates in the lap-shear test.

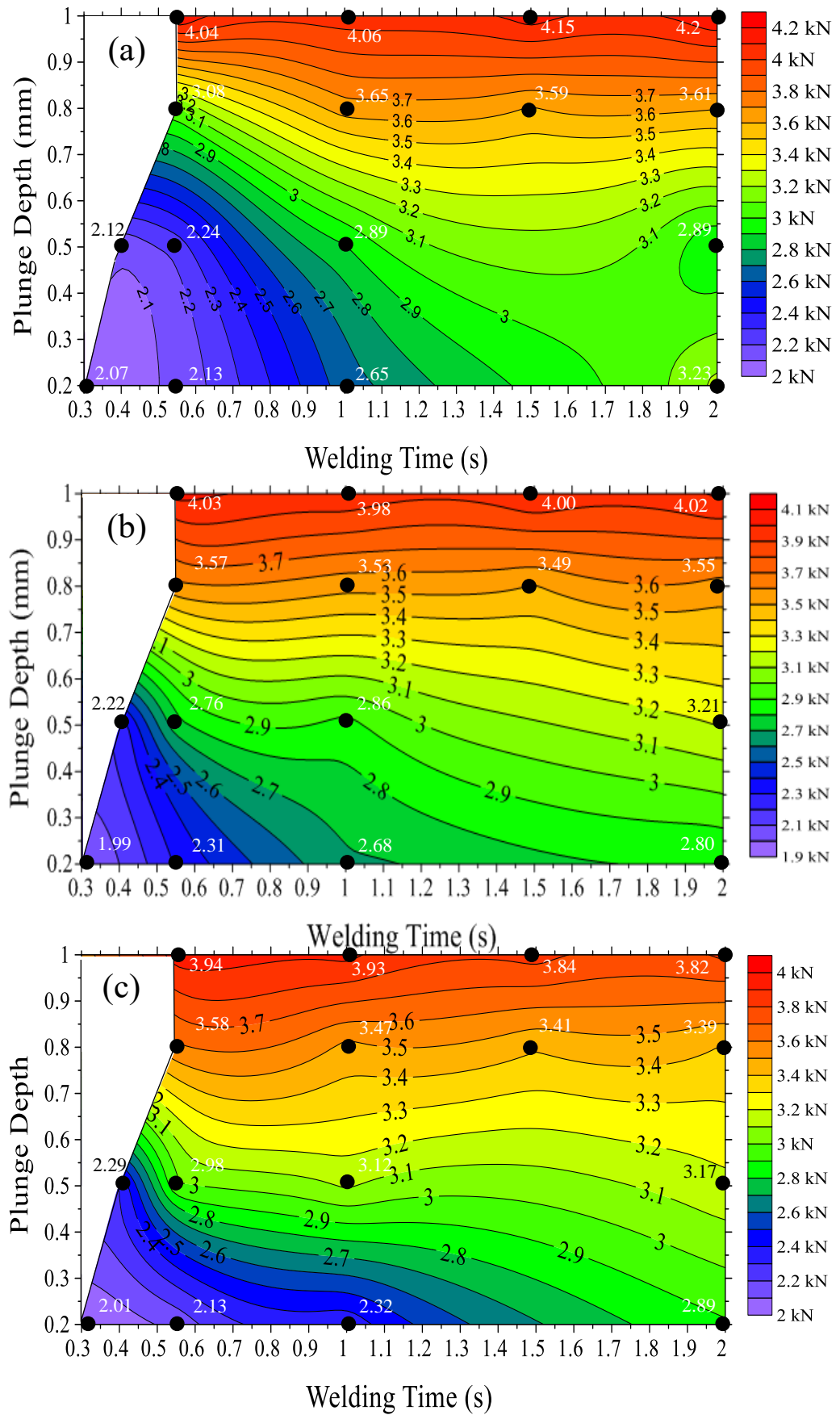


Figure 4-27: Effect of welding time and sleeve plunge depth on the joints' average lap-shear test peak load, in the as-welded condition, with different tool rotation rates: (a) 1500 rpm, (b) 2000 rpm and (c) 2500 rpm.

The effect of the welding conditions on the average fracture energy of the welded joints in the as-welded condition is shown in Figure 4-28. The total failure energy was calculated by integration of the load-extension curves (see Figure 4-26). An average of the fracture energy for three samples was again taken. Figure 4.28 shows that the failure energies have a similar trend to the effect of welding parameters on the average peak load (Figure 4-27) where the fracture energy of the joints increased with both longer welding times and greater plunge depths, especially when using low plunge depths (0.2 and 0.5 mm) or short welding times (0.3 to 1.0 s). For example, increasing the plunge depth from 0.2 mm to 1.0 mm, when using the same welding time of 0.55 s, resulted in an increase in average fracture energy from about 0.74 kN.mm to about 5.57 kN.mm. Meanwhile, an increase in welding time from 0.3 s to 2.0, while keeping the plunge depth constant at 0.2 mm, increased the average fracture energy from 0.6 kN.mm to 4.92 kN.mm. These results reflect the effect of increasing the area of the metallurgical bond on the values of the average fracture energy, where the bond area increases with increasing the sleeve plunge depth (see Figure 4-3) and/or welding time (Shen, et al., 2015).

Contrary to the above, the fracture energies showed some fluctuation with increasing the tool rotation rate from 1500 rpm (Figure 4-28 a) to 2000 rpm or 2500 rpm (Figure 4-28 b and c), especially when using deep plunge depths (0.8 and 1.0 mm). For example, the average fracture energy of the welds produced using a 0.8 mm plunge depth increased with increasing the tool rotation rate from 1500 to 2500 rpm, and also with increasing welding time. However, when using tool rotation rates of 2000 rpm the values of the average fracture energy showed an inconsistent fluctuation with increasing welding time, compared with welds produced using other tool rotation rates with the same plunge depth and welding time. Overall, it is apparent that high fracture energies result from the strongest welds, which show a very long decline curve after reaching peak load, while the lower fracture energy welds show a more sudden failure (Bakavos, et al., 2011) (see Figure 4-26).



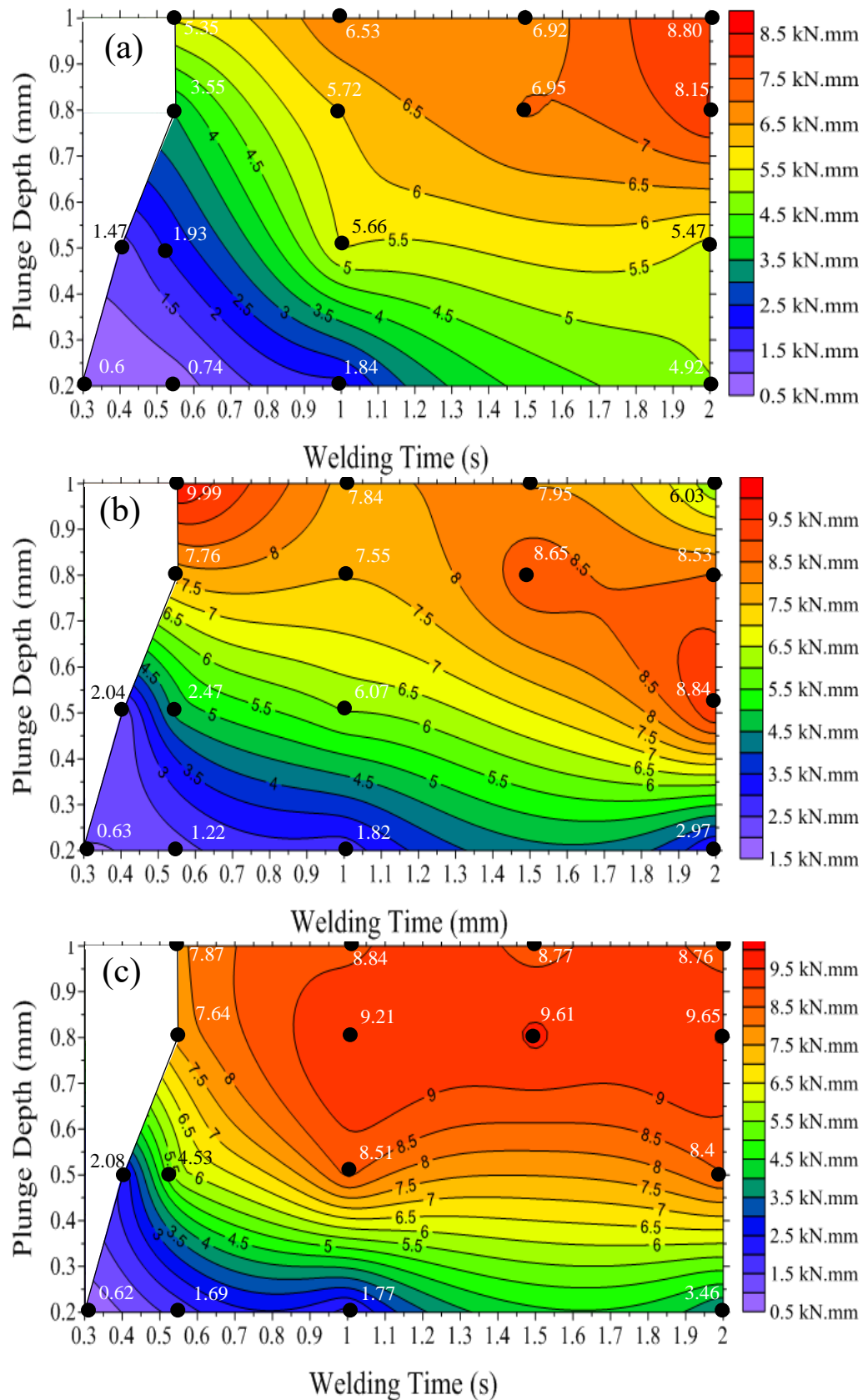


Figure 4-28: Effect of welding time and sleeve plunge depth on the average fracture energy of the joints in the as-welded condition, with different tool rotation rates: (a) 1500 rpm, (b) 2000 rpm and (c) 2500 rpm.

## 4.8 Effect of Natural and Artificial Ageing on Weld Strength

To study the effect of heat treatment on the performance of the RFSSW joints, lap-shear samples were produced using different welding parameters and then subjected to two types of heat treatments -natural ageing and artificial ageing- using a simulated paint bake cycle. For the natural ageing, the samples were kept at room temperature for 30 days. The paint bake cycle (PBC), as it is frequently referred to in the automotive industry, is an artificial ageing treatment which is used to increase the final strength of the alloy. To simulate this cycle, the samples were heat treated directly after welding at 180 °C for 30 min.

Figure 4-29 shows examples of typical load-extension curves for the tensile lap-shear test of RFSSW joints of an AA6111 alloy in as-welded, naturally aged, and artificially aged conditions. In general, the strength level of the welded samples shows an increasing improvement with natural and artificial ageing compared to the as-welded condition. The artificially aged samples showed the highest average peak load of 6.89 kN (for a sample welded using a 2500 rpm tool rotation rate, 1.5 s welding time, and 1.0 mm plunge depth) compared to 5.15 kN for the naturally aged sample, and 3.84 kN when tested immediately after welding.

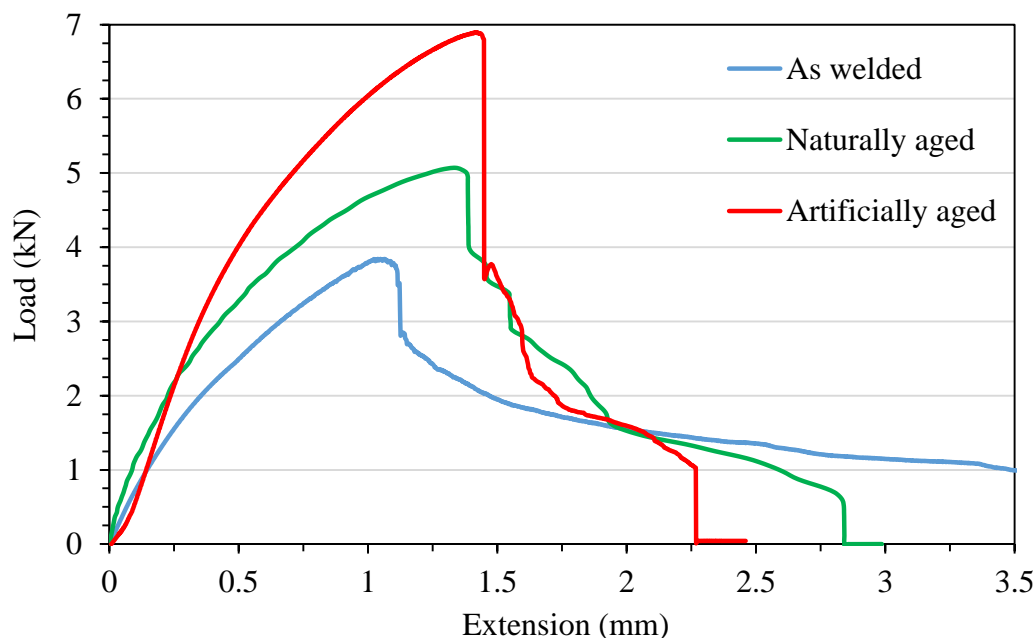


Figure 4-29: Example of load-extension curves for the tensile-shear test from RFSSW joints in the as-welded, naturally aged, and artificially aged conditions. The welding parameters were a 2500 rpm tool rotation rate, 1.0 mm plunge depth, and a 1.5 s welding time.

The effect of the welding conditions on the peak load of the welded joints in as-welded, naturally aged and artificially aged conditions is shown in Figure 4-30. The welding time and tool rotation rate were varied in a range of 0.55 to 2.0 s and 1500 to 2500 rpm, respectively, while a constant sleeve plunge depth of 1.0 mm was used. The peak load of the samples in the as-welded condition was only slightly affected by the welding time, and slightly increased with increasing welding time when using a lower tool rotation rate (1500 rpm) but, conversely, decreased with increasing welding time with a higher tool rotation rate (2500 rpm). This difference occurred due to the effects of two competing factors. The first factor is the material flow, which is important in refilling the annular cavity left by sleeve retraction, and if the material does not have enough plasticity then incomplete refilling will lead to weld defects that reduce the joint strength (see Figure 4-8 a, c, g, and h). To increase the material plasticity, the temperature to which it is heated during the weld cycle can be increased, by increasing the welding time, which is especially important for welds produced using lower tool rotation rates (around 1500 rpm) (see Figure 4-16). On the other hand, welds prepared with higher tool rotation rates (around 2500 rpm) did not develop refill defects (see Figures 4-8 e and f) because the temperature was already high enough for the material to flow more easily (see Figure 4-16).

The second factor which affects the peak load of the samples in aged conditions is the local changes in material properties at the periphery of welds and, in particular, the HAZ formed as a result of the thermal cycle of the weld. The use of a high rotation rate (2500 rpm) resulted in an increase in peak temperature in all of the weld regions, which was further increased by increasing the welding time (see Figure 4-16). This greater heat input led to further deterioration of the local yield strength in the HAZ (see Figures 4-20 and 4-22) (Wang, et al., 2003; Bakavos, et al., 2011).

Figure 4-30 shows the clear impact of the welding time and the tool rotation rate on the joint strength of the naturally and artificially aged samples, where the peak load for these samples in these conditions increased with welding time from 0.55 to 1.5 s, for both conditions. For example, the average peak load of the naturally aged samples produced using 1500 rpm increased from 4.69 to 5.14 kN when the welding time was increased from 0.55 to 1.5 s. This effect of welding time on the strength of the joints became more significant when using post weld artificial ageing. For instance, in the

welds produced using a tool rotation rate of 2500 rpm, the weld strength increased from 5.61 to 6.43 kN by increasing the welding time from 0.55 to 1.5 s.

The tool rotation rate exhibited an effect on the strength of the naturally and artificially aged welds similar to that produced by different welding time. In general, the weld strength after heat treatment increased on increasing the tool rotation rate (except when using a 2000 rpm rotation rate and a 0.55 welding time, and artificial ageing). For example, the weld strength increased from 5.89 to 6.43 kN by increasing the tool rotation rate from 1500 to 2500 rpm and keeping the welding time constant at a level of 1.5 s. However, this behaviour is completely different to that shown for the samples in the as-welded condition, where the weld strength decreased with increasing the tool rotation rate, especially when using long welding times.

This increase in joint strength seen after natural or artificial ageing occurs because the local mechanical properties in the HAZ (the weakest region in the joint) and other regions are greatly improved (see Figures 4-23 and 4-25). This improvement comes as a result of the re-precipitation of GPZs and clustering on natural ageing, or  $\beta''$  on artificial ageing (Chen, et al., 2012 a), which were dissolved during the weld cycle. The increase in peak load caused by increasing the welding time and tool rotation rate occurs because an increase in any of these welding parameters leads to an increase in the welds' peak temperatures (see Figure 4-16). This temperature increase in turn results in dissolution of more strengthening precipitates and increases the saturation of the solute atoms in solid solution, which results in a higher tendency towards post-weld natural or artificial ageing (Wang, et al., 2003; Raeisinia, et al., 2006; Chen, et al., 2012 a). Figure 4-30 shows a clear difference in the average peak loads between the samples in the naturally and artificially aged conditions; this difference is because the higher temperature reached during artificial ageing (180 °C) translates to an increase in the diffusivity of the solute atoms during artificial ageing and a subsequent acceleration of the ageing kinetics.

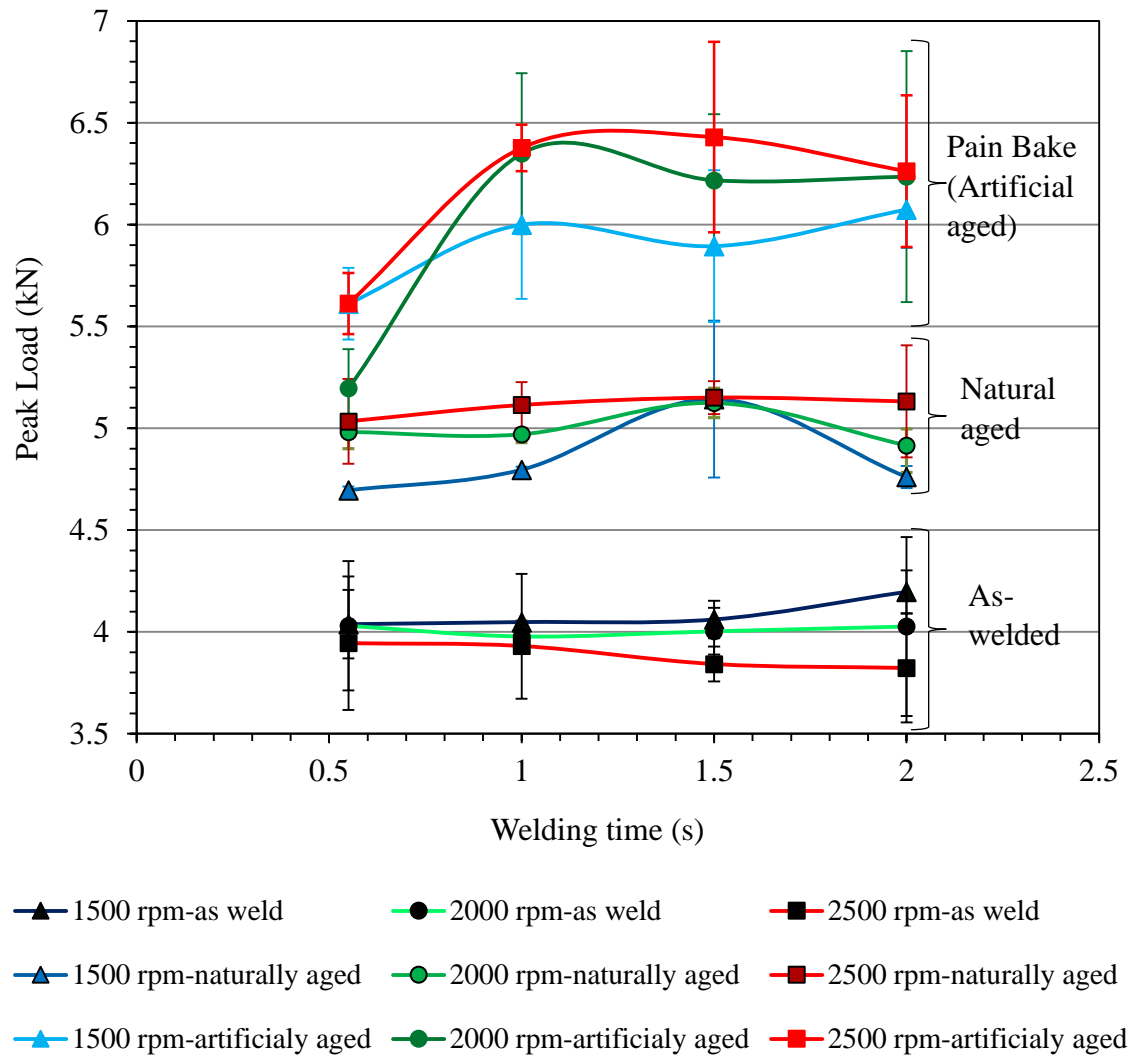


Figure 4-30: Effect of welding time and rotation rate on average peak load in the lap-shear tests of RFSSW joints in the as-welded, naturally aged, and artificially aged conditions. Welds were produced using 1.0 mm sleeve plunge depth.

Figure 4-31 shows the effect of welding time and tool rotation rate on the average fracture energy of the welded joints in the as-welded, naturally aged and artificially aged conditions. It can be seen that the average failure energies of the joints produced using the lower rotation rate (1500 rpm) increased with increasing welding time. However, when using a higher rotation rate (2500 rpm) the naturally and artificially aged samples showed some fluctuation in the average fracture energy with increasing welding time. In addition, the average failure energies of the welded joints in the naturally aged condition were on the whole higher than the energies produced under the other conditions. However, in Figure 4-31 it is important to note that there is less differentiation between the levels of the average fracture energy for the samples subjected to different treatments than that seen in Figure 4-30 for the average peak

loads, where the levels were clearly divided into three distinct groups (the as-welded, naturally, and artificially aged conditions). A possible reason for this phenomenon is that in the as-welded samples the failure propagated through soft material leading to a very long extension after the peak load (see Figures 4-26 and 4-29). This resulted in a larger area under the load-extension curve and a higher fracture energy. On the other hand, the naturally and artificially aged samples exhibited much shorter extensions after the peak load, but had higher peak loads due to the increase in strength seen for the softest weld region (HAZ) (see Figure 4-29). This behaviour thus also resulted in a similar large area under the load-extension curve, as well as high fracture energy.

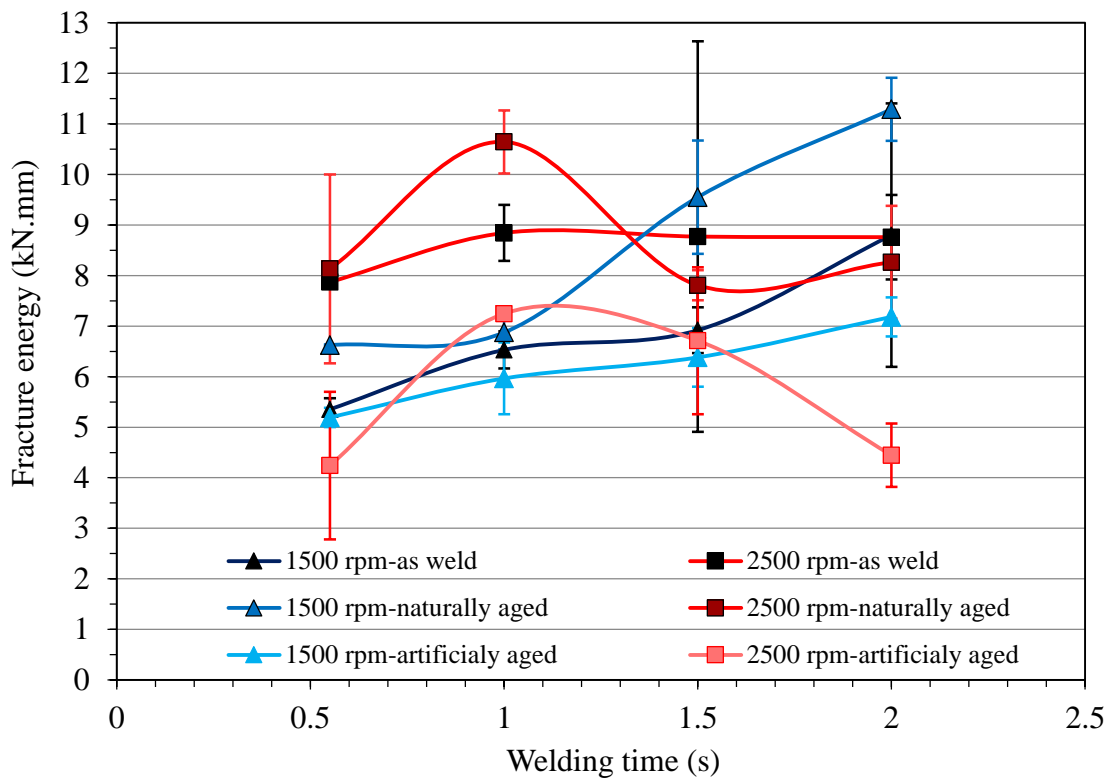


Figure 4-31: Effect of welding time and rotation rate on the average fracture energy of the RFSSW joints in the as-welded, naturally, and artificially aged conditions.

## **4.9 Weld Fracture Surfaces and Cross-Sections in the As-Welded, Naturally Aged, and Artificially Aged Conditions**

A range of fracture modes have been observed in tensile lap-shear tests of RFSSW joints (Rosendo, et al., 2015; Li, et al., 2016). However, the tensile lap-shear test itself is sensitive to the thickness of the welded sheets. The tensile shear test of spot welded thin sheets normally results in the joint being bent out of the plane. Therefore, in addition to the pure shear, the joint is subjected to a normal tensile component to the joint, or a 'peel' force, which is at its highest at the nugget edge (Bakavos, et al., 2011).

Generally, the fracture behaviours reported for RFSSW joints can be classified into three main modes (Rosendo, et al., 2015; Li, et al., 2016):

- 1- Shear fracture mode, where the failure follows the line of the joint between the two welded sheets in the same plane of the sheet.
- 2- Shear-plug fracture mode, sometimes referred to as a mixed cleavage failure (Bakavos, et al., 2011). In this mode, the failure starts with cleavage of the interface between the two sheets at the edge of the weld zone, and then due to the high strength of the join line, the crack turns upwards and propagates through the interface between the SZ and TMAZ.
- 3- Nugget pull out fracture mode. In this mode, the join line does not fail and either the upper or lower sheet tears around the edge of the weld zone. The crack nucleates at the interface between the two sheets and propagates through the weakest region (e.g. the TMAZ/HAZ interface), leading to separation of the two sheets. The weld nugget then remains attached to one of the two sheets.

Examples of typical fracture behaviours for samples welded using different welding parameters, after lap-shear testing in the as-welded condition are shown in Figure 4-32. The failed samples produced with the same welding parameters were found to have a similar appearance in repeated tests. All of the fracture modes mentioned above were noted in the samples after the tensile-shear tests, depending on the sleeve plunge depth. As can be seen from Figure 4-32 a, when using a sleeve plunge depth of 0.2 mm, the fracture showed an interfacial shear mode because the metallurgically bonded area (the size of the join line) was not large enough to withstand the interfacial crack propagation (see Figures 4-3 and 4-9). When sleeve plunge depth was increased to 0.5 mm the

fracture mode changed to the transitional mode, or partial- nugget pull-out (Figure 4-32 b), due to the increase in the metallurgically bonded area (see Figures 4-3 and 4-9). With an additional increase in sleeve plunge depth to 0.8 mm (Figure 4-32 c), the metallurgically bonded area became much larger and stronger than the through-thickness region around the SZ, especially at the TMAZ/HAZ interface where the weakest material is located. Therefore, after the nucleation of a crack, it tended to grow through the thickness of the upper sheet along the TMAZ/HAZ interface and propagate around the weld nugget, resulting in a fully nugget pull-out fracture mode (Rosendo, et al., 2015; Li, et al., 2016).

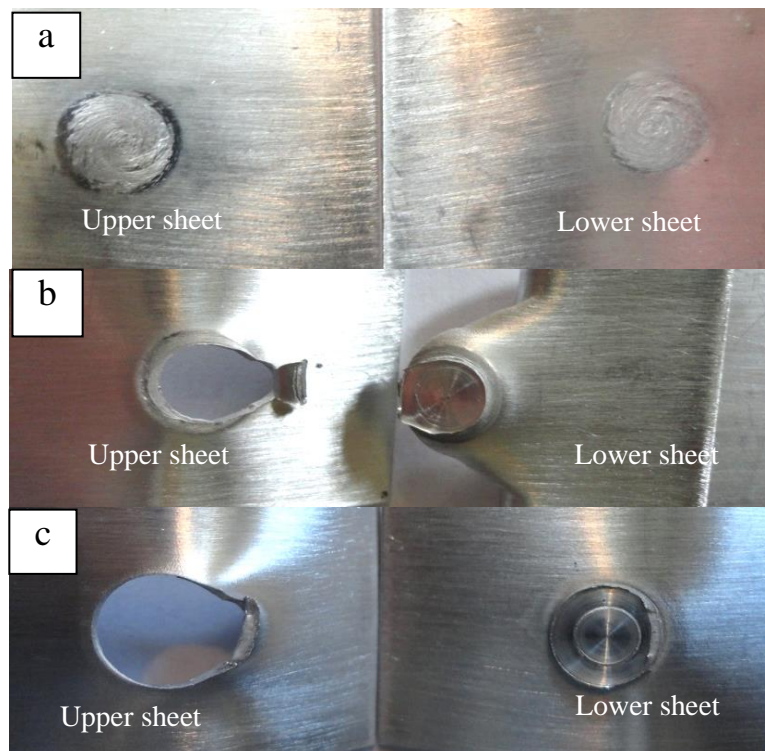


Figure 4-32: Examples of joint failure behaviours, showing both halves of the fractured lap-shear test samples welded with a 2000 rpm rotation rate and different plunge depths of (a) 0.2 mm (shear mode), (b) 0.5 mm (mixed mode), and (c) 0.8 mm (pull out mode).

A plug pull-out fracture mode was noted under tensile-shear loading in all cases when using a 1.0 mm sleeve plunge depth. In most cases, the failure crack propagated through the thickness of the lower sheet, as shown in Figure 4.33, because the hook that formed at the interface between the two sheets was mainly bent downwards (Cao, et al., 2016) (see Figure 4-10). In this fracture mode, the hook feature has a very important influence since the crack generally nucleates at the tip of the hook or at the weld defect (Rosendo, et al., 2015) and then propagates in the same direction as the hook to the sheet surface.



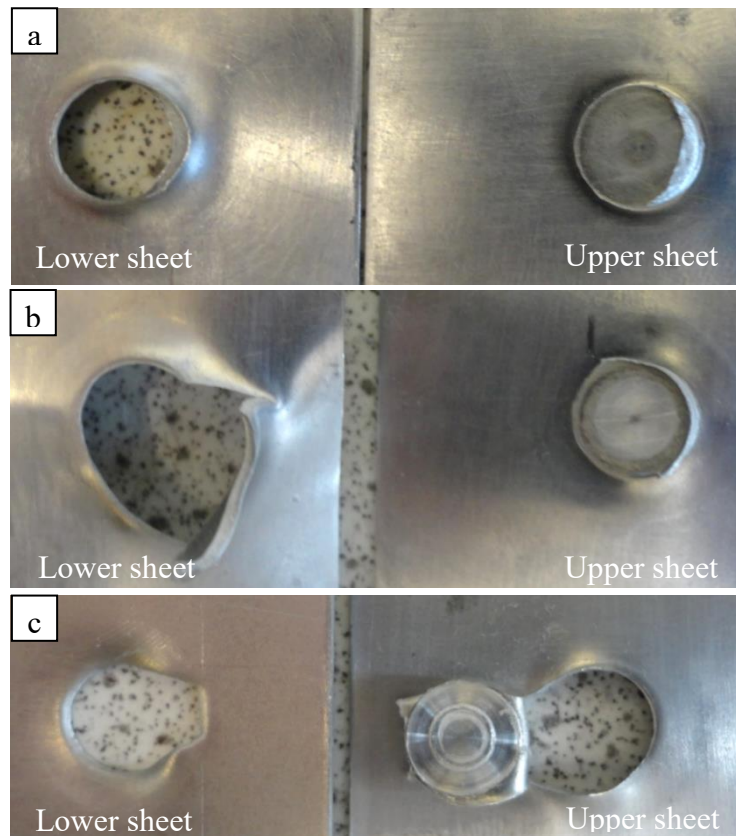


Figure 4-33: Examples of the failure behaviour showing both halves of the fractured lap-shear test samples welded with different welding parameters and tested in the as-welded condition: (a) 0.55 s at 1500 rpm, (b) 2.0 s at 1500 rpm, and (c) 1.5 s at 2000 rpm.

Figure 4-34 shows examples of cross-sections through the joint centre lines of fractured samples in the as-welded, naturally aged, and artificially aged conditions, for welds produced using a 1.0 mm sleeve plunge depth. The RFSSW joints continued to show a plug pull-out fracture mode after natural and artificial ageing, but some differences could be seen compared to the as-welded samples. For example, in the as-welded condition, the lower sheet of the sample showed greater plastic deformation before fracture. This phenomenon can be observed on the fractured side of the lower sheet, where local ‘necking’ of the lower sheet at the failure point can be observed. This is likely to have occurred because the material had the lowest hardness after welding (see Figure 4-20) and, as a result, higher ductility. In comparison, the naturally and artificially aged samples exhibited more of a shear failure, since this region (TMAZ and HAZ) partially or completely recovers its strength (see Figure 4-23 and 4-25). There was thus a greater tendency for failure through the lower sheet where the crack path changed to  $\sim 45^\circ$  to the sheet surface (Li, et al., 2016).

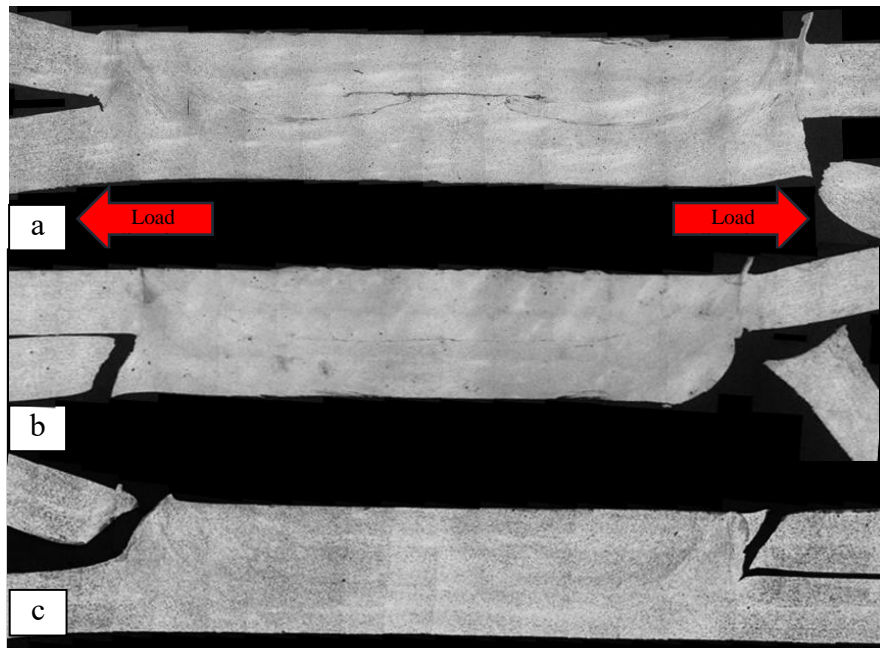


Figure 4-34: Macroscopic cross-sections through the weld centre lines for fractured samples: (a) in the as-welded condition (2.0 s, 2000 rpm, and 1.0 mm); (b) naturally aged for 30 days (0.55 s, 2000 rpm, and 1.0 mm); and (c) artificially aged at 180 °C for 30 min. (2.0 s, 2000 rpm, 1.0 mm).

#### 4.10 Summary and Conclusions

In this chapter, the refill friction stir spot welding (RFSSW) parameters (sleeve plunge depth, tool rotation rate, and welding time) were assessed in terms of their effect on the material flow, temperature distribution and microstructure, and their subsequent effect on the mechanical properties of similar AA6111-T4 automotive aluminium alloy joints.

To further understand the process and the effect of process parameters on joint formation, several material flow experiments were implemented by using two different types of markers and monitoring methods; dissimilar aluminium alloys and X-ray tomography. The results showed that the size of the metallurgically bonded area of the joint increased with increasing plunge depth up to 1.0 mm, and the material mixing (layering) mostly occurred near the tip of the sleeve, where the highest plastic deformation occurs near the internal edge of the sleeve. At this point, much thinner marker layers were observed compared to those found in other SZ regions. Moreover, the mixing of the upper part of the joint material was found to stop once it entered the sleeve cavity during the plunging stage.

The formation of a hooking defect was found to take place during the sleeve plunging stage, increasing in severity with increasing plunge depth due to greater displacement of

material from under the sleeve. On the other hand, other weld defects, such as incomplete refill and a lack of mixing, have been shown to result from insufficient plasticity of the material during the refilling stage. Moreover, an unbonded interface weld defect was also observed at the centre of the joint and was found to be caused by pin retraction during the early stage of the welding process.

The effect of welding parameters on heat generation was studied, due to the effect of heat input and the peak weld temperatures on the microstructure and local mechanical properties of the material being joined. The measured temperatures showed a rapid increase during the sleeve plunging stage of the welding cycle, with a rate of about  $1450^{\circ}\text{C/s}$ . This very high rate of increase in temperature resulted from the use of a very high plunge rate (4 mm/s), which led to a very high strain rate. However, the rate of increase in temperature decreased to about  $73^{\circ}\text{C/s}$  during the dwell stage. This decline is likely to be because, during this stage, most of the plastic deformation occurs near the bottom of the sleeve and the high local temperature causes material softening in this region, which reduces the amount of heat generated. The peak temperature was increased by increasing the tool rotation rate and/or welding time. For all welds, the highest peak temperatures were measured at a distance of 3 mm from the weld centre, under the sleeve position. The highest peak temperature measured at this location was  $580^{\circ}\text{C}$ , when the highest rotation rate of 2500 rpm and the longest welding time of 2.0 s were used.

RFSSW for the AA6111 aluminium alloy revealed three distinct weld microstructure zones: the stir zone (SZ), which was characterised by very refined equiaxed grains; the thermo-mechanically affected zone (TMAZ), observed from the distortion of the grains compared with the base material; and the heat affected zone (HAZ) and the base metal (BM), which had much bigger grains compared to those in the SZ and TMAZ. The SEM investigation revealed that the HAZ contained a very low density of very small widely spaced precipitates in the as-welded condition; these spheroidised precipitates are probably  $\beta$  phase. Conversely, in the artificially aged sample, the HAZ showed a greater volume fraction of coarser, but still very fine, precipitates. However, for short welding times, virtually no HAZ was observed.

In general, the hardness profile across the welds in the as-welded condition showed a typical W-shape, similar to that usually seen in friction stir spot welds in the same alloy and other heat-treatable alloys. The HAZ reached a minimum value of about 60 HV,

compared to an average hardness of about 89 HV for the base material. The HAZ width also showed a clear increase with increasing welding time and tool rotation rate. The hardness level in the SZ and HAZ increased after natural and artificial ageing in comparison to the hardness levels in the as-welded condition, but samples that were welded for longer still exhibited a lower hardness level in the HAZ after natural ageing. Overall, the HAZ damage was found to be minimal because of the very rapid thermal cycle, which greatly limited the effects of over-ageing.

By optimising the welding parameters, sound joint strengths could be achieved while using very short welding times of 0.55 s. However, a wide window of suitable process parameters was found that could result in joints with a nugget pull-out failure mode, especially when using a sleeve plunge depth of 0.8 mm or more. All load-extension curves showed ductile behaviour under the tensile lap-shear test. It was found that the mechanical properties of the joints in the as-welded condition were optimised when welding parameters of 1500 rpm and a 1.0 mm plunge depth were used with a range of welding times from 0.55 to 2.0 s. This is because the welds produced using the lower tool rotation rate (1500 rpm) had the narrowest HAZ (the weakest region in the joint). Therefore, by reducing the size of the HAZ, the strength of the joints was increased. By adding the effect of either natural or artificial ageing, the joint strengths were further improved, but the welding parameters that resulted in the optimum mechanical properties of the joint changed to a 2500 rpm tool rotation rate, a 1.5 s welding time and a 1.0 mm plunge depth, resulting in peak loads of 5.15 and 6.43 kN in the naturally aged and artificially aged conditions, respectively. This increase in joint strength seen after natural or artificial ageing occurs because the local mechanical properties in the HAZ and other regions are greatly improved. This improvement comes as a result of the re-precipitation of GPZs and clustering on natural ageing, or  $\beta''$  on artificial ageing, which were dissolved during the weld cycle. Under optimised conditions, the joints resulting from the RFSSW process for the AA6111 aluminium alloy were found to have higher strengths than those obtained using other welding processes, such as FSSW with a peak load of 3-3.5 kN (Bakavos & Prangnell, 2009), USW with a peak load of 3.4 kN in the optimum condition (Panteli, et al., 2012), or RSW with a peak load of about 1.7-3 kN (Briskham, et al., 2006; Han, et al., 2010).

The high performance of the joints found under optimised conditions will be discussed further in chapter 6, where modelled results of the lap-shear test are presented.

## **Chapter 5: Refill Friction Stir Welding of Mg-Al Dissimilar and Mg-Mg Similar Welding (Results and Discussion)**

---

### **5.1 Introduction**

This chapter presents the results of the investigation into the optimisation of dissimilar magnesium to aluminium joints produced with short welding times using refill friction stir spot welding (RFSSW). The effects of a range of welding parameters including the sleeve plunge depth, tool rotation rate, and welding time (the ranges of which are summarised in Table 3-2) were assessed for both conventional and modified RFSSW processes, by conducting lap tensile-shear tests on the joints. For the modified RFSSW, process a final shallow pin plunge stage was added as an additional step to the conventional process, in order to eliminate weld defects resulting after the standard welding cycle. The main focus of this research was to optimise the RFSSW process for the purpose of obtaining sound welds when rapid welding thin sheets (about 1.0 mm thickness) of the AA6111-T4 aluminium alloy and AZ31-H24 magnesium alloy (more details of which, including the chemical composition can be seen in section 3.2). Rapid welding (with a welding time of less than one second) was targeted as it is important for industrial applications, but also because it can reduce the intermetallic reaction in dissimilar metal welds.

To obtain a more detailed understanding of the performance of the welded joints and the possible reasons for their mechanical behaviour, several experiments were conducted, to ascertain the effect of the welding parameters on the thermal profile and thermal history at the joint interface, and the consequent influence of the thermal history on the microstructure and the hardness profiles across the welded joints. The effect of the welding variables on the strength of the weld and fracture mode was also assessed. The chapter also discusses the effect of the process parameters on the strength of Mg to Mg similar welds produced for the purpose of a baseline comparison with Mg to Al dissimilar welds.

## 5.2 Welding Optimisation and RFSSW Modification

RFSSW of dissimilar aluminium to magnesium sheets presents different challenges to those seen when welding similar combinations of an AA6111 aluminium alloy. In initial trials, it was found that the welding parameter window obtained from the welding experiments explained in section 4.2 could not be used for dissimilar welding of the AA6111 aluminium alloy to AZ31 magnesium. This result was found to be because the nugget was observed to always be pulled-out of its location as it stuck to the tool, leaving the weld zone with a large hole, as can be seen in Figure 5-1. To solve this problem, initially a thicker 2.0 mm gauge aluminium upper sheet with a 1.0 mm Mg lower sheet was used. In spite of the ability to obtain welds without pulling the nugget out and with an average peak load of around 2.0 kN, with these welds, the average fracture energy was still low, in the region of 0.8 kN.mm. This was attributed to an extremely thick IMC layer which formed at the weld interface and extended to the upper edges of the weld, as seen in Figure 5-2. This layer was mainly produced as a result of the very long welding time required to obtain a good bond (2.5 s, in addition to a 1.0 s heating time prior to plunging the sleeve), which led to an increase in the heat input and encouraged the IMC reaction. This very thick IMC layer (Figure 5-2 b) was the main reason for the poor mechanical properties, because it acted as a preferred crack path, as can be seen in Figure 5-2 c.

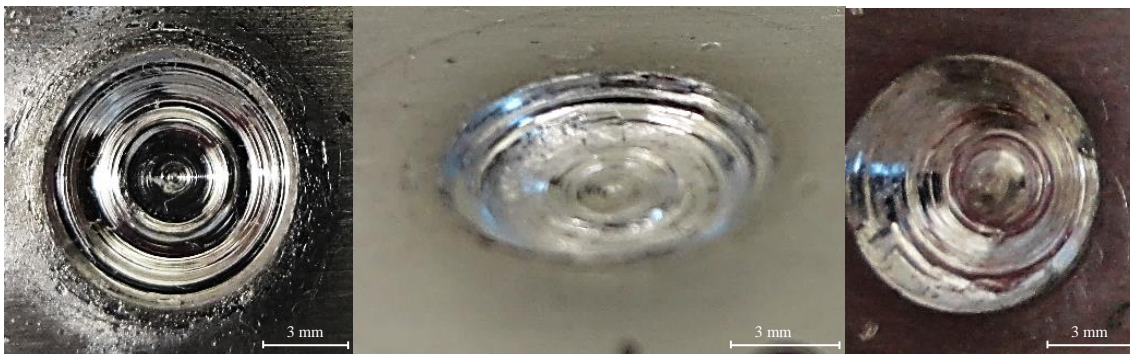


Figure 5-1: Examples of nugget pull-out holes left after RFSSW of 1.0 mm AA6111 aluminium alloy to AZ31 magnesium alloy.



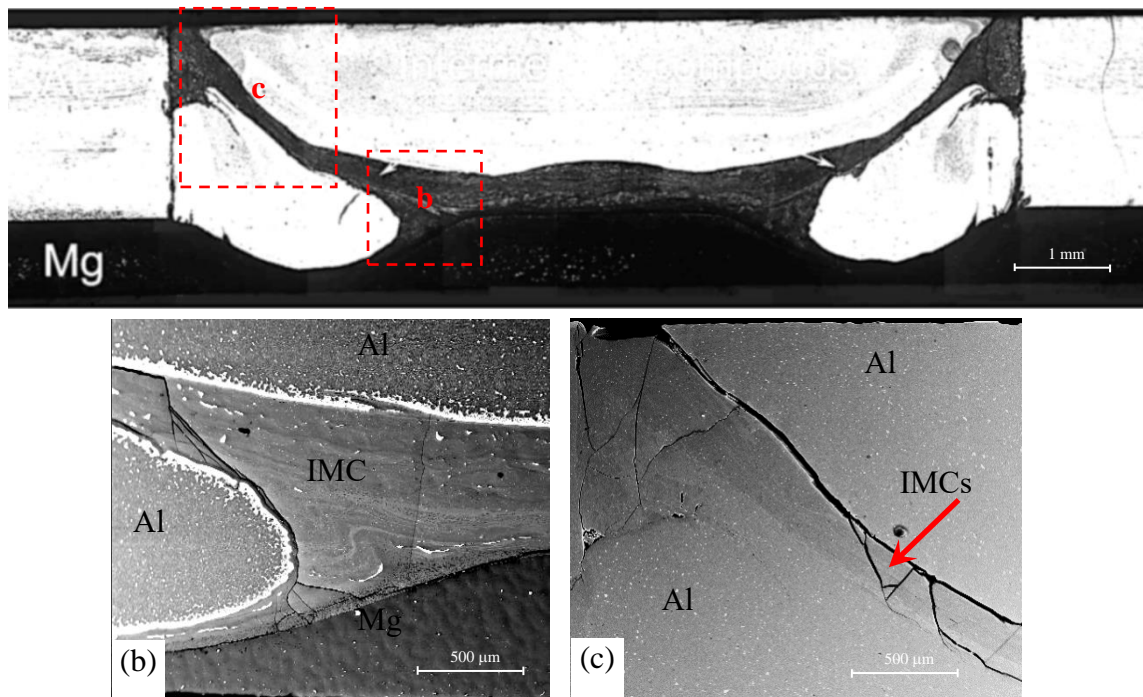


Figure 5-2: Macrostructure of a cross-section of an early RFSSW dissimilar Al to Mg joint produced with a 2.0 mm thick Al upper sheet, using a 2500 rpm tool rotation rate and 2.5 s welding time; (b) the thick IMC layer formed at the joint interface; and (c) example of cracks propagated through the IMC layer.

After attempting several different approaches in order to obtain higher quality joints, it was found that changing the welding configuration by welding magnesium to aluminium with the magnesium on top (i.e. so that the tool plunged into the magnesium sheet) led to a major improvement. As a result, a wide range of welding parameters could then be used to obtain joints with acceptable mechanical properties (see Table 5-1). However, when sectioning the welded samples for metallographic investigation, unacceptably large voids were detected at the edges of the SZ (as shown in Figure 5-6 a). These voids represent a preferred location for crack propagation, which would lead to a deterioration in the mechanical properties of the joints. To solve this problem, the understanding obtained from the material flow investigations in chapter 4 (see section 4-3) was used. A solution was explored based on adding an additional step to the weld cycle after finishing the standard refill step, when the sleeve and pin reached the zero position. This step included a shallow plunge of the pin into the SZ to force the material to fill the voids retained after the refill step, as seen in Figure 3-6. This step required a very short time (about 0.15 s or less) and it did not affect the total time of the welding cycle because it could be compensated for by subtracting the same time from the previous steps. As a result of this modification to the RFSSW process, joints with improved mechanical properties and welds that were almost free of defects could be

obtained. The mechanical properties and weld defects seen for samples welded using both the conventional method and this new modified RFSSW approach will be discussed in this chapter.

Table 5-5-1: The range of welding parameters used in the RFSSW and modified RFSSW process for welding AZ31 to AA6111 dissimilar joints.

Welding Parameter							
Tool Rotation Rate (rpm)	Plunge Depth (mm)		Welding Time (s)				
	Sleeve	Pin*	Sleeve Plunge	Dwell	Retraction & Pin Plunge	2 <sup>nd</sup> Retraction*	Total
1300- 2800	0.8- 1.6	0.2	0.25-0.5	0.05-1.35	0.25-0.45	0.15	0.7- 2.0

\* Only for modified RFSSW

### 5.3 Effect of Welding Variables on the Weld Thermal Field and Thermal History of Mg-Al Dissimilar Joints

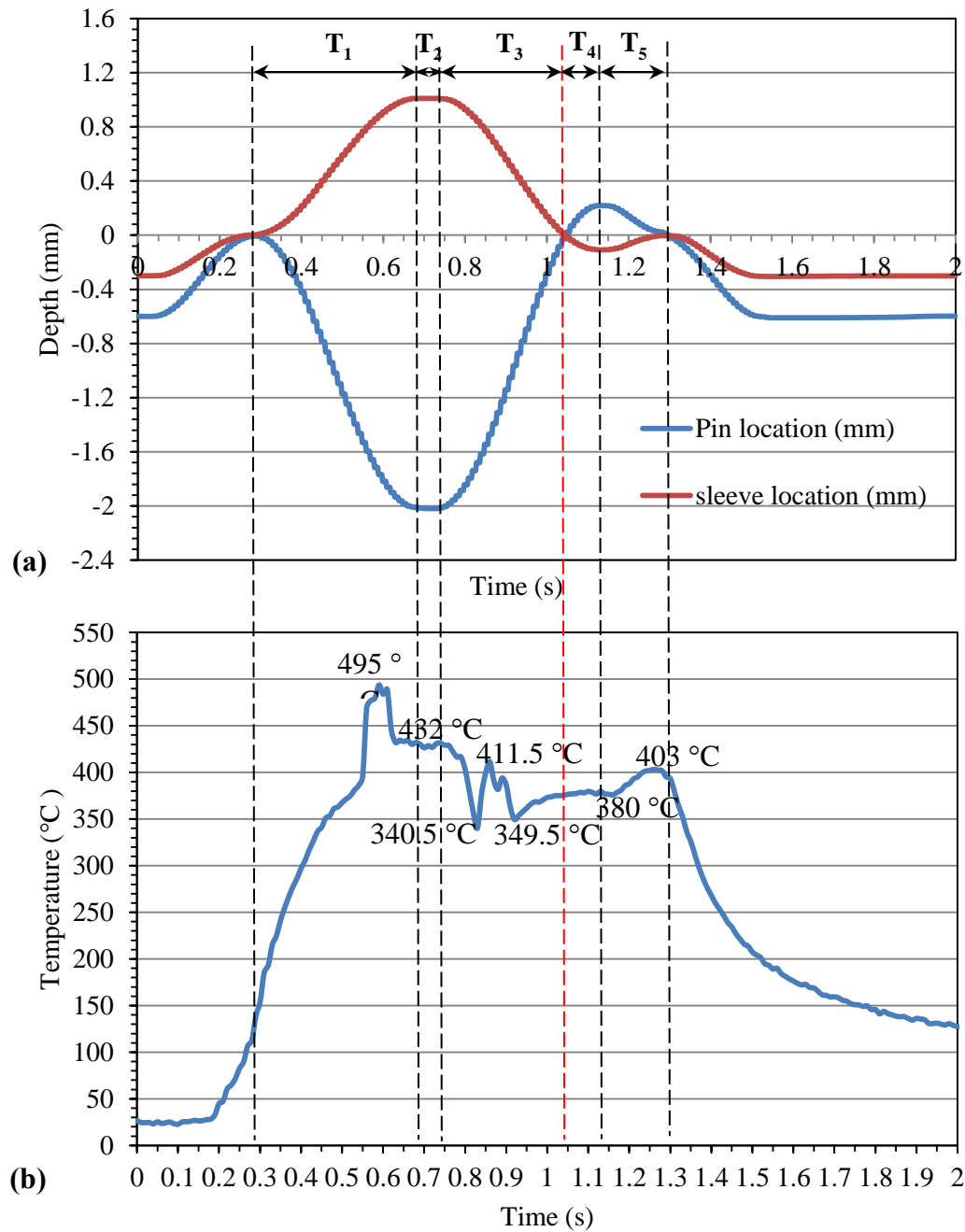
To measure the temperatures reached at the weld interface during a welding cycle for welds produced using different parameters, a thermocouple was located exactly under the sleeve and between the two welded sheets with a distance of 3.0 mm from the weld centre, as shown in Figure 3-8. This location was selected based on the results obtained from the temperature measurements of AA6111 similar welds shown in Figure 4-16, because the highest peak temperatures were measured at this distance for all welding parameters.

Figure 5-3 shows a typical temperature history curve for the modified RFSSW process. The weld was produced using a 2800 rpm tool rotation rate, 1.0 s welding time, and 1.0 mm plunge depth. This figure also shows the vertical positions of the sleeve and pin during the welding cycle. During the first sleeve plunging stage (step b in Figure 3-6), marked by T<sub>1</sub> in Figure 5-3 a, the temperature increased rapidly at an average rate of about 1300 °C/s to reach a peak temperature of 495 °C, as a result of the high rate of plastic shear induced by the rotating tool and the high plunging rate (2.5 mm/s), in addition to the friction between the sleeve and the magnesium alloy. However, the temperature then suddenly fell to 432 °C. This rapid decrease in temperature occurred when eutectic melting took place between the  $\alpha$ -Mg solid solution and the Mg<sub>17</sub>Al<sub>12</sub>



phase at a temperature of 437 °C (Gerlich, et al., 2005). As a result of local melting of the material at the interface between the two sheets, on cooling a eutectic structure was found to form; this occurs because the eutectic reaction temperature represents the lowest melting point in the Al–Mg binary system (Okamoto, 1998), as shown in Figures 2-58 and 5-10. The formation of a liquid phase greatly decreases the viscosity of the material near the joint interface, leading to a drop in the generation of frictional heating, which significantly affected the heating rate. Therefore, the temperature was self-limited and dropped to 432 °C (Gerlich, et al., 2005; Suhuddin, et al., 2013 a). The temperature then remained at approximately the same level with some small fluctuations during the short dwell time, which represents the second stage of the welding cycle and is marked by  $T_2$  in Figure 5-3 a. This temperature level is very close to that of the eutectic reaction (437 °C) (Okamoto, 1998; Gerlich, et al., 2005); therefore, it is expected that the continued formation of eutectic liquid at the joint interface during this stage of welding limited the energy input and caused temperature stabilisation. However, it should be noted that for eutectic melting to occur both the  $\alpha$ -Mg and  $Mg_{17}Al_{12}$  phases must first have been present at the weld interface. Therefore, eutectic liquation must have been preceded by some solid-state inter-diffusion and IMC reaction.

During the third stage of the weld cycle when the sleeve retraction occurs, which is marked by  $T_3$  in Figure 5-3 a (step c in Figure 3-6), the temperature decreased rapidly to reach 340.5 °C. This occurred partially because the cavity left by the sleeve retracting during this stage was then refilled with colder material, which acts as a heat sink that reduced the temperature. In addition, as the sleeve is withdrawn, the contact area of the fastest moving outer surface of the tool is reduced, decreasing the heat input. This then would have led to solidification of the liquid interface region. Therefore, the viscosity of the plasticised material in the SZ near the joint interface would have increased as a result of solidification, leading to a greater rate of plastic work and more frictional heating, which would have increased the temperature again to about 411.5 °C. The temperature was then relatively stable during stage 3 before gradually increasing again at the end of the refilling stage (Suhuddin, et al., 2013 a).



$T_1$ : sleeve plunging & pin retraction time = 0.4 s.       $T_2$ : dwell time = 0.05 s.  
 $T_3$ : sleeve retraction and pin plunging = 0.3 s.       $T_4$ : pin plunging & sleeve retraction = 0.1 s.  
 $T_5$ : pin retraction & sleeve plunging = 0.15 s.

Figure 5-3: Example of a thermal history measured for the modified RFSSW process for Mg-Al, showing in (a) the vertical location of the sleeve and pin during the weld cycle. For the thermal measurement (b) the thermocouple was located between the two sheets at a distance of 3.0 mm from the weld centre, with a 2800 rpm tool rotation rate, 1.0 mm sleeve plunge depth, 0.2 mm pin plunge depth, and 1.0 s total welding time.

The fourth and fifth stages, marked with  $T_4$  and  $T_5$  in Figure 5-3 a (steps d and e in Figure 3-6), represent the final pin plunging and retraction stages, added as a modification to the conventional RFSSW process to eliminate the voids produced at the joint edges at the end of the refilling stage. Normally, it is expected that the pin plunge would generate some heat, but only a very small increase in temperature was detected during this stage ( $T_4$ ). This likely to be because of the shallow plunge of the pin used (0.2 mm) and the increased distance between the pin, and sleeve surface as a source of heat generation from the thermocouple position. In addition, the surface velocity of the pin is significantly lower than that of the sleeve, because the total energy generated during friction stir spot welding ( $Q_{total}$ ) shows an  $R^3$  dependency on the pin/sleeve base contact area (see equation 2-2). However, the temperature still gradually increased to about 403 °C during this final stage (pin retraction and sleeve plunging, marked by  $T_5$ ) due to the sleeve plunge, which generated some additional heat. Finally, when the tool head was withdrawn, the temperature cooled down rapidly after the end of the welding process.

The same criteria were applied to determine whether the individual temperature measurements were reliable, or not, as had been used in the case of the RFSSW of similar aluminium alloys described in section 4.4. Namely, the welded joints were sectioned after the end of the welding cycle to check the location of the thermocouples and to be sure that they remained at the correct location at the interface of the joint. However, results from the dissimilar welds that included fluctuations in the temperature measured during the dwell stage, where eutectic melting occurred, were accepted.

Figure 5-4 shows the effect of tool rotation rate (1900, 2200, 2500 and 2800 rpm) on the peak temperature measured at the interface between the two sheets at a distance of 3.0 mm from the weld centre, for welds produced with a 1.0 mm sleeve plunge depth and 1.0 s total welding time. Initially, the peak temperature increased rapidly with increasing tool rotation rate from 1900 rpm to 2200 rpm, but then the rate of increase slowed down and became less affected by tool rotation rate on increasing the rotation rate from 2500 rpm to 2800 rpm. The main reason behind this rapid increase in peak temperature is that the tool rotation rate is one of the most important factors that affects the heat generation during FSSW processes (Schmidt & Hattel, 2008), as it increases the material shear rate. Therefore, with an increasing tool rotation rate it is expected that the temperature will increase (see Figure 4-16). However, using tool rotation rates greater

than 2500 rpm did not increase the temperature significantly, because the peak temperatures associated with these high tool rotation rates were above 437 °C, which corresponds to the eutectic reaction temperature in the Mg-Al binary system (Okamoto, 1998; Suhuddin, et al., 2013 a). Therefore, local melting at the interface between magnesium and aluminium occurred which limited the heat generation, as there would be a rapid drop in material viscosity and the temperature would reach a self-limiting steady state, near the eutectic temperature (Suhuddin, et al., 2013 a).

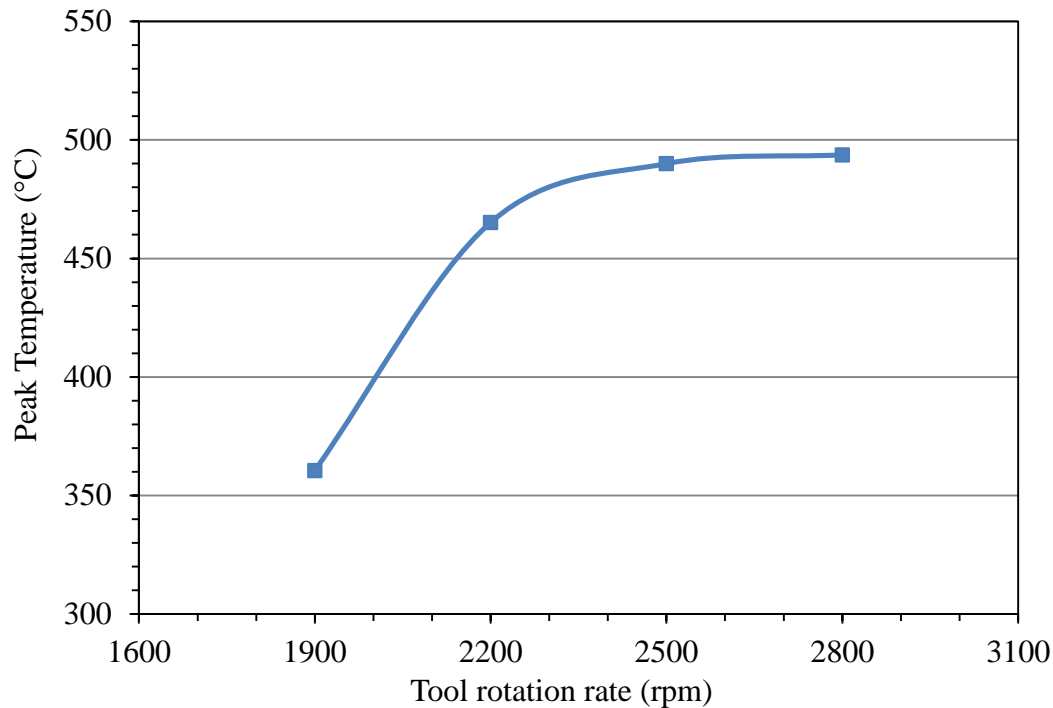


Figure 5-4: The effect of tool rotation rate on the peak temperature measured for the modified RFSSW process produced using a 1.0 mm plunge depth and 1.0 s welding time. The thermocouple was located between the two sheets at a distance of 3.0 mm from the weld centre.

#### 5.4 Effect of Welding Variables on Joint Hardness Profile of the Mg-Al Dissimilar Weld in the As-Welded Condition

To discover the effect of the RFSSW process on the local mechanical properties of the joint cross-sections, microhardness tests were carried out on samples in the as-welded condition. Hardness measurements were made in the form of two parallel lines passing through the cross-sections of the weld located at the mid-thickness of the upper and lower sheets, as shown in Figure 3-9, and following the procedure explained in section 3-6.

Figure 5-5 shows a typical example of the effect of RFSSW on the microhardness profiles of dissimilar joints between the AZ31-H24 magnesium and AA6111-T4 aluminium alloys. The weld was produced with magnesium as the upper sheet and aluminium as the lower sheet. The joint was produced using the modified RFSSW process with welding conditions of a 2500 rpm tool rotation rate, a 1.0 s welding time, 1.0 mm sleeve plunge depth, and 0.2 mm pin plunge depth in the additional final stage. The microhardness was measured immediately after welding to try to prevent the effect of natural ageing in the AA6111 sheet.

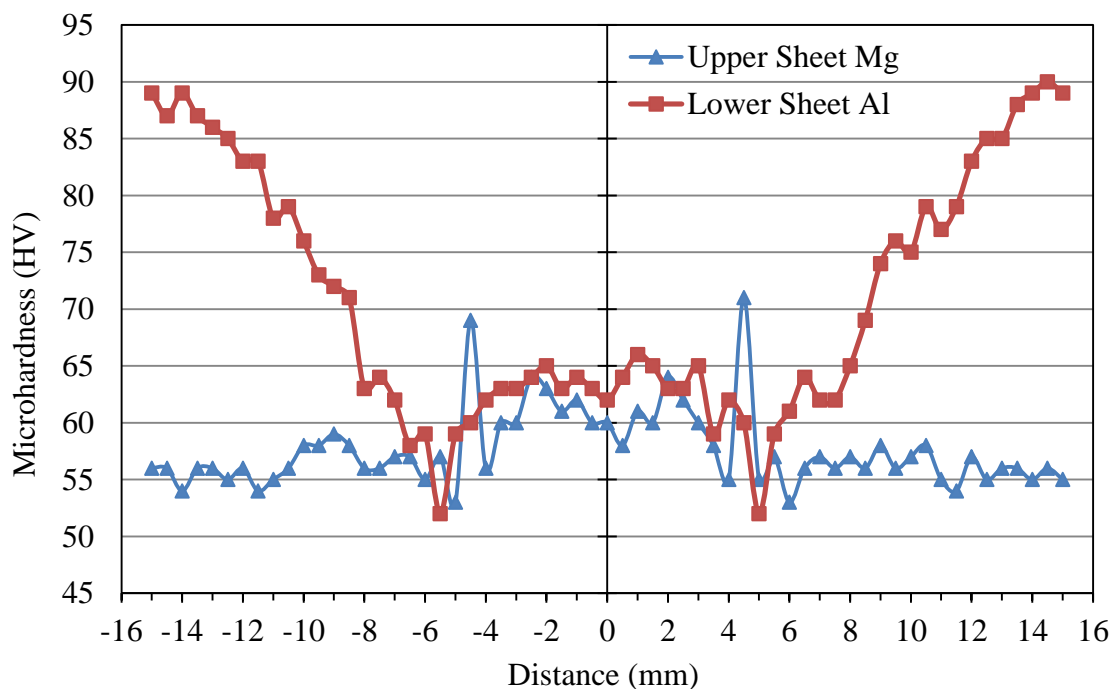


Figure 5-5: Hardness profiles of cross-sections across a typical Mg-Al joint in the as-welded condition. The weld was produced using modified RFSSW with a 2500 rpm rotation rate, 1.0 s welding time, 1.0 mm sleeve plunge depth, and 0.2 mm pin plunge depth.

The hardness profiles of the two alloys were influenced by the welding process in different ways. Generally, the microhardness of the AA6111-T4 aluminium alloy sheet in the as-welded condition showed a W-shaped profile across a weld, which is typical for this alloy, and other heat-treatable aluminium alloys when welded using a friction stir spot welding process (Bakavos & Prangnell, 2009) and was similar to that seen in the welding of the similar AA6111-T4 aluminium alloy using RFSSW (discussed in section 4.6). For example, the average microhardness of the base material (AA6111-T4) was about 89 HV, while the HAZ showed a minimum value of about 52 HV, but moving towards the weld centre the microhardness increased to reach a level of 65 HV. The observed decrease in hardness level in the HAZ is associated with the intermediate temperature reached in this region. In an AA6111 alloy, in the T4 temper, this mainly occurs due to reversion of the GPZs and solute clustering plus some limited overageing (as discussed in section 4.6) (Bakavos & Prangnell, 2009; Parra, et al., 2011; Chen, et al., 2012 a). On the other hand, the high strain rate and the higher temperature reached in the SZ led to dynamic recrystallisation and grain refinement in this region, as well as full solutionisation and some subsequent natural ageing. Therefore, the SZ shows a higher hardness level than the HAZ (Bakavos, et al., 2011). Further details concerning the effect of RFSSW on the microhardness distribution found in AA6111-T4 aluminium alloy welds have previously been outlined in section 4.6.

In contrast, the microhardness level of the AZ31 magnesium alloy was less affected by the welding process. No HAZ could be detected because this alloy is non-heat-treatable. Nonetheless, the stir zone showed a higher microhardness level, with an average of about 60 HV, compared to the microhardness of the base metal, which had an average of about 56 HV. The main reason for this effect is the high deformation rate and the high temperature (about 490 °C), which leads to dynamic recrystallisation of the stir zone and grain refinement (Campanelli, et al., 2012b). Moreover, the edges of the stir zone showed noticeably higher microhardness compared with the centre of the stir zone and base metal. At this position, the measurements taken were in line with the sleeve plunge and retraction position, where very high levels of plastic deformation occurred and very fine grains could be detected (see regions 2 and 3 in Figure 4-18).

## **5.5 Effect of Welding Variables on the Interface Microstructure of the Mg-Al Dissimilar Welds**

The interface between several Mg to Al welds were analysed using SEM and TEM. The interface appearance, weld defects (voids), and the thickness of the reaction layer will be discussed in this section, with attention paid to how the interface region was affected by the welding parameters.

The magnesium to aluminium dissimilar welds were produced with a range of tool rotation rates, using both the conventional and modified RFSSW processes. Scanning electron micrographs were taken of the cross-sections using backscattered electron imaging, focusing on the joint interface. From Figure 5-6, which shows SEM images for two welds produced using conventional and modified RFSSW using welding conditions of a 1900 rpm tool rotation rate, 1.0 s welding time, and 1.0 mm plunge depth, void defects can be clearly seen at the edges of the weld zone for both welding approaches, due to incomplete refilling. The main reason for this is the low plasticity of the Mg metal at low temperatures, which affected the material flow during the refilling stage. This low plasticity resulted from the comparatively low peak temperature of about 360°C (at a distance of 3 mm from the weld centre) seen when using 1900 rpm as a rotation rate (see Figure 5-4). Figure 5-6 c shows that some Al fragments have also been transported into the Mg base material during the refilling stage. On the other hand, with this low level of heat generation, it was difficult to measure the thickness of the interfacial reaction layer as seen in Figure 5-6 f, because it was very thin and discontinuous as the low peak temperature inhibited the IMC reaction. Welding also took place entirely in the solid state and the peak temperature was much lower than the eutectic reaction temperature (Suhuddin, et al., 2013 a). Therefore, the IMC layer was expected to be very thin, in addition to the effect of the material flow which could have caused the break of the IMC layer that generated during the early stages of the welding process.

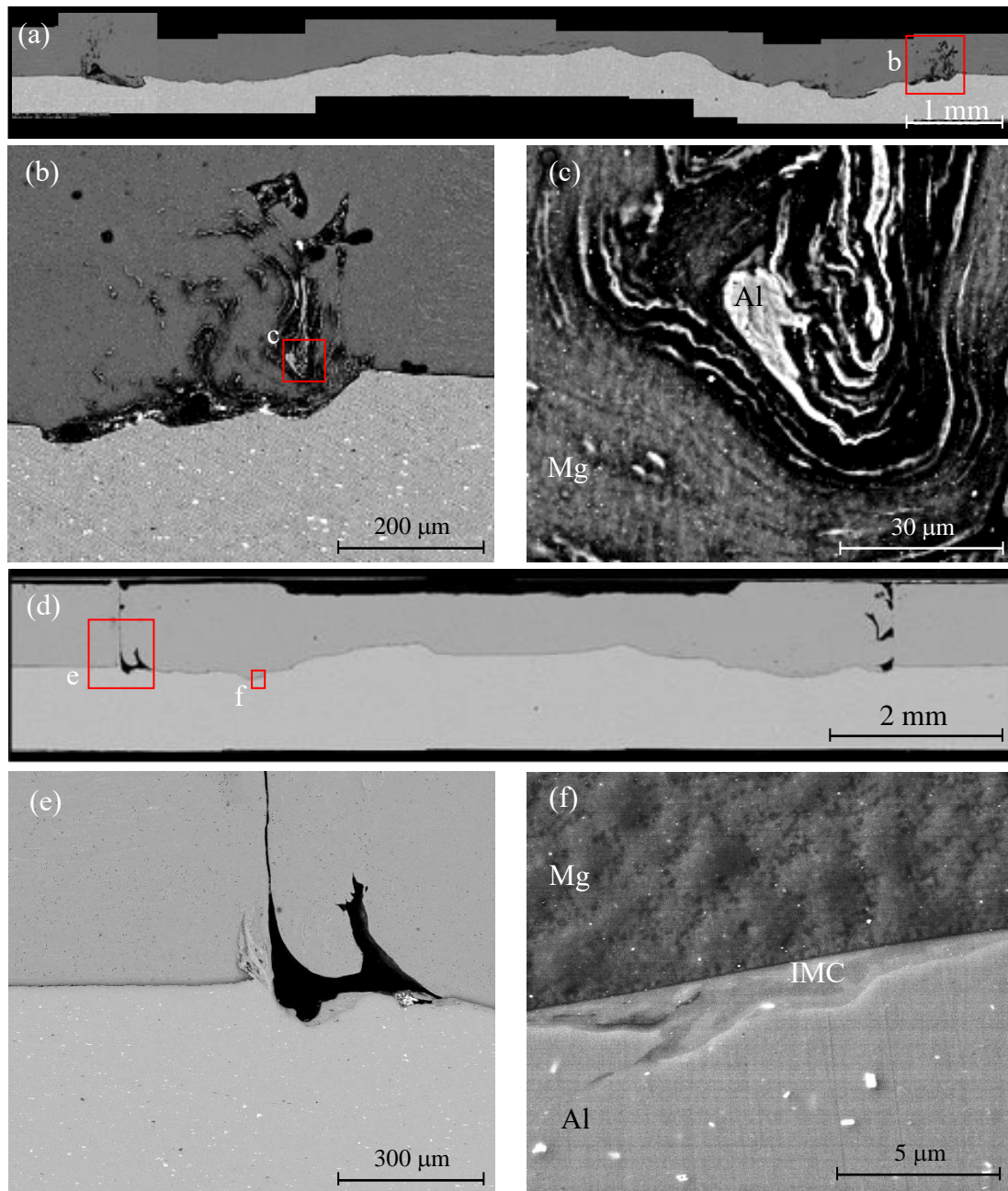


Figure 5-6: Backscattered SEM micrographs of the cross-section of Mg to Al welds produced using welding conditions of 1900 rpm, 1.0 s, 1.0 mm with Mg on the top: (a) with the conventional RFSSW process, showing (b) defects at the edge of weld (a); (c) Al fragments at the edge of weld (a) and (d) using the modified RFSSW process, showing (e) voids at the edge of weld (d); and (f) joint interface, marked by the red rectangle in (d).

On increasing the tool rotation rate to 2500 rpm, overall, the cross-section of the welded joints showed fewer weld defects (voids) (as seen in Figure 5-7) compared with the joints produced using a low rotation rate (1900 rpm) (Figure 5-6). Increasing the tool rotation rate increased the peak temperature in the SZ to about 490 °C (see Figure 5-4), which led to an improvement in the refilling stage by increasing the plasticity of the Mg material. However, the cross-section of the joint produced using conventional RFSSW



(Figure 5-7 a and c) still showed some weld defects, such as voids and hooking at the weld edges. In comparison, the cross-section of the joint produced using the modified RFSSW process appeared to be free from defects (Figure 5-7 d), although Al fragments could still be found in the Mg, especially near the edge of the weld zone.

The rapid formation of intermetallic phases during the spot welding of aluminium to magnesium is a well-known problem that has been widely cited for different welding methods, such as friction stir welding (Sato, et al., 2010; Choi, et al., 2011), ultrasonic welding (Panteli, et al., 2012; Panteli, 2012), and RFSSW (Suhuddin, et al., 2013 b; Suhuddin, et al., 2014). A reaction layer present at the interface between the two sheets can clearly be identified because in the SEM with BSE imaging it is a contrasting shade to the magnesium and aluminium alloys. In the example shown in Figure 5-7 for a 1.0-second weld produced with high tool rotation rate of 2500 rpm the reaction layer can be seen to be neither uniform in thickness nor continuous, and shows 'islands' at the interface. Nonetheless, in general, the reaction layer was predominantly detected under the sleeve and near the interface between the pin and the sleeve, about 2.0 mm from the edge of the joint, where the highest peak temperature was measured (see Figure 4-16). The maximum thickness was about 11  $\mu\text{m}$  for this welding condition, with an average thickness of about 7.8  $\mu\text{m}$  in the region with the highest temperature. The Mg to Al dissimilar joints produced using the modified RFSSW process, with magnesium on top, exhibited a much thinner reaction layer compared to that reported in other studies. For example, an IMC phases with a thickness of about 500  $\mu\text{m}$  has been reported for Al to Mg dissimilar joints produced using RFSSW with aluminium on top at the weld centre by Suhuddin, et al., (2013 b). This reaction layer was, in fact, composed of two distinct sub-layers, with a thicker layer on the magnesium side, as seen in Figure 5-7 f.

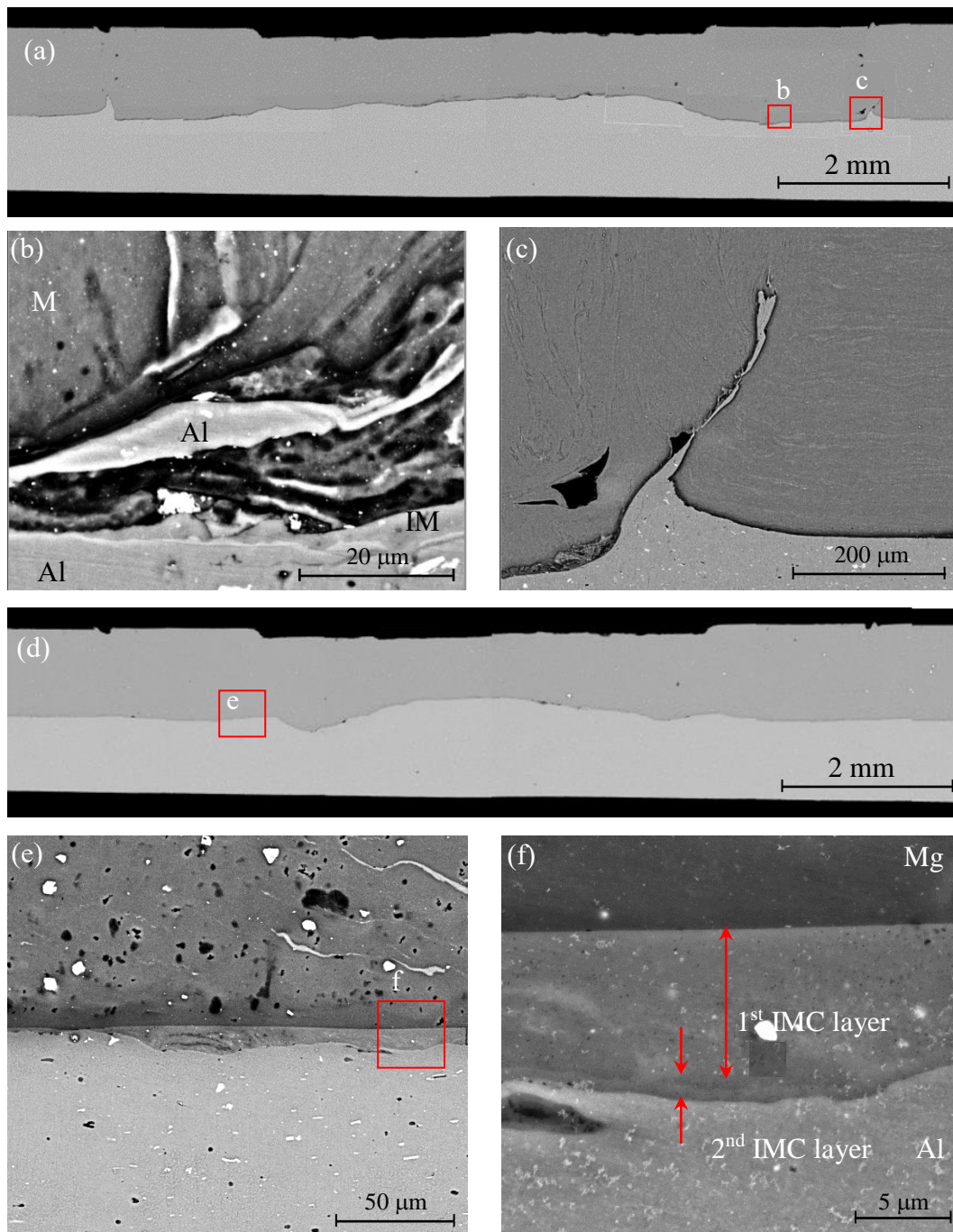


Figure 5-7: Backscattered SEM micrographs of the cross-section of Mg to Al welds produced using the welding condition of 2500 rpm, 1.0 s, and 1.0 mm, with the Mg sheet on top: (a) conventional RFSSW; (b) Al fragments and the interfacial IMC layer at the location under the sleeve, as marked in (a); (c) voids at the edge of weld as marked in (a); and (d) a weld produced by the modified RFSSW process, showing (e) the interfacial IMC layer in a location under the sleeve from the modified weld as marked in (d), and (f) a higher mag. view of the IMC layer marked by the red rectangle in (e).

In spite of the fact that the temperature reached about 490 °C (see Figure 5-4) when using the welding parameters of a tool rotation rate of 2500 rpm, a 1.0 s welding time, and 1.0 mm sleeve plunge depth, which is much higher than the eutectic temperature for the Al-Mg system of 437 °C (Okamoto, 1998; Gerlich, et al., 2005) no eutectic structure

could be detected at, or near the joint interface. The main reason for this is the very short time for which the temperature exceeded the eutectic temperature during the sleeve plunging stage of the welding cycle (less than 0.1 s). This short time period means that the heat input was not high enough to generate a detectable liquid phase, even though the peak temperature reached was higher than the eutectic temperature, and if a small amount of liquid phase formed during this early stage, it is likely that it mixed with the SZ material during the later welding stages.

To determine the composition of the interfacial reaction layer of the joint, EDS line scans were taken using the EDS facility on the Quanta 650 SEM across the interface region of the Mg to Al joints, produced using a tool rotation rate of 2500 rpm, 1.0 s welding time, and 1.0 mm sleeve plunge depth. As shown in Figure 5-8, the line scan for the chemical composition revealed that the IMC reaction layer had an Mg composition ranging from 50 to 60 in wt. %, on the side of the magnesium alloy. The layer with this composition was about 8  $\mu\text{m}$  wide, while on the side of the aluminium sheet the IMC layer had a lower Mg content, with a range of 30 to 50 wt. %.

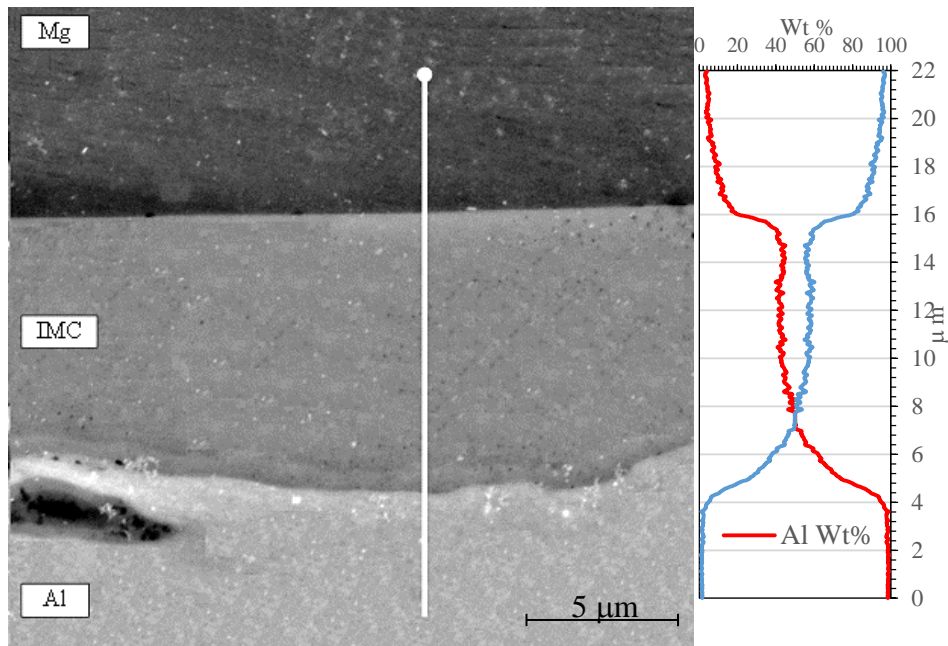


Figure 5-8: Backscattered SEM micrographs of the interfacial reaction IMC layer seen between the Mg and Al sheets, from welds produced using the modified RFSSW process with welding condition of 2500 rpm, 1.0 s, and 1.0 mm time with the Mg on top.

As mentioned in chapter 2 (section 2-14), the Al-Mg system contains several intermetallic phases (Schurmann & Voss, 1981; Murray, 1982; Su, et al., 1997; Okamoto, 1998). There is also still some uncertainty about the nature of the phase types



and structure in the composition range of 40-60 at %Mg (Saunders, 1990). However, there is general agreement that two intermetallic compounds exist in the Al-Mg phase diagram: the  $\beta$ -Al<sub>3</sub>Mg<sub>2</sub> phase, with a range of composition of 37-40 at %Mg and the  $\gamma$ -Al<sub>12</sub>Mg<sub>17</sub> phase with a wider range of solid solubility (Saunders, 1990). Only these two phases have ever been detected in Al-Mg joints produced by different spot welding techniques (Sato, et al., 2010; Choi, et al., 2011; Panteli, et al., 2012; Suhuddin, et al., 2013 b; Suhuddin, et al., 2014). In this project, it has also been shown that  $\beta$ -Al<sub>3</sub>Mg<sub>2</sub> and  $\gamma$ -Al<sub>12</sub>Mg<sub>17</sub> were the only phases detected in the IMC layer at the interface of the Mg-Al joint. This can clearly be seen in Figure 5-9, which shows a TEM image of a sample taken from the same interface region of Figure 5-7 e.

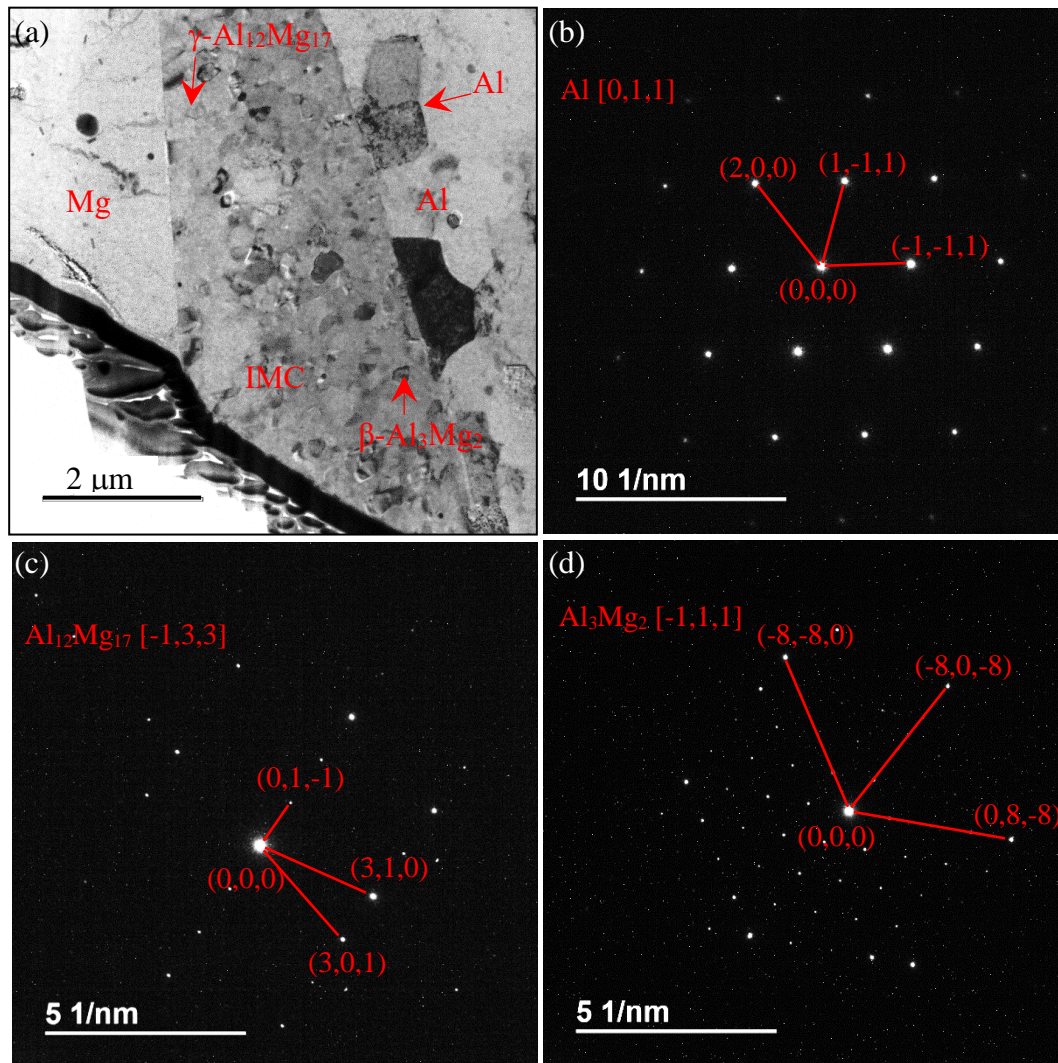


Figure 5-9: (a) TEM image of the bond-line between the Mg and Al sheets showing the IMC layer. The weld was produced using the modified RFSSW process with Mg on top and welding conditions of 2500 rpm, 1.0 s, and 1.0 mm; (b),(c) and (d) Selected area diffraction patterns are shown for each phase in (a).

The TEM sample was prepared using the FIB technique, following the procedure explained in section 3.8.6. Figure 5-9 shows a clearly distinct IMC layer with a non-uniform thickness. By selected area diffraction in the TEM, this IMC layer was found to consist of two sub-layers; an Al-rich layer on the aluminium side composed of the  $\beta$ - $\text{Al}_3\text{Mg}_2$  phase, and an Mg-rich IMC layer on the magnesium side, composed of the  $\gamma$ - $\text{Al}_{12}\text{Mg}_{17}$  phase.

As can be seen from Figures 5-6 and 5-7, increasing the tool rotation rate from 1900 to 2500 rpm helped in reducing the size of the voids located at the joint edges, in the case of the conventional RFSSW process and eliminated them when the modified RFSSW technique was used. However, a further increase in tool rotation rate to 2800 rpm, resulted in a significant change in the joint interface. As can be seen in Figures 5-10 b, d, and e, surprisingly the IMC layer between the magnesium and aluminium became thinner, compared to that seen in Figures 5-7 e, and f, with a larger variation in thickness. This decline in the thickness of the IMC layer was contrary to expectations, in that it was expected that with an increase in the tool rotation rate the temperature would increase and result in an increase in the thickness of the IMC layer. However, the presence of a solidified eutectic microstructure seen in Figure 5-10 c, showed clear evidence of much more significant interface melting within this region, because the material exceeded the eutectic temperature (see Figure 5-4) (Suhuddin, et al., 2013 a). It can also be seen that this melted material had been displaced through the magnesium due to the material flow during the refilling step of the welding process. This resulted in the formation of a eutectic structure near the weld interface, as shown in Figures 5-10 c, d, and e, which removes the ambiguity about the issue of the decrease in the thickness of the IMC, where most of the eutectic liquid was mixed with the magnesium during the welding process and formed a dispersed eutectic structure.

The eutectic structure was found to be mostly generated near the interface in a region within the magnesium between the pin and the sleeve, near the internal edge of the sleeve, where the maximum peak temperature was measured (see Figures 4-16 and 5-4). According to the equilibrium Al-Mg phase diagram (see Figure 2-58), there are two possible eutectic reactions:  $\alpha$ -Al with  $\beta$ - $\text{Al}_3\text{Mg}_2$  and  $\gamma$ - $\text{Al}_{12}\text{Mg}_{17}$  with  $\delta$ -Mg, with a difference in temperature of about 13 °C (the reactions occur at 450 °C and 437 °C, respectively) (Zuo & Chang, 1993; Okamoto, 1998). Therefore, the eutectic structure at the interface of the weld could contain  $\gamma$ - $\text{Al}_{12}\text{Mg}_{17}$  and  $\delta$ -Mg (Suhuddin, et al., 2013 b;

Suhuddin, et al., 2013). The existence of the  $\gamma$ -Al<sub>12</sub>Mg<sub>17</sub> with  $\delta$ -Mg eutectic structure has been also reported by Suhuddin et al. (2013 b; 2014) in the microstructure of Al-Mg dissimilar RFSSWs (see Figure 2-41) (Suhuddin, et al., 2013 b; Suhuddin, et al., 2014).

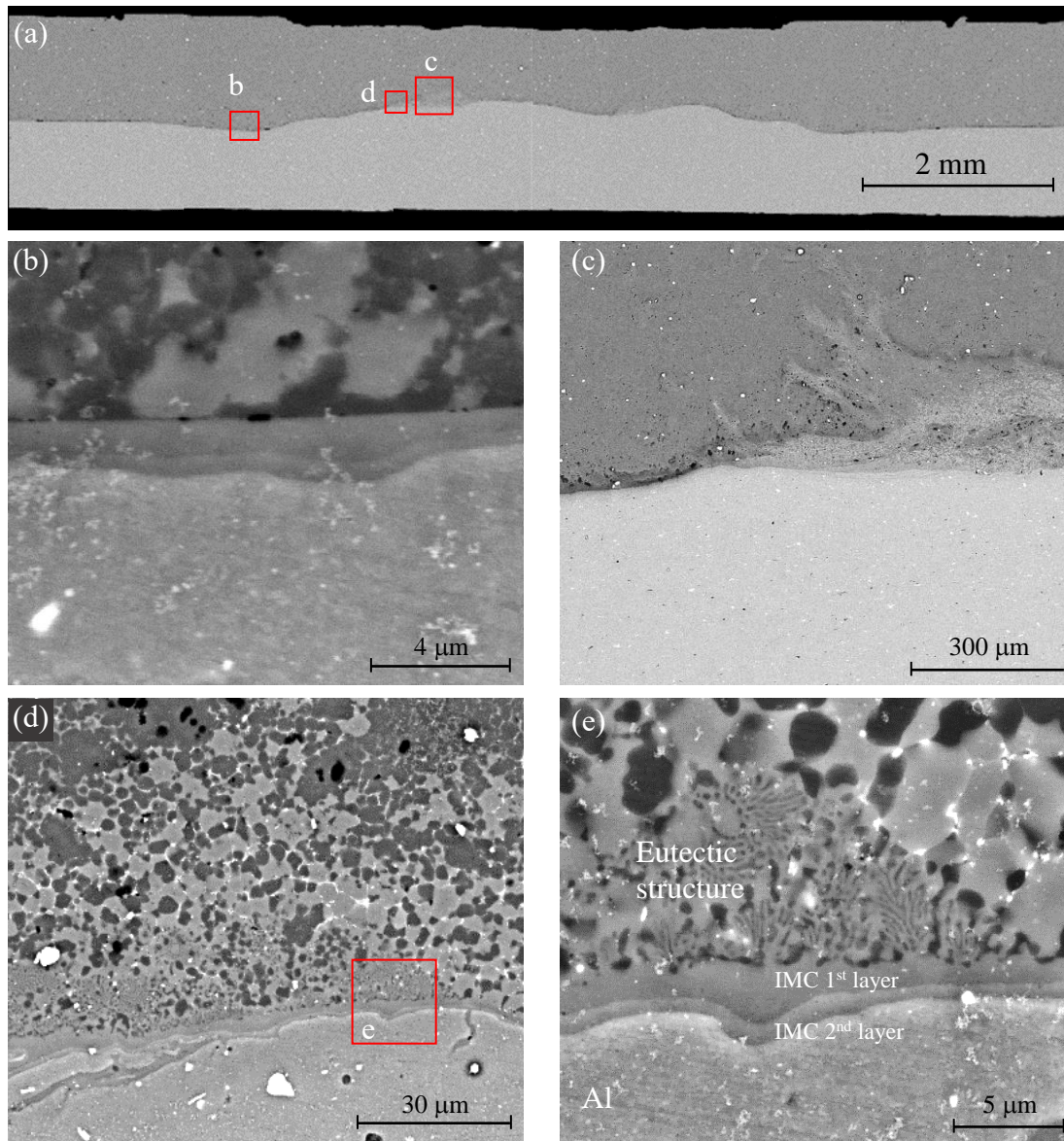


Figure 5-10: Backscattered SEM micrographs of the cross-section of Mg to Al joints produced using the modified RFSSW process with welding conditions of 2800 rpm, 1.0 s, 1.0 mm, with Mg on top: (a) full joint cross-section, (b) an interfacial IMC layer in a location under the sleeve, as marked in (a); (c) a solidified eutectic region; (d) the interfacial IMC layer and eutectic structure; and (e) higher mag. of the IMC layer and eutectic structure from the region marked in (d).

As mentioned above, the thickness of the IMC layer shows noticeable variation with changing welding parameters. Figure 5-11 shows an example of the effect of one of the welding parameters, the tool rotation rate on the thickness of the IMC layer. Thickness measurements were taken using ImageJ software. In spite of the non-uniform

distribution and discontinuity of the reaction layer, the maximum thickness could be detected under the sleeve at the joint interface at a distance of about 2 mm from the edge of the joint. Therefore, this location was taken as a reference for comparison of the thickness of the reaction layer for joints produced using different tool rotation rates. Figure 5-11 shows that with increasing tool rotation rate from 1900 to 2500 rpm, the average thickness of the reaction layer increased rapidly from about 1.7  $\mu\text{m}$  to 7.8  $\mu\text{m}$ , by using the same welding time of 1.0 s and a plunge depth of 1.0 mm. Beyond a 2500 rpm tool rotation rate, the average thickness then decreased to about 2.8  $\mu\text{m}$  when using a tool rotation rate of 2800 rpm. The average thicknesses also showed less variation in different samples in welds produced with lower rotation rates (1900 rpm). However, variation in the average thicknesses increased when increasing the tool rotation rate. It was expected that the thickness of the reaction layer would increase with increasing the tool rotation rate due to the increase in the peak temperature of the weld. However, what was not expected was the rapid decrease in the thickness with increasing the tool rotation rate to 2800 rpm, in spite of the increase in the weld heat input. The main reason for this decrease in thickness is the onset of significant eutectic melting and dispersal of the eutectic liquid due to the tool pressure, as discussed above (see Figure 5-10 e).

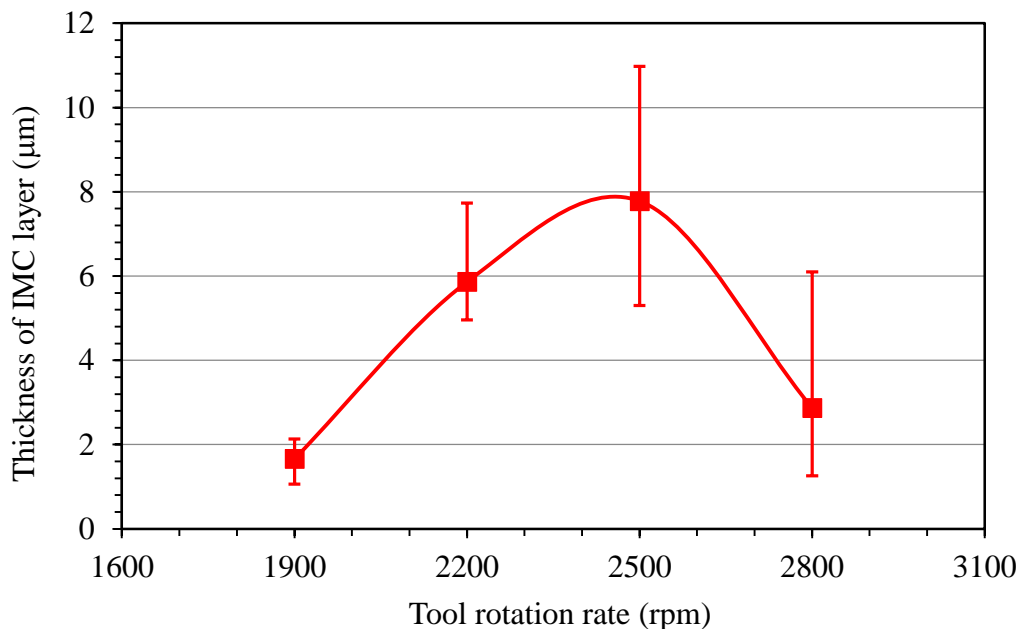


Figure 5-11: Effect of tool rotation rate on the thickness of the interfacial IMC reaction layer in the Mg-Al joints. The welds were produced using the modified RFSSW process with Mg on top and welding conditions of a 1.0 s welding time and 1.0 mm sleeve plunge depth.



Finally, Figure 5-12 shows a series of micrographs of the development of weld defects, as a function of sleeve plunge depth. No weld defects were detected when using the modified RFSSW process with the optimum conditions of a 1.0 mm sleeve plunge depth, 2500 rpm tool rotation rate, and a 1.0 s welding time (see Figure 5-7 d).

However, under these welding conditions, weld defects became noticeable when using plunge depths of 1.2 mm, or more. As seen in Figure 5-12, the size of the voids at the edges and the height of the hook increased significantly with increasing plunge depth. Since the hook is formed by deforming the interface between the two sheets, due to the vertical material flow in the region out of the sleeve, as shown in Figure 4-7a (region 1), a deeper plunge results in more displacement of the interface and leads to a bigger hook. On the other hand, void formation is closely linked to poor material flow back in to refill the SZ, which depends on the plasticity of the SZ material. Refilling the annular sleeve cavity is more difficult if the plasticity of the material (Mg alloy) that came from the upper sheet is insufficient. Therefore, some regions remained unfilled, and the size of these regions increased with increasing sleeve plunge depth, due to the increase in the volume of material required to refill the annular cavity.

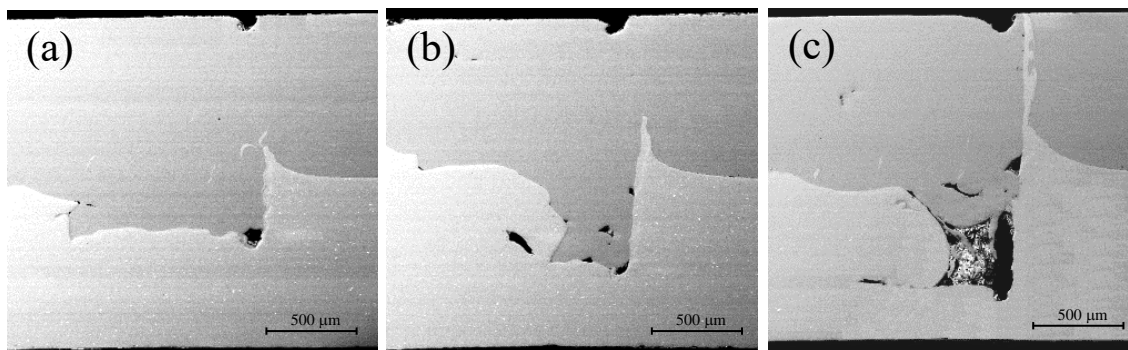


Figure 5-12: Backscattered SEM micrographs showing the development of weld defects (voids and hooks) at the edge of Mg and Al joints, as a function of the sleeve plunge depth. Welds were produced using the modified RFSSW process with welding condition of 2500 rpm, 1.0 s, and a plunge depth of (a) 1.2 mm, (b) 1.4 mm, and (c) 1.6 mm.

## **5.6 Effect of Welding Variables on the Weld Strength of Mg-Al RFSSWs and Modified RFSSWs**

To evaluate the mechanical performance of the dissimilar Mg-Al and similar Mg-Mg lap joints, numerous spot welds were produced using the conventional and modified RFSSW processes with a wide range of welding parameters (see Table 5-1). A tensile lap shear test was used to assess the mechanical properties of the joints, which were



produced using the dimensions shown in Figure 3-11. All the measurements were implemented at room temperature immediately after welding (within one hour), using a machine crosshead speed of 1.0 mm/min.

Figure 5-13 shows examples of the typical load-extension curves for the lap-shear tests of conventional and modified RFSSW joints produced by the dissimilar AZ31 alloy welded to the AA6111 alloy, in addition to similar welds of the AZ31 alloy for the purpose of comparison. The welded joints were produced using the same welding conditions of a 2500 rpm rotation rate, 1.0 mm sleeve plunge depth, and 1.0 s total welding time. The curves of the similar Mg-Mg joint and modified RFSSW Mg-Al joint show some ductile behaviour, where the samples deformed plastically before the formation of a crack at the peak load, whereas the Mg-Al joint produced using conventional RFSSW shows much less ductile behaviour, with evidence of cracking before the peak load (see inflections in the loading curve in Figure 5-13). Subsequent to the peak load, this sample also showed a rapid decrease in the load. This rapid decrease in load is characteristic of a brittle fracture in the joint. However, the Mg-Al joint produced using the modified RFSSW process showed a two-step failure in its loading curve, with a transitional shape between a fully brittle failure and ductile failure, shown by similar Mg-Mg and similar Al-Al joints (see Figure 4-29).

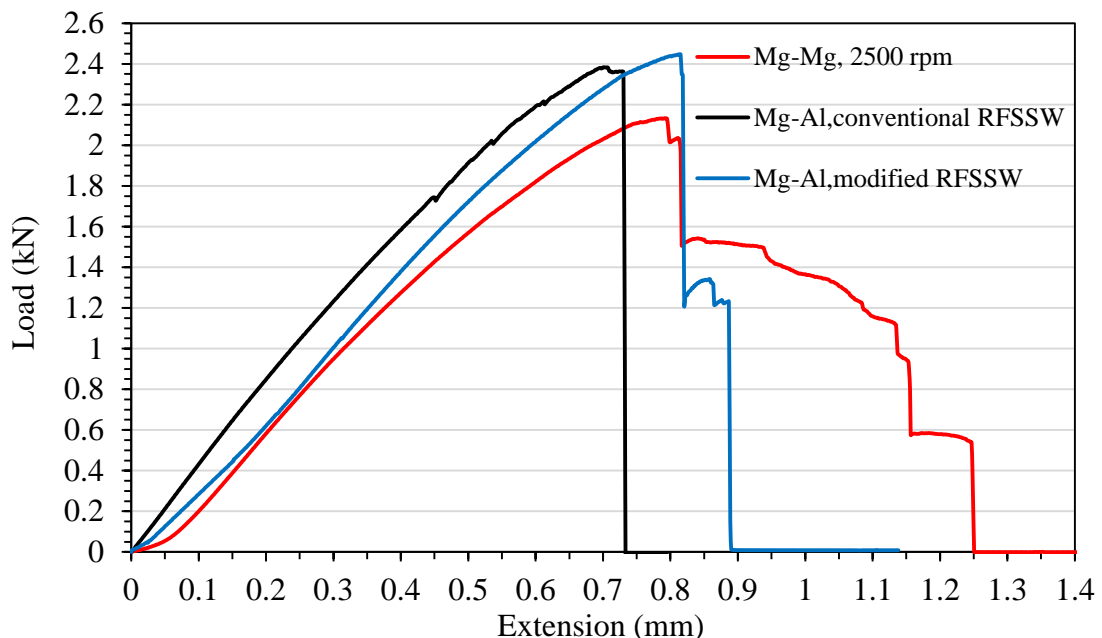


Figure 5-13: Example load-extension curves for the tensile-shear test from dissimilar Mg-Al and similar Mg-Mg joints. The joints were produced using the conventional and modified RFSSW processes, with the welding conditions of a 2500 rpm tool rotation rate, a 1.0 mm sleeve plunge depth, and a 1.0 s total welding time.

The effect of the welding conditions on the peak load of the dissimilar Mg-Al joints welded by the conventional RFSSW and modified RFSSW processes are shown in Figure 5-14. Figure 5-14 a shows that the average peak loads of the samples welded using conventional RFSSW were increased by increasing the tool rotation rate for low plunge depths (1.0 and 1.2 mm) while the deeper plunge depths (1.4 and 1.6 mm) show some fluctuation in the values of the average peak loads. On the other hand, both the tool rotation rates and plunge depths had a clear impact on the weld strength of the joints produced using the modified RFSSW process as shown in Figure 5-14 b. From this figure, it can be noted that the average peak load increased with increasing tool rotation rate, to reach a maximum value at 2500 rpm. The peak load level then decreased on increasing the tool rotation rate to 2800 rpm, when using all plunge depths except the smallest (0.8 mm). This behaviour resulted from the effects of two competing factors. The first factor is the material flow, which is important for refilling the annular cavity left by retraction of the sleeve. If the material does not have enough plasticity due to insufficient heat generation, when using an excessively low tool rotation rate, then incomplete refilling will occur and lead to weld defects, such as voids at the weld edges (see Figure 5-6), which reduce the strength of the joint. The plasticity of the SZ material can be increased through increasing the heat input, which could be achieved by increasing the tool rotation rate (see Figure 5-4). However, welds produced with the conventional RFSSW process still showed a lower average peak load compared to those produced with the modified RFSSW process. For example, the average peak load improved by about 10 % when using modified RFSSW at the optimum conditions of 2500 rpm tool rotation rate, 1.0 mm sleeve plunge depth, and 1.0 s total welding time, compared to welds produced with the conventional RFSSW process and the same welding parameters. The main reason for this difference is that the modified process resulted in defect free samples when using the optimum conditions (see Figure 5-7).

The second factor that affected the strength of the samples was the formation of a brittle IMC layer and the eutectic structure at the joint interface. The presence of both an IMC layer and a eutectic structure containing a large volume fraction of brittle intermetallic phases will affect the strength of the joints. However, a significant eutectic layer could only be detected when using tool rotation rates of 2800 rpm (see Figure 5-10), due to the higher heat input. This resulted in deterioration of the joint strengths for all the plunge depths, except the depth of 0.8 mm.

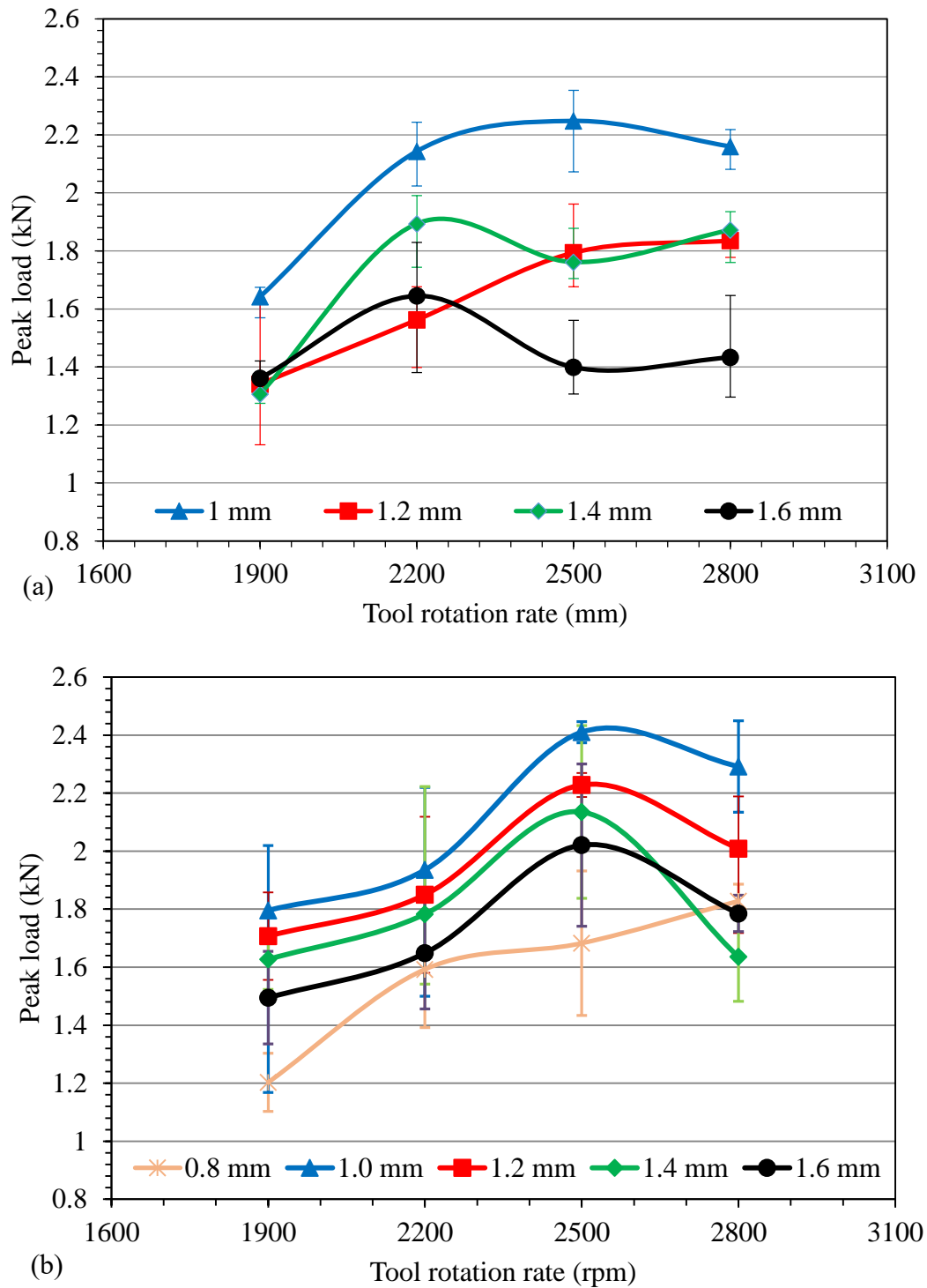


Figure 5-14: Effect of tool rotation rate and sleeve plunge depth on the average lap shear peak load of Mg-Al joints produced using a 1.0 s total welding time with (a) conventional RFSSW, and (b) the modified RFSSW process.

The effect of sleeve plunge depth on the strength of the dissimilar Mg-Al joints produced using modified RFSSW is shown in Figure 5-15. An increase in the sleeve plunge depth from 0.8 mm to 1.0 mm led to a rapid increase in weld strength for all tool rotation rates. This is due to the increase in the metallurgical bond area between the two

sheets, as when using a sleeve plunge depth of 0.8 mm, the sleeve does not reach the interface between the two sheets, which results in weaker joints. By plunging the sleeve deeper than 1.0 mm the average peak load showed a gradual decrease, with a nearly linear relationship for most tool rotation rates. This result is likely due to the increase in weld defects, and especially the void size, with increasing plunge depth that results from the diminishing ability to refill the sleeve cavity (see Figure 5-12). The average peak load of the joints welded using the modified RFSSW process showed similar behaviour as a function of the welding time, as can be seen in Figure 5-16. When using a welding time of less than 1.0 s, this resulted in the weakest joint because the time was not sufficient for the material to heat up enough to flow and produce a defect-free joint. The strength of the joints increased significantly once the welding time was increased to 1.0 s, which resulted in defect free joints, especially when using optimum welding conditions (see Figure 5-7 d). However, with a further increase in welding time, the average peak load decreased gradually due to the increase in the thickness of the IMC layer when using tool rotation rates of 2500 rpm or less, and the thickness of the interfacial eutectic structure when using 2800 rpm as a tool rotation rate (Suhuddin, et al., 2013 a; Suhuddin, et al., 2013 b; Suhuddin, et al., 2014).

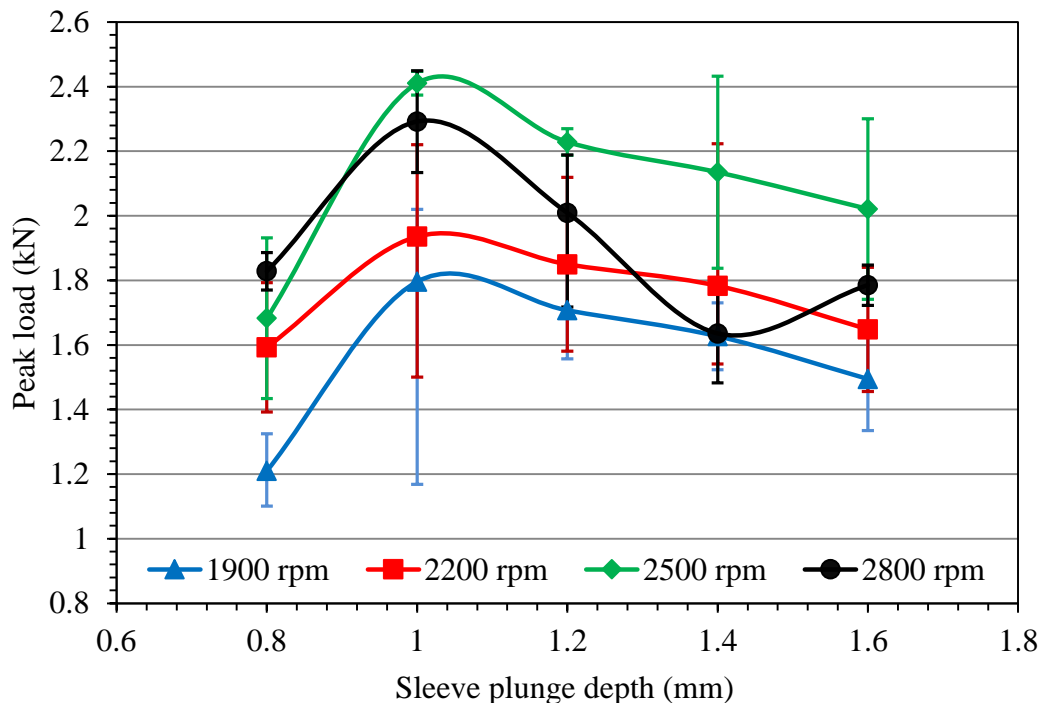


Figure 5-15: Effect of sleeve plunge depth and tool rotation rate on the average lap shear peak load of Mg-Al joints produced using the modified RFSSW process with a 1.0 s total welding time.

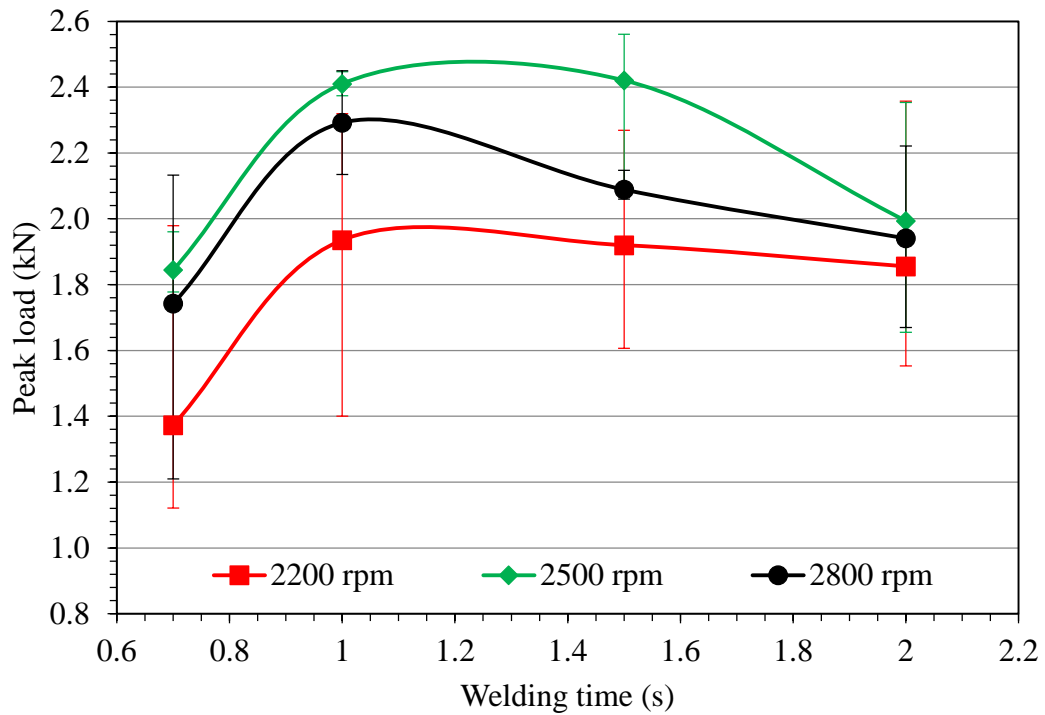
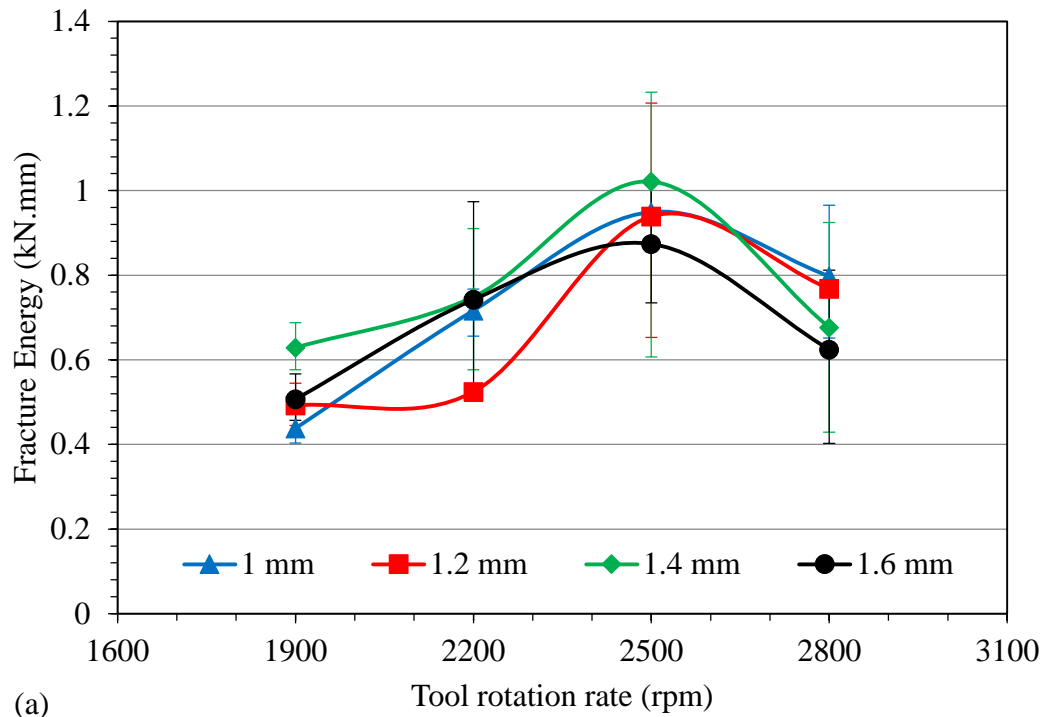
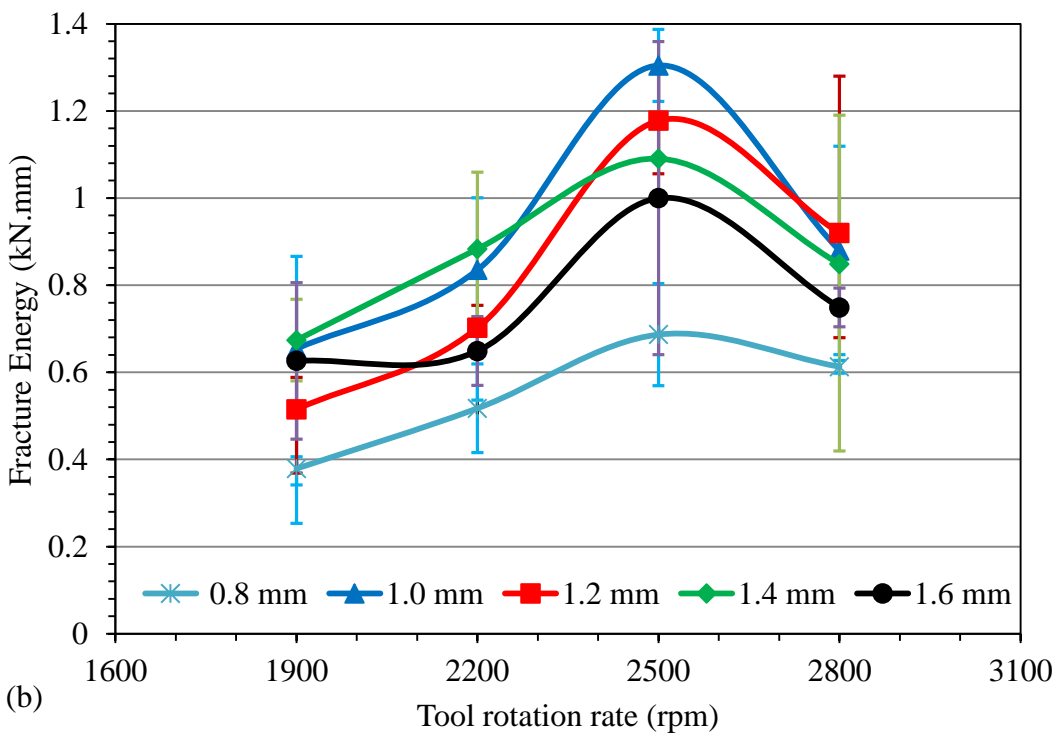


Figure 5-16: Effect of total welding time and tool rotation rate on the average lap shear peak load of Mg-Al joints produced using the modified RFSSW process with a 1.0 mm sleeve plunge depth.

The effect of the welding conditions on the average fracture energy of the welded joints produced using the conventional and modified RFSSW processes is shown in Figures 5-17, 5-18, and 5-19. The total failure energy was calculated by integration of the load-extension curves. Figure 5-17 shows that the failure energies gave a similar trend to that for the effect of welding parameters on the average peak load (shown in Figure 5-14), especially for the joints produced using the modified RFSSW process (see Figures 5-14 b, and 5-17 b), where the fracture energy of the joints was increased by increasing the tool rotation rate to 2500 rpm, while a further increase in tool rotation rate to 2800 rpm led to a decrease in the fracture energy. Moreover, the joints produced using the modified RFSSW process show an increase in fracture energy compared to those produced by the conventional RFSSW process, using the same welding parameters. For instance, at the optimum welding condition (i.e. with a tool rotation rate of 2500 rpm, total welding time of 1.0 s, and a sleeve plunge depth of 1.0 mm) the modification made to the process improved the fracture energy by about 27 %.



(a)



(b)

Figure 5-17: Effect of tool rotation rate and sleeve plunge depth on the average fracture energy of Mg-Al joints produced using a 1.0 s total welding time with (a) conventional RFSSW, and (b) the modified RFSSW process.

From Figures 5-18, and 5-19 it can be noted that the sleeve plunge depth and welding time had the same effect on the average fracture energy of the joints as that seen on the average peak load (see Figures 5-15, and 5-16), as the fracture energy showed the lowest values when using the shortest welding time (0.7 s) or a shallower sleeve plunge depth (0.8 mm) and increased rapidly with increasing welding time to a maximum at 1.0 s and a plunge depth of 1.0 mm. However, after these optimum conditions the fracture energy of the joints showed a gradual decrease with longer weld durations or deeper plunge depths similar to the behaviour of the peak fracture loads.

A possible reason behind the similarity between the trends of the fracture energy and peak load data is that all the samples showed nearly the same load-extension curve behaviour ( see Figure 5-13), and since the fracture energy represents the area under this curve, the fracture energy can be understood to scale with the value of the peak load.

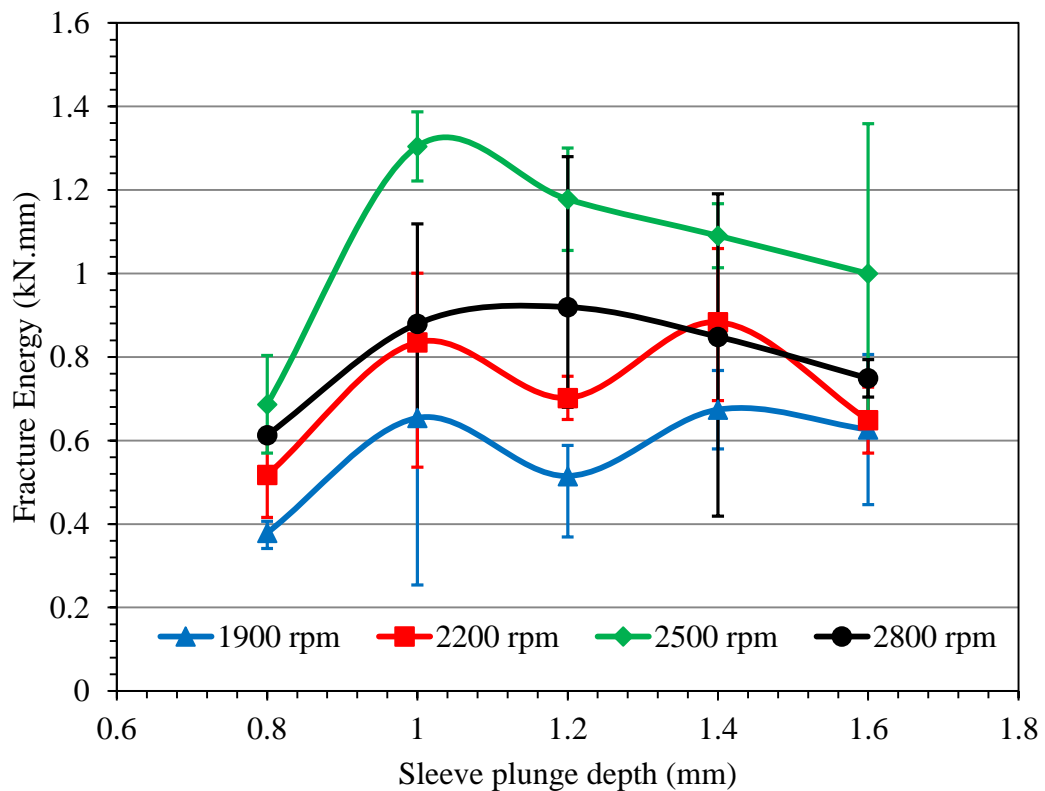


Figure 5-18: Effect of sleeve plunge depth and tool rotation rate on the average fracture energy of Mg-Al joints produced using the modified RFSSW process with a 1.0 s total welding time.

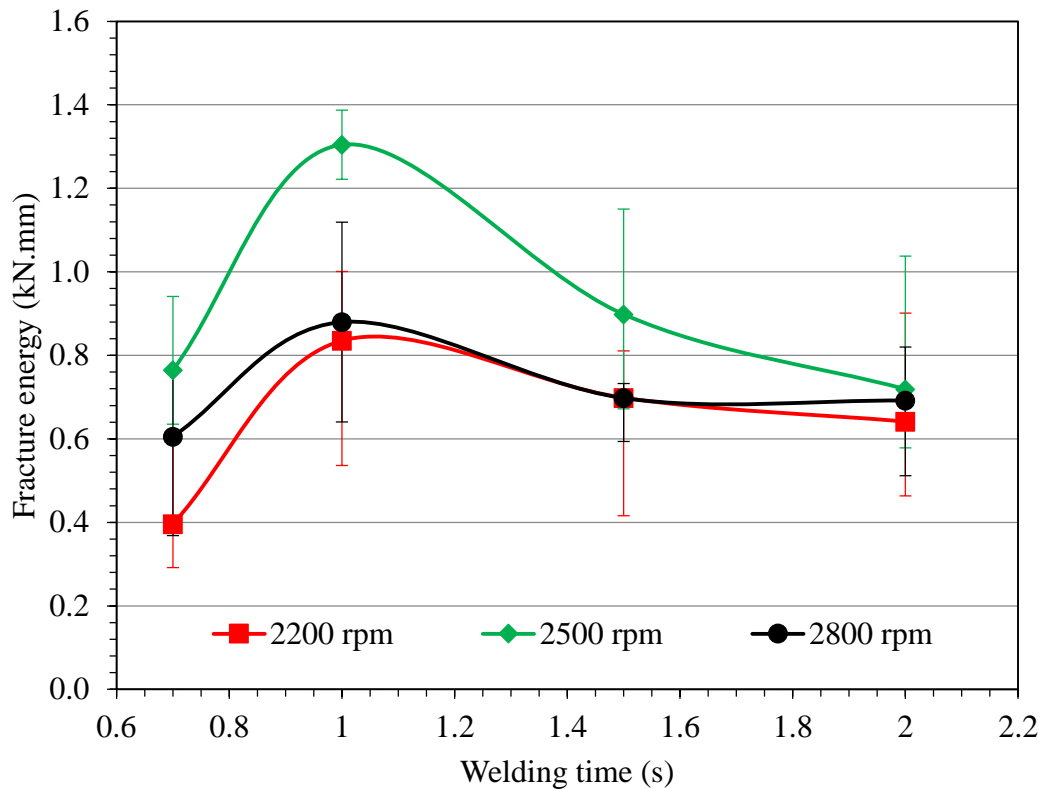


Figure 5-19: Effect of total welding time and tool rotation rate on the average fracture energy of Mg-Al lap joints produced using the modified RFSSW process with a 1.0 mm sleeve plunge depth.

## 5.7 Comparison of the Effect of the Tool Rotation Rate on the Strength of Mg-Al and Mg-Mg Modified RFSSWs

To compare the effect of the welding conditions on similar welds of Mg to Mg with dissimilar welds of Mg to Al, several welds were produced with a 1.0 mm plunge depth, 1.0 s welding time, and a range of tool rotation rates (1900-2800 rpm).

Figure 5-20 compares the effect of tool rotation rate on the peak load in the lap-shear tests for the Mg-Mg and Al-Mg joints. It can be seen that the level of the average peak load of the Mg-Al joints is comparable to that of the Mg-Mg welds, especially for high tool rotation rates (2500 and 2800 rpm). The strength of the Mg-Mg joint is relatively constant but shows a slight decrease with increasing tool rotation rate. A possible reason for this is that softening occurs in the AZ31-H24 weld zone of the similar joints, due to the greater heat input when using high tool rotation rates (see Figure 5-4). Conversely, a greater heat input is needed to remove defects from the Mg-Al dissimilar welds.



However, the difference in the level of the average fracture energy between the Mg-Mg and Mg-Al joints was much greater, as shown in Figure 5-21, where the similar Mg-Mg joints have at least a 50% higher fracture energy and show a clear increase with increasing tool rotation rate, while the dissimilar Mg-Al welds show an optimum peak. This difference is due to the difference in the fracture mode of the samples, as the Mg-Al joints were fractured by the interfacial fracture mode, while the fracture showed a full nugget pull-out mode for the Mg-Mg joints. Both of these fracture modes will be discussed in more detail in the next section, where figures with examples of these phenomena are shown.

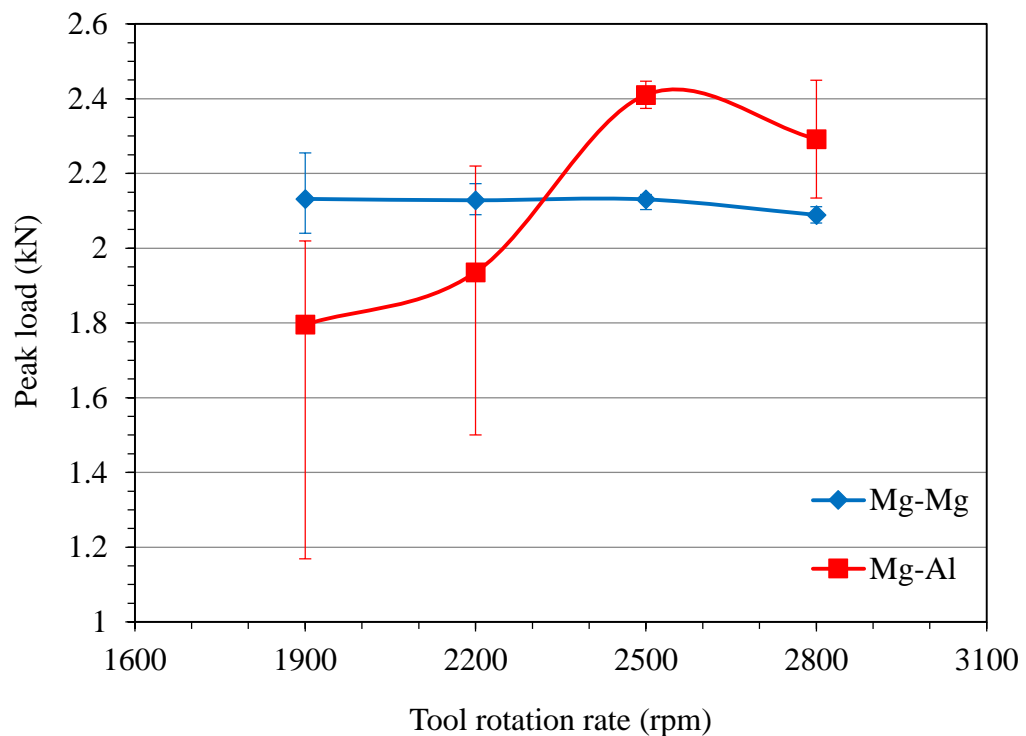


Figure 5-20: Effect of tool rotation rate on the average peak load of the Mg-Mg and Mg-Al joints produced using the modified RFSSW process with a 1.0 mm sleeve plunge depth and 1.0 s total welding time.

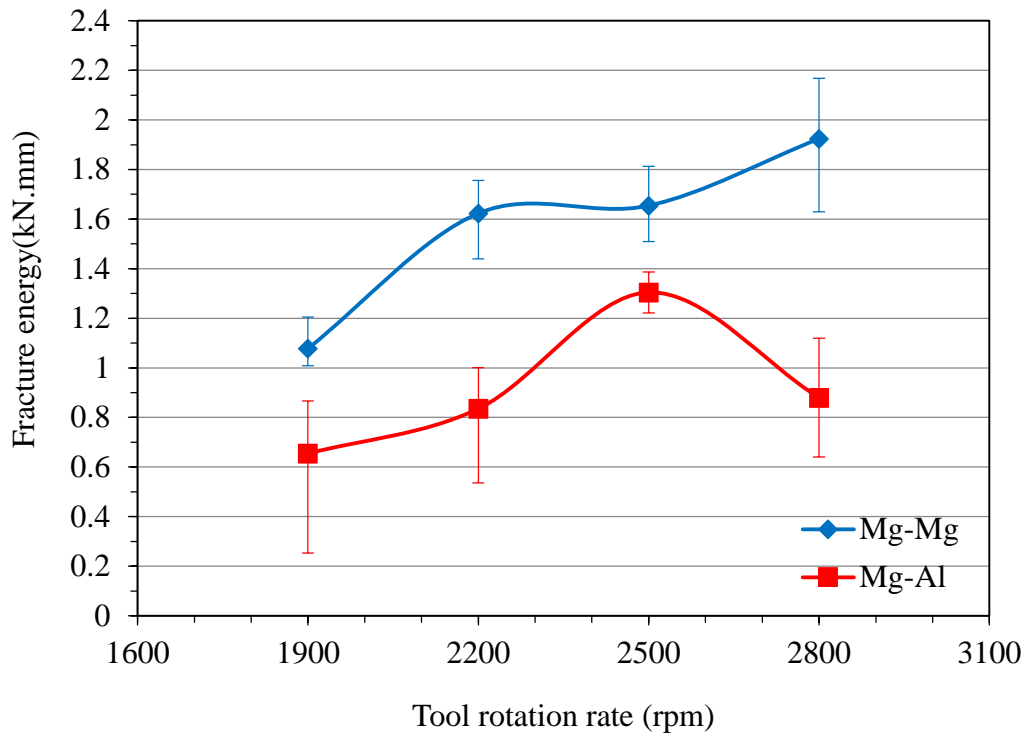


Figure 5-21: Effect of tool rotation rate on the average fracture energy of the Mg-Mg and Mg-Al joints produced using the modified RFSSW process with a 1.0 mm sleeve plunge depth and 1.0 s total welding time.

## 5.8 Weld Failure Modes

Examples of typical fracture behaviours of the dissimilar Mg-Al joints produced using the conventional and modified RFSSW processes with different welding parameters, after lap shear testing in the as-welded condition, are shown in Figure 5-22. An interfacial fracture mode was noted under the tensile-shear loading for most of the joints produced with different welding parameters, for two reasons: firstly, the voids present at the edges of the joint, especially, when using the conventional RFSSW or lower rotation rates act as vulnerable locations for the creation of cracks, which lead to failure. Secondly, the interfacial fracture of the samples is caused by the formation of an IMC layer, or a eutectic structure at the joint interface. These structures exhibit much more brittle behaviour than the parent materials (magnesium and aluminium); therefore, cracks easily propagate through them, which results in low fracture energy during lap-shear tests (Sato, et al., 2010). However, some welds with high strength exhibited a partial nugget pull-out failure mode, especially when using the optimum welding parameters, as can be seen on the side of the AZ31 alloy in Figure 5-22 b.

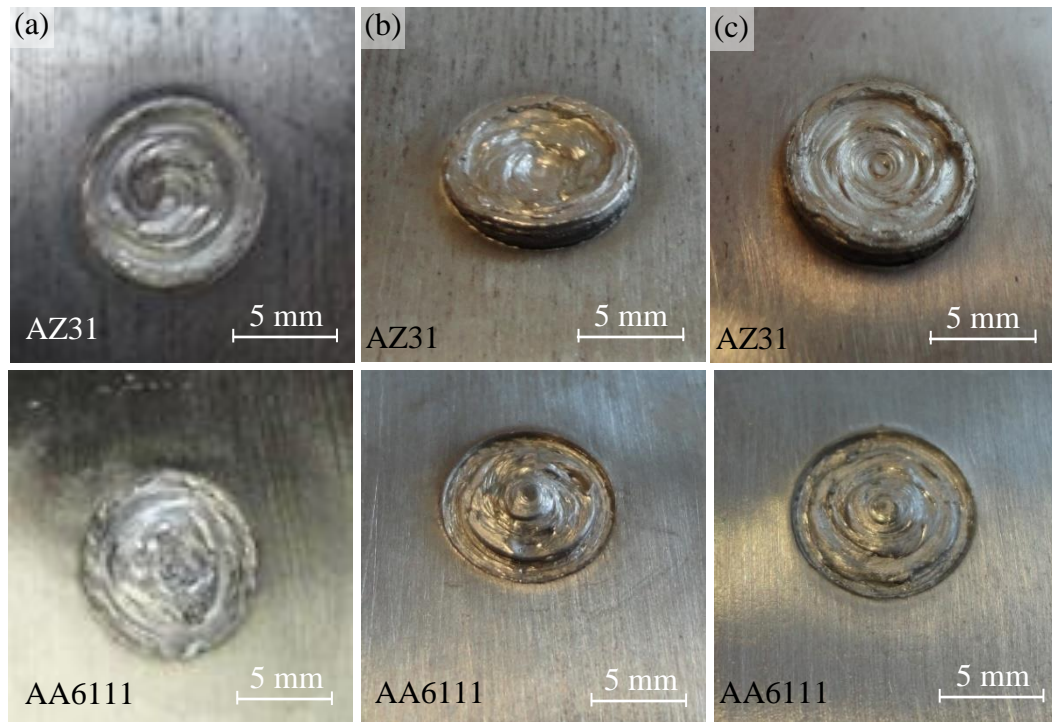


Figure 5-22: Examples of typical joint failure behaviours, showing both halves of the fractured lap shear test samples produced using a 1.0 mm sleeve plunge depth and 1.0 s welding time: (a) for the conventional RFSSW process with a 2500 rpm tool rotation rate; (b) the modified RFSSW with a 2500 rpm tool rotation rate; and (c) the modified RFSSW process with a 2800 rpm tool rotation rate.

Figure 5-23 shows backscattered SEM micrographs and EDS maps for a quarter of both halves of the fractured Mg to Al welds produced using the modified RFSSW, produced with the welding condition of a 2500 rpm tool rotation rate, 1.0 mm sleeve plunge depth, and 1.0 s total welding time. These images show an uneven distribution of the IMC layer over the interface of the joint. However, an important point to note is that the crack path passed through the IMC layer, not through any of the metals (Sato, et al., 2010). The evidence of this is that an IMC layer containing aluminium can be seen on the fractured surface of the magnesium sheet (Figure 5-23 b) and the same IMC layer containing magnesium can be seen on the fractured surface of the aluminium sheet (Figure 5-23 d).



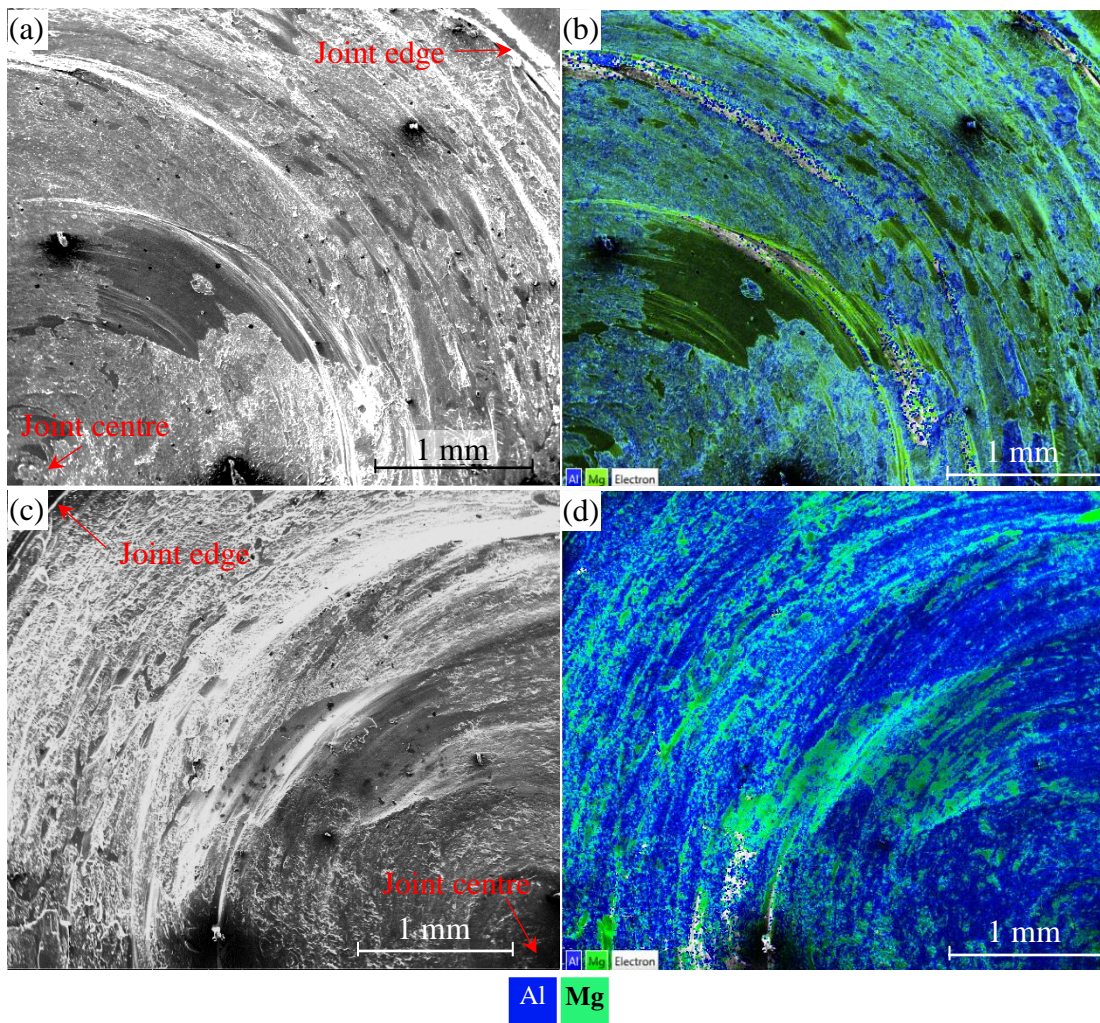


Figure 5-23: Backscattered SEM micrographs and EDS maps of a quarter of both halves of the fractured Mg to Al welds, produced using the modified RFSSW process with welding parameters of a 2500 rpm tool rotation rate, 1.0 mm sleeve plunge depth, and 1.0 s total welding time: (a) SEM micrograph of the upper sheet (Mg); (b) EDS map of the upper sheet (Mg); (c) SEM micrograph of the lower sheet (Al); (d) EDS map of the lower sheet (Al).

Unlike the fracture mode of the dissimilar Mg-Al joints, a plug pull-out fracture mode was noted under tensile lap-shear loading in all cases for the Mg-Mg joints produced using a 1.0 mm sleeve plunge depth and 1.0 s total welding time, as shown in Figure 5-24, which presents some examples of the typical failure behaviour for the Mg-Mg joints. This type of fracture mode was also reported as a typical mode observed in sound joints made from the same AZ31 alloy welded using the RFSSW technique by Campanelli et al. (Campanelli, et al., 2013a). Due to the high strength of the joint, the failure crack propagated through the thickness of either the lower or upper sheet. In this fracture mode, the hook feature has a very important influence, since the crack generally

nucleates at the tip of the hook (or at the weld defect) (Rosendo, et al., 2015) and then propagates in the same direction as the hook towards the sheet surface.

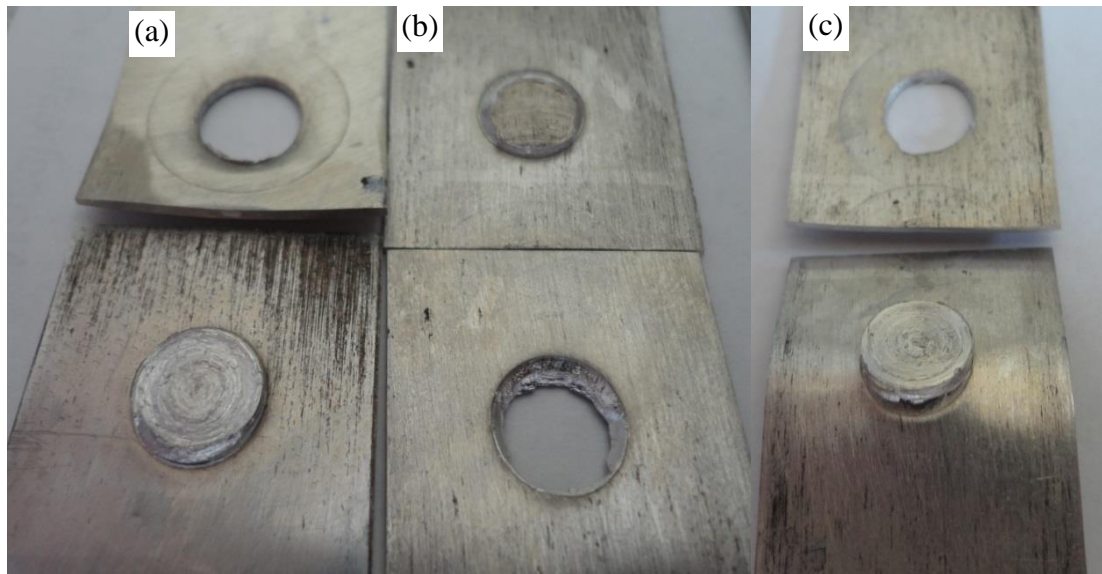


Figure 5-24: Examples of typical joint failure behaviours from similar Mg-Mg welds showing both halves of the fractured lap-shear test samples produced using modified RFSSW with a 1.0 mm sleeve plunge depth, 1.0 s welding time, and a tool rotation rates of (a) 2200 rpm, (b) 2500 rpm, and (c) 2800 rpm.

## 5.9 Summary and Conclusions

In this chapter, the RFSSW process was assessed, in terms of its ability to produce dissimilar welds between AZ31 and AA6111 alloys. The aim of the preliminary work focused on the use of this technique to obtain a sound defect-free joint. Due to the sticking of the weld nugget to the tool when welding from the side of the aluminium sheet of the dissimilar RFSSWs, which was found to always be pulled-out of its location after completion of the welding cycle, the welding configuration was adapted to weld from the magnesium side, which was found to be the best solution and resulted in a major improvement. With this alternative welding configuration, joints of thin Mg and Al sheets with acceptable mechanical properties could be achieved using a wide range of welding parameters. However, the metallographic investigation revealed unacceptably large voids at the edges of these joints. This problem was solved by adapting the welding cycle with an additional step, which involved a very quick (about 0.15 s) shallow plunge (0.2 mm) of the pin to force the material to fill the voids that remained after the refill step. This modification to the RFSSW process resulted in

almost entirely defect-free welds with improved mechanical properties using a wide range of the process parameters, especially when the optimum conditions were used (a 1.0 mm sleeve plunge depth, 2500 rpm tool rotation rate, and a 1.0 s total welding time).

To further understand the modified RFSSW process and the effect of the process parameters (sleeve plunge depth, tool rotation rate, and welding time) on joint formation, the effect of these parameters was assessed in terms of the weld's temperature histories, weld defects, and the microstructure of the interface and the subsequent effect on the mechanical properties of the dissimilar AZ31-H24 magnesium to AA6111-T4 automotive aluminium alloy joints.

The temperature measured during the cycle of the modified RFSSW process showed a rapid increase during the sleeve plunge stage of the welding cycle at a rate of about 1300 °C/s to reach a peak temperature of 495 °C, due to the use of a high plunge rate (2.5 mm/s), which led to a high plastic deformation rate. The temperature then fell to 432 °C, due to local melting of the material at the interface between the two sheets, which decreased the material viscosity and led to a fall in the generation of heat. During the dwell time, the temperature continued at approximately the same level of the eutectic reaction temperature (437 °C) suggesting that melting self-limits the heat input. However, the temperature was found to decrease during the sleeve retraction (refilling) stage, because the 'colder' material from the sleeve cavity acted as a heat sink that reduced the temperature. The final pin plunging and retraction stages showed a very slow gradual increase in temperature to about 403 °C.

The peak temperature showed a significant increase with increasing tool rotation rate from 1900 rpm to 2500 rpm, because the increase in the tool rotation rate increased the material shear rate and resulted in increased heat generation during the welding process. However, a further increase of the tool rotation rate to 2800 rpm showed less effect on the rate of increase in temperature, due to local melting of the material at the joint interface, which limited the increase in temperature and caused the formation of eutectic structures of  $\alpha$ -Mg solid solution and  $\text{Mg}_{17}\text{Al}_{12}$  at the weld interface after cooling of the molten material.

An IMC reaction layer was found to be present at the interface between the two sheets which was neither uniform in thickness, nor continuous, and showed 'islands' at the

interface. Nonetheless, in general, this layer was mainly detected at a location under the sleeve, about 2 mm from the edge of the joint. The thickness of the IMC layer showed a significant increase from about 1.7  $\mu\text{m}$  to 7.8  $\mu\text{m}$  with increasing tool rotation rate from 1900 to 2500 rpm, due to the increase in the peak temperatures of the welds, which enhanced the reaction between the two metals. Despite the increase in the peak temperature of the weld with increasing the tool rotation rate to 2800 rpm, the thickness of the IMC layer showed a rapid decrease to about 2.8  $\mu\text{m}$ , because of the onset of significant eutectic melting and dispersal of the eutectic liquid due to the tool pressure. However, overall the rapid dissimilar joints of Mg to Al produced using the modified RFSSW process yielded a much thinner reaction layer compared to that reported in other studies; for example a total thickness of the IMC phases of about 500  $\mu\text{m}$  has been reported for Al to Mg dissimilar joints produced using the RFSSW process by Suhuddin et al. (2013 b). The IMC layer was found to be composed of two sub-layers: an Al-rich layer on the aluminium side composed of a  $\beta\text{-Al}_3\text{Mg}_2$  phase, and an Mg-rich IMC layer on the side of magnesium, composed of a  $\gamma\text{-Al}_{12}\text{Mg}_{17}$  phase.

The microhardness of the AA6111-T4 aluminium alloy in the as-welded condition showed a W-shaped profile across the weld. The SZ showed an average microhardness of about 63 HV, while the HAZ reached a minimum value of about 52 HV, compared to an average hardness of about 89 HV for the base material. The decrease in hardness level in the HAZ is associated with the intermediate temperatures reached in this region, which led to coarsening and dissolution of the strengthening particles. Due to the high strain rate and the higher temperature reached in the SZ, dynamic recrystallisation and grain refinement occurs in this region, as well as full solutionisation and subsequent natural ageing. Therefore, the SZ showed a greater hardness level than the HAZ. In contrast, no HAZ could be detected in the AZ31 magnesium alloy sheet, because this alloy is non-heat-treatable. Nonetheless, the SZ showed an average microhardness level of about 60 HV, compared to an average microhardness of about 55 HV in the base metal. The main reason for this effect is the high deformation rate and the high temperature (about 490 °C), which led to dynamic recrystallisation and grain refinement.

Load-extension curves of the Mg-Al samples produced using the modified RFSSW process showed a two-step failure process with a transition between a fully brittle failure, shown by the samples produced using conventional RFSSW, and a ductile



failure, shown by the similar Mg-Mg joints. Generally, the dissimilar joints showed an interfacial fracture mode under lap tensile-shear test loading due to the presence of voids, and an IMC layer, or eutectic structure, at the interface of the joint, depending on the process variant used and the welding parameters. However, joints produced using the modified RFSSW process with the optimum welding parameters (2500 rpm, 1.0 s, and 1.0 mm) showed a partial nugget pull-out failure mode and had high strength.

The average peak load increased with increasing tool rotation rate, to reach a maximum value at 2500 rpm, and decreased on further increasing of tool rotation rate to 2800 rpm. This result is likely due to two competing factors: the material flow, which is affected by the material plasticity, and the formation of the IMC layer and the eutectic structure at the joint interface. Both of these factors are affected by the heat generation. Lower heat is generated when using low rotation rates and results in the formation of voids because the material plasticity is insufficient. Increasing the tool rotation rate increased the material plasticity and the thickness of the IMC layer, as well as promoting eutectic melting, which reduced the strength of the joint. Therefore, the balance between these two factors resulted in the optimum weld conditions (2500 rpm, 1.0 s, and 1.0 mm) for the modified RFSSW with an average peak load of 2.4 kN and average fracture energy of 1.3 kN.mm, which represents an improvement of about 10 % and 27 %, respectively, compared to welds produced using the conventional RFSSW process. The main reason for this difference is that the modified process resulted in defect free samples when using the optimum conditions. Moreover, these values represent about 112 % of the average peak load and about 78 % of the fracture energy of Mg-Mg similar joints produced using the same welding conditions.



## **Chapter 6: FE Modelling of the Mechanical Behaviour of Refill Friction Stir Spot Welds (Al-Al and Mg-Al)**

---

### **6.1 Introduction**

This chapter presents the results of a numerical investigation, based on finite element modelling (FEM), which aimed to model the mechanical behaviour of similar AA6111-T4 aluminium and dissimilar AA6111-T4 aluminium to AZ31-H24 magnesium lap joints, produced using RFSSW, under ‘simple’ lap-shear tension test loading conditions. The main aim of this work was to help improve understanding of the failure behaviour of dissimilar joints in lap shear tests and to see if the use of dissimilar materials could affect the stress state generated within the test itself.

The chapter starts by outlining the characteristics of the model used to define the geometry of the lap-shear sample. This section includes details of the geometries and dimensions of the weld regions (SZ, TMAZ, HAZ, and BM), which were taken from the results of material flow experiments for similar and dissimilar welds. The following section reviews results of the simulation of the mechanical properties of different regions by using the output of the microhardness tests, different heat treatments, and a simple uniaxial tension test. To complete the model, the next step involved the assembly of the parts and setting the contact conditions between them, in addition to assigning the mesh geometry and boundary conditions for all samples. Finally, the results obtained from the models will be discussed and compared with the experimental results.

### **6.1 Model Characteristics**

In order to simulate the RFSSW joint behaviour under lap-shear loads, a full model of the test specimen was developed. To reduce the total number of finite element calculations and consequently reduce the computational resources required for the numerical simulation, just one-half of the actual lap-shear sample (see Figure 3-11) was modelled, due to the symmetry of both its geometry and the loads about the x-y plane. Model containing the geometry of the 3D solid component partitions, their assembly, and specification of the contact condition between them, in addition to the mesh characteristics and boundary conditions, were carried out using Abaqus-CAE software.

### **6.1.1 Geometry and Dimensions of the Similar Al-Al Lap-Shear Specimen and Weld Regions (SZ, HAZ, BM)**

Because the weld regions develop different material properties after welding, the modelled RFSSW joint of the similar Al alloy specimen was composed of five different parts: the lower and upper parent sheet, the heat affected zone of the lower and upper sheet (HAZ lower and HAZ upper), and the stir zone (SZ), as seen in the sample configuration shown in Figure 6-1. The geometry and dimensions used for each part in the model were identical to the dimensions used to produce the samples in the experimental work for the weld to which each model was compared. The first and second parts are the lower and upper sheets (see Figure 6-1 a and b). Both of them had a rectangular shape with dimensions of 100 x 25 x 1.0 mm. Two spacers with a length of 25 mm were used at each end of the samples, similar to in the real mechanical tests (see Figure 3-11) for the purpose of preventing the misalignment of the sheets during testing; these spacers were assumed to be tightly connected to the sheets. Each of the two sheets also contained a hole with a diameter of 17 mm, which represented the location where the other material partitions were located to represent the weld zones (e.g. HAZ).

The third and fourth parts of the model were the HAZ of the lower and upper sheets; their dimensions were confirmed from the hardness distribution around the SZ, which was discussed in section 4.6. However, the geometries of the two HAZs were different. The upper HAZ region was assumed to have a constant width around the SZ; with a hollow disc shape (see Figure 6-1 e) as the sheet thickness was only about 1.0 mm, therefore the small difference in hardness value through the thickness was neglected (see Figure 4-20). On the other hand, the lower HAZ was also defined with a disc shape, but with a central feature with an almost semi-spherical shape. This shape corresponded to the hole remaining when the SZ was removed (see Figure 6-1 d). This shape was adopted to be as close to that of the stir zone nugget shape as possible (see Figures 4-3 and 4-4).

The last and most important part was the stir zone (SZ), or spot weld nugget (see Figure 6-1 f). Two factors were used to identify the geometry and dimensions of this region. The first factor was the different local mechanical properties of the material, as measured by the microhardness measurements in Figure 4-20. The SZ geometry determined by using this factor was found to be a simple disc shape, as can also be seen

in the work of Mazzaferro et al. (2009); Campanelli et al. (2013b); Rosendo et al. (2015). The second factor, which was used in this project to identify the geometry and dimensions of the SZ, was the observation from the material flow experiments (see section 4-3), where the deformation patterns showed that the SZ had a shape of a convex lens (see Figures 4-3 and 4-4).

An idealised welded joint was assumed to be free from any weld defects, such as voids, incomplete refill, the lack of mixing, or partial bonding. However, to simulate the effect of the critical specific weld defect (a hook), a modified model was also developed containing a hook, by bending the interface between the upper and lower HAZs near the SZ down, as shown in Figure 6-2. The surfaces of the upper and lower sheets in the hook region were assumed to be completely separated so this represented an extreme case as partial metallurgical bonding can occur across the hook (Cao, et al., 2016). The geometry and dimensions of the hook were taken from Figure 4-10 c.

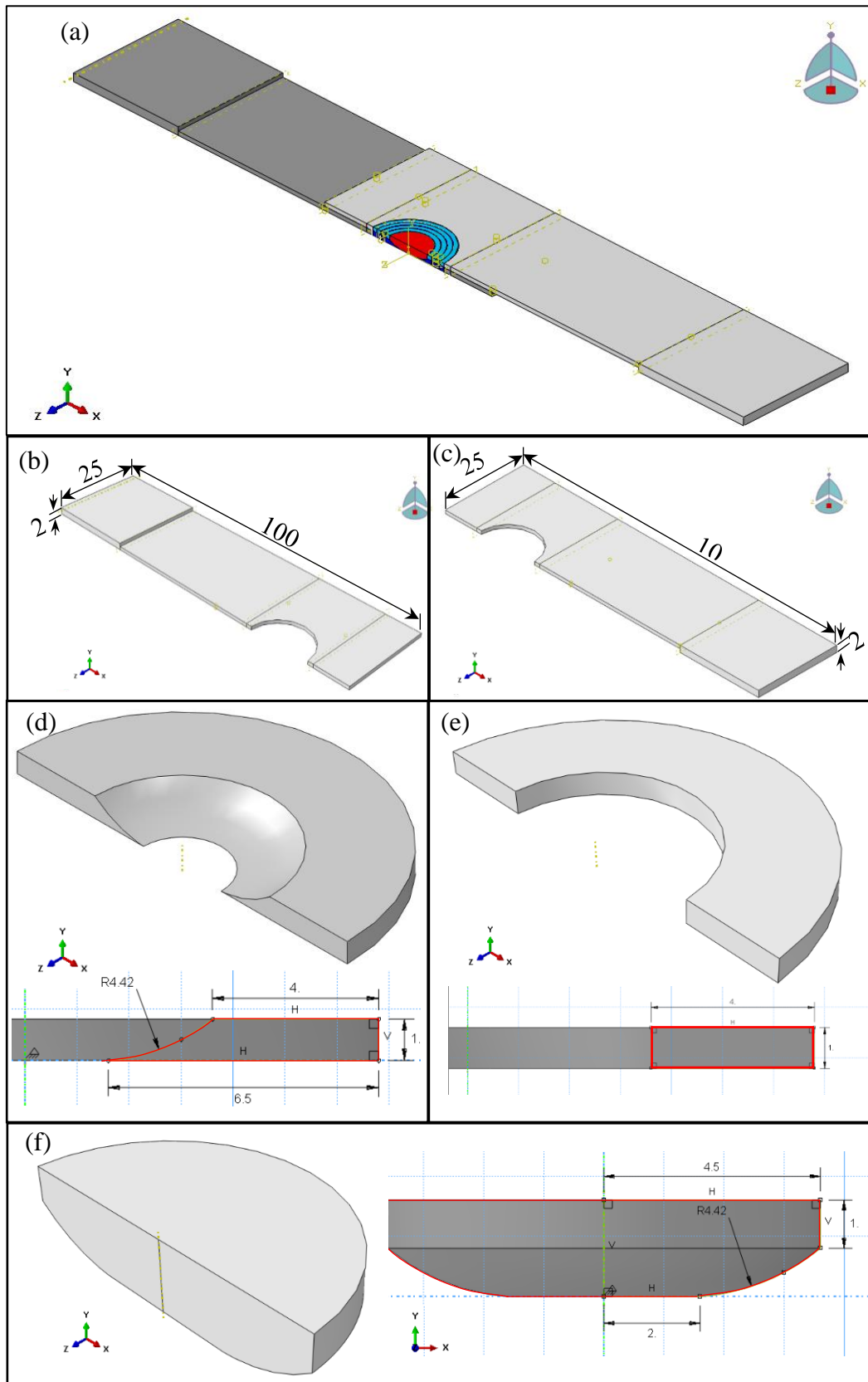


Figure 6-1: Geometry definition of the different material partition zones used for the similar AA6111 aluminium alloy RFSSW joint model of the lap-shear test: (a) full sample, (b) lower sheet with spacer, (c) upper sheet with spacer, (d) HAZ of the lower sheet, (e) HAZ of the upper sheet, and (f) the SZ.

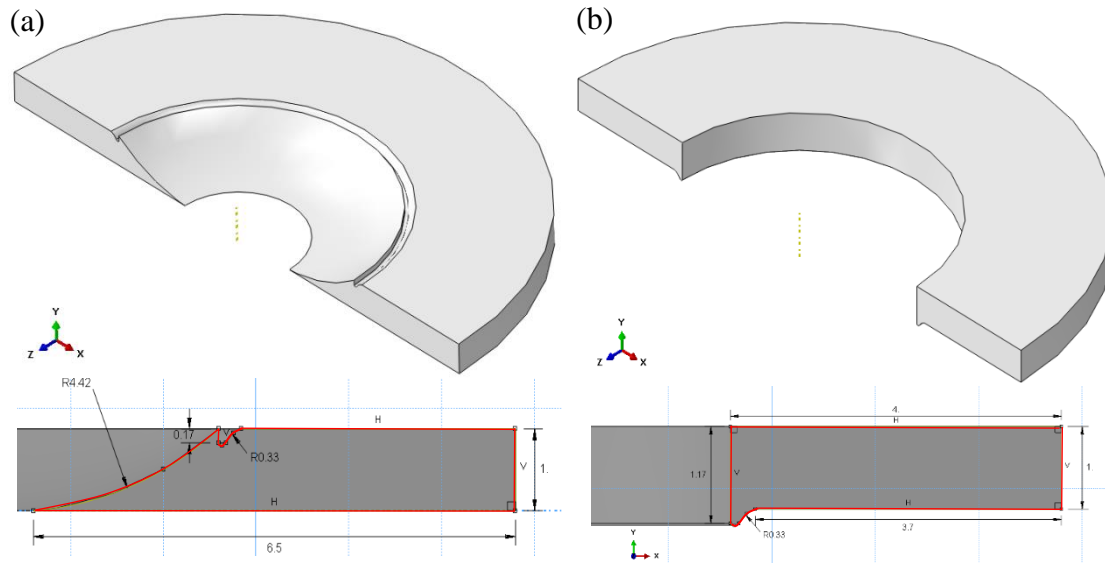


Figure 6-2: Geometry definition of the heat-affected zones for a similar RFSSW joint of AA6111 aluminium alloy for modelling a lap-shear test, showing the detail of the hook defect: (a) lower sheet, and (b) upper sheet.

### 6.1.2 Geometry and Dimensions of Dissimilar Mg-Al Lap-Shear Specimen and Weld Regions (SZ, HAZ, BM)

Since the AZ31 magnesium alloy, used in the dissimilar joints of Mg to Al produced using the RFSSW process was a non-heat-treatable, the modelled specimen, in this case, was composed of five different parts: the lower and upper sheet, lower HAZ, stir zone (SZ) of the upper sheet (Mg alloy), and the stir zone (SZ) of the lower sheet (aluminium alloy). The geometry and dimensions used for both the lower and upper sheets were identical to those used for the model of the Al-Al similar joint, except that the half-width was adjusted to 12.5 mm because the different sample dimensions used in this test to save material. Moreover, two spacers with the same configuration stated in section 6.1.1 were also used.

The main difference between the models of the similar and dissimilar joints was that, as can be seen from Figure 6-1, the SZ of the similar was weld composed of one part. However, the SZ in the model for the dissimilar joints was split into two distinct parts, because unlike during welding similar metals, the two materials did not greatly mix during the welding cycle. Again, the geometry and dimensions of both SZs were taken from the metallographic investigations for the weld cross-section (see Figures 5-6, 5-7,

and 5-10). The lower SZ (Figure 6-3 a) had a disc shape and was slightly lower in height than the lower sheet in the outer region of the zone, while the centre was given a slightly higher curved feature, to correspond the material displaced during the sleeve plunging stage of the weld cycle. The upper SZ (Figure 6-3 b) also has a disc shape, but with a concavity in the centre to match the shape of the lower SZ.

To simplify the model, it was assumed that there was no IMC layer at the joint interface and the joint was free from any weld defects, such as voids or partial bonding.

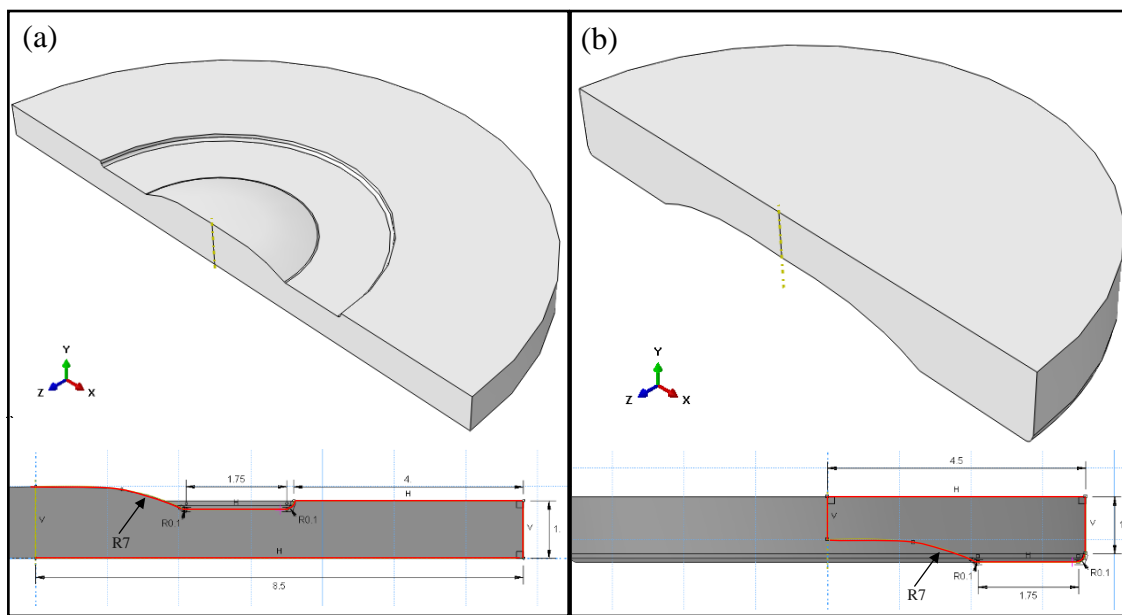


Figure 6-3: Geometry definition of the SZ of the dissimilar AZ31 magnesium to AA6111 aluminium alloy RFSSW joint, for modelling the lap-shear test: (a) the lower part of the SZ and HAZ of the lower aluminium sheet with the HAZ of the lower sheet, (b) the upper part of the SZ (magnesium side).

## **6.2 Material Properties**

### **6.2.1 Al-Al welds**

As stated in chapter 4, the RFSSW joint and the adjacent regions in the as-welded condition can be divided into four distinct regions, in terms of their microstructure and material properties: the SZ, TMAZ, HAZ and the BM (see sections 2.10, 4.5, and 4.6). It is difficult to evaluate the material strength of the SZ, TMAZ and HAZ regions because they are narrow and show gradients in microstructure (Nguyen, et al., 2011). However, the local mechanical properties can be assessed using the Vickers microhardness test (see section 4.6). Figure 6-4 shows hardness profile across an optimised joint produced using RFSSW with welding parameters of a 1.0 mm plunge depth, 2000 rpm tool rotation rate, and 1.0 s welding time. These welding parameters were used because they represented the average of the optimum tool rotation rates and welding times, respectively, used to produce Al-Al joints in this study (see Table 4-1). As can be seen in Figure 6-4, the hardness profile across the weld show a typical W-shape in the as-welded condition, whereas the SZ showed an almost constant hardness level. On the other hand, the hardness showed a rapid gradient in the TMAZ and HAZ regions between the level of the base material, which exhibited an average hardness value of about 89 HV, and the hardness minima of about 59 HV at a point near the nugget.

To simulate the material properties in these regions in the finite-element model used in this study, the TMAZ and HAZ were assumed to be one region, in terms of their mechanical properties, since the width of the TMAZ was less than 0.2 mm. Due to the very large gradient in the hardness of the HAZ, which was expected to result in high stress concentration in the model when moving from the BM to the SZ, the HAZ was further divided into four sub-regions with a step difference in hardness level of about 10%. On the other hand, the hardness levels of the BM and SZ could be assumed to be constant at a level of 89 HV and 66 HV respectively, as shown in Figure 6-4.

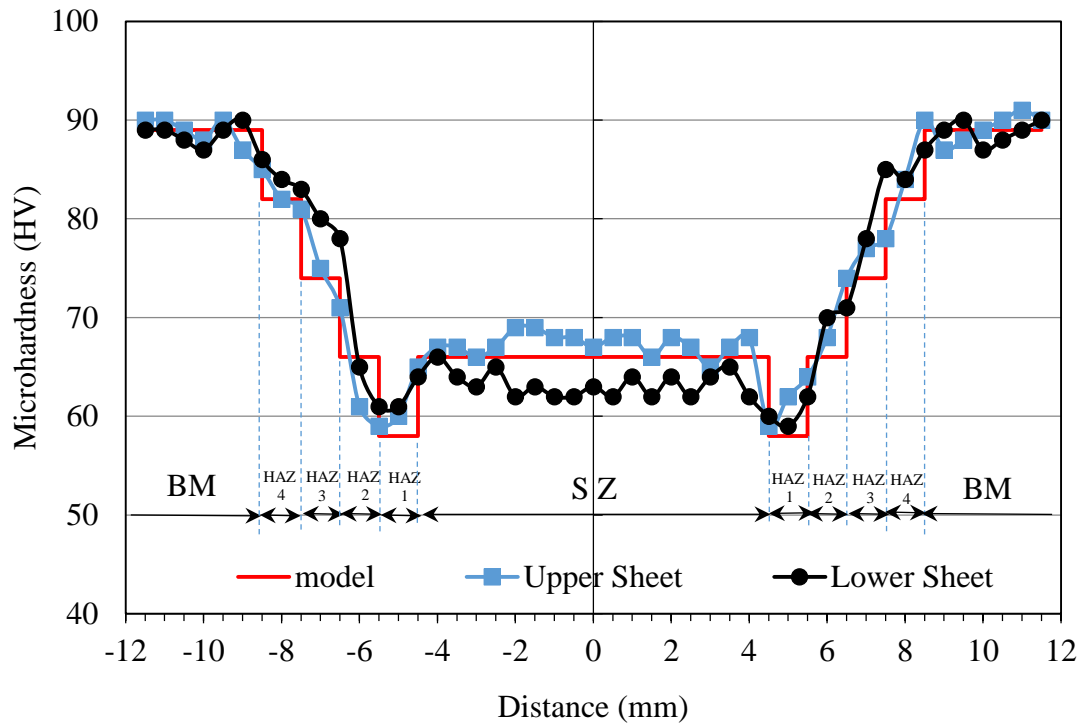


Figure 6-4: Hardness profiles of an RFSSW joint produced using a 2000 rpm tool rotation rate, 1.0 s welding time and 1.0 mm sleeve plunge depth, measured immediately after welding (within one hour), showing the partitioning used of the material properties in the FE simulations.

Heat-treatments were also implemented on several AA6111 samples to simulate the hardness level for each region in tensile test samples. Initially, the heat-treatments were carried out using the corresponding peak temperature measured in each region (as discussed in section 4.4, see Figure 4-6). Unfortunately, the control of the hardness level when using these heat treatments was very difficult and all the samples showed nearly the same highly over-aged minimum hardness level (under 60 HV) even when applying a heat-treatment for time periods as short as 1.0 s. Therefore, another approach was used, involving a new heat-treatment that included the solution-heat-treatment for samples at 500 °C for 20 min. and quenching in water, followed by artificial ageing at 140 °C for different times (0, 25, 45, and 53 min.). These heat treatments resulted in samples with the required hardness levels of about 58, 66, 74, and 82 HV, which represent the hardness levels of the HAZ sub-regions and the SZ.

To convert the hardness measurements to tensile stress-strain data, the next step was to prepare several standard tensile test samples from the AA6111-T4 aluminium alloy. Some of these samples were heat-treated using the treatments explained above, to obtain



the required hardness levels. Other samples were kept in the as-received condition (AA6111-T4) to simulate the mechanical properties of the BM. To implement the tensile test, the samples were tested using the same machine and test parameters used for the welded samples; which were a crosshead travel speed of 1.0 mm/min and the data was collected at 50 Hz (see section 3.7 for further details). The resultant engineering stress-strain curves of the samples following the above heat-treatments (SHT at 500 °C for 20 min. + artificial ageing at 140 °C for 0, 25, 45, and 53 min.) in addition to a sample in the T4 condition, are shown in Figure 6-5.

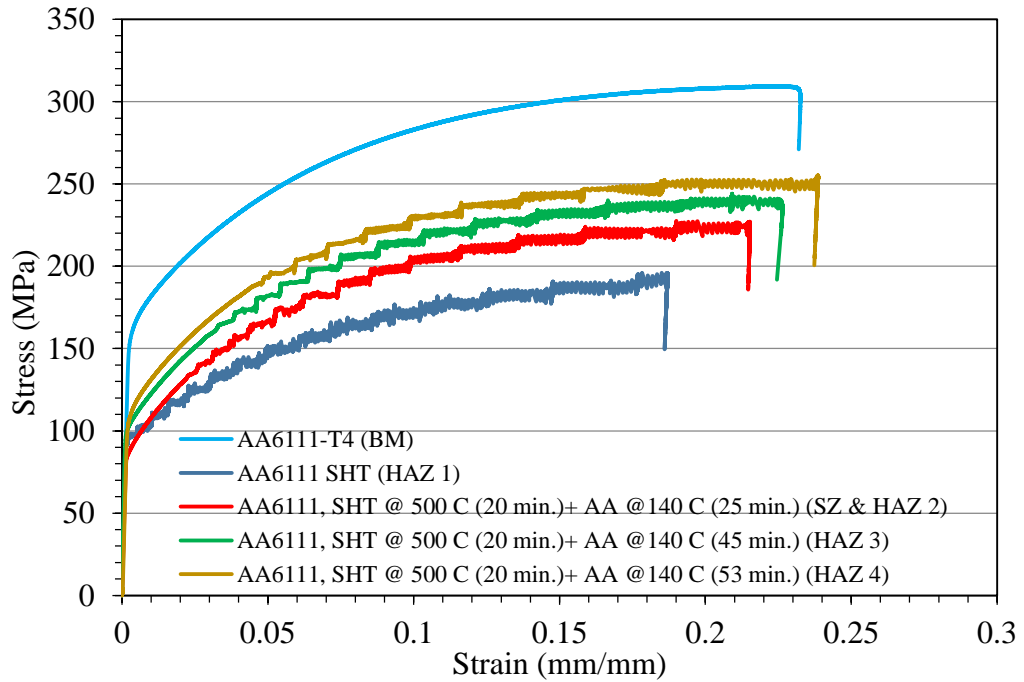


Figure 6-5: Stress-strain curves for AA6111 aluminium alloy heat-treated using different treatments. Samples were tested immediately after heat treatment (within one hour).

Equations 6-1 and 6-2 (Ling, 1996) were then used to transform the engineering stress-strain curves to true stress-strain curves, which were required to extract the data for the model.

$$\epsilon_{\text{true}} = \ln(1 + \epsilon_{\text{eng.}}) \quad \text{Equation 6-1}$$

$$\sigma_{\text{true}} = \sigma_{\text{eng.}}(1 + \epsilon_{\text{eng.}}) \quad \text{Equation 6-2}$$

where:  $\epsilon_{\text{true}}$ : True strain  
 $\epsilon_{\text{eng.}}$ : Engineering strain  
 $\sigma_{\text{true}}$ : True stress  
 $\sigma_{\text{eng.}}$ : Engineering stress

To define the material property in the model, separate curves had to be fitted for the elastic region and plastic region. Therefore, the offset yield point was located using 0.2% of the plastic strain. From the elastic region, the only data required were the elastic modulus ( $E=70$  GPa) and Poisson's ratio ( $\nu = 0.33$ ). On the other hand, for the plastic deformation region smooth-curves of this region were fitted to eliminate the fluctuations in stress due to the Portevin-Le Chatelier effect, which is a well-known phenomenon in 6000 series of aluminium alloy (McCormick, 1971), as seen in Figure 6-6. The fitting process reduced the number of data points from several thousand to only a hundred points. However, the total number of data points was then reduced again to eleven points for each curve, to reduce the time required to process the model, as seen in Table 6-1.

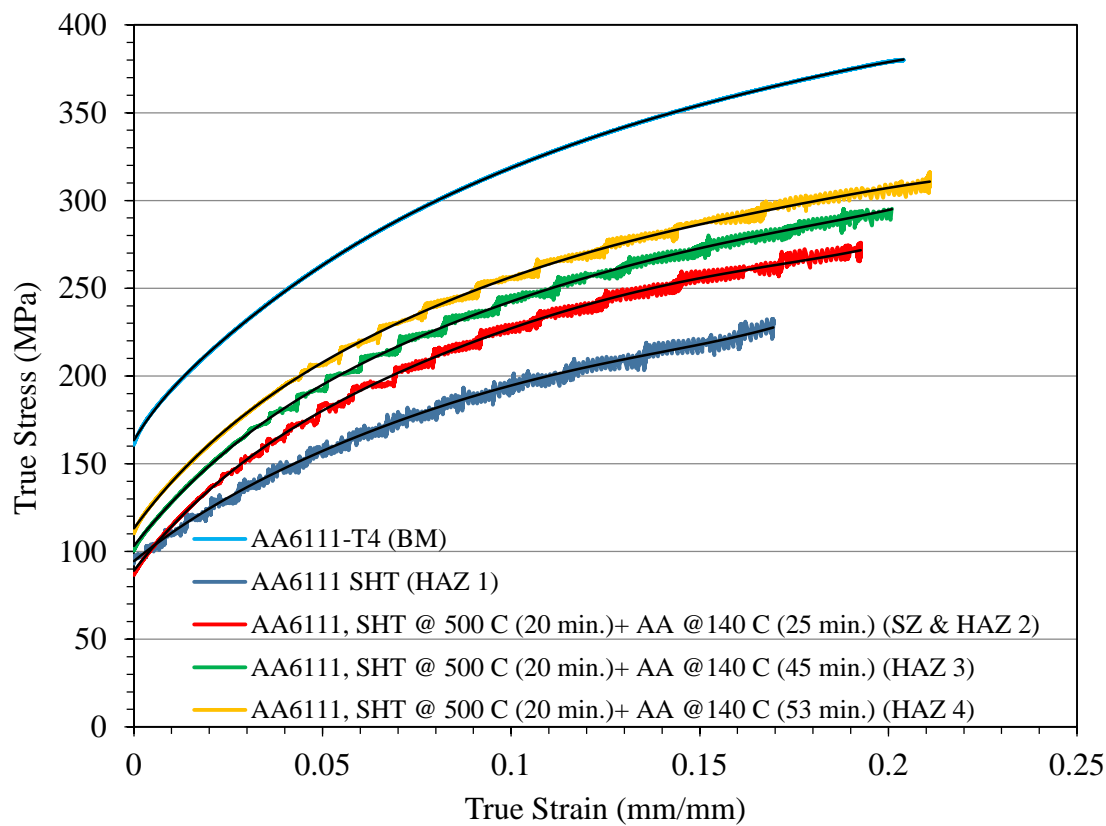


Figure 6-6: Plastic region of the true stress-strain curves and their curve fits (black lines) for AA6111 aluminium alloy heat-treated using different treatments. Samples were tested immediately after heat treatment (within one hour).

To simulate the mechanical properties of the RFSSW joint after the paint-bake treatment, the same procedures used for the joint in the as-welded condition was used. Figure 6-7 shows the hardness profile for an RFSSW joint produced using welding parameters of a 2000 rpm tool rotation rate, 1.0 s welding time, and 1.0 mm sleeve

plunge depth, after artificially ageing at 180 °C for 30 min. This figure reveals that after the simulated paint-bake treatment the SZ had a significantly higher hardness level than the adjacent regions. Therefore, by using a step difference in hardness level of about 10%, the hardness profile was divided into three regions, namely the SZ (art. aged), HAZ 1 (art. aged), and BM (art. aged).

Table 6-1: True stress-strain data used for modelling the RFSSW joint in the as-welded condition.

T4 (BM)		SHT (HAZ 1)		SHT @ 500 °C, 20 min. + art. ageing @ 140 °C, 25 min. ( SZ & HAZ 2)		SHT @ 500 °C, 20 min. + art. ageing @ 140 °C, 45 min. (HAZ 3)		SHT @ 500 °C, 20 min. + art. ageing @ 140 °C, 53 min. (HAZ 4)	
Strain	Stress (Pa)	Strain	Stress (Pa)	Strain	Stress (Pa)	Strain	Stress (Pa)	Strain	Stress (Pa)
0	163406000	0	94474900	0	89046600	0	103179000	0	113158000
0.0103	192964000	0.00856	108403000	0.00973	113599000	0.01015	128314000	0.01066	141047000
0.02988	231247700	0.024824	130326000	0.028219	149154100	0.029432	165214400	0.030901	180019000
0.050488	263529100	0.041946	149315900	0.047681	177097900	0.049725	194362000	0.052211	210153000
0.071094	289746400	0.059066	165249600	0.067141	198750900	0.070025	216742500	0.073522	233431400
0.0917	310956300	0.076186	178870000	0.086603	216493000	0.090325	234804700	0.094833	252232100
0.11231	328696900	0.093306	190477400	0.106065	231373200	0.110615	249880200	0.116143	267533300
0.132916	343681700	0.110428	200219700	0.125526	243673100	0.130915	262595200	0.137454	279971500
0.153521	356270000	0.127548	208379800	0.144987	253467900	0.151215	273285900	0.158765	290328400
0.17413	367243400	0.144668	215664500	0.164449	261190800	0.171508	282411400	0.180076	299446300
0.20401	380349000	0.16949	227616000	0.19267	271641000	0.20094	295003000	0.21098	310743000

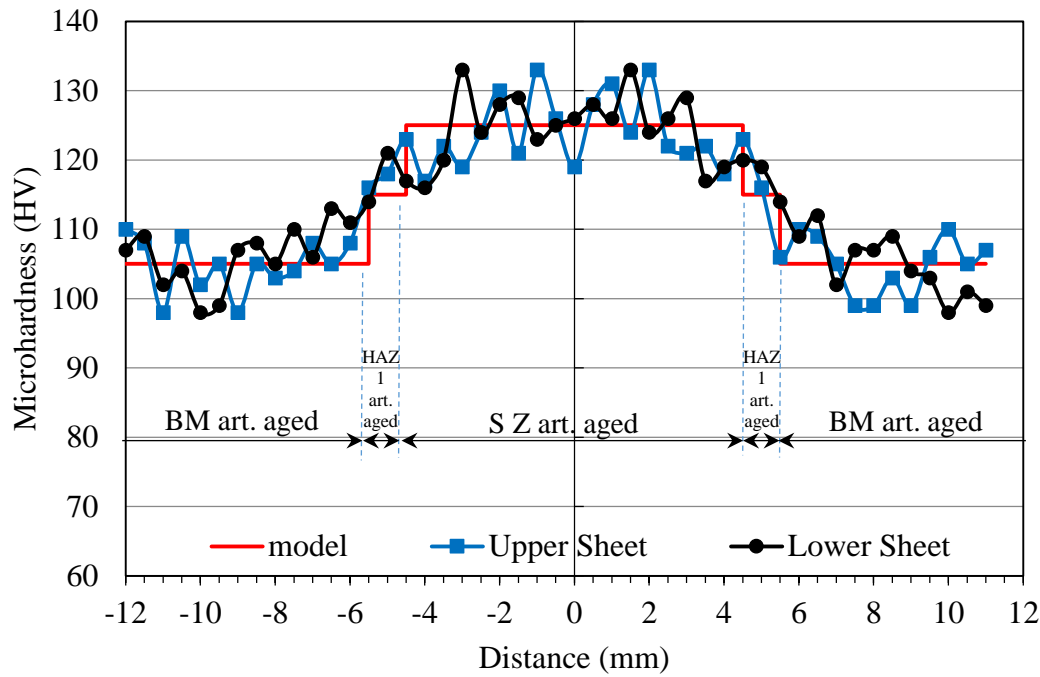


Figure 6-7: Hardness profiles of an RFSSW joint produced using a 2000 rpm tool rotation rate, 1.0 s welding time, and 1.0 mm sleeve plunge depth. The sample was artificially aged at 180 °C for 30 min. immediately after welding (within one hour).

To achieve the required hardness levels in tensile test samples for each of these weld zones, three heat-treatments were implemented. The first heat-treatment included artificial ageing of the samples in the as-received (T4) condition at 180 °C for 30 min.; to simulate the effect of the paint-baking treatment on the BM. The second and third heat-treatments were implemented to simulate the mechanical properties of the HAZ 1 and SZ after heat-treatment, and included solution-heat-treatment at 500 °C for 20 min. followed by artificial ageing at 180 °C for 20 and 30 min., respectively.

The tensile samples were then tested using the same test procedure stated above and the resultant engineering stress-strain curves are shown in Figure 6-8 a. These curves were also transformed to the true stress-strain curves using equations 6-1 and 6-2 (see Figure 6-8 b). The next step was fitting of the plastic regions of each curve and reducing the number of data points to eleven for each curve, as seen in Table 6-2.

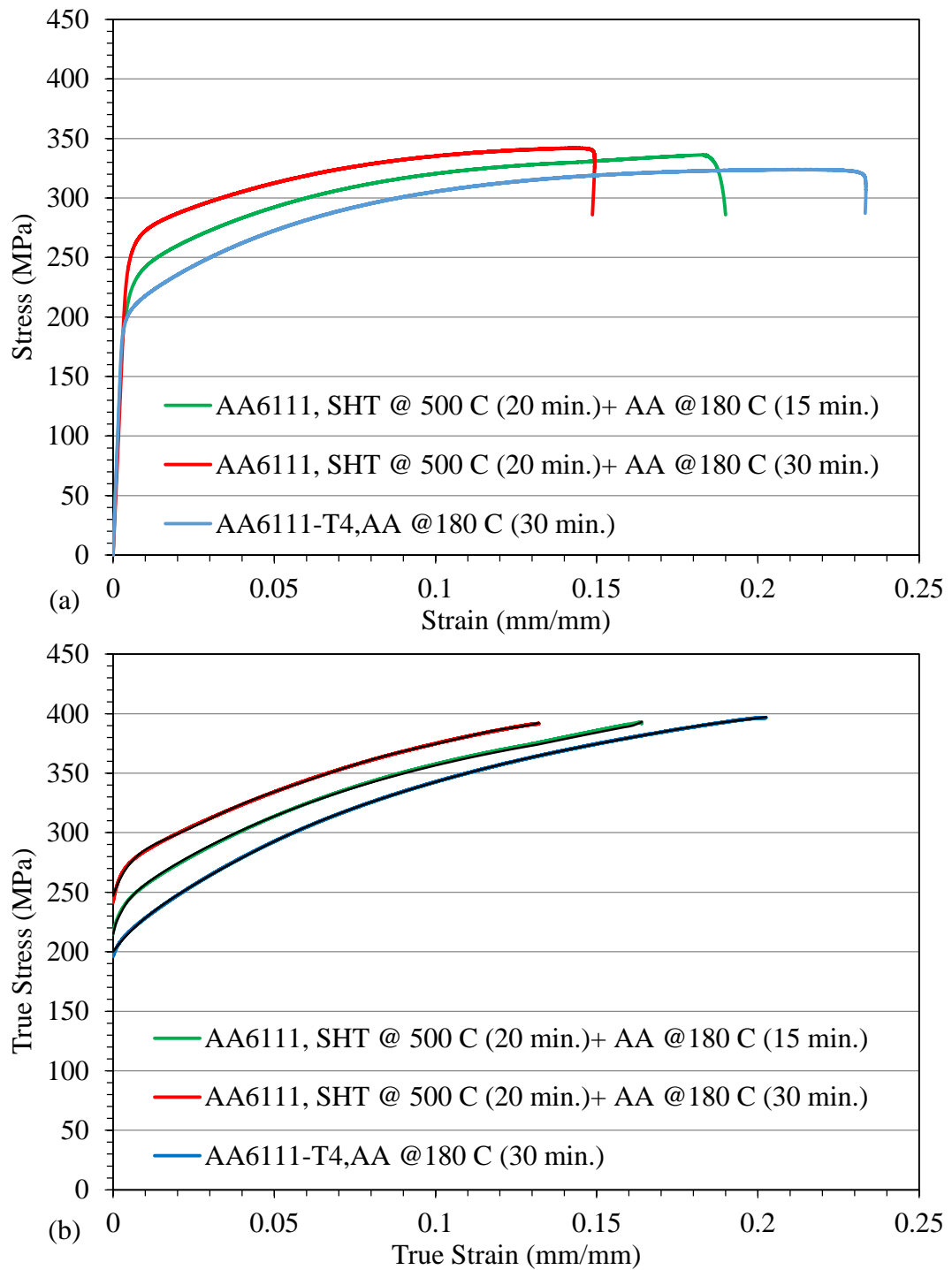


Figure 6-8: Stress-strain curves for the simulated paint-baked for the AA6111 aluminium alloy weld zones. Samples were tested immediately after heat treatment (within one hour): (a) engineering stress-strain, and (b) plastic region of the true stress-strain curves and their curve fits (black lines).

Table 6-2: True stress-strain data used for modelling the RFSSW joint in the paint-baked (artificially aged) condition.

T4 + art. aged @ 180 °C 30 min.		SHT @ 500 °C, 20 min. + art. aged @ 180 °C, 15 min. (HAZ 1 art. aged)		SHT @ 500 °C, 20 min. + art. aged @ 180 °C, 30 min. (SZ art. aged)	
Strain	Stress (Pa)	Strain	Stress (Pa)	Strain	Stress (Pa)
0	200221000	0	215311000	0	247077000
0.01023	228886000	0.001218	226027340	0.00667	278495000
0.029667	263276000	0.003931	240020230	0.019345	298275000
0.050127	292585600	0.012069	260663200	0.032687	315103200
0.070586	316277900	0.033771	294143070	0.046027	330308900
0.091045	335221700	0.055473	319666200	0.059369	343125700
0.111505	351136500	0.077175	339813420	0.072711	355106500
0.131965	364516500	0.098877	355764130	0.086052	365588000
0.152425	375731300	0.120579	368517610	0.099393	374245800
0.172885	385763300	0.142281	379914240	0.112735	382505700
0.20255	397113000	0.163983	393067560	0.13208	392283000

### 6.2.2 Mg-Al welds

The hardness profile across a typical Mg-Al dissimilar RFSSW joint in the as-welded condition shown in Figure 5-5. This revealed that only the aluminium lower sheet showed a significant change in hardness level, while the difference in the average hardness between the SZ of the magnesium side and the other region of the magnesium sheet (BM) was less than 10 %. Therefore, the aluminium lower sheet was assumed to have the same partitions and the corresponding material properties as that used in the model for the similar Al-Al joints, in the as-welded condition, as discussed in section 6.1.1. As the Mg side of the joint showed little hardness variations, all the regions of the magnesium side of the weld were assumed to have the same elastic-plastic properties as the as-received AZ31-H24 alloy.

Several samples were produced and the tension test was implemented using the test procedure discussed in section 6.2.1. Figure 6-9a shows the stress-strain curve for the AZ31-H24 magnesium alloy, and Figure 6-9b shows the plastic region of the true stress-strain curve for the same alloy in addition to the fitting curve. Table 6-3 shows the data used in the model after reducing the total number of points to eleven only.

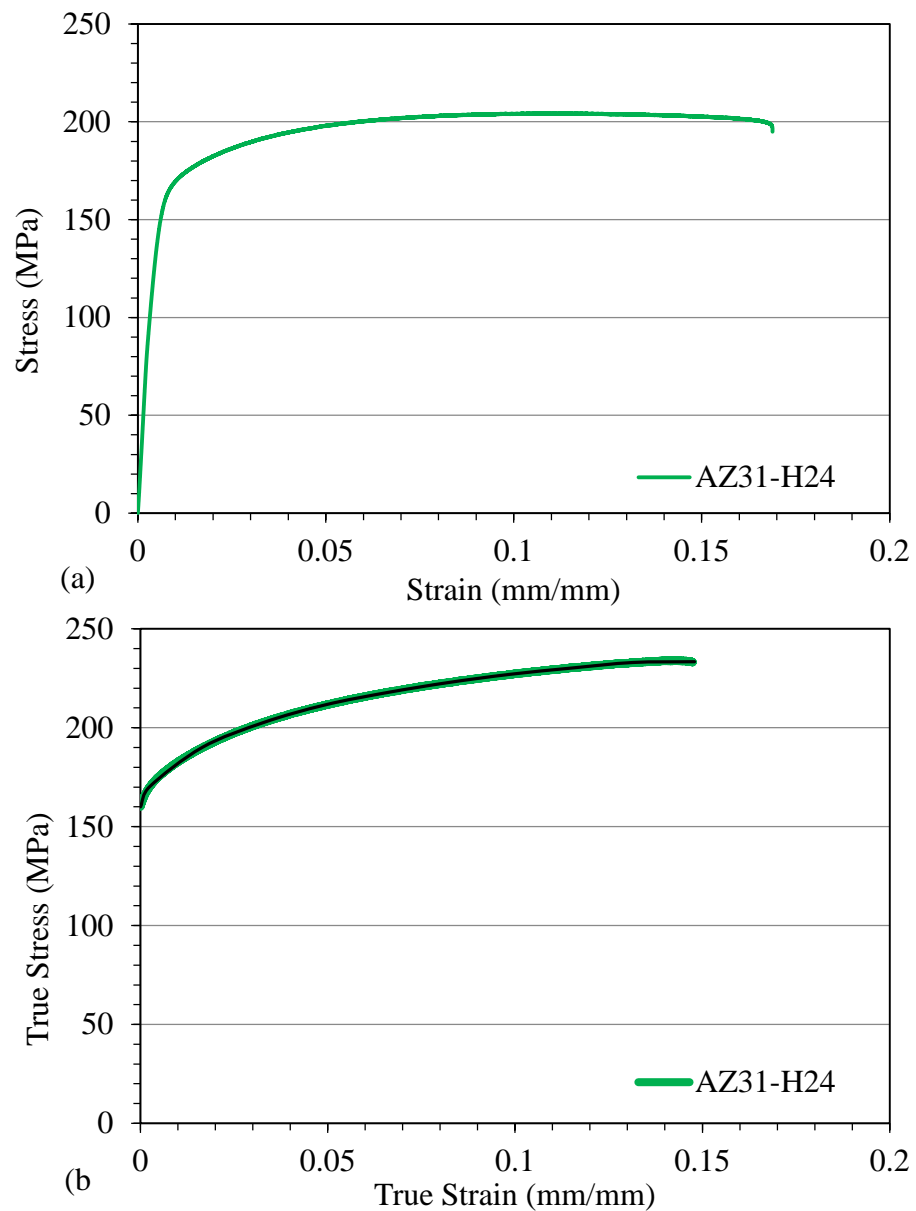


Figure 6-9: (a) Stress-strain curve for the AZ31-H24 magnesium alloy, and (b) plastic region of the true stress-strain curve for the AZ31-H24 magnesium alloy and its curve fit.

Table 6-3: True stress-strain data used for modelling the AZ31-H24 magnesium alloy in the dissimilar RFSSW joint of Mg-Al.

AZ31-H24	
Strain	Stress (Pa)
0	160000000
0.002419964	170171364
0.01644	190024860
0.03287	202656330
0.04931	211565340
0.06574	217749990
0.08218	222850120
0.09861	227000430
0.11505	230180440
0.13148	232991810
0.14792	233380470

### **6.3 Boundary Loading Conditions in the Model**

To simulate the actual situation of the lap- tensile shear test, the model was assumed to be subjected to a displacement/rotation type boundary condition. An extension was applied at one of the ends of the welded sample while the other end was fixed.

Therefore, three boundary conditions were applied to the model: two to simulate the gripping of the fixed end and the pulled end and the third for the plane of symmetry, as seen in Figure 6-10 a. The boundary conditions of the fixed end, which represents the end of the lower sheet and the spacer (highlighted by a red box in Figure 6-10 b), were restricted in all degrees of freedom (i.e.  $U_1 = U_2 = U_3 = 0$ ).

For the simulation of the tensile displacement in the lap shear test, loading on the samples was not directly defined using an applied force, but through the use of an extension condition by pulling one of the sample ends, in order to replicate the experimental test conditions. At the pulled end, which represents the end of the upper sheet (the spacer and highlighted by a red box in Figure 6-10 c), the motion was restricted in all directions (i.e.  $U_2 = U_3 = 0$ ) except in the direction of the applied load. The maximum extension in the x-direction was assumed to be 1.5 mm. This value was chosen because it was higher by 20% than the maximum extension at peak fracture load for most of the experimentally tested samples. The velocity of the pulled end was set to  $1.0 \text{ mm.min}^{-1}$ , which is equal to the travel speed of the moving cross-head during the lap tensile-shear tests. It should be noted that the effect of gravity was neglected because it was very small compared to the load applied during the test.

As mentioned in section 6.2, due to the symmetry of the geometry of the sample about the x-y plane and the uniaxial loads in the x-direction, only one-half of the actual lap-shear sample was modelled to reduce the computational resources required for the numerical simulation and the time of calculation. To simulate the symmetry of the sample, the motion of the plane of symmetry (surfaces highlighted in red in Figure 6-10 d) in the z-direction was restricted (i.e.  $U_3 = 0$ ).



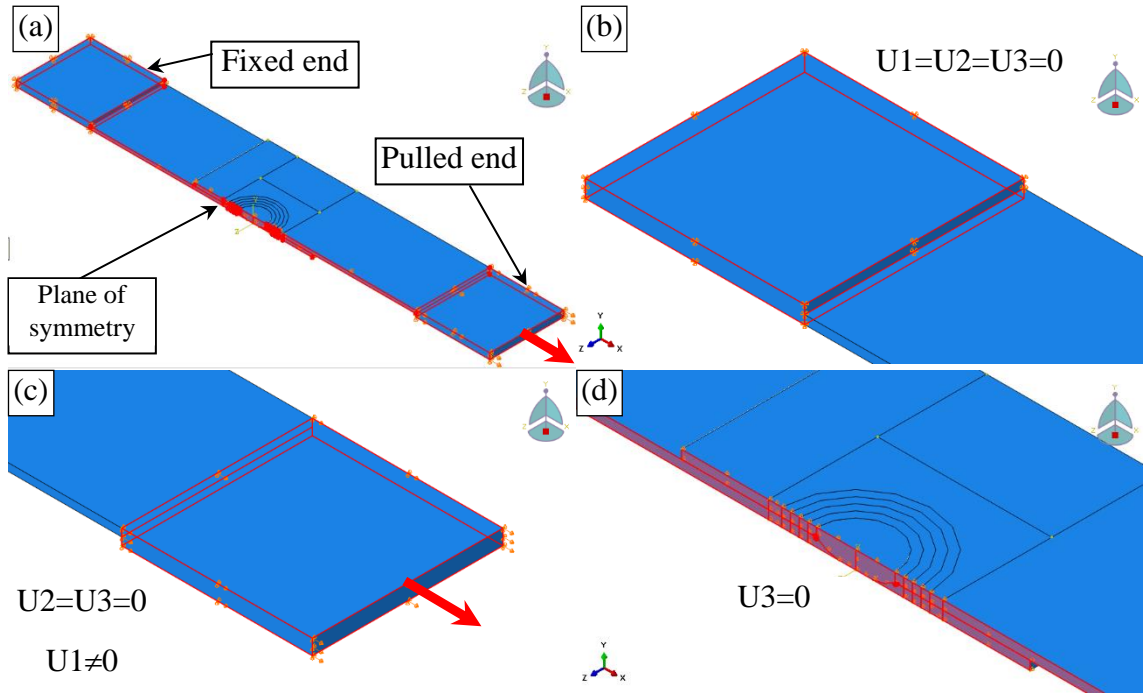


Figure 6-10: Boundary condition applied to the model: (a) full sample with boundary conditions, (b) fixed end (lower sheet), (c) pulled end (upper sheet), and (d) plane of symmetry (XY plane).

## 6.4 Mesh building

A tetrahedral structured mesh was created in all the regions of the welded joint where ten-node C3D10M elements were used (see Figure 6-11). The tetrahedral elements were used because they are geometrically versatile and the software did not allow the use of a simpler hexahedral structured mesh, due to the presence of the concave interfaces between the SZ and HAZ of the lower sheet (see Figure 6-1 d).

After the selection of the type of element, it was important to pay attention to two important factors that affect the stress distribution and concentration. Firstly, the highest stresses are developed in the SZ (region 4 in Figure 6-11 b), HAZ (region 3 in Figure 6-11 b) and BM between the HAZ at the opposite sides of the sample (region 2 in Figure 6-11 a), therefore, the mesh density should be greater in this region. Secondly, full coherency should be ensured between adjacent elements in the different parts. It should be noted that the dimensions in the x, y and z directions of the elements in each region were not equal because the thickness-to-length ratio for the sample was very low. For example, the elements in region 1 in Figure 6-11 a had dimensions of 2.5x0.33x1.25 mm in the x, y, and z directions.

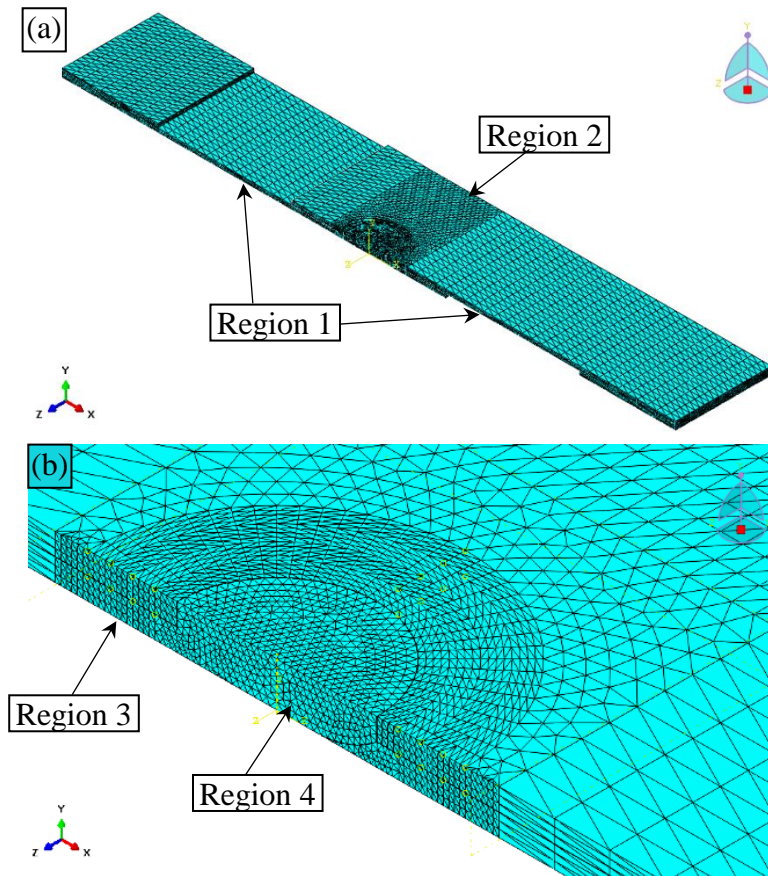


Figure 6-11: Mesh distribution for the similar Al joint: (a) full sample; and (b) detailed view of the joint area.

To ensure the highest possible accuracy for the model, the effect of mesh number on the behaviour of the sample was tested. The criterion that was used to determine accuracy was the difference between the force resulting from the model ( $F_{\text{mod.}}$ ) and those resulting from the experimental test ( $F_{\text{exp.}}$ ). This is shown in Figure 6-12, which also shows the effect of increasing the mesh number on the computing time for the model. From Figure 6-12, it can be noted that increasing the total mesh number from about 7500 to about 26000 reduced the difference between the measured and predicted forces from about 1.95 to about 0.97 kN, which represents a decrease of 48%. On the other hand, the computing time increased from 298 to 1551 s, which represents an increase in processing time of 420%. However, with a further increase in mesh number to about 63000, which represents an increase of about 750 %, the difference between the measured and predicted forces became 0.77 kN, or a 58% decrease, compared to the starting point. Conversely, the processing time increased to about 7700 s representing an increase of about 2500% with respect to the time used at the starting point. Therefore, it was found that further increase in mesh number increased the time required for processing without a comparable increase in the accuracy of the model. The

significant difference that still occurred between the model prediction, when it became stable with mesh refinement, and the experimental load will be discussed further below (section 6.6.1). Thus, the mesh density that had a total number of about 63000 was applied to the model, with the distribution shown in Figure 6-11.

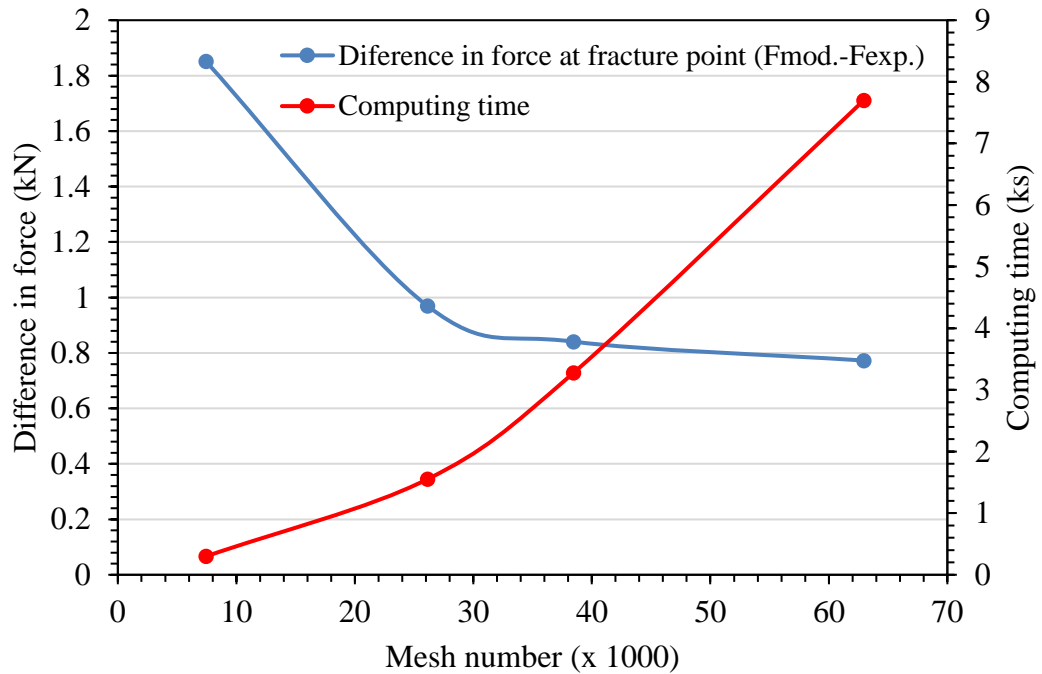


Figure 6-12: The effect of mesh number on computing time and the difference between the force predicted by the model and the experimentally measured force at the peak load.

The number of mesh elements used for the models that contained a hook defect was slightly higher than 63000, this was because a finer mesh was required in the region of the hook to allow for the effect on the stress concentration, as shown in Figure 6-13. A similar total number of mesh elements of about 60000 was used for the model of the dissimilar joint of Mg to Al. In spite of the fact that the width of the sample was only 12.5 mm, which is only half the width of the Al similar joints. In this case, this higher mesh density was used due to the requirement of a higher mesh density in the joint region near the interface between the two metals, as shown in Figure 6-14.

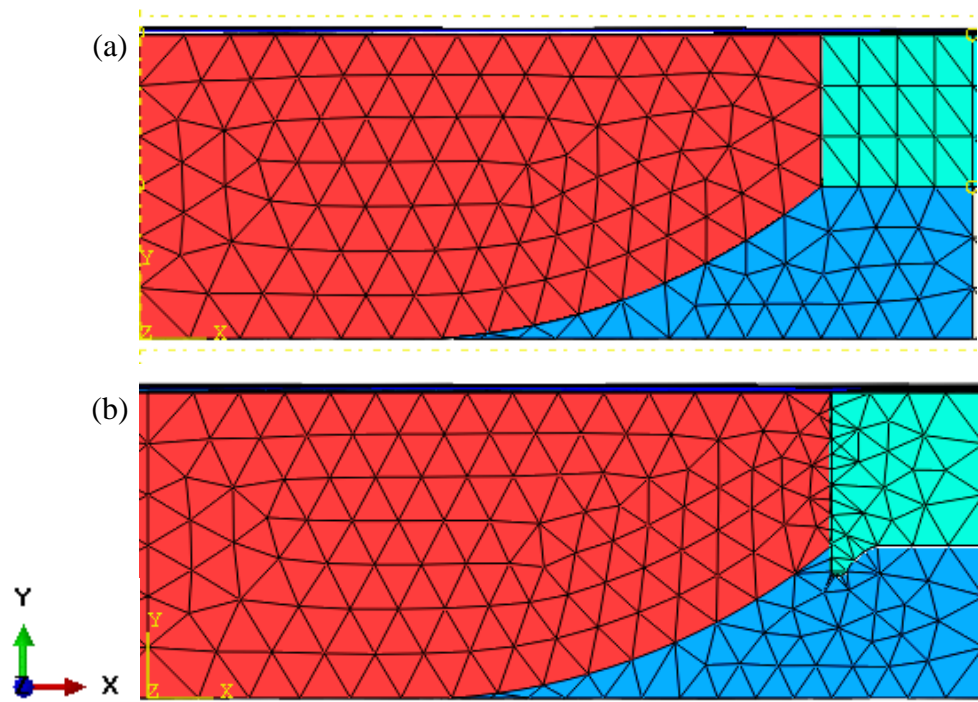


Figure 6-13: Mesh distribution through the cross-section of Al-Al joints; (a) without a hook, and (b) with a hook.

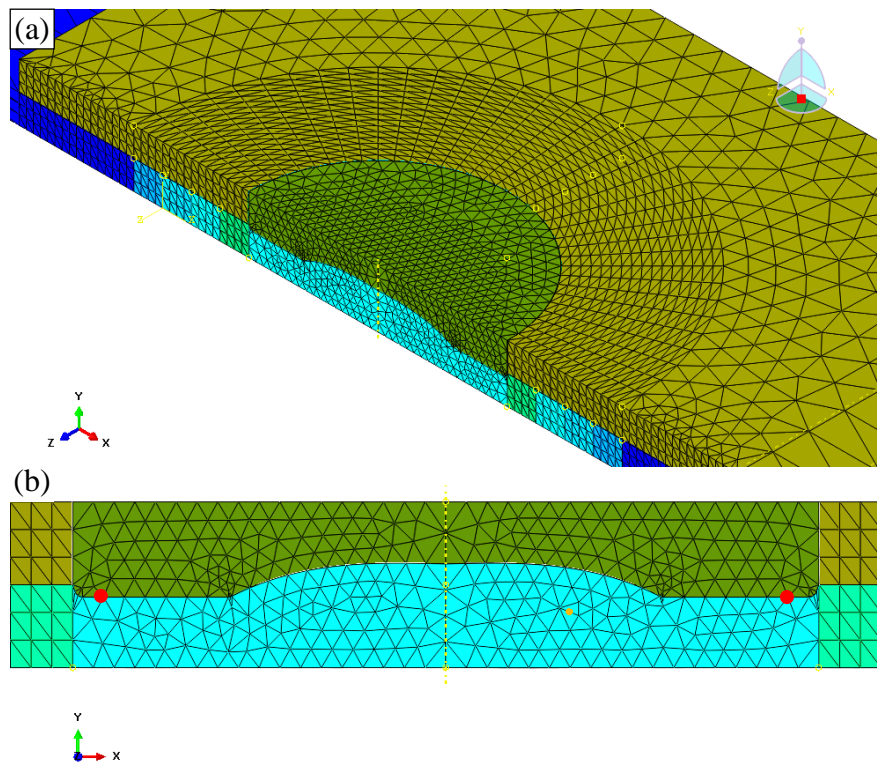


Figure 6-14: Mesh distribution through the cross-section of the model used to replicate a dissimilar joint of Mg to Al; (a) full joint region and (b) detailed view of the cross-section of the joint.

## **6.5 Results and Discussion**

It is important for all spot joining methods to investigate the stress distribution and deformation in the welded components under tensile-shear loading in order to improve the quality and predict the mechanical properties of the joint, and especially the failure load. In addition, the lap-shear test does not load a material in a pure shear (Bakavos, et al., 2011) so it is important to understand how using dissimilar materials with different properties (e.g. Young's moduli) affects the actual test itself.

As discussed in section 6.4, in order to perform the tension-shear test, the tension load was applied at one end of the joined sample while the other end was fixed. As a result of this configuration similar to in an actual test, the weld was subjected to tension and a shear condition, which encouraged the nugget to rotate to align with the ends of the sample. This rotation of the nugget changed the loading mode to a mixture of tension and shear, instead of pure shear.

### **6.5.1 As-welded similar Al joints**

Figure 6-15 shows the distribution of Von-Mises equivalent stress (Figure 6-15, column a) and the distribution of equivalent plastic strain (Figure 6-15, column b) at different stages of the analysis for the longitudinal cross section of the sample, in the as-welded condition without a hook defect. From column a, of Figure 6-15, it can be noted that the stress mostly concentrated in the vicinity of the nugget region near the end of the bonding zone, at the interface between the two sheets. With increasing the extension high stress from this region propagated from the interface between the two sheets to the upper surface of the upper sheet and in the opposite direction for the lower sheet. The stress concentration in this region affected the development of the failure of the RFSSW joint because this region had the lowest yield strength in the as welded condition, compared to all other regions of the joint (see Figure 6-4). The effect of the stress concentration and material properties on the behaviour of this region can be clearly seen in column b of Figure 6-15, which shows the development of the effective strain as a function of extension. The highest strain was also observed at the interface near the edge of the nugget; the strain then propagated to the upper and lower surfaces of the upper and lower sheet, respectively. However, the strain map showed a greater concentration in the region of the lowest yield strength (the HAZ), compared to the stress map and less penetration of the strain through the stronger nugget region.



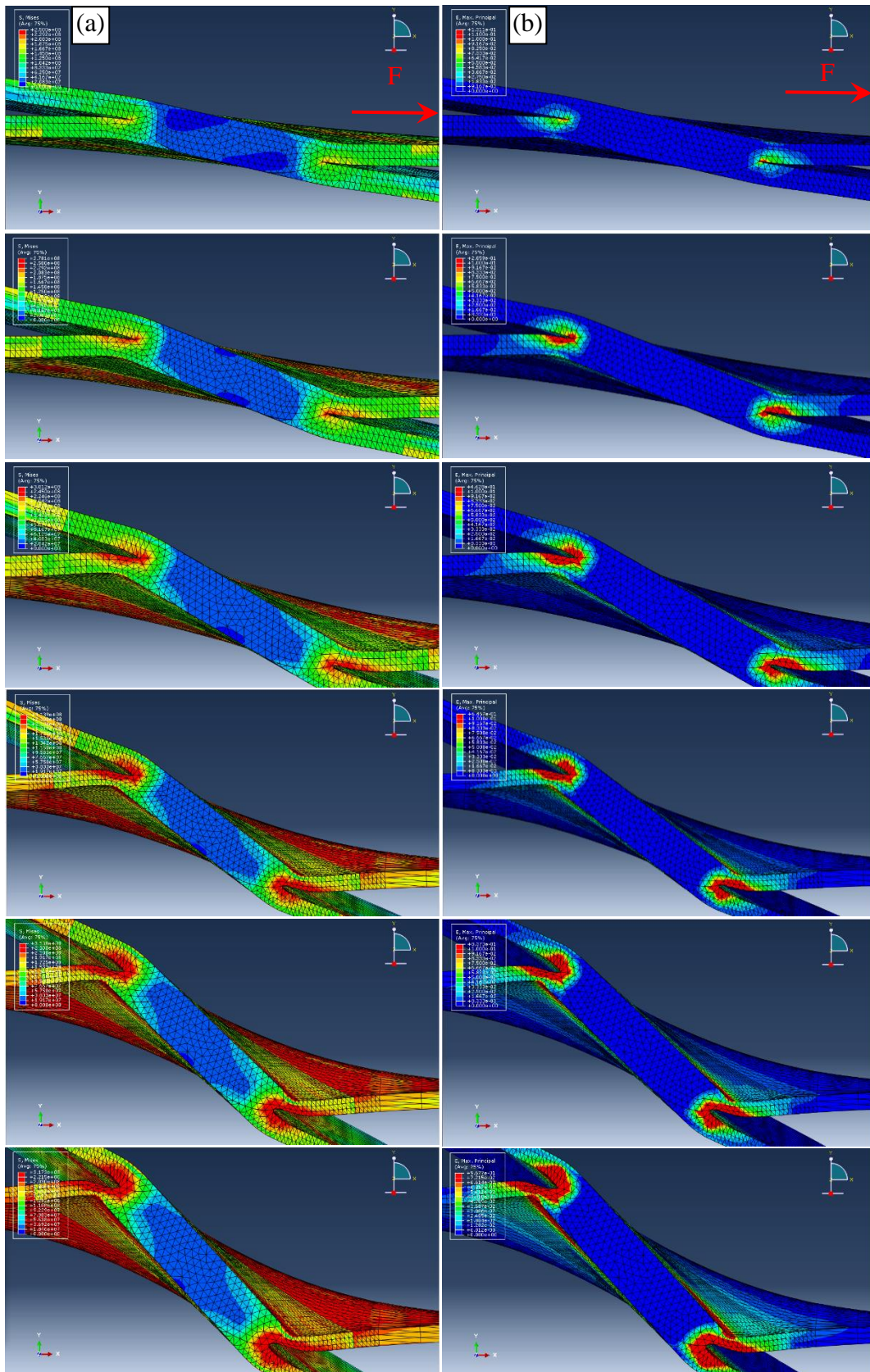


Figure 6-15: Stress and strain distribution on the longitudinal cross-section of an RFSSW joint under tensile-shear loading: column (a) Von-mises equivalent stress distribution, and column (b) strain distribution.

The stress and strain distributions shown in Figure 6-15 provide evidence of the failure path, which was found to be through the thickness of the sheet at the HAZ/nugget boundary (see Figure 4-34) rather than through the nugget which shows low-stress levels with no noticeable strain at its centre. The mechanical properties of the HAZ are thus significantly more important than those of other regions in determining the performance of the joint. In addition, if the centre of the joint contains any weld defects, such as holes or unbonded regions, the presence of such defects will not affect the strength of the welded joint. This assertion was proved experimentally in chapter 4 (see Figure 4-34 a).

Figure 6-16 shows a top view of the stress and strain distribution on the surface of the upper sheet. After propagation of the region of highest stress concentration through the thickness of the two sheets reached the upper and lower surfaces of the upper and lower sheet near the weld centre line, it tended to propagate around the joint to form an annular zone. As shown in column a, in Figure 6-16, at the beginning the highest stress region had a crescent shape, but then began to grow in two directions, annularly around the weld nugget through the HAZ. With the further extension, the nugget became completely surrounded by a cylindrical surface region with a high stress concentration and the region of the highest stress level then begins to extend laterally to the outer sides of the sample. The region that deforms plastically showed approximately the same propagation behaviour as that for stress distribution, but with a greater concentration in an annular region near the periphery of the nugget. This region agrees well with the path of observed cracks, which resulted in the failure of the joints in the form of a full plug pull-out fracture mode, similar to that shown in the experimentally tested samples in Figure 4-33. These model predictions also agree with similar results to those achieved by other researchers, when using the same welding method with different materials and sheet thicknesses, such as Mazzaferro et al., Rosendo et al., and Lacki & Derlatka (Mazzaferro, et al., 2009; Rosendo, et al., 2015; Lacki & Derlatka, 2016).

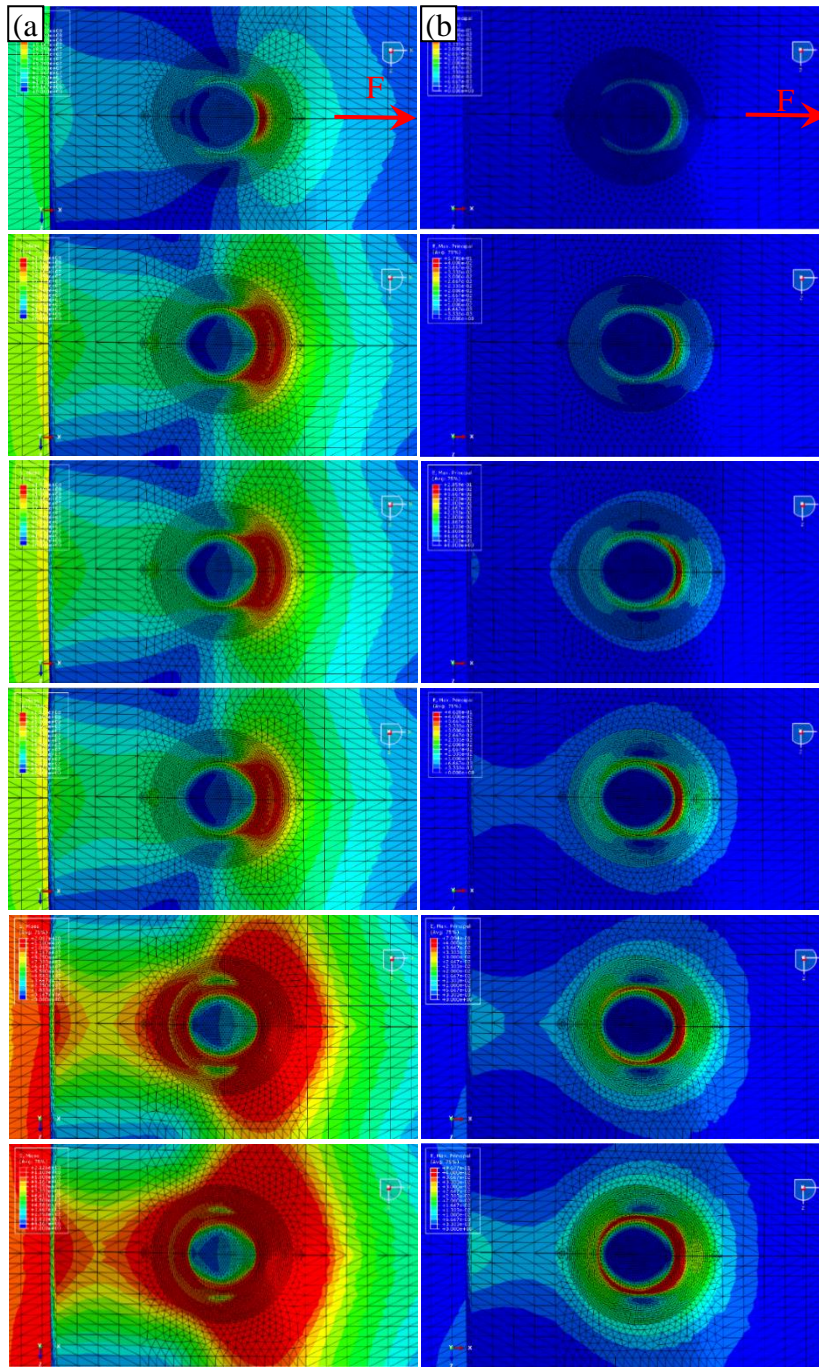


Figure 6-16: Predicted Von-mises stress and strain distribution in an RFSSW joint under tensile-shear loading (top view): column (a) stress distribution, and column (b) strain distribution.

It was found that adding the hook defect to the sample did not affect the overall stress and strain distribution, in terms of their concentration at the interface between the sheets at the beginning of the test and the growth of the regions of highest stress and strain at the upper and lower surfaces of the upper and lower sheet respectively, as shown in Figure 6-17. However, when a hook was included less symmetry in the stress and strain distribution was observed between the two sheets (like that in Figure 6-15). This result is likely due to the higher stress concentration near the edge of the hook, which leads to



an increase in the strain in this region of the lower sheet. This region of high strain localisation originated at the end of the hook and propagated through the thickness of the lower sheet and then around the nugget to form an annular strain concentration. This much more localised highly strained area is probably the origin of the tears seen in the lower sheet in the experimental results in Figure 6-18. The experimental results also showed the crack to be first initiate and follow the hook through to the lower sheet surface in Figure 4-34.

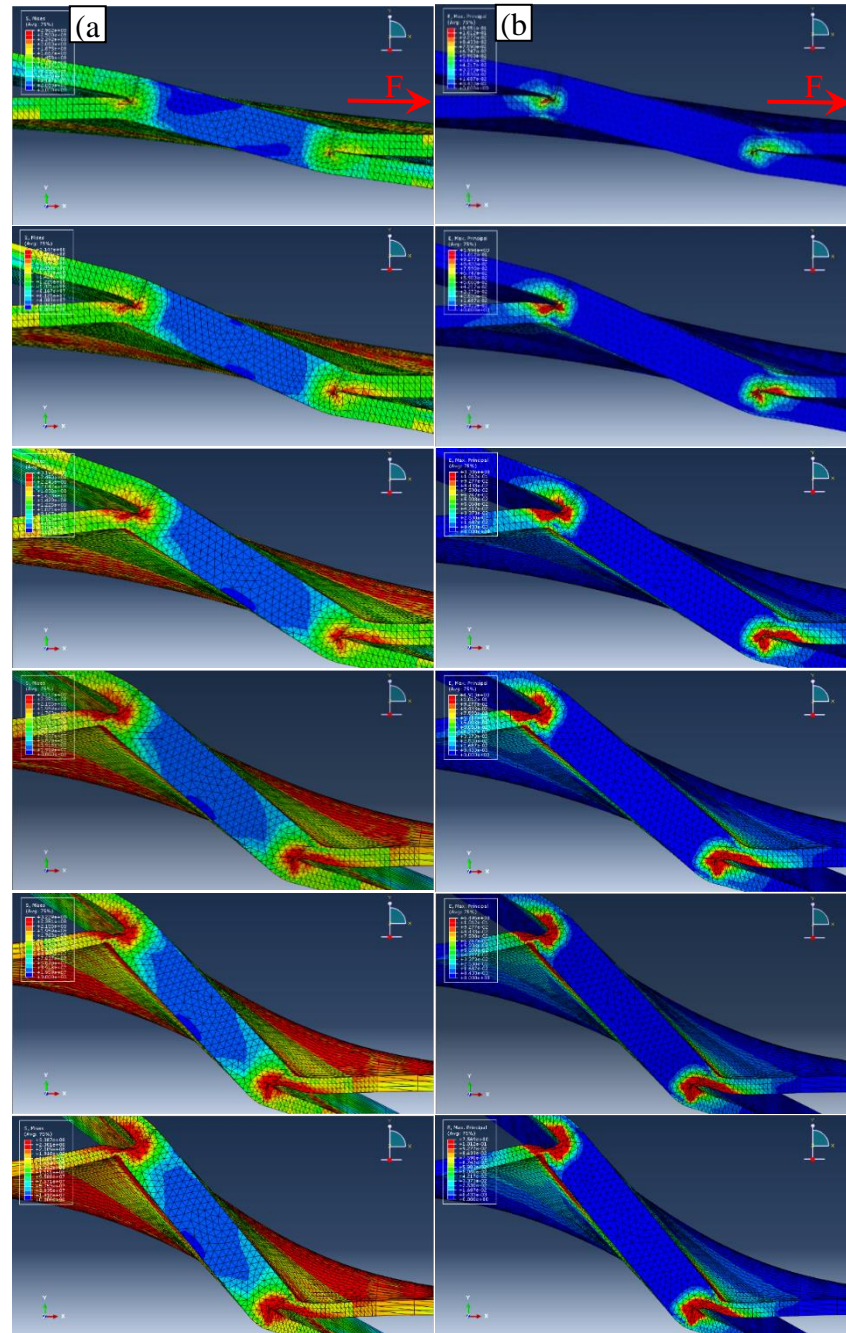


Figure 6-17: Effect of a hook defect on the stress and strain distribution on the longitudinal cross-section of an RFSSW joint under tensile-shear loading: column (a) stress distribution, and column (b) strain distribution.

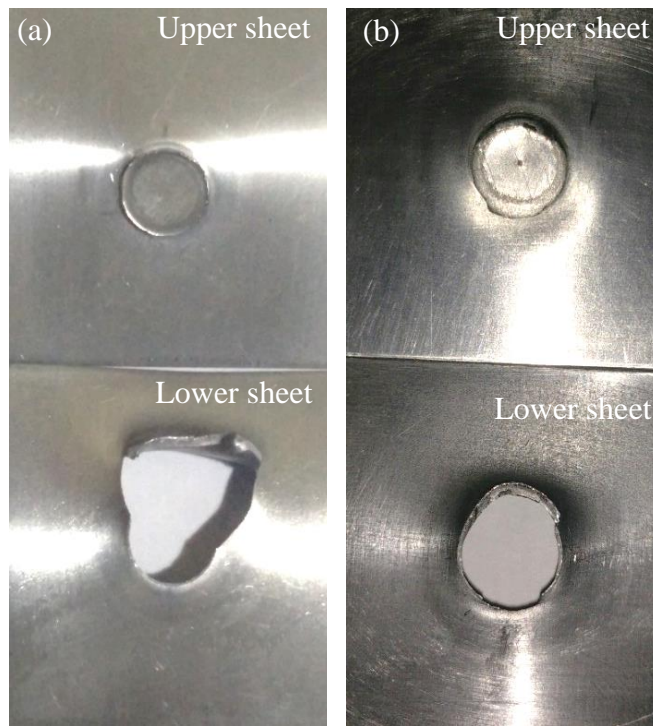


Figure 6-18: Examples of the failure behaviour, showing both halves of the fractured lap shear test samples welded using welding parameters of 2000 rpm, 1.0 s, and 1.0 mm. The samples were tested in the (a) as-welded condition, and (b) after artificial ageing at 180°C for 30 min.

For comparison, Figure 6-19 shows the stress and strain distribution on the longitudinal cross-section of an RFSSW joint, with and without, the hook defect. The figure clearly shows how the local maximum stress and strain increased in the lower sheet near the hook, which shows greater plastic deformation and a local ‘necking’ behaviour, similar to that observed in the experimentally tested samples (see Figure 4-34 a). This explains why most of the samples tended to fail through the nugget pull-out from the lower sheet (see section 4.9). Figure 6-20 also shows a comparison of the stress and strain distributions predicted in two lines of nodes along the longitudinal cross-section 0.33 mm above and below the interface of an RFSSW joint under tensile-shear loading (with and without a hook). These two figures show more clearly the effect of the hook defect on increasing the local maximum stress and strain concentration in the lower sheet near the hook with about 87% and 60%, respectively.

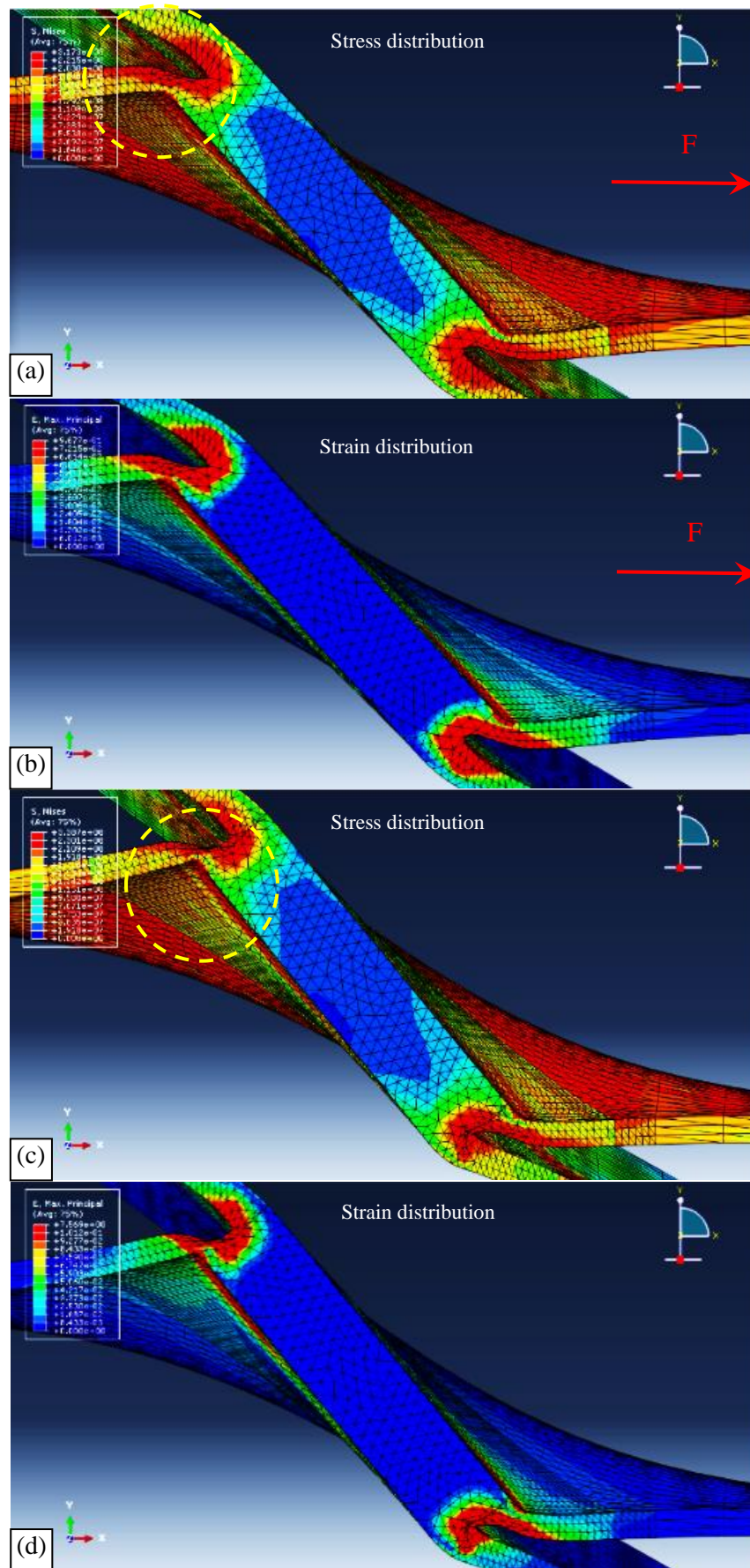


Figure 6-19: Comparison of the stress and strain distribution predicted in the longitudinal cross-section of an RFSSW joint under tensile-shear loading: (a) and (b) without a hook, and (c) and (d) with a hook.

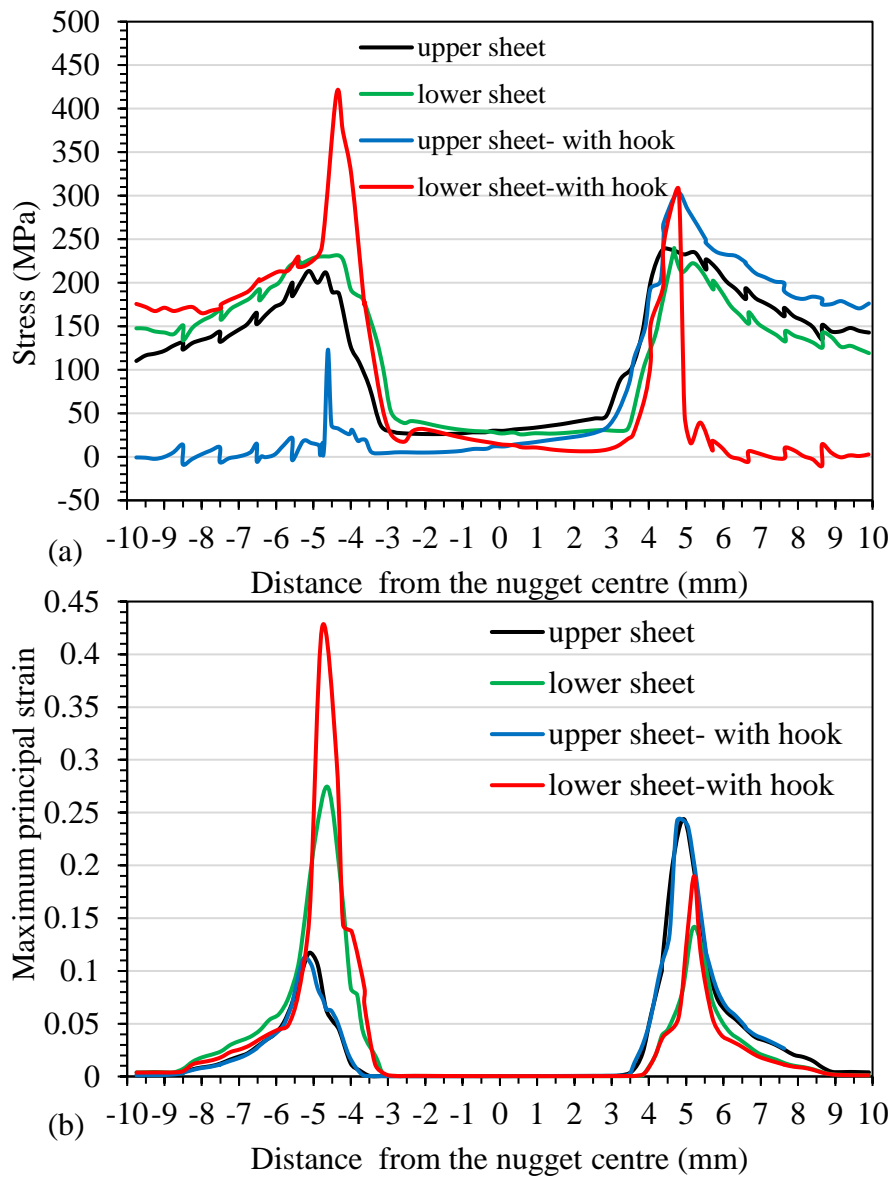


Figure 6-20: Comparison of the stress and strain distribution predicted in two lines of nodes passing through the longitudinal cross-section at 0.33 mm above and below the interface of an RFSSW joint in the as-welded condition, under tensile-shear loading (with and without a hook): (a) stress distribution, and (b) strain distribution.

Overall force-extension curves were used to evaluate the performance of the model by comparison to the experimental results. The stress and extension values were taken as an average from a total number of 135 nodes, which represents the first set of nodes in a vertical plane parallel to the y-z plane and adjacent to the pulled side of the sample (i.e. 2.5 mm from the pulled side, or 27.5 from the end of the sample). The force obtained from multiplying the average stress of all the 135 nodes by the total cross-sectional area (i.e. 50 mm<sup>2</sup>).



Figure 6-21 a shows an experimental and numerical force-extension curves (with and without hook) for the tensile lap shear test of RFSSW joints in the as-welded condition. The experimentally tested weld was produced using the welding conditions modelled, of 2000 rpm, 1.0 s, and 1.0 mm. It can be noted from this figure that the calculated force shows a higher level compared to the experimentally measured force, in both model approaches, especially for the extensions up to 0.3 mm. However, the force-extension for the model containing a hook shows a behaviour approaching that of the experimental curve, when the extension exceeded 0.4 mm with a difference of only about 0.2 kN, or about 6.6%.

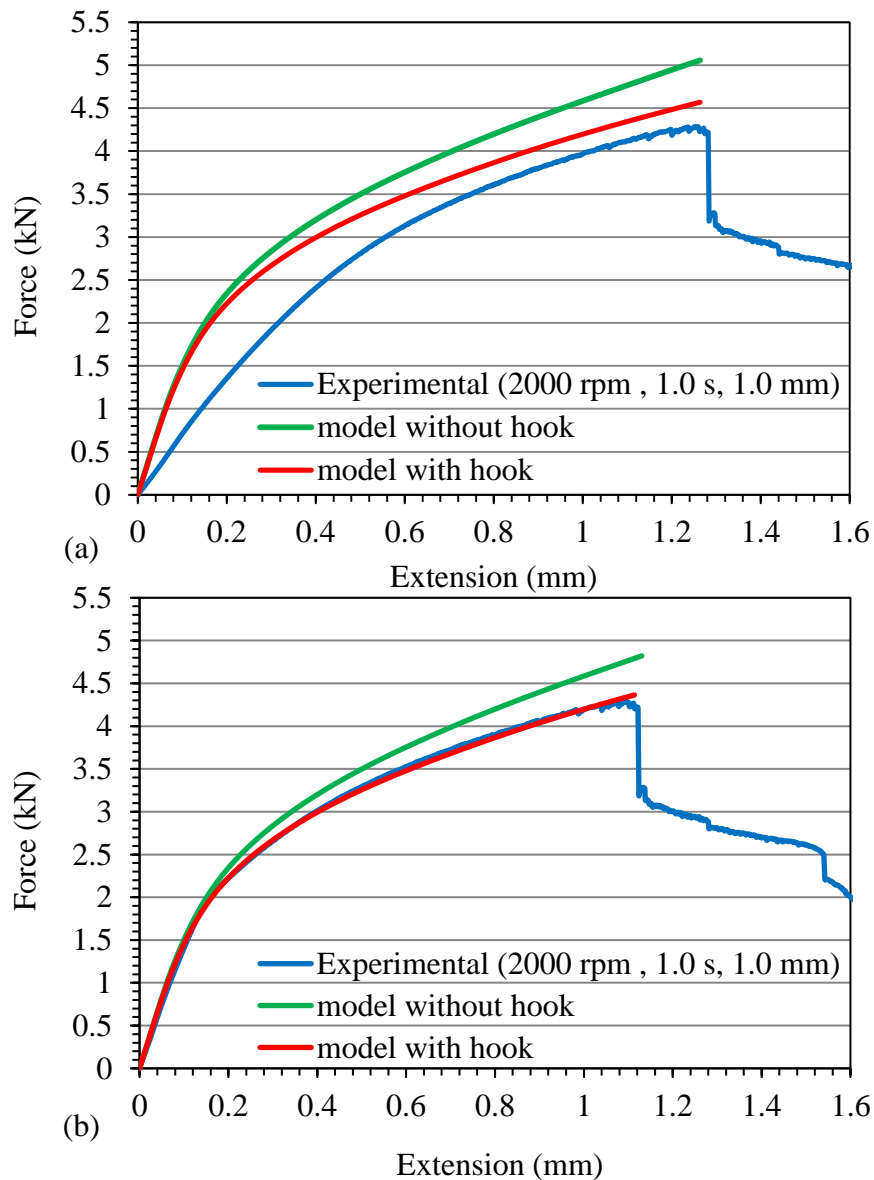


Figure 6-21: Comparison of experimental and modelled (with and without hook) force-extension curves for the tensile lap shear test of RFSSW joints in the as-welded condition. The experimentally tested weld was produced using welding conditions of 2000 rpm, 1.0 s, and 1.0 mm: (a) before correction of the experimental results, and (b) after correction for machine compliance.

The main reason for the difference in behaviour between the modelled samples, with and without a hook, is the presence of the hook defect, which reduces the force required for a certain extension through the separation between the lower sheet and the SZ reduces the effective thickness of the lower sheet. However, overall the model still over-predicts the force-extension behaviour due to the effect of the machine compliance during the experimental test, which results in a change in the slope of the curve in the elastic region. Due to the difficulty of measuring the machine compliance with such samples, to solve this problem, the experimental curve was corrected by assuming its true slope in the elastic region should agree with that predicted by the model. As a result, when the displacement was corrected for the inferred machine compliance, the predicted force-extension curve for the model with a hook showed complete matching with the corrected experimental curve, as can be seen in Figure 6-21 b.

### **6.5.2 Artificially-aged Similar Joints**

The model of the artificially-aged similar Al-Al joints showed a significant similarity to the model of the samples in the as-welded condition, in both approaches, with and without the hook defect. Figure 6-22 shows an example of the stress and strain distribution in the longitudinal cross-section of the model for an artificially-aged RFSSW joint, without a hook, in two different steps under tensile-shear loading. This figure shows that the stress was concentrated near the edge of the nugget at the interface between the two sheets. The highest strain was also observed in this region, and with further extension the region of highest stress and strain propagated through the thickness to the upper and lower surfaces of the upper and lower sheets, respectively. This behaviour can also be seen in the model of the sample with the hook, as shown in Figure 6-23, but with less symmetry due to the effect of the hook, which again resulted in a higher stress concentration in the lower sheet at the side opposite to the direction of the load. This was also the failure point seen in the actual weld samples (see Figures 4-34 and 6-18).

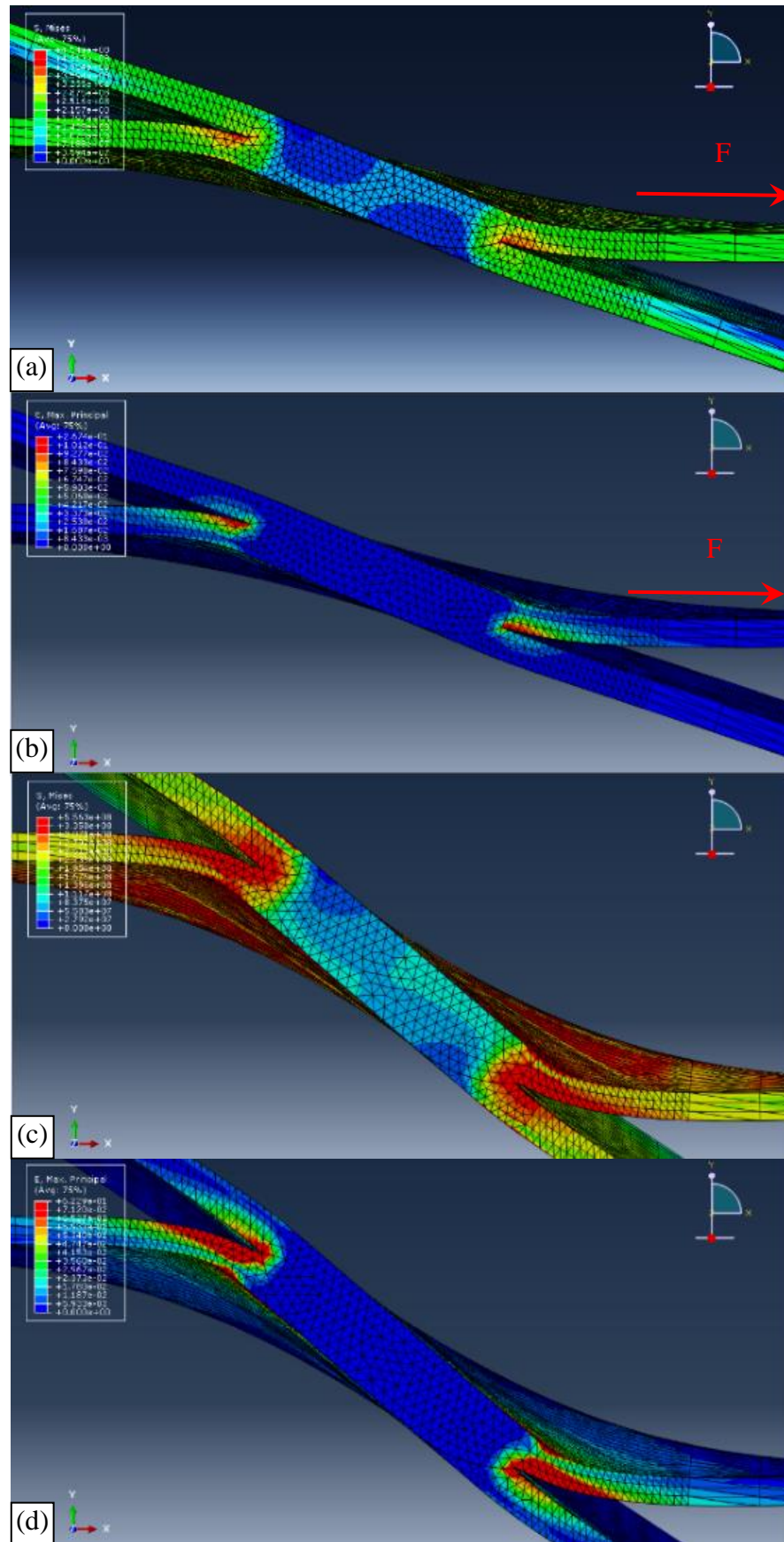


Figure 6-22: Stress and strain distribution modelled in the longitudinal cross section of an artificially-aged RFSSW joint in two different steps under tensile-shear loading: (a) and (c) stress distribution, and (b) and (d) strain distribution.

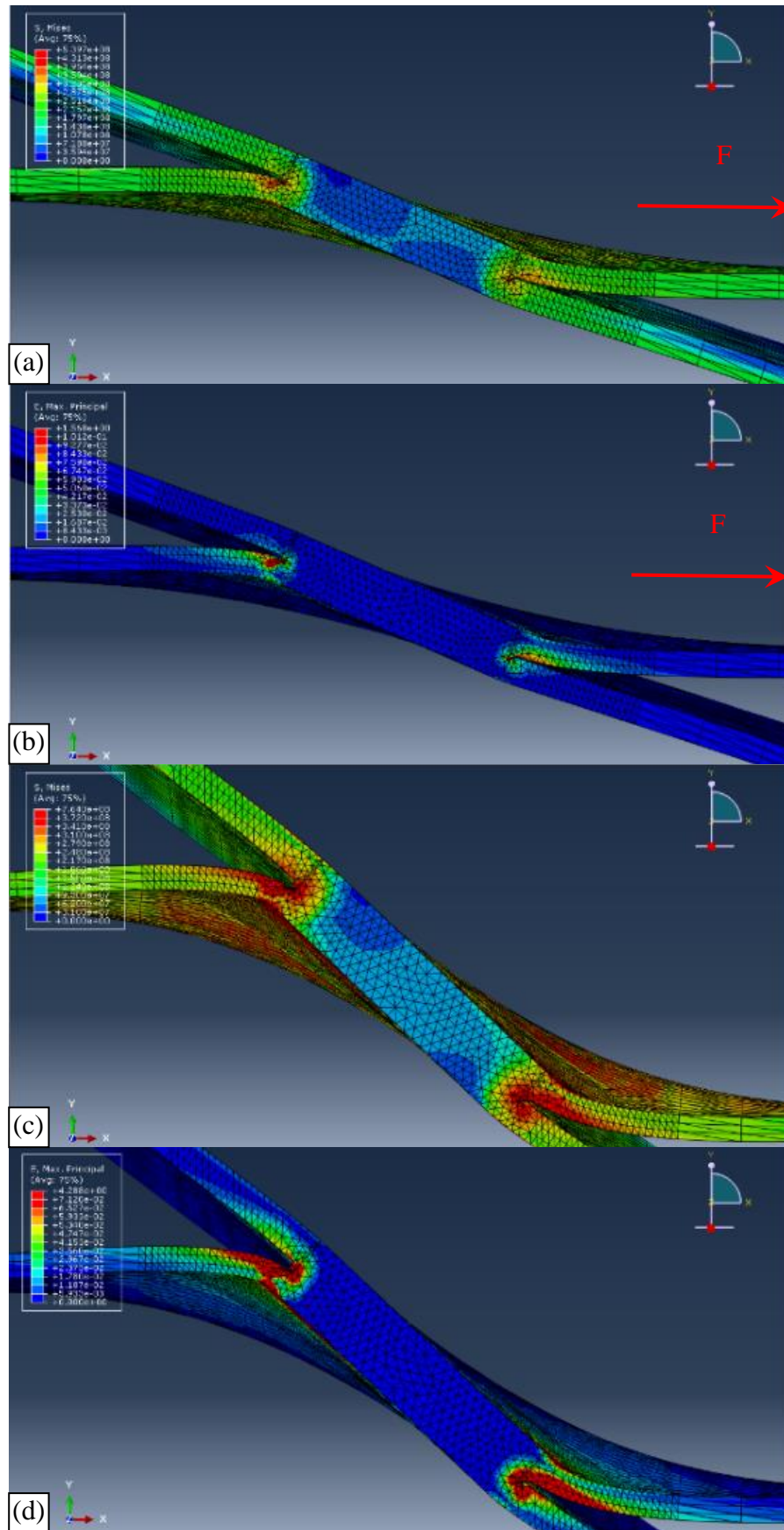


Figure 6-23: Effect of the hook defect on the stress and strain distribution modelled in the longitudinal cross-section of an artificially-aged RFSSW joint in two different steps under tensile-shear loading: (a) and (c) stress distribution, and (b) and (d) strain distribution.



Figures 6-24 shows a comparison of the predicted stress and strain distributions from the model in two lines of nodes along the longitudinal cross-section in a 0.33 mm, above and below the interface of an RFSSW joint in the artificially aged condition and subjected to a tensile-shear loading (with and without a hook). In this case, the effect of the adding of the hook defect on increasing the local maximum strain compared to the local maximum stress in the lower sheet near the hook is much clearer with an increase of about 95% compared to the model without a hook.

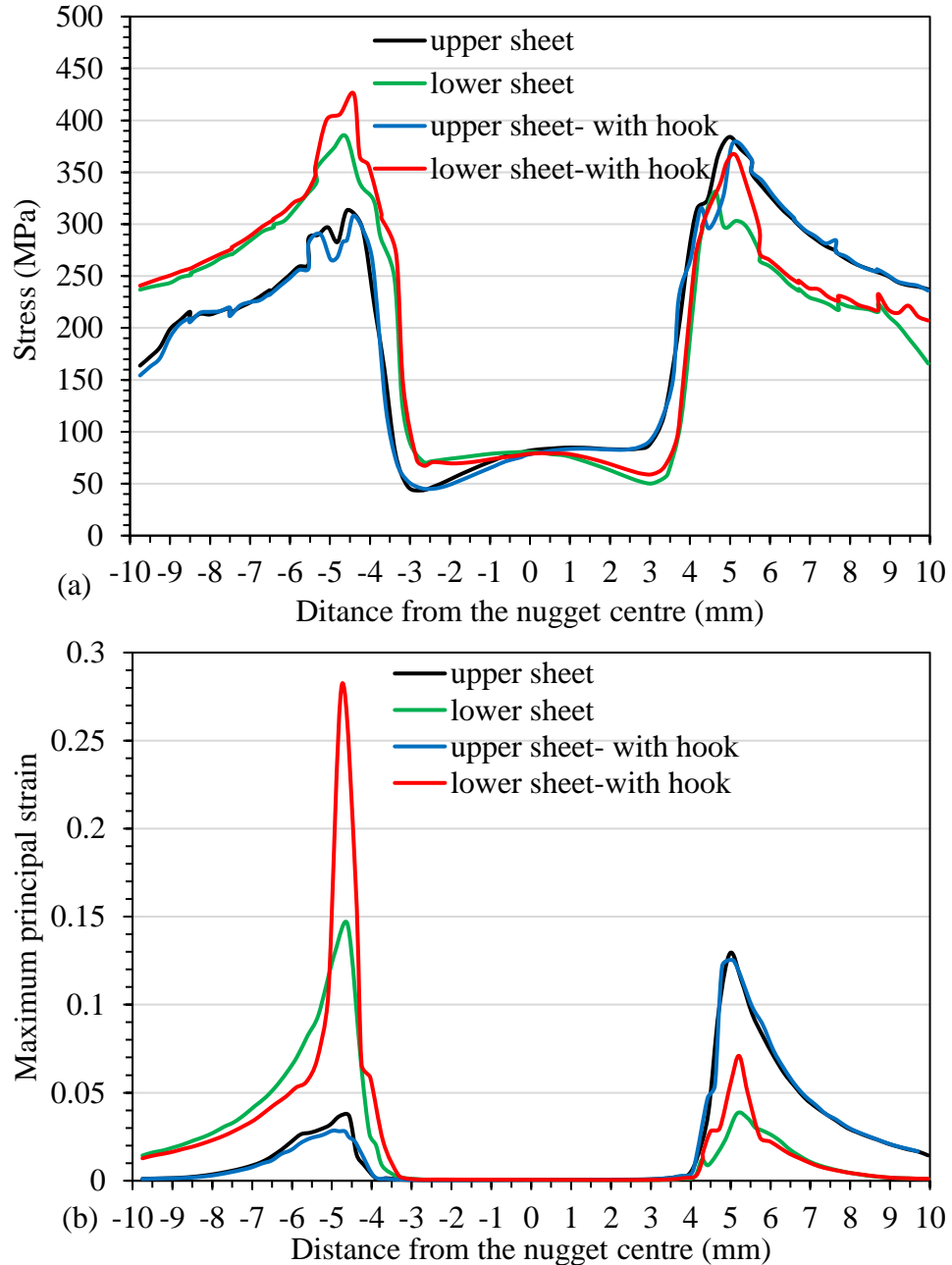


Figure 6-24: Comparison of the stress and strain distribution predicted in two lines of nodes passing through the longitudinal cross-section at 0.33 mm above and below the interface of an RFSSW joint in the artificially aged condition, under tensile-shear loading (with and without a hook): (a) stress distribution, and (b) strain distribution.

Figure 6-25 shows an example of the stress and strain distribution for a top view of the upper sheet in two different steps of the model for the same sample. The region of the highest stress and strain begins from the edge of the nugget at the line of symmetry of the sample and then propagates in two directions: around the nugget, which is much clearer in the strain maps, and to the outer sides of the sample. In spite of the difference in the local mechanical properties of the regions of the artificially-aged joint, compared to those for the joint modelled in the as-welded condition (especially for the HAZ region near the nugget; see Figures 6-4 and 6-7), the two samples in the as-welded and artificially-aged conditions showed a very similar behaviour, in terms of the stress and strain distribution. This means that the geometry of the joint had a greater effect on the strain localisation and performance of the similar joints than any difference in local material properties. Therefore, the experimentally tested artificially aged samples still showed a full plug pull-out fracture mode, as shown in Figures 4-34 c and 6-18.

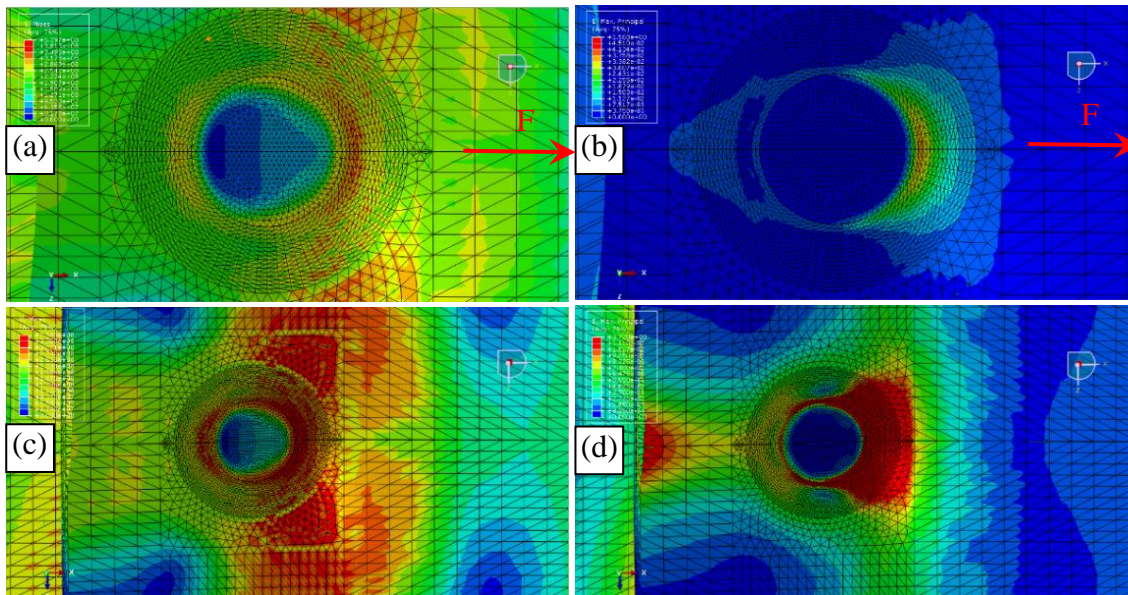


Figure 6-25: Stress and strain distribution on an artificially-aged RFSSW joint in two different steps under tensile-shear loading (top view): (a) and (c) stress distribution, and (b) and (d) strain distribution.

To predict the overall force-extension curves, the same procedure was used to calculate the force for the samples in the as-welded condition. Figure 6-26a compares the curves of the results of the experimental and modelled tensile lap shear test (with and without a hook) for RFSSW joints produced using welding conditions of 2000 rpm, 1.0 s, and 1.0 mm, followed by artificial-ageing at 180°C for 30 min. It can be noted that, again, the force calculated by the model still shows a higher level compared to that resulted from the experimental test by about 1.0 kN at the fracture point. In general, both the experimental and modelled results showed significantly higher levels of force compared

to those of the samples in the as-welded condition (see Figure 6-26 b); due to the effect of artificial ageing, which improved the local mechanical properties, especially in the HAZ (see sections 4-8). The force-extension curve for the model with a hook defect showed an approximately a similar but still constant difference from the experimental curve, especially for extensions higher than 0.2 mm. However, after correction for machine compliance, the predicted force-extension curve for the model with a hook shows a complete matching with the corrected experimental curve, as shown in Figure 6-26 b.

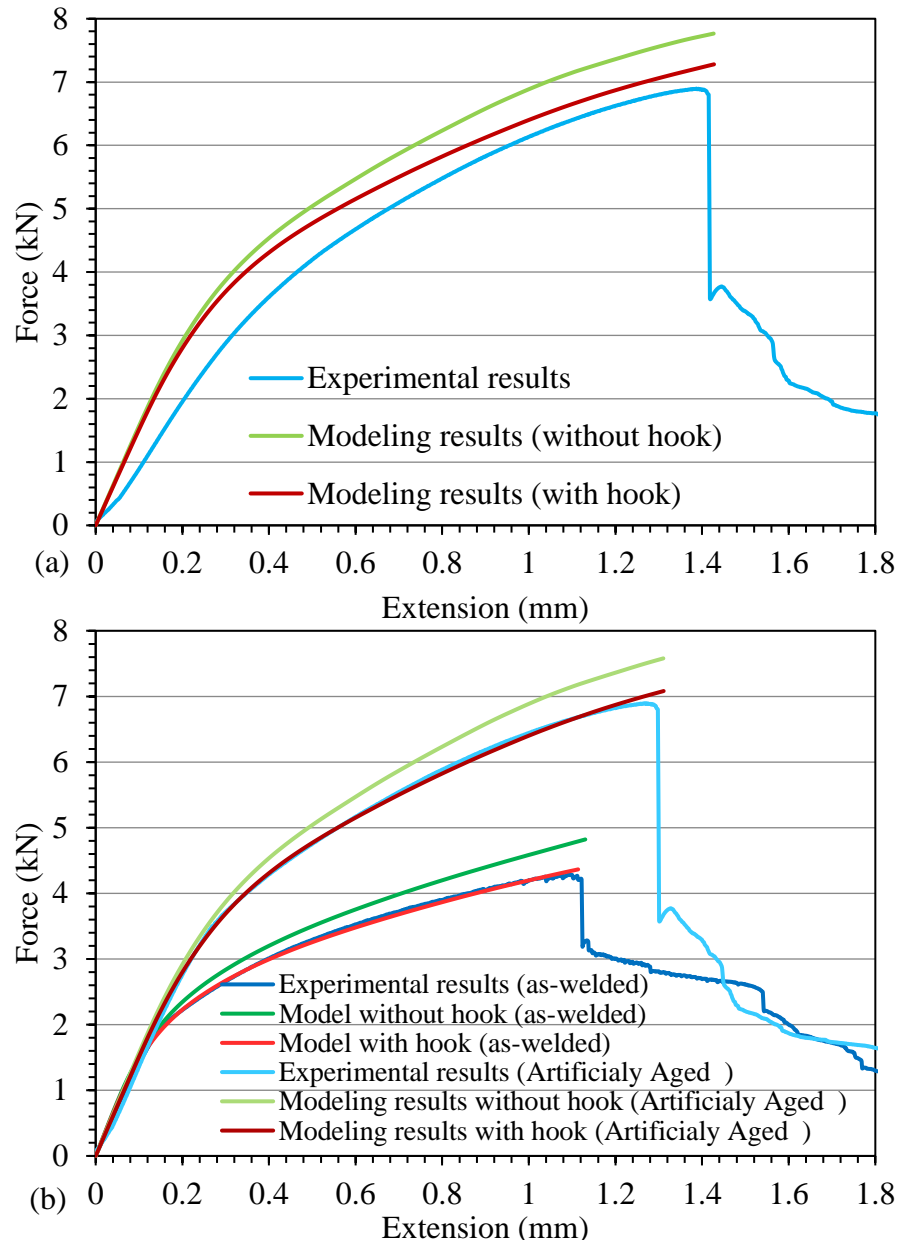


Figure 6-26: Experimental and modelled (with and without hook) force-extension curves for the tensile lap shear test of RFSSW joints in the as-welded and artificially aged conditions at 180 °C for 30 min. The experimentally tested weld was produced using the welding conditions of 2000 rpm, 1.0 s, and 1.0 mm: (a) before correction of the experimental results, and (b) after correction for machine compliance.

### **6.5.3 Mg-Al Dissimilar Welds**

Modelling of the dissimilar material Mg-Al joint, was more challenging than the similar material welds, due to the difference in the failure mechanisms and the very different mechanical properties of the two metals.

Figure 6-27 shows the predicted stress and strain distribution in the longitudinal cross section of an RFSSW joint of a dissimilar Mg-Al weld in two different steps, under tensile-shear loading. Both the stress and strain maps show asymmetrical shapes in the two steps, where the upper sheet (Mg) shows a higher stress level than the lower sheet (Al), in both cases. In contrast, the lower sheet (Al) shows a significantly higher strain, due to the lower yield stress of the aluminium in the HAZ adjacent to the SZ (see Figure 5-5). However, the region of the highest stress and strain still begins at the interface between the two sheets and then propagates to the outer surfaces. The other important point to note is that the weld centre does not show high levels of stress or strain because the two metals were assumed to be completely connected by the nugget without the presence of any weld defect or the IMC layer and deformation initiates at the edge of the edge of the joint region; i.e. the model treated the joint as a continuous material with two regions with different mechanical properties.

Figures 6-28 shows a comparison of the predicted distribution of stress and strain in two lines of nodes along the longitudinal cross-section in a 0.33 mm above and below the interface of an RFSSW dissimilar Mg-Al joint subjected to a tensile-shear loading. From 6-28 a, it can be noted that the magnesium shows an asymmetric higher maximum stress than aluminium at the edge of the joint. However, the lower sheet (Al) shows a significantly higher maximum strain of about 70% compared to the magnesium, as shown in Figure 6-28 b. This is because of the lower yield stress of the aluminium, in the HAZ adjacent to the SZ in the as-welded condition, which transfers load to the Mg sheet.

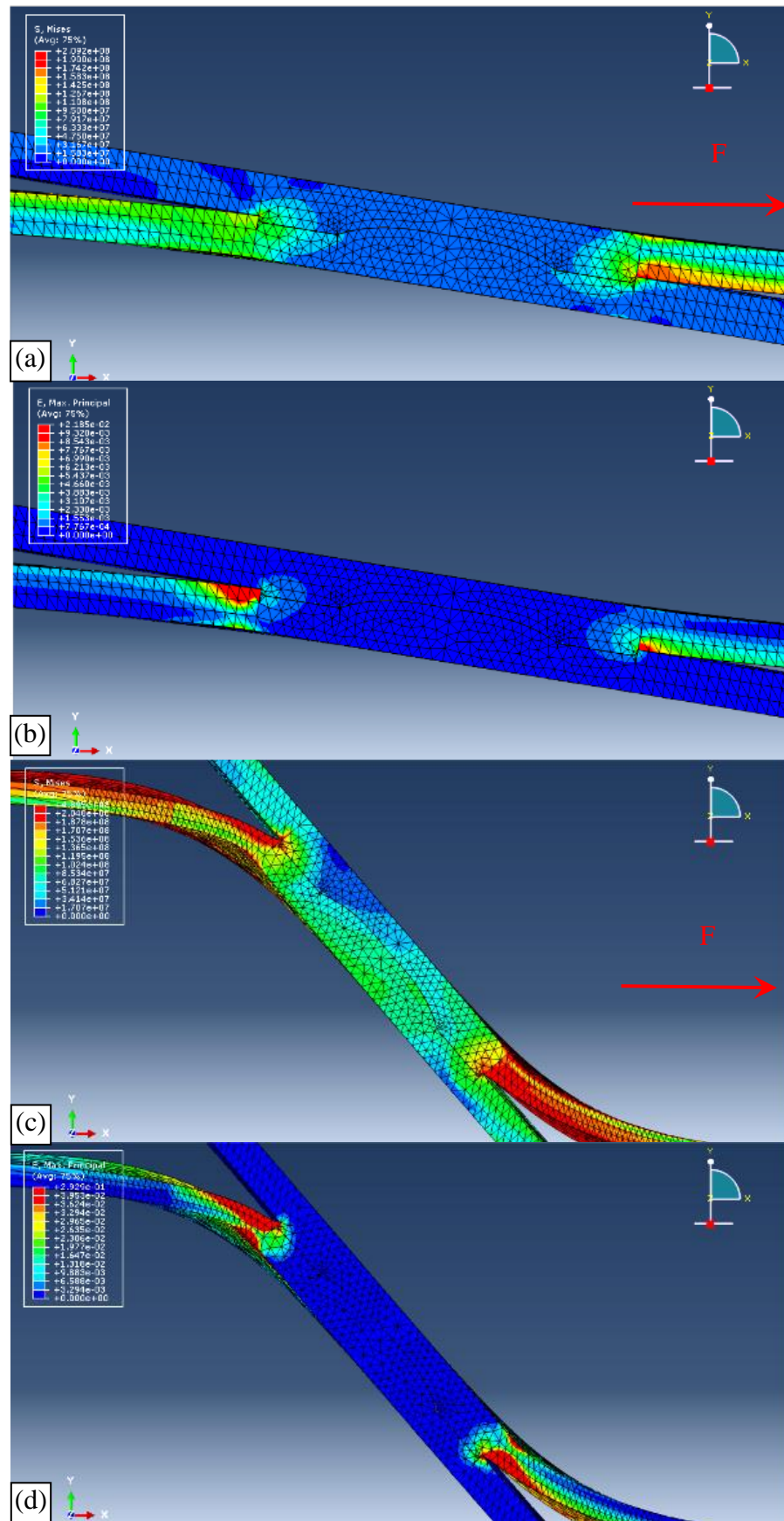


Figure 6-27: Predicted stress and strain distribution in the longitudinal cross section of an RFSSW dissimilar Mg-Al joint, in two different steps under tensile-shear loading: (a) and (c) stress distribution, and (b) and (d) strain distribution.

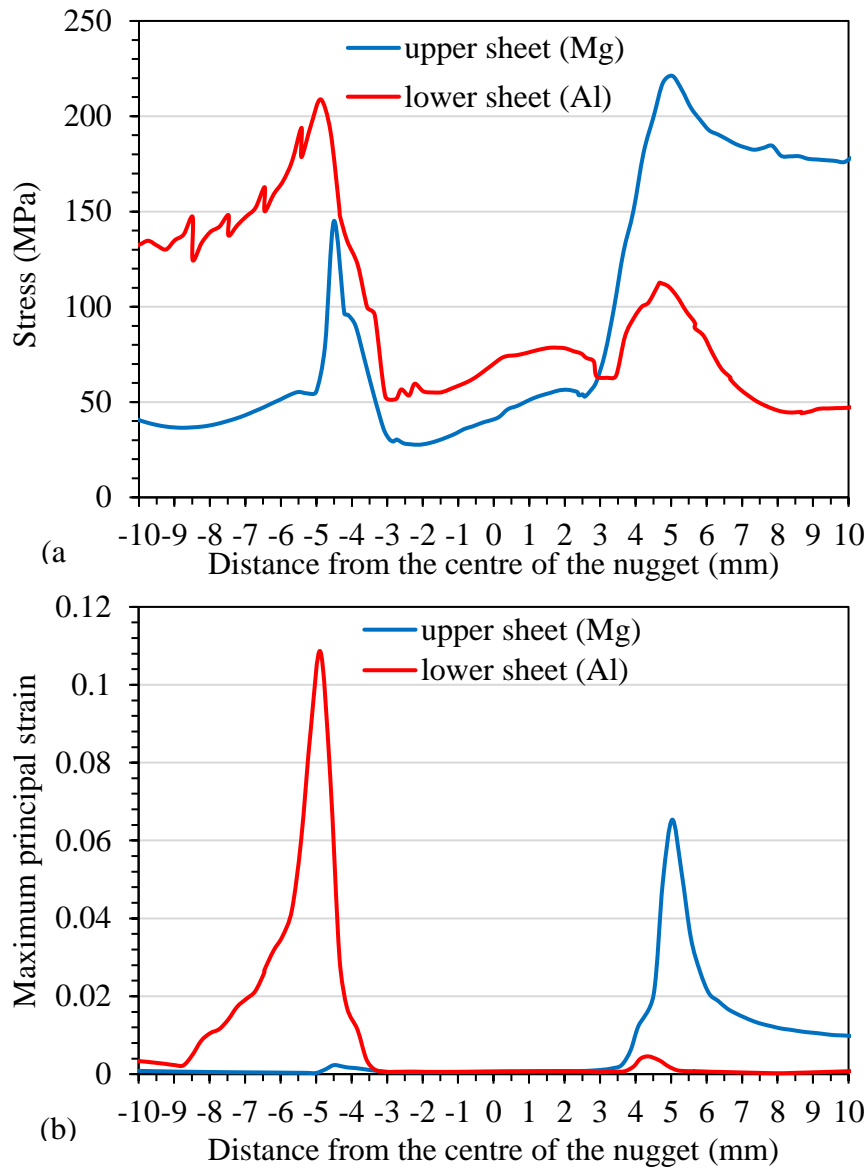


Figure 6-28: Comparison of the stress and strain distributions predicted in two lines of nodes passing through the longitudinal cross-section at 0.33 mm above and below the interface of a dissimilar Mg-Al RFSSW joint of under tensile-shear loading: (a) stress distribution, and (b) strain distribution.

Dissimilar Mg-Al spot joints usually fail by brittle fracture through the interface when they are subjected to tensile-shear loading. Therefore, it is important to understand the behaviour of the interface of the joint under the tensile-shear loading. Figure 6-29 shows examples of predicted maximum principal stress-strain curves for two nodes in a dissimilar Mg-Al RFSSW joint under tensile-shear loading, which can be seen as the red points in Figure 6-14 b and are located at the interface at 0.35 mm from the edges of the joint. In spite of the symmetry in the location of the two nodes, the node on the side of the fixed end shows a significantly higher level of stress, and strain, due to the higher



strain level in the lower sheet in this region (Al) (see Figures 6-27 d and 6-28 b). This different in maximum principal stress is likely to be the reason for start the interface to fail from the edge on the aluminium sheet side.

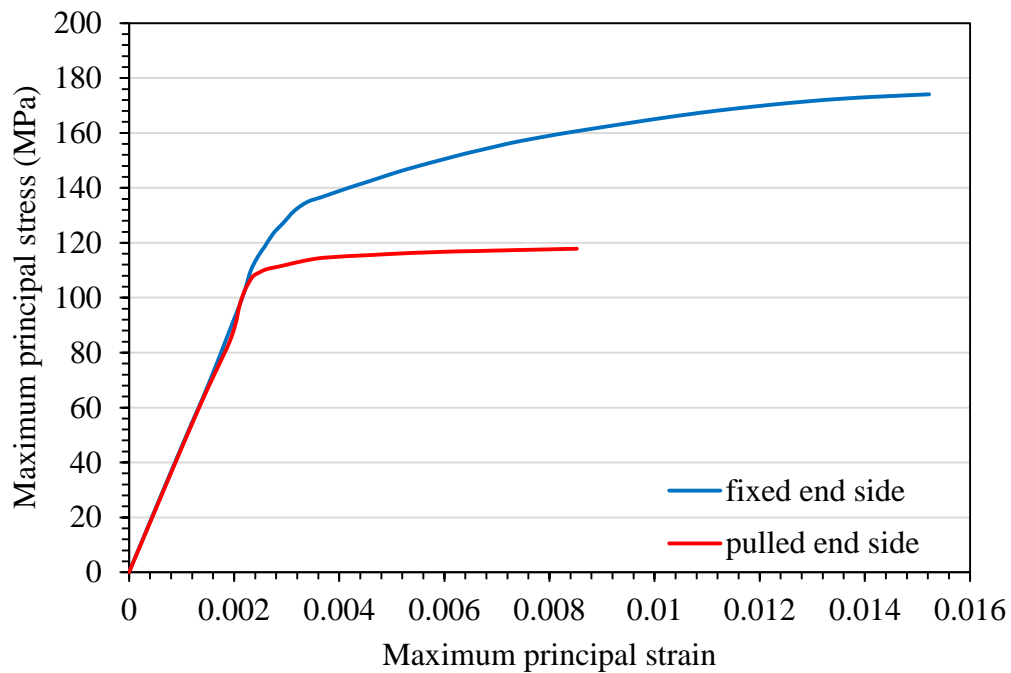


Figure 6-29: Comparison of the predicted maximum principal stress-strain curves in two nodes located at the interface at 0.35 mm from the edges of the dissimilar Mg-Al RFSSW joint (shown as red points in Figure 6-14 b), under tensile-shear loading.

The top and bottom views shown in Figures 6-30 and 6-31 also show the difference in the response of the Mg and Al sheets to shear loading. Similar to that discussed for the cross-section, the upper sheet (Mg) shows a higher stress level and lower strain level in both cases. However, the most important point to notice in these figures is that the region of highest stress extended to the sides of the sample, instead of propagating around the nugget. This is likely to have occurred because of sample size, in this case, had a width of 25 mm compared to the 50 mm width of the similar Al joints. This reduction in sample width reduced the load-bearing area of the cross-section and increased the stress in the adjacent sheet, making direct comparison problematic.

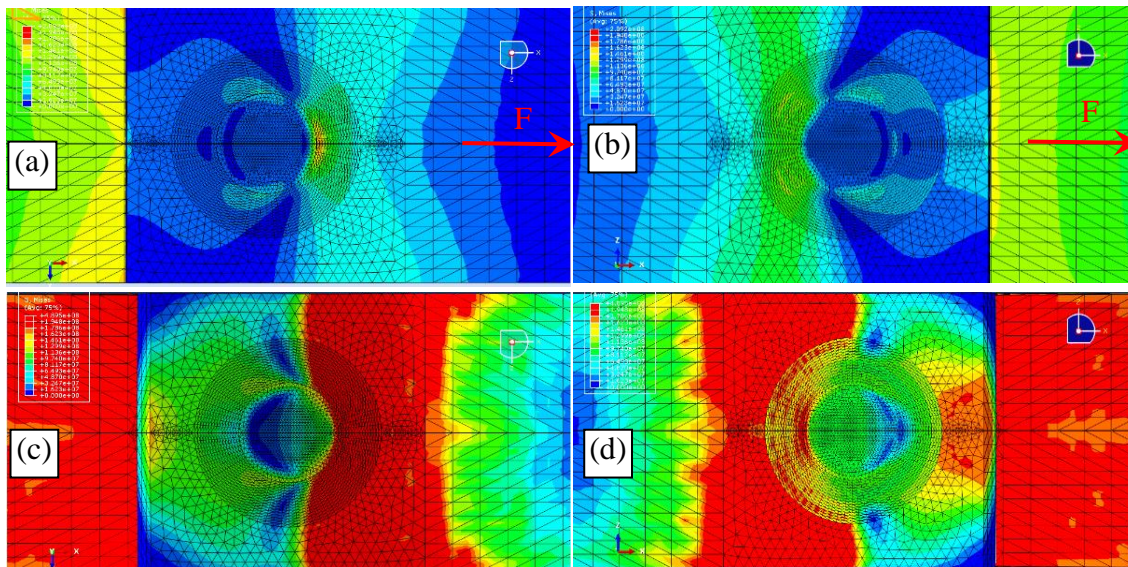


Figure 6-30: Predicted stress distribution in an RFSSW dissimilar Mg-Al joint in two different steps under tensile-shear loading: (a) and (c) Mg upper sheet, and (b) and (d) Al lower sheet.

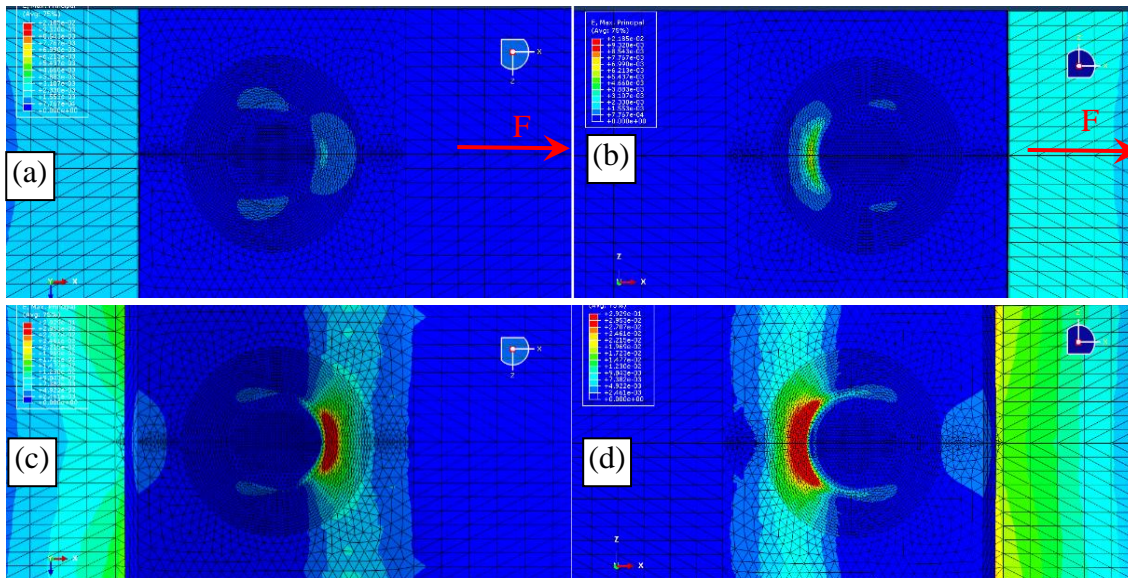


Figure 6-31: Predicted strain distribution in an RFSSW dissimilar Mg-Al joint in two different steps under tensile-shear loading: (a) and (c) Mg upper sheet, and (b) and (d) Al lower sheet.

Figure 6-32a shows a comparison of an experimental and predicted tensile lap shear test force-displacement curves from the dissimilar Mg-Al joints produced using the modified RFSSW process with welding conditions of 2500 rpm, 1.0 s, and 1.0 mm. The force-extension curve calculated by the model show a much more ductile behaviour compared to the approximately linear relationship of the experimental curve, especially during the early stages of the test up to an extension of 0.4 mm. Nevertheless, after this value of the extension, the model force-extension curve became approximately parallel to the experimental curve with a difference of about 0.5 kN until the point of fracture.



After compliance correction of the curve for the experimental test, the behaviour of the modelled overall load-displacement agreed well with the results of the experimental curve, until the point of fracture (as shown in Figure 6-32 b).

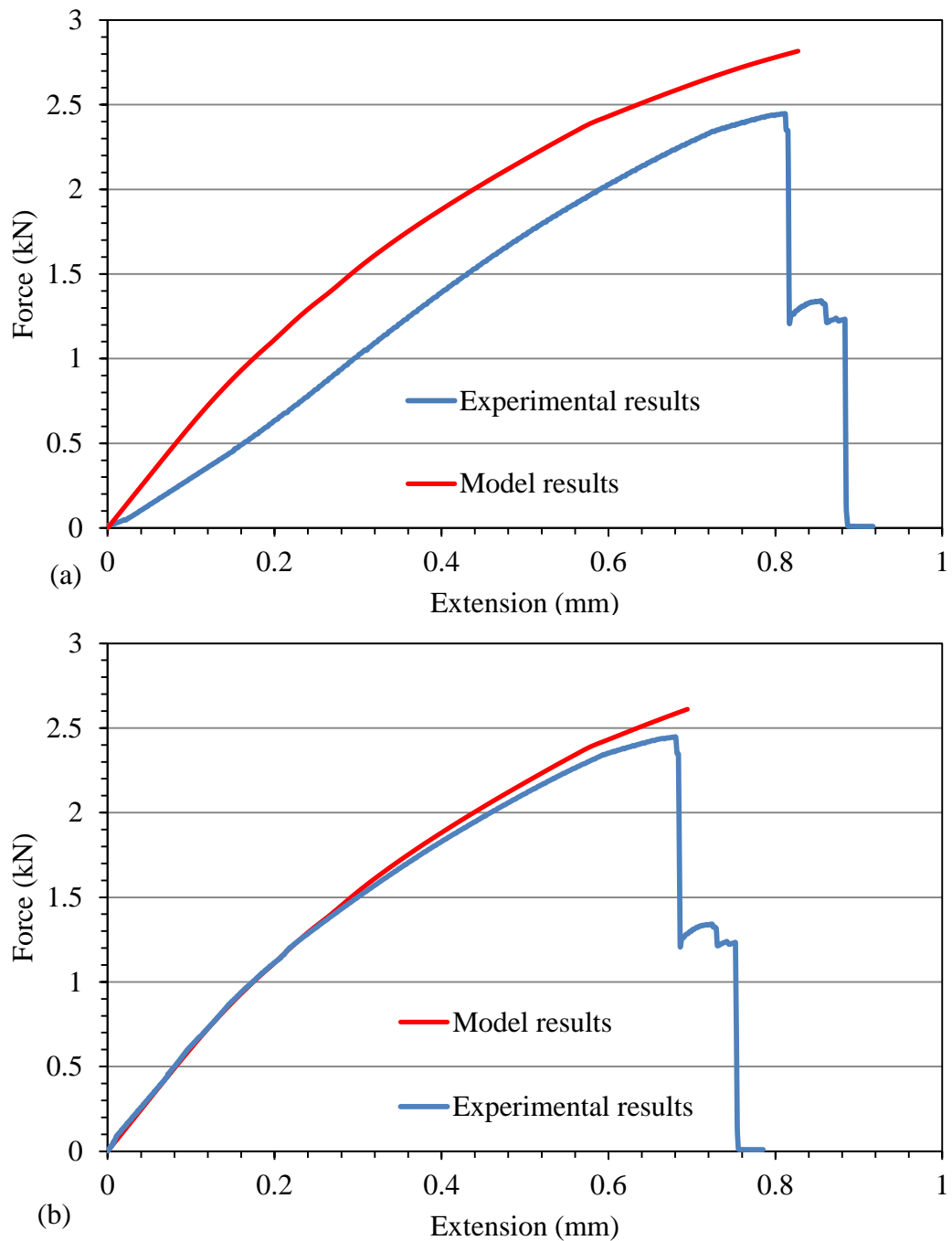


Figure 6-32: Experimental and numerical force-extension curves for the tensile lap shear test of RFSSW joints of dissimilar Mg-Al. The experimentally tested weld was produced using the modified RFSSW process with welding conditions of 2500 rpm, 1.0 s, and 1.0 mm.

## **6.6 Summary and Conclusions**

In this chapter, finite-element models of similar AA6111 and dissimilar AA6111 to AZ31 RFSSW joints were developed, to investigate the behaviour of the joints under tensile-shear loading conditions through numerical analysis.

The modelled sample was divided into an upper sheet, lower sheet, upper HAZ, lower HAZ, and SZ, depending on the variation of mechanical properties in these regions. The local hardness level was taken as an initial reference for the local mechanical properties. The HAZ was then divided into four sub-regions, due to the very large gradient in hardness. Several heat treatments were conducted to simulate these hardness levels in tensile samples to obtain stress-strain curves. These curves were then transformed into the true stress-strain plastic response curves that were required for the model.

To simulate the gripping in the lap tensile-shear test, one of the ends of the modelled sample was assumed to be fixed and the other pulled by an applied force. Only one-half of the actual sample was modelled, so as to reduce the computing time and a third boundary condition was assumed on the plane of symmetry to restrict the movement perpendicular to this plane and simulate the presence of the other half of the sample.

A tetrahedral structured mesh was chosen for all regions of the sample. However, the sizes of the elements were not equal in all regions: it was reduced in the SZ, HAZ, and the adjacent region due to the high stress concentration and the importance of these regions.

Both the modelled samples in the as-welded and the artificially-aged conditions showed nearly the same behaviour, in terms of their stress and strain distributions, which were mostly concentrated in the vicinity of the SZ at the interface between the two sheets. It was found that increasing the extension causes the regions of high stress and strain to propagate to the outer surfaces of the two sheets. These regions then propagated in two other directions: radially through the HAZ and annularly around the weld nugget. As a result, the nugget became completely surrounded by a cylindrical highly deformed region with a high stress concentration, which corresponded well with the full plug pull-out fracture mode, shown by the experimentally tested samples. The addition of the effect of the hook defect did not significantly alter the general behaviour, but increased the stress concentration in the region near its tip, resulting in more plastic deformation

for a lower applied load, reducing the strength of the joints. It also showed why failure always occurred in the lower sheets in the real tests.

FE analysis was successful in replicating the behaviour of the similar AA6111 RFSSW joints when subjected to lap tensile-shear loading. The force-extension curves showed good agreement between the model predictions and experimental results in both cases of the as-welded and artificially aged conditions; this was especially true for the model with the hook defect which showed a difference of about 6.6% compared to the experimental results in the as-welded condition. Moreover, after the correction of the experimental results the predicted force-extension curve for the model with a hook showed a full matching with the experimental curve in the as-welded and artificially aged conditions.

The model of the dissimilar Mg to Al weld showed approximately the same behaviour as that seen in the similar Al joints, in terms of the stress and strain distribution, but with higher stress and lower strain levels seen in the magnesium side of the joint. This occurred because the softer Al HAZ region transferred load to the Mg side of the joint at the edge of the nugget. Tensile stresses of the order of 100 MPa were generated at the weld interface, which would be expected to be responsible for initiating fracture through the IMC layer. In general, this model could be used for predicting the behaviour during the early stages of the test, but a failure criterion would be needed to predict the fracture of the joint, because this type of joint usually fails by a brittle fracture through the interface and was affected by several factors such as weld defects, the IMC layer and partial melting.



## **Chapter 7: Conclusions and Recommendations for Further Work**

---

### **7.1 General Conclusion**

Prior to this project refill friction stir spot welding (RFSSW) was a new and poorly-understood solid state joining technique. Due to the advantages of this process for joining similar and dissimilar combination of materials, it has become the focus of growing interest and investigation. However, before this project understanding was still limited in several areas for which further improvement was required, such as to reduce the long welding time (found to be  $\sim 4$  seconds in most of the literature), by controlling the material flow during the process, to control, or reduce, the effect of the interfacial brittle intermetallic phases formed in the joining of dissimilar material combinations.

In the present study, RFSSW has been used to join 1.0 mm gauge sheets of two material combinations: similar AA6111-T4 automotive aluminium alloy joints and dissimilar AA6111-T4 aluminium to AZ31-H24 magnesium alloys. The following conclusions have been made with regard to improving current understanding, to allow optimisation of the process for similar and dissimilar welding of light alloys.

#### **7.1.1 Al to Al similar welds**

The role of the process parameters, including sleeve plunge depth, tool rotation rate, and welding time were systematically assessed, in terms of their effect on the material flow, temperature distribution and microstructure, and their subsequent effect on the mechanical properties and failure mode of the joints.

The results of the experiments on the material flow, when using the contrast method, showed that the size of the area where the joint was metallurgical bonded increased with increasing plunge depth up to 1.0 mm. It has been observed that most mixing in the SZ occurred near the internal edge of the sleeve. This region showed much thinner marker layers compared to those found in other SZ regions, such as the upper region of the SZ, which was found to stop deforming once it entered the sleeve cavity during the plunging stage. Moreover, the material flow was shown to have a major role in the formation of

weld defects, such as the hooking, which was found to take place during the sleeve plunging stage, and increased in severity with increasing plunge depth.

The thermal history of a typical weld showed that the measured temperature highly depends on the vertical movement of the sleeve during the weld cycle, which affected the rate of plastic deformation. During the sleeve plunging stage, the temperature increased rapidly with a rate of about  $1450^{\circ}\text{C/s}$ . The rate of increase then decreased to about  $73^{\circ}\text{C/s}$  during the dwell stage. The temperature then decreased during the retraction stage. All welds showed the same location where the highest peak temperatures were measured. This point was located exactly under the sleeve position at a distance of 3 mm from the weld centre under the position of the internal edge of the sleeve, which was the main source of heat generation. This occurred because the sleeve surface had the highest velocity relative to the workpiece, and largest contact area. Moreover, this region was subjected to a very high plastic deformation and it was affected by the heat generated at both the inner and bottom surfaces of the sleeve. The effect of these factors together resulted in increasing the peak temperature in this region compared to other regions of the SZ. When increasing the tool rotation rate and/or welding time, the peak temperature showed a significant increase due to the increase in the rate of plastic deformation with increasing the tool rotation rate and increasing the amount of the heat accumulation with increasing welding time. Consequently, the highest peak temperature of  $580^{\circ}\text{C}$ , equivalent to the melting point of the alloy used, was measured when the highest rotation rate of 2500 rpm and the longest welding time of 2.0 s were used.

Investigation of the welded joints revealed three distinct weld microstructure regions in the as-welded condition: the first region was the stir zone (SZ) that contained very refined equiaxed grains as a result of dynamic recrystallization caused by the high strain reached during the sleeve plunging stage and the high temperature during the welding cycle; the second region was the thermo-mechanically affected zone (TMAZ), which could be observed from the distortion of the grains compared with the base material. This structure resulted from the effect of the more moderate temperature due the heat transferred from the stir zone, in addition to the more moderate strain caused by the shear gradient from the material that was coupled to the rotated and plunged tool, relative to the surrounding colder constraining material. In the third region, represented by the heat affected zone (HAZ) only thermal effects were observed. Further

investigation for the HAZ using the SEM revealed that it contained a very low density of very small widely spaced precipitates. These spherodised precipitates are probably  $\beta$  phase. Conversely, after the artificially ageing treatment, the same region showed a greater volume fraction of slightly coarser precipitates.

The hardness profile across the welds in the as-welded condition showed a typical W-shape. With a minimum value of about 60 HV at the HAZ border, compared to an average hardness of about 89 HV for the base material. The decrease in hardness level was caused by two factors; depending on the temperature, namely: the coarsening and the partial solutionisation of the hardening precipitates in the naturally aged parent material. Over-ageing occurred in the outer regions of the HAZ, because the maximum temperature reached during the welding cycle in this region was less than 300 °C. The region of the HAZ closer to the weld centre where the peak temperature reached a level higher than 300 °C, showed partial solutionisation, combined with a greater rate of coarsening because the peak temperatures in these zones did not reach the  $\beta$  phase solvus (540°C). Despite expected coarsening of the precipitate in the TMAZ, this region shows a slightly higher hardness level due to the effect of some strain hardening that resulted from the plastic deformation. The dynamic recrystallisation of the stir zone and grain refinement due to the high strain rate and higher temperature reached in the SZ (420 to 580 °C), caused near complete re-solutionisation, which resulted in subsequent rapid natural aging, all of these factors led to a slightly higher hardness level compared to the HAZ and TMAZ. The HAZ width also showed a clear increase with increasing welding time and tool rotation rate, due to the expansion of the thermal field and increase in peak temperature in regions more distant from the weld centre, which resulted in greater coarsening of the strengthening particles, or even solutionisation of strengthening precipitates in the regions where the peak temperatures exceed the solvus temperatures. The hardness level in the SZ and HAZ increased after natural and artificial ageing in comparison to the hardness levels in the as-welded condition, due to the precipitation of GPZs and solute clustering with ageing time, but samples that were welded for longer still exhibited a lower hardness level in the HAZ after natural ageing. Overall, the HAZ damage was found to be minimal because of the very rapid thermal cycle, which greatly limited the effects of over-ageing.

A wide window of suitable process parameters was found for the RFSSW process that resulted in joints with high strengths, even when using very short welding time (as short

as 0.55 s). The optimum conditions for the joints in the as-welded condition, which resulted in joints with a strength of about 4.2 kN, were found to be 1500 rpm and a 1.0 mm plunge depth used with a range of welding times from 0.55 to 2.0 s. In addition, when using a sleeve plunge depth of 0.8 mm, or more, all samples showed a nugget pull-out failure mode due to the increase in the bonded area. Natural and artificial ageing further improved the strength of the joints due to the improvement of the local mechanical properties in the HAZ and other regions, which resulted from the re-precipitation of GPZs and clustering on natural ageing, or  $\beta''$  on artificial ageing. The weld strength achieved when using welding parameters of a 2500 rpm tool rotation rate, a 1.5 s welding time and a 1.0 mm plunge, were peak loads of 5.15 and 6.43 kN in the naturally and artificially aged conditions, respectively. These strength levels are higher than those measured in any competing process.

### **7.1.2 Mg to Al dissimilar welds**

The application of RFSSW of thin Mg and Al sheets by welding from the magnesium side resulted in joints with acceptable mechanical properties, using a wide range of welding parameters. However, large non-acceptable voids at the edges of these joints were revealed by the metallographic investigation. To solve this problem, a modification to the RFSSW process was developed, that included adapting the welding cycle by adding an additional step that involved a very quick (about 0.15 s) shallow plunge (0.2 mm) of the pin to force the material to fill the voids retained after the refill step. As a result, nearly defect-free joints were produced with improved mechanical properties using a wide range of the process parameters.

The temperature measured during the cycle of the modified RFSSW process of the dissimilar joints showed different profiles than that of the similar welds. The temperature increased rapidly during the sleeve plunge stage with a rate of about 1300 °C/s to reach a peak temperature of 495 °C when using a tool rotation rate of 2800 rpm. However, due to local melting of the material at the interface between the two sheets, the temperature then fell to 432 °C. During the later steps, the temperature continued approximately at the same level of the eutectic reaction temperature (437 °C), suggesting melting self-limits the heat input. However, it decreased during the sleeve retraction (refilling) stage. The final pin plunging and retraction stages showed a low gradual increase in temperature to about 403 °C. Increasing the tool rotation rate had a



significant effect on increasing the peak temperature of the welds, especially in the range of 1900 rpm to 2500 rpm. However, a further increase of tool rotation rate to 2800 rpm showed less effect on the rate of increase in temperature, due to local melting of the material at the joint interface, which limited the increase in temperature and caused the formation of eutectic structures of  $\alpha$ -Mg solid solution and  $Mg_{17}Al_{12}$  at the weld interface after cooling down of the molten material.

In the dissimilar welds a non-uniform and non-continuous IMC reaction layer was found to be present at the interface of the joint. In general, 'islands' of the IMC layer were mainly detected at the interface under the sleeve, about 2 mm from the edge of the joint. The IMC layer was found to be composed of two sub-layers; an Al-rich layer on the aluminium side composed of  $\beta$ - $Al_3Mg_2$  phase, and an Mg-rich IMC layer on the side of magnesium, composed of  $\gamma$ - $Al_{12}Mg_{17}$  phase. The thickness of the IMC layer showed a significant increase, from about 1.7  $\mu m$  to 7.8  $\mu m$  with increasing tool rotation rate from 1900 to 2500 rpm due to the increase in the peak temperature. However, the thickness of the IMC layer showed a rapid decrease to about 2.8  $\mu m$  on increasing the tool rotation rate to 2800 rpm, because of the onset of significant eutectic melting and dispersal of the eutectic liquid due to the tool pressure.

The average peak load increased with increasing tool rotation rate, to reach a maximum value at 2500 rpm due to the increase of the material plasticity leading to eliminating the weld defects. However, the average peak load decreased on further increasing of tool rotation rate to 2800 rpm due the eutectic melting at the weld interface. Therefore, the optimum weld condition was found to be: 2500 rpm, 1.0 s, and 1.0 mm, for the modified RFSSW with an average peak load of 2.4 kN and average fracture energy of 1.3 kN.mm, which represent an improvement of about 10 % and 27 %, respectively, compared to welds produced with the conventional RFSSW process. Moreover, these values represent about 112 % of the average peak load and about 78 % of the fracture energy of Mg-Mg similar joints produced using the same welding conditions.

### **7.1.3 FE Model of the Similar and Dissimilar Joints**

The FE model developed was successful in increasing understanding of the behaviour of the RFSSW joints when subjected to lap tensile-shear loading, especially for the similar AA6111 alloy, in both the as-welded and the artificially aged conditions. The

stress and strain distribution in the modelled samples showed approximately the same overall behaviour as the real welds, with the highest concentration occurring in the region of the confluence of the SZ with the two sheets. With increasing extension, these regions of highest stress and strain propagated through the weak HAZ material of the edge of the weld to the outer surfaces of the two sheets away from the interface. This was followed by an annular propagation around the weld nugget. This annular ring of high strain concentration agreed well with the failure path and results in a full plug pull-out fracture mode, similar to that shown by the experimentally tested samples. Moreover, after compliance correction the numerical predictions of the force-extension curves using the model also showed good agreement with the experimental results, especially when including the effect of the hook defect. Full matching was achieved between the predicted force-extension curve for the model with a hook and the experimental curve in both cases: the as-welded and artificially aged conditions, whereas, the models without a hook over-predicted the joint strength by about 6%. Therefore, it is essential to accurately capture the hook defect to replicate the welds mechanical behaviour.

The stress and strain distribution in the model of the dissimilar Mg-to-Al weld also showed an approximately similar behaviour to that for the Al-Al model. However, the magnesium sheet showed higher stress and lower strain levels compared to the aluminium sheet. Currently, a failure criterion for the fracture of the interface has not been included in the model, but by correcting the curve of the experimental test, the behaviour of the overall load-displacement of the model agreed well with the results of the experimental curve until the point of fracture.

## **7.2 Recommendations for Further Work**

- Use the in-situ the X-Ray Computational Tomography Technique (XCT) to clarify the material flow behaviour during the different stages of RFSSW process and the failure behaviour during the tensile-shear test
- Use the TEM to increase the understanding of the mechanism of dissolution and re-precipitation of the hardening precipitates especially in the HAZ which is affected the changes in the Al-Al weld properties.
- Investigate the effect preheating and of the cooling during welding process on the properties of the similar and dissimilar welded joint.
- Evaluating the performance of welded joint using various mechanical testing techniques such as fatigue and impact test.
- Use the RFSSW process to join other combinations of materials such as welding aluminium to titanium or aluminium to steel.
- Develop a full FE model by adding a failure criterion to predict the failure load with taking into consideration the effect of welding defects, especially for the dissimilar joints, such as the voids in the edges of the weld zone.



## **Chapter 8: References**

- Abe, Y., Kato, T. & Mori, K., 2006. Joinability of aluminium alloy and mild steel sheets by self piercing rivet. *Journal of Materials Processing Technology*, Volume 177, p. 417–421.
- Abe, Y., Kato, T. & Mori, K., 2007. Joining of Aluminium Alloy and Mild Steel Sheets Using Mechanical Clinching. *Materials Science Forum*, Volume 561-565, pp. 1043-1046.
- Abe, Y., Kato, T. & Mori, K., 2009 a. Self-piercing riveting of high tensile strength steel and aluminium alloy sheets using conventional rivet and die. *journal of materials processing technology*, Volume 209, p. 3914–3922.
- Abe, Y., Kato, T. & Mori, K., 2009 b. Aluminium Alloy Self-Pierce Riveting for Joining of Aluminium Alloy Sheets. *Key Engineering Materials*, Volume 410-411, pp. 79-86.
- ACEA, 2015 a. *CO2 from Cars and Vans*. [Online]  
Available at: <http://www.acea.be/industry-topics/tag/category/co2-from-cars-and-vans>  
[Accessed 26 Jan 2016].
- ACEA, 2015 b. *Reducing CO2 emissions from cars and vans*. [Online]  
Available at: <http://www.acea.be/publications/article/backgrounder-reducing-co2-emissions-from-cars-and-vans>  
[Accessed 26 Jan 2016].
- Aghion, E. & Bronfin, B., 2000. Magnesium Alloys Development towards the 21st Century. *Materials Science Forum*, Volume 350-351, pp. 19-30.
- Aghion, E., Bronfin, B. & Eliezer, D., 2001. The role of magnesium industry in protecting environment. *Journal of Material Processing Technology*, Volume 117, pp. 381-385.
- Amancio-Filho, S. T. et al., 2011 b. On the feasibility of friction spot joining in magnesium/fiber-reinforced polymer composite hybrid structures. *Materials Science and Engineering A*, Volume 528, p. 3841–3848.
- Amancio-Filho, S. T. et al., 2011 a. Preliminary Investigation of the Microstructure and Mechanical Behaviour of 2024 Aluminium Alloy Friction Spot Welds. *Materials Transactions*, 52(5), pp. 985-991.
- Awang, M. & Mucino, V. H., 2010. Energy Generation during Friction Stir Spot Welding (FSSW) of Al 6061-T6 Plates. *Materials and Manufacturing Processes*, 25(1-3), pp. 167-174.
- Babout, L., 2006. X-ray tomography imaging: a necessary tool for materials science. *Automatyka/Akademia Górniczo-Hutnicza im. Stanisława Staszica w Krakowie*, Volume 10, pp. 117-124.
- Babu, S. et al., 2012. Microstructures and Mechanical Properties of Friction Stir Spot Welded Aluminum Alloy AA2014. *Journal of Materials Engineering and Performance*, 18 4.

- Badarinarayan, H., Shi, Y., Li, X. & Okamoto, K., 2009. Effect of tool geometry on hook formation and static strength of friction stir spot welded aluminium 5754-O sheets. *International Journal of Machine Tools & Manufacture*, Volume 49, p. 814–823.
- Bakavos, D. & Prangnell, P. B., 2009. Effect of reduced or zero pin length and anvil insulation on friction stir spot welding thin gauge 6111 automotive sheet. *Science and Technology of Welding and Joining*, 14( 5), pp. 443-456.
- Bakavos, D., Chen, Y., Babout, L. & Prangnell, P., 2011. Material Interactions in a Novel Pinless Tool Approach to Friction Stir Spot Welding Thin Aluminum Sheet. *Metallurgical and Materials Transactions A*, 42(A), pp. 1266-1282.
- Bakavos, D. & Prangnell, P. B., 2010. Mechanisms of joint and microstructure formation in high power ultrasonic spot welding 6111 aluminium automotive sheet. *Materials Science and Engineering A*, Volume 527, p. 6320–6334.
- Barnes, T. A. & Pashby, I. R., 2000a. Joining techniques for aluminium spaceframes used in automobiles Part I - solid and liquid phase welding. *Journal of Materials Processing Technology*, Volume 99, pp. 62-71.
- Barnes, T. A. & Pashby, I. R., 2000b. Joining techniques for aluminium spaceframes used in automobiles Part II - adhesive bonding and mechanical fasteners. *Journal of Materials Processing Technology*, Volume 99, pp. 72-79.
- Benedyk, J. C., 2010. Aluminum alloys for lightweight automotive structures. In: P. K. Mallick, ed. *Materials, design and manufacturing for lightweight vehicles*. s.l.:Woodhead publishing limited, pp. 70-113.
- Bilici, M. K. & Yüklér, A. I., 2012. Influence of tool geometry and process parameters on macrostructure and static strength in friction stir spot welded polyethylene sheets. *Materials and Design*, Volume 33, p. 145–152.
- Blawert, C., Hort, N. & Kainer, K. U., 2004. Automotive Applications Of Magnesium And Its Alloys. *Trans. Indian Inst. Met.*, 57(4), pp. 397-408.
- Borrisutthekul, R., Miyashita, Y. & Mutoh, Y., 2005. Dissimilar material laser welding between magnesium alloy AZ31B and aluminum alloy A5052-O. *Science and Technology of Advanced Materials*, Volume 6, p. 199–204.
- Bozzi, S. et al., 2010. Influence of FSSW parameters on fracture mechanisms of 5182 aluminium welds. *Journal of Materials Processing Technology*, Volume 210, p. 1429–1435.
- Briskham, P. et al., 2006. Comparison of self-pierce riveting, resistance spot welding and spot friction joining for aluminium automotive sheet. *SAE 2006 congress, Technical paper, 2006-01-0774*.
- Buffa, G., Fratini, L. & Piacentini, M., 2008 b. On the influence of tool path in friction stir spot welding of aluminum alloys. *journal of materials processing technology*, Volume 208, p. 309–317.
- Buffa, G., Fratini, L. & Shivpuri, R., 2008 a. Finite element studies on friction stir welding processes of tailored blanks. *Computers and Structures* 86, Volume 86, p. 181–189.

- Burger, G. B., Gupta, A. K., Jeffrey, P. W. & Lloyd, D. J., 1995. Microstructural Control of Aluminum Sheet Used in Automotive Applications. *Materials Characterization*, Volume 35, pp. 23-39.
- Campanelli, L. C. et al., 2013b. Lap Shear Test of a Magnesium Friction Spot Joint: Numeric Modeling. *Tecnol. Metal. Mater. Miner.*, 10(2), pp. 97-102.
- Campanelli, L. C., de Alcântara, N. G. & dos Santos, J. F., 2011. Solid State Spot Welding of Lightweight Alloys. *Soldag. insp. São Paulo*, 16(3), pp. 300-307.
- Campanelli, L. C., Suhuddin, U. F., dos Santos, J. F. & Alcântara, N. G., 2012b. Preliminary investigation on friction spot welding of AZ31 magnesium alloy. *Materials Science Forum*, Volume 706–709, p. 3016–3021.
- Campanelli, L. C. et al., 2013a. Metallurgy and mechanical performance of AZ31 magnesium alloy friction spot welds. *Journal of Materials Processing Technology*, Volume 213, p. 515– 521.
- Campanelli, L. C. et al., 2013a. Metallurgy and mechanical performance of AZ31 magnesium alloy friction spot welds. *Journal of Materials Processing Technology*, Volume 213, p. 515– 521.
- Campanelli, L. C., Suhuddin, U. F. H., dos Santos, J. F. & de Alcântara, N. G., 2012a. Parameters Optimization for Friction Spot Welding of AZ31 Magnesium Alloy by Taguchi Method. *Soldag. Insp.*, Jan/Mar, 17(1), pp. 026-031.
- Cao, J. Y., Wang, M., Kong, L. & Guo, L. J., 2016. Hook formation and mechanical properties of friction spot welding in alloy 6061-T6. *Journal of Materials Processing Technology*, Volume 230, p. 254–262.
- CAR, 2011. *Automotive Technology: Greener Products, Changing Skills, Lightweight Materials & Forming Report*, s.l.: Driving Change.
- Carle, D. & Blount, G., 1999. The suitability of aluminium as an alternative material for car bodies. *Materials and Design*, Volume 20, pp. 267-272.
- Chao, Y. J., Qi, X. & Tang, W., 2003. Heat Transfer in Friction Stir Welding- Experimental and Numerical Studies. *Journal of Manufacturing Science and Engineering*, February, Volume 125, pp. 138-145.
- Chen, Y.-C., Bakavos, D., Gholinia, A. & Prangnell, P. B., 2012 a. HAZ development and accelerated post-weld natural ageing in ultrasonic spot welding aluminium 6111-T4 automotive sheet. *Acta Materialia*, Volume 60, p. 2816–2828.
- Chen, Y.-C., Bakavos, D., Gholinia, A. & Prangnell, P. B., 2012 a. HAZ development and accelerated post-weld natural ageing in ultrasonic spot welding aluminium 6111-T4 automotive sheet. *Acta Materialia*, Volume 60, p. 2816–2828.
- Chen, Y.-C., Bakavos, D., Gholinia, A. & Prangnell, P. B., 2012b. HAZ development and accelerated post-weld natural ageing in ultrasonic spot welding aluminium 6111-T4 automotive sheet. *Acta Materialia*, Volume 60, p. 2816–2828.
- Chen, Y. C., Gholinia, A. & Prangnell, P. B., 2012 b. Interface structure and bonding in abrasion circle friction stir spot welding: A novel approach for rapid welding aluminium

alloy to steel automotive sheet. *Materials Chemistry and Physics*, Volume 134, p. 459–463.

Chen, Y. C., Liu, S. F., Bakavos, D. & Prangnell, P. B., 2013. The effect of a paint bake treatment on joint performance in friction stir spot welding AA6111-T4 sheet using a pinless tool. *Materials Chemistry and Physics*, Volume 14, pp. 768-775.

Choi, D.-H. et al., 2011. Formation of intermetallic compounds in Al and Mg alloy interface during friction stir spot welding. *Intermetallics*, Volume 19, pp. 125-130.

Chowdhury, S. H. et al., 2013. Lap shear strength and fatigue behavior of friction stir spot welded dissimilar magnesium-to-aluminum joints with adhesive. *Materials Science & Engineering A*, Volume 562, p. 53–60.

Colegrove, P. A., Shercliff, H. R. & Zettler, R., 2007. Model for predicting heat generation and temperature in friction stir welding from the material properties. *Science and Technology of Welding and Joining*, 12(4), pp. 284-297.

Cole, G. S. & Sherman, A. M., 1995. Lightweight Materials for Automotive Applications. *Materials Characterization*, Volume 35, pp. 3-9.

Commin, L., Dumont, M., Masse, J. -E. & Barrallier, L., 2009. Friction stir welding of AZ31 magnesium alloy rolled sheets: Influence of processing parameters. *Acta Materialia* 57, p. 326–334.

Cui, X., Wang, S. & Hu, S. J., 2008. A method for optimal design of automotive body assembly using multi-material construction. *Materials and Design*, Volume 29, p. 381–387.

Czerwinski, F., 2011. *Magnesium Alloys - Design, Processing and Properties*. Edited Volume ed. s.l.:InTech.

De Noirfontaine, M. -N. et al., 2010. High Temperature Oxidation of the Al<sub>3</sub>Mg<sub>2</sub> Complex Metallic Alloy. *Oxid Met*, Volume 73, p. 219–232.

Dodman, D., 2009. Blaming cities for climate change? An analysis of urban greenhouse gas emissions inventories. *Environment & Urbanization*, 21(1), p. 185–201.

Dong, H. et al., 2016. Refilled friction stir spot welding of aluminum alloy to galvanized steel sheets. *Materials and Design*, Volume 94, pp. 457-466.

Douglas, C. H. & Kenneth, S. V., 2007. Thermal history analysis of friction stir processed and submerged friction stir processed aluminum. *Materials Science and Engineering A*, 465(1–2), p. 165–175.

Elangovan, K., Balasubramanian, V. & Babu, S., 2008. Predicting tensile strength of friction stir welded AA6061 aluminum alloy joints by a mathematical model. *Materials and Design*, 30(1), p. 188–193.

Elangovan, S., Semeer, S. & Prakasan, K., 2009. Temperature and stress distribution in ultrasonic metal welding—An FEA-based study. *Journal of materials processing technology*, Volume 209, p. 1143–1150.



- Esmaceli, S., Wang, X., Lloyd, D. J. & Poole, W. J., 2003. On the Precipitation-Hardening Behavior of the Al-Mg-Si-Cu Alloy AA6111. *Metallurgical and Materials Transactions A*, March , 34(A), pp. 751-763.
- Esteves, J. V. et al., 2015. Friction spot joining of aluminum AA6181-T4 and carbon fiber-reinforced poly(phenylene sulfide): Effects of process parameters on the microstructure and mechanical strength. *Materials and Design*, Volume 66, p. 437–445.
- Fanelli, P., Vivio, F. & Vullo, V., 2012. Experimental and numerical characterization of Friction Stir Spot Welded joints. *Engineering Fracture Mechanics*, Volume 81, p. 17–25.
- FEI, 2007. *FEI Company. Quanta 3 D FEG User Operation Manual*, -: -.
- Feuerbacher, M. et al., 2007. The Samson phase, b-Mg<sub>2</sub>Al<sub>3</sub>, revisited. *Z. Kristallogr.*, Volume 222, p. 259–288.
- Fontaras, G. & Samaras, Z., 2007. A quantitative analysis of the European Automakers' voluntary commitment to reduce CO<sub>2</sub> emissions from new passenger cars based on independent experimental data. *Energy Policy*, Volume 35, p. 2239–2248.
- Fridlyander, I. N. et al., 2002. Aluminum Alloys: Promising Materials in the Automotive Industry. *Metal Science and Heat Treatment*, Volume 44, pp. 365-370.
- Fuchs, E. R., Field, F. R., Roth, R. & Kirchain, R. E., 2008. Strategic materials selection in the automobile body: Economic opportunities for polymer composite design. *Composites Science and Technology*, Volume 68, p. 1989–2002.
- Fukumoto, S. et al., 2003. Effects of Electrode Degradation on Electrode Life in Resistance Spot Welding of Aluminum Alloy 5182. *Welding Journal*, Volume Welding Research. Supplement to the Welding Journal, November 2003, pp. 307S-312S.
- Gao, C., Gao, R. & Ma, Y., 2015. Microstructure and mechanical properties of friction spot welding aluminium–lithium 2A97 alloy. *Materials & Design*, Volume 83, p. 719–727.
- Gerlich, A., Avramovic-Cingrara, G. & North, T. H., 2006. Stir zone microstructure and strain rate during Al 7075-T6 friction stir spot welding. *Metallurgical and Materials Transactions A*, 37(A), pp. 2773-2786.
- Gerlich, A. P. & Shibayanagi, T., 2009. Grain boundary sliding during friction stir spot welding of an aluminum alloy. *Scripta Materialia*, Volume 60, p. 236–239.
- Gerlich, A., Su, P. & North, T. H., 2005. Peak temperatures and microstructures in aluminium and magnesium alloy friction stir spot welds. *Science and Technology of Welding and Joining*, 10(6), pp. 647-652.
- Gerlich, A., Su, P., Yamamoto, M. & North, T. H., 2007. Effect of welding parameters on the strain rate and microstructure of friction stir spot welded 2024 aluminum alloy. *Journal of Materials Science*, July, 42(14), pp. 5589-5601.
- Gerlich, A., Su, P., Yamamoto, M. & North, T. H., 2008. Material flow and intermixing during dissimilar friction stir welding. *Science and Technology of Welding and Joining*, 13(3), pp. 254-264.

- Ghassemieh, E., 2011. Materials in Automotive Application, State of the Art and Prospects. In: M. Chiaberge, ed. *New Trends and Developments in Automotive Industry*. Croatia: InTech, pp. 365-390.
- Ghosh, M., Kumar, K., Kailas, S. & Ray, A., 2010. Optimization of friction stir welding parameters for dissimilar aluminum alloys. *Materials and Design* 31, p. 3033–3037.
- Gopalakrishnan, S. & Murugan, N., 2011. Prediction of tensile strength of friction stir welded aluminium matrix TiC p particulate reinforced composite. *Materials and Design*, Volume 32, p. 462–467.
- Gould, J. E., 2012. Joining Aluminum Sheet in the Automotive Industry – A 30 Year History. *Welding Journal*, Volume 91, pp. 23-s - 34-s.
- GOV.UK, 2015. *2010 to 2015 government policy: transport emissions - GOV.UK*. [Online]  
Available at: <https://www.gov.uk/government/publications/2010-to-2015-government-policy-transport-emissions/2010-to-2015-government-policy-transport-emissions>  
[Accessed 26 Jan 2016].
- Greene, D. L., 2006. *Reducing Greenhouse Gas Emissions From Transportation*, Raleigh, North Carolina: A presentation to the Legislative Commission on Global Climate Change.
- Greene, D. L. & Plotkin, S. E., 2011. *Reducing Greenhouse Gas Emissions from U.S. Transportation*, s.l.: The Pew Center on Global Climate Change.
- Haddadi, F., Strong, D. & Prangnell, P. B., 2012. Effect of zinc coatings on joint properties and interfacial reactions in aluminium to steel ultrasonic spot welding. *JOM*, 64(3), pp. 407-413.
- Hadley, S. W., Das, S. & Miller, J. W., 2000. *Aluminium R&D for Automotive Uses And the Department of Energy's Role*, s.l.: U.S. Department of Energy.
- Han, L., Thornton, M., Boomer, D. & Shergold, M., 2010. Effect of aluminium sheet surface conditions on feasibility and quality of resistance spot welding. *Journal of Materials Processing Technology*, 210(8), pp. 1076-1082.
- Han, L., Thornton, M. & Shergold, M., 2010. comparative study between self-piercing riveting and resistance spot welding of aluminium sheets for the automotive industry. *Materials & Design*, 31(3), pp. 1457-1467.
- Hatamleh, O., 2008. Effects of peening on mechanical properties in friction stir welded 2195 aluminum alloy joints. *Materials Science and Engineering*, 492(A), p. 168–176.
- Hayat, F., 2011. The effects of the welding current on heat input, nugget geometry, and the mechanical and fractural properties of resistance spot welding on Mg/Al dissimilar materials. *Materials and Design*, 32(4), pp. 2476-2484.
- He, X., Pearson, I. & Young, K., 2008. Self-pierce riveting for sheet materials: State of the art. *journal of materials processing technology*, Volume 199, p. 27–36.
- Hirsch, J., 2011. Aluminium in Innovative Light-Weight Car Design. *Materials Transactions*, 52(5), pp. 818-824.

Hoang, N. -H., Porcaro, R., Langseth, M. & Hanssen, A. -G., 2010. Self-piercing riveting connections using aluminium rivets. *International Journal of Solids and Structures*, Volume 47, p. 427–439.

Hovanski, Y., Santella, M. L. & Grant, G. J., 2007. Friction stir spot welding of hot-stamped boron steel. *Scripta Materialia*, Volume 57, p. 873–876.

ICCT, 2014. *EU CO2 Emission Standards for Passenger Cars and Light-Commercial Vehicles, Policy Update*, S.L.; s.l.: International Council on Clean Transportation.

Jahn, R., Cooper, R. & Wilkosz, D., 2007. The Effect of Anvil Geometry and Welding Energy on Microstructures in Ultrasonic Spot Welds of AA6111-T4. *Metallurgical and Materials Transactions*, 38(A), pp. 570-583.

Jambhale, S., Kumar, S. & Kumar, S., 2015. Effect of Process Parameters & Tool Geometries on Properties of Friction Stir Spot Welds: A Review. *Universal Journal of Engineering Science*, 1(3), pp. 6-11.

Jambor, A. & Beyer, M., 1997. New cars - new materials. *Materials & Design*, 18(4/6), pp. 203-209.

Jeglič, P. et al., 2007. *PHYSICAL REVIEW*, 75(B), pp. 1-15.

Johnson, R. & Kallee, S., 2013. *m.com The A to Z of Materials*. [Online] Available at: <http://www.azom.com/article.aspx?ArticleID=1170> [Accessed 9 April 2016].

Juchmann, P., 2006. Rolling and Shut Forming. In: H. E. Friedrich & B. L. Mordike, eds. *Magnesium Technology Metallurgy, Design Data, Applications*. Berlin Heidelberg: Springer-Verlag, pp. 269-288.

Kalagara, S. & Muci-Küchler, K. H., 2010. Visualization of Material Flow in a Refill Friction Stir Spot Welding Process Using Marker Materials. *SAE International Journal of Materials and Manufacturing*, 3(1), pp. 628-651.

Kallee, S. & Nicholas, D., 2003. <http://materialteknologi.hig.no/Lettvektdesign/joining%20methods/joining-welding-friction%20stir%20weld.htm>. [Online] [Accessed 14 August 2012].

Kammer, C., 2006. Wrought Alloys. In: H. E. Friedrich & B. L. Mordike, eds. *Magnesium Technology: Metallurgy, Design Data, Applications*. Berlin Heidelberg: Springer-Verlag, pp. 204-214.

Karthikeyan, R. & Balasubramanian, V., 2010. Predictions of the optimized friction stir spot welding process parameters for joining AA2024 aluminum alloy using RSM. *Int J Adv Manuf Technol*, Volume 51, p. 173–183.

Kaya, A. A., 2013. Physical metallurgy of magnesium. In: M. O. Pekguleryuz, K. U. Kainer & A. A. Kaya, eds. *Fundamentals of magnesium alloy metallurgy*. s.l.: Woodhead Publishing Limited, pp. 33-84.

Kelkar, A., Roth, R. & Clark, J., 2001. Automobile Bodies: Can Aluminum Be an Economical Alternative to Steel?. *JOM*, 53(8), pp. 28-32.

- Khan, J. A., Xu, L., Chao, Y.-J. & Broach, K., 2000. Numerical Simulation of Resistance Spot Welding Process, Numerical Heat Transfer, Part A: Applications. *An International Journal of Computation and*, 37(5), pp. 425-446.
- Khan, M. I., 2007. *Welding Science and Technology*. New Delhi: New Age International (P) Limited, Publishers.
- Kim, D. et al., 2010. Numerical simulation of friction stir butt welding process for AA5083-H18 sheets. *European Journal of Mechanics A/Solids*, Volume 29, p. 204–215.
- Kou, S., 2003. *Welding Metallurgy*. 2nd ed. New Jersey: John Wiley & Sons, Inc.
- Kulekci, M. K., Esme, U. & Er, O., 2011. Experimental Comparison of Resistance Spot Welding and Friction-Stir Spot Welding Processes For the En Aw 5005 Aluminum Alloy. *Materials and technology*, 45(5), p. 395–399.
- Kumar, N., Yuan, W. & Mishra, R. S., 2015. *Friction Stir Welding of Dissimilar Alloys and Materials*. 1st ed. Oxford: Elsevier Inc.
- Lacki, P. & Derlatka, A., 2016. Experimental and numerical investigation of aluminium lap joints made by RFSSW. *Meccanica*, Volume 51, p. 455–462.
- Lashof, D. A. & Ahuja, D. R., 1990. Relative contributions of greenhouse gas emissions to global warming. *Nature*, Volume 344, pp. 529-531.
- Lathabai, S., Painter, M. J., Cantin, G. M. & Tyagi, V. K., 2006. Friction spot joining of an extruded Al–Mg–Si alloy. *Scripta Materialia*, Volume 55, p. 899–902.
- Lee, W.-B. et al., 2005. Microstructural investigation of friction stir welded pure titanium. *Materials Letters* 59, p. 3315 – 3318.
- Lee, Y.-W. et al., 2011. *Characterization of Friction Stir Spot Welding of Aluminum Alloys using Acoustic Emissions*. Maui, Hawaii, USA, the International Society of Offshore and Polar Engineers (ISOPE).
- Liang, X.-p. et al., 2012. Study on the microstructure in a friction stir welded 2519-T87 Al alloy. *Materials and Design* 35, p. 603–608.
- Ling, Y., 1996. Uniaxial True Stress-Strain after Necking. *AMP Journal of Technology*, Volume 5, pp. 37-48.
- Liu, H. J., Zhang, H. J. & Yu, L., 2011. Effect of welding speed on microstructures and mechanical properties of underwater friction stir welded 2219 aluminum alloy. *Materials and Design* 32, p. 1548–1553.
- Liu, L., Ren, D. & Liu, F., 2014. A Review of Dissimilar Welding Techniques for Magnesium Alloys to Aluminum Alloys. *Materials*, Volume 7, pp. 3735-3757.
- Liyanage, T., Kilbourne, J., Gerlich, A. P. & North, T. H., 2009. Joint formation in dissimilar Al alloy/steel and Mg alloy/steel friction stir spot welds. *Science and Technology of Welding and Joining*, 14(6), pp. 500-508.
- Li, Y., Lin, Z., Jiang, A. & Chen, G., 2003. Use of high strength steel sheet for lightweight and crashworthy car body. *Materials and Design* , Volume 24, p. 177–182.

- Li, Y., Lin, Z., Jiang, A. & Chen, G., 2004. Experimental study of glass-fiber mat thermoplastic material impact properties and lightweight automobile body analysis. *Materials and Design*, Volume 25, p. 579–585.
- Li, Z. et al., 2016. Fracture mechanism of refill friction stir spot-welded 2024-T4 aluminum alloy. *Int J Adv Manuf Technol*, Volume published online: 16 January 2016, pp. 1-8.
- Lum, I. et al., 2004. Electrode Pitting in Resistance Spot Welding of Aluminum Alloy 5182. *Metallurgical and Materials Transactions*, 35(A), pp. 217-226.
- Lutsey, N., 2010. *Review of Technical Literature and Trends Related to Automobile Mass-Reduction Technology*, s.l.: Institute of Transportation Studies ° University of California, Davis.
- Maire, E. et al., 2001. On the Application of X-ray Microtomography in the Field of Materials Science. *Advanced Engineering Materials*, 3(8), pp. 539-546.
- Mai, T. A. & Spowage, A. C., 2004. Characterisation of dissimilar joints in laser welding of steel–kovar, copper–steel and copper–aluminium. *Materials Science and Engineering A*, Volume 374 , p. 224–233.
- Maitland, T. & Sitzman, S., 2006. Electron Backscatter Diffraction (EBSD) Technique and Materials Characterization Examples. In: W. Zhou & Z. L. Wang, eds. *Scanning Microscopy for Nanotechnology Techniques and Applications*. New York: Springer, pp. 41-75.
- Malafaia, A. M. S., Milan, M. T., Oliveira, M. F. & Spinelli, D., 2010. Fatigue behavior of friction stir spot welding and riveted joints in an Al alloy. *Procedia Engineering*, Volume 2, pp. 1815-1821.
- Mandal, S., Rice, J. & Elmustafa, A., 2008. Experimental and numerical investigation of the plunge stage in friction stir welding. *Journal of Materials Processing Technology*, 18 July, 203(1–3), p. 411–419.
- Manladan, S. M., Yusof, F., Ramesh, S. & Fadzil, M., 2016. A review on resistance spot welding of magnesium alloys. *Int J Adv Manuf Technol*.
- Mascarin, A. et al., 2015. *Vehicle Lightweighting: 40% and 45% Weight Savings Analysis: Technical Cost Modeling for Vehicle Lightweighting*, Idaho Falls, Idaho: Idaho National Laboratory.
- Mathers, G., 2002. *The welding of aluminium and its alloys*. 1st ed. Cambridge England: Woodhead Publishing Limited.
- Matsuoka, S.-i. & Imai, H., 2009. Direct welding of different metals used ultrasonic vibration. *Journal of Materials Processing Technology*, Volume 209, p. 954–960.
- Mazzaferro, J. A. E., Rosendo, T. d. S., Mazzaferro, C. C. P. & Ramos, F. D., 2009. Preliminary Study on the Mechanical Behavior of Friction Spot Welds. *Soldagem Insp.*, Jul/Set, 14(3), pp. 238-247.
- McCormick, P. G., 1971. The Portevin-Le Chatelier Effect in an Al-Mg-Si Alloy. *Acta Metallurgica*, Volume 19, pp. 463-471.

- Meinshausen, M. et al., 2009. Greenhouse-gas emission targets for limiting global warming to 2 °C. *Nature*, Volume 458, pp. 1158-1162.
- Meran, C., 2006. The joint properties of brass plates by friction stir welding. *Materials and Design* 27, p. 719–726.
- Mercedes-Benz.USA, 2016. *AMG SL63 2016 Convertible Roadster / Mercedes-Benz*. [Online]  
Available at: <http://www.mbusa.com/mercedes/vehicles/model/class-SL/model-SL63>  
[Accessed 26 Jan 2016].
- Michael, B. P. et al., 2006. Residual stress measurements in a thick, dissimilar aluminum alloy friction stir weld. *Acta Materialia* 54, p. 4013–4021.
- Miller, W. S. et al., 2000. Recent development in aluminium alloys for the automotive industry. *Materials Science and Engineering*, Volume A280, p. 37–49.
- Mishra, R. & Ma, Z., 2005. Friction stir welding and processing. *Materials Science and Engineering: R: Reports*, p. 1–78.
- Mitchell, R. A., Woolley, R. M. & Baker, S. M., 1975. *Finite Element Analysis of Spotwelded, Bonded and Weldbonded Lap Joints*, Washington, D. C.: National Bureau of Standards.
- Mitlin, D. et al., 2006. Structure–properties relations in spot friction welded (also known as friction stir spot welded) 6111 aluminum. *Materials Science and Engineering A* (), Volume 441, p. 79–96.
- Mordike, B. L. & Lukác, P., 2006. Physical Metallurgy. In: H. E. Friedrich & B. L. Mordike, eds. *Magnesium Technology: Metallurgy, Design Data, Applications*. Berlin Heidelberg: Springer-Verlag , pp. 63-108.
- Murray, J. L., 1982. The Al-Mg (aluminium-magnesium) system. *Bulletin of Alloy Phase Diagrams*, 3(1), pp. 60-74.
- Nami, H., Adgi, H., Sharifitabar, M. & Shamabadi, H., 2011. Microstructure and mechanical properties of friction stir welded Al/Mg 2 Si metal matrix cast composite. *Materials and Design* 32, p. 976–983.
- Nandan, R., DebRoy, T. & Bhadeshia, H., 2008. Recent advances in friction-stir welding – Process, weldment structure and properties. *Progress in Materials Science*, Volume 53, p. 980–1023.
- Nguyen, N.-T., Kim, D.-Y. & Kim, H. Y., 2011. Assessment of the failure load for an AA6061-T6 friction stir spot welding joint. *Proceedings of the Institution of Mechanical Engineers, Part B: Journal of Engineering Manufacture*, 225(10), pp. 1746-1756.
- Nie, J.-F., 2014. Physical Metallurgy of Light Alloys. In: D. E. Laughlin & K. Hono, eds. *Physical Metallurgy*. 5th ed. Oxford ,UK: Elsevier, pp. 2009-2156.
- Okamoto, H., 1998. Al-Mg (Aluminum-Magnesium). *Journal of Phase Equilibria*, 19(6), p. 598.

- Oliveira, P. H., Amancio-Filho, S. T., dos Santos, J. F. & Jr, E. H., 2010. Preliminary study on the feasibility of friction spot welding in PMMA. *Materials Letters*, Volume 64, p. 2098–2101.
- Panteli, A., 2012. *Friction Joining of Aluminium-to-Magnesium for Lightweight Automotive Applications*. Ph.D. Thesis: The University of Manchester.
- Panteli, A., Robson, J. D., Brough, I. & Prangnell, P. B., 2012. The effect of high strain rate deformation on intermetallic reaction during ultrasonic welding aluminium to magnesium. *Materials Science & Engineering A*, Volume 556, p. 31– 42.
- Parra, B. et al., 2011. An Investigation on Friction Spot Welding in AA6181-T4 Alloy. *Tecnol. Metal. Mater. Miner.*, jul.-set., 8(3), pp. 184-190.
- Patel, V. K., Bhole, S. D. & Chen, D. L., 2011. Influence of ultrasonic spot welding on microstructure in a magnesium alloy. *Scripta Materialia*, Volume 65, p. 911–914.
- Patel, V. K., Bhole, S. D. & Chen, D. L., 2012 a. Improving weld strength of magnesium to aluminium dissimilar joints via tin interlayer during ultrasonic spot welding. *Science and Technology of Welding and Joining*, 17(5), pp. 342-347.
- Patel, V. K., Bhole, S. D. & Chen, D. L., 2012 b. Microstructure and mechanical properties of dissimilar welded Mg–Al joints by ultrasonic spot welding technique. *Science and Technology of Welding and Joining*, 17(3), pp. 202-206.
- Peilin, L. et al., 2012. Mechanical properties and microstructure analysis of refilling friction stir welding on 2219 aluminium alloy. *Acta Metall. Sin.(Engl. Lett.)*, June, 25(3), pp. 225-234.
- Pekguleryuz, M., 2013. Alloying behavior of magnesium and alloy design. In: M. O. Pekguleryuz, K. U. Kainer & A. A. Kaya, eds. *Fundamentals of magnesium alloy metallurgy*. s.l.:Woodhead Publishing Limited, pp. 152-196.
- Pereira, A. M. et al., 2010. Effect of process parameters on the strength of resistance spot welds in 6082-T6 aluminium alloy. *Materials and Design*, Volume 31, p. 2454–2463.
- Polmear, I. J., 2007. *Light Alloys*. 4th ed. s.l.:Butterworth-Heinemann.
- Porcaro, R., Hanssen, A. G., Aalberg, A. & Langseth, M., 2004. Joining of aluminium using self-piercing riveting: Testing, modelling and analysis. *International Journal of Crashworthiness*, 9(2), pp. 141-154.
- Porcaro, R., Hanssen, A. G., Langseth, M. & Aalberg, A., 2006. Self-piercing riveting process: An experimental and numerical investigation. *Journal of Materials Processing Technology*, Volume 171, p. 10–20.
- Pouranvari, M. & Marashi, S. P. H., 2013. Critical review of automotive steels spot welding: process, structure and properties. *Science and Technology of Welding and Joining*, 18(5), pp. 361-403.
- Powell, B., Krajewski, P. & Luo, A., 2010. Magnesium alloys for lightweight powertrains and automotive structures. In: M. P. K., ed. *Materials, design and manufacturing for lightweight vehicles*. Cambridge UK: Woodhead Publishing Limited, pp. 114-173.

- Prakash, S. J. & Muthukumaran, S., 2011. Refilling Probe Hole of Friction Spot Joints by Friction Forming. *Materials and Manufacturing Processes*, Volume 26, p. 1539–1545.
- Prangnell, P. B. & Bakavos, D., 2010. Novel Approaches to Friction Spot Welding Thin Aluminium Automotive Sheet. *Materials Science Forum*, Volume 638-642, pp. 1237-1242.
- Qiao, F., Cheng, K., Wang, L. & Guo, L., 2015. An experimental investigation on the dissimilar joining of AA6061 and 1Cr18Ni9Ti by refill friction stir spot welding and its mechanical properties. *J Engineering Manufacture*, Volume Proc IMechE Part B, pp. 1-7.
- Qiu, R., Iwamoto, C. & Satonaka, S., 2009. Interfacial microstructure and strength of steel/aluminum alloy joints welded by resistance spot welding with cover plate. *Journal of Materials Processing Technology*, Volume 209, p. 4186–4193.
- Raeisinia, B., Poole, W. J. & Lloyd, D. J., 2006. Examination of precipitation in the aluminum alloy AA6111 using electrical resistivity measurements. *Materials Science and Engineering*, 420(A), p. 245–249.
- Rajakumar, S., Muralidharan, C. & Balasubramanian, V., 2011. Influence of friction stir welding process and tool parameters on strength properties of AA7075-T 6 aluminium alloy joints. *Materials and Design* 32, p. 535–549.
- Ratanathavorn, W., 2015. *Development and evaluation of hybrid joining for metals to polymers using friction stir welding*, Licentiate Thesis. Stockholm, Sweden: KTH Royal Institute of Technology, Industrial Engineering and Management, Department of Production Engineering.
- Reilly, A., Shercliff, H., Chen, Y. & Prangnell, P., 2015. Modelling and visualisation of material flow in friction stir spot welding. *Journal of Materials Processing Technology*, Volume 225, p. 473–484.
- Rosado, L. S. et al., 2010. Advanced technique for non-destructive testing of friction stir welding of metals. *Measurement* 43, p. 1021–1030.
- Rosendo, T. et al., 2011. Mechanical and microstructural investigation of friction spot welded AA6181-T4 aluminium alloy. *Materials and Design*, Volume 32, p. 1094–1100.
- Rosendo, T. et al., 2015. Mechanical performance of AA6181 refill friction spot welds under Lap shear tensile loading. *Fatigue Fract Engng Mater Struct*, Volume 38, p. 1443–1455.
- Salvo, L. et al., 2010. 3D imaging in material science: Application of X-ray tomography. *C. R. Physique*, Volume 11, p. 641–649.
- Samson, S., 1965. The Crystal Structure of the Phase II Mg<sub>2</sub>Al<sub>3</sub>. *Acta Cryst.*, Volume 19, pp. 401-413.
- Sanderson, A., Punshon, C. S. & Russell, J. D., 2000. Advanced welding processes for fusion reactor fabrication. *Fusion Engineering and Design*, p. 77–87.



- Santos, T. G., Vilac, a, P. & Miranda, R. M., 2011. Electrical conductivity field analysis for evaluation of FSW joints in AA6013 and AA7075 alloys. *Journal of Materials Processing Technology* 211, p. 174–180.
- Sato, Y. S. et al., 2010. Effect of interfacial microstructure on lap shear strength of friction stir spot weld of aluminium alloy to magnesium alloy. *Science and Technology of Welding and Joining*, 15(4), pp. 319-324.
- Saunders, N., 1990. A Review and Thermodynamic Assessment of The Al-P& and Mg-Li systems. *CALPHAD*, 14(1), pp. 61-70.
- Schmidt, H. B. & Hattel, J. H., 2008. Thermal modelling of friction stir welding. *Scripta Materialia*, Volume 58, p. 332–337.
- Schumann, S. & Friedrich, H., 2006. Engineering Requirements, Strategies and Examples: Automotive Applications in Europe. In: H. E. Friedrich & B. L. Mordike, eds. *Magnesium Technology: Metallurgy, Design Data, Applications*. Berlin Heidelberg: Springer-Verlag, pp. 499-569.
- Schurmann, E. & Voss, H. J., 1981. Untersuchung der Schmelzgleichgewichte von Magnesium-Lithium-. *Giessereiforschung*, Volume 33, pp. 43-46.
- Sha, G., Marceau, R. K. & Ringer, S. P., 2011. Precipitation and solute clustering in aluminium: advanced characterisation techniques. In: R. Lumley, ed. *Fundamentals of aluminium metallurgy Production, processing and applications*. Cambridge: Woodhead Publishing Limited, pp. 345-366.
- Shen, J., Min, D. & Wang, D., 2011. Effects of heating process on the microstructures and tensile properties of friction stir spot welded AZ31 magnesium alloy plates. *Materials and Design*, Volume 32, p. 5033–5037.
- Shen, Z. et al., 2015. Influence of processing parameters on microstructure and mechanical performance of refill friction stir spot welded 7075-T6 aluminium alloy. *Science and Technology of Welding and Joining*, 20(1), pp. 48-57.
- Shen, Z. et al., 2014. Microstructure and mechanical properties of friction spot welded 6061-T4 aluminum alloy. *Materials and Design*, Volume 54, p. 766–778.
- Shen, Z. et al., 2013. Microstructure and failure mechanisms of refill friction stir spot welded 7075-T6 aluminum alloy joints. *Materials and Design*, Volume 44, p. 476–486.
- Shercliff, H. R. & Colegrove, P. A., 2007. Process Modeling. In: R. S. Mishra & M. W. Mahoney, eds. *Friction Stir Welding and Processing*. Ohio: ASM International, pp. 187-217.
- Shivaraj, K. M., Dinakaran, V. & Mahadevan, V., 2011. *Frictional Stir Welding on Aluminum Alloys AA2024-T4 and AA7075-T6*. s.l., IEEE Xplore, pp. 1-5.
- Silcock, J. M., Heal, T. J. & Hardy, H. K., 1954. Structural Ageing Characteristics of Binary Aluminium-Copper Alloys. *J. Inst. Metals*, Volume 82, pp. 239-248.
- Singh, R., 2016. *Applied Welding Engineering: Processes, Codes, and Standards*. 2nd ed. s.l.:Elsevier.

- Singh, R. et al., 2011. The microstructure and mechanical properties of friction stir welded Al–Zn–Mg alloy in as welded and heat treated conditions. *Materials and Design* 32, p. 682–687.
- Smallman, R. E. & Ngan, A. H. W., 2014. *Modern Physical Metallurgy*. Eighth ed. Oxford: Elsevier Ltd.
- Solomon, S., Plattner, G.-K., Knutti, R. & Friedlingstein, P., 2009. Irreversible climate change due to carbon dioxide emissions. *PNAS*, 106(6), p. 1704–1709.
- Sooriyamoorthy, E., John Henry, S. P. & Kalakkath, P., 2011. Experimental studies on optimization of process parameters and finite element analysis of temperature and stress distribution on joining of Al–Al and Al–Al<sub>2</sub>O<sub>3</sub> using ultrasonic welding. *Int J Adv Manuf Technol*, Volume 55, p. 631–640.
- Su, H. L. et al., 1997. Experimental Investigation of the Mg-Al Phase diagram from 47 to 63 at.% Al. *Journal of Alloys and Compounds*, Volume 217, pp. 57-65.
- Suhuddin, U. F., Fischer, V. & dos Santos, J. F., 2013 a. The thermal cycle during the dissimilar friction spot welding of aluminium and magnesium alloy. *Scripta Materialia*, Volume 68, p. 87–90.
- Suhuddin, U. F., Fischer, V. & dos Santos, J. F., 2013 a. The thermal cycle during the dissimilar friction spot welding of aluminium and magnesium alloy. *Scripta Materialia*, Volume 68, p. 87–90.
- Suhuddin, U. F., Fischer, V. & dos Santos, J. F., 2013. The thermal cycle during the dissimilar friction spot welding of aluminium and magnesium alloy. *Scripta Materialia*, Volume 68, p. 87–90.
- Suhuddin, U., Fischer, V. & dos Santos, J., 2013 b. Formation of Intermetallic Compounds in Dissimilar Friction Spot Weld of Al to Mg Alloys. *Materials Science Forum*, Volume 765, pp. 731-735.
- Suhuddin, U., Fischer, V., Kroeff, F. & dos Santos, J. F., 2014. Microstructure and mechanical properties of friction spot welds of dissimilar AA5754 Al and AZ31 Mg alloys. *Materials Science & Engineering A*, Volume 590(, p. 384–389.
- Suhuddin, U., Fischer, V. & Santos, J. d., 2013 b. Formation of Intermetallic Compounds in Dissimilar Friction Spot Weld of Al to Mg Alloys. *Materials Science Forum*, Volume 765, pp. 731-735.
- Suhuddin, U., Kroeff, F. & dos Santos, J. F., 2011. *Dissimilar Friction Spot Welding of Al/Mg Alloys*. Manchester, UK, Challenges for Joining Lightweight Dissimilar Materials for Automotive Applications Conference.
- Sun, Y. F., Fujii, H., Takaki, N. & Okitsu, Y., 2013. Microstructure and mechanical properties of dissimilar Al alloy /steel joints prepared by a flat spot friction stir welding technique. *Materials and Design*, Volume 47, p. 350–357.
- Su, P., Gerlich, A., North, T. H. & Bendzsak, G. J., 2006 b. Material flow during friction stir spot welding. *Science and Technology of Welding and Joining*, 11(1), pp. 61-71.

Su, P., Gerlich, A., North, T. H. & Bendzsak, G. J., 2006a. Energy utilisation and generation during friction stir spot welding. *Science and Technology of Welding & Joining*, March, 11(2), pp. 163-169.

Su, P., Gerlich, A., North, T. H. & Bendzsak, G. J., 2007. Intermixing in Dissimilar Friction Stir Spot Welds. *Metallurgical and Materials Transactions A*, March, 38(A), pp. 584-595.

T&E, 2007. *Reducing CO2 emissions from new cars, 2006 progress report on the car industry's voluntary commitment*, s.l.: European Federation for Transport and Environment.

T&E, 2008. *CO2 Emissions from New Cars, Position paper in response to the European Commission proposal*, s.l.: T&E – European Federation for Transport and Environment AiSBL.

Thomas, W. et al., 1991. Friction stir butt welding. *GB Patent No. 9125978.8, International Patent No. PCT/GB92/02203.*

Thoppu, S. D. & Gibson, R. F., 2009. Mechanical characterization of spot friction stir welded joints in aluminum alloys by combined experimental/numerical approaches, Part I: Micromechanical studies. *Materials Characterization*, Volume 60, p. 1342–1351.

Tier, M. D. et al., 2013. The influence of refill FSSW parameters on the microstructure and shear strength of 5042 aluminium welds. *Journal of Materials Processing Technology*, Volume 213, p. 997– 1005.

Tolle, C. R. et al., 2008. *Experimental Investigation of Material Flows Within FSWs Using 3D Tomography*. Idaho Falls, Idaho, USA, Idaho National Laboratory.

Tozaki, Y., Uematsu, Y. & Tokaji, K., 2007. Effect of processing parameters on static strength of dissimilar friction stir spot welds between different aluminium alloys. *Fatigue Fract Engng Mater Struct*, Volume 30, p. 143–148.

Tozaki, Y., Uematsu, Y. & Tokaji, K., 2010. A newly developed tool without probe for friction stir spot welding and its performance. *Journal of Materials Processing Technology*, Volume 210, p. 844–851.

Tran, V. -X., Pan, J. & Pan, T., 2008. Fatigue behavior of aluminum 5754-O and 6111-T4 spot friction welds in lap-shear specimens. *International Journal of Fatigue*, Volume 30, p. 2175–2190.

Tran, V.-X., Pan, J. & Pan, T., 2009. Effects of processing time on strengths and failure modes of dissimilar spot friction welds between aluminium 5754-O and 7075-T6 sheets. *journal of materials processing technology*, Volume 209, p. 3724–3739.

TWI Ltd., 2016. *TwI-global.com*. [Online]  
Available at: <http://www.twi-global.com/capabilities/joining-technologies/friction-processes/friction-stir-welding/benefits-and-advantages/>  
[Accessed 12 April 2016].

Uematsu, Y. & Tokaji, K., 2009. Comparison of fatigue behaviour between resistance spot and friction stir spot welded aluminium alloy sheets. *Science and Technology of Welding and Joining*, 14(1), pp. 62-71.

- Uematsu, Y. et al., 2008. Effect of re-filling probe hole on tensile failure and fatigue behaviour of friction stir spot welded joints in Al–Mg–Si alloy. *International Journal of Fatigue*, Volume 30, p. 1956–1966.
- Uematsu, Y. et al., 2009. Effect of post-heat treatment on the fatigue behaviour of a friction stir spot-welded Al–Mg–Si alloy. *Welding International*, Volume 23:7, pp. 481–489.
- Verastegui, R. N., Mazzaferro, J. A. E., Mazzaferro, C. C. P. & Strohaecker, T. R., 2015. Welding of Aluminum to DP600 Steel Plates by Refill Friction Stir Spot Welding Process (Refill FSSW): Preliminary Results. *Advanced Materials Research*, Volume 1082, pp. 123–132.
- Villars, P., 2014.  $\epsilon$ -Al30Mg23 (Mg23Al30 ht) *Crystal Structure*, Vitznau, Switzerland: SpringerMaterials.
- Voutou, B. & Stefanaki, E. C., 2008. Electron Microscopy: The Basics. *Physics of Advanced Materials Winter School*, pp. 1–11.
- Wang, X. et al., 2003. Precipitation Strengthening of the Aluminum Alloy AA6111. *Metallurgical and Materials Transactions A*, December , 34(A), pp. 2913– 2924.
- Watt., I. M., 1997. *The Principles and Practice of Electron Microscopy*.. 2nd ed. Cambridge: Cambridge University Press.
- Weatherly, G. C. et al., 2001. The Precipitation of the Q Phase in an AA6111 Alloy. *Metallurgical and Materials Transactions A*, February, 32(A), p. 214— 218.
- Wei, Y. et al., 2012. Microstructures and mechanical properties of magnesium alloy and stainless steel weld-joint made by friction stir lap welding. *Materials and Design* 33, p. 111–114.
- Wirth, R., 2009. Focused Ion Beam (FIB) combined with SEM and TEM: Advanced analytical tools for studies of chemical composition, microstructure and crystal structure in geomaterials on a nanometre scale. *Chemical Geology*, Volume 261, p. 217–229.
- Wolnya, J., Kozakowski, B., Duda, M. & Kusz, J., 2008. Stacking of hexagonal layers in the structure of B-Mg2Al3. *Philosophical Magazine Letters*, 88(7), p. 501–507.
- Woo, W. et al., 2007. In situ neutron diffraction measurements of temperature and stresses during friction stir welding of 6061-T6 aluminium alloy. *Science and Technology of Welding & Joining*, May, 12(4), pp. 298–303.
- Yang, H. G. & Yang, H. J., 2013. Experimental Investigation on Refill Friction Stir Spot Welding Process of Aluminum Alloys. *Applied Mechanics and Materials*, Volume 345, pp. 243–246.
- Yang, Q., Mironov, S., Sato, Y. S. & Okamoto, K., 2010. Material flow during friction stir spot welding. *Materials Science and Engineering A*, Volume 527, p. 4389–4398.
- Yang, Y. S. & Lee, S. H., 1999. A study on the joining strength of laser spot welding for automotive applications. *Journal of Materials Processing Technology*, Volume 94, pp. 151–156.

- Yazdanian, S., Chen, Z. W. & Littlefair, G., 2012. Effects of friction stir lap welding parameters on weld features on advancing side and fracture strength of AA6060-T5 welds. *J Materials Sci*, p. 1251–1261.
- Yuan, W. et al., 2012. Material flow and microstructural evolution during friction stir spot welding of AZ31 magnesium alloy. *Materials Science and Engineering A*, Volume 543, p. 200– 209.
- Yuan, W. et al., 2012. Material flow and microstructural evolution during friction stir spot welding of AZ31 magnesium alloy. *Materials Science and Engineering A*, Volume 543, p. 200– 209.
- Yuan, W. et al., 2011. Effect of tool design and process parameters on properties of Al alloy 6016 friction stir spot welds. *Journal of Materials Processing Technology*, Volume 211, p. 972–977.
- Zhang, C. Q., Robson, J. D., Ciuca, O. & Prangnell, P. B., 2014. Microstructural characterization and mechanical properties of high power ultrasonic spot welded aluminum alloy AA6111–TiAl6V4 dissimilar joints. *Materials Characterization*, Volume 97, p. 83–91.
- Zhang, D., Suzuki, M. & Maruyama, K., 2005. Microstructural evolution of a heat-resistant magnesium alloy due to friction stir welding. *Scripta Mater*, p. 899–903.
- Zhang, H. T. & Song, J. Q., 2011. Microstructural evolution of aluminum/magnesium lap joints welded using MIG process with zinc foil as an interlayer. *Materials Letters*, Volume 65, p. 3292–3294.
- Zhang, M. -X., Huang, H., Spencer , K. & Shi, Y. -N., 2010. Nanomechanics of Mg–Al intermetallic compounds. *Surface & Coatings Technology*, Volume 204, p. 2118–2122.
- Zhao, H., White, D. R. & DebRoy, T., 1999. Current issues and problems in laser welding of automotive aluminium alloys. *International Materials Reviews*, 44(6), pp. 238-266.
- Zhao, Y. et al., 2016. Study of temperature and material flow during friction spot welding of 7B04-T74 aluminum alloy. *Int J Adv Manuf Technol*, 83(9), pp. 1467-1475.
- Zhong, Y., Yang, M. & Liu, Z.-K., 2005. Contribution of first-principles energetics to Al–Mg thermodynamic modeling. *Computer Coupling of Phase Diagrams and Thermochemistry*, Volume 29, p. 303–311.
- Zhou, W., Apkarian, R. P., Wang, Z. L. & Joy, D., 2007. Fundamentals of Scanning Electron Microscopy. In: W. Zhou & Z. L. Wang, eds. *Scanning Microscopy for Nanotechnology*. New York: Springer, pp. 1-40.
- Zuo, Y. & Chang, Y. A., 1993. Thermodynamic Calculation of the Al-Mg Phase Diagram. *Calphad*, 17(2), pp. 161-174.